

# Mechanochemically synthesised metal-organic frameworks as nanovehicles for drug delivery

PhD

School of Chemistry, Pharmacy, and Food

Jethro Beamish-Cook

January 2020

## Abstract

In recent years MOFs have attracted a lot of attention for their permanent porous properties. MOFs are traditionally synthesised using a solvothermal synthesis method, but a “green” synthesis method has recently emerged, mechanochemical synthesis, which can produce MOFs using a fraction of the solvent compared to solvothermally synthesised counterparts.

MOFs have the potential to revolutionise several fields, most notably gas-storage and catalysis. In this thesis the potential drug loading applications of MOFs which have been mechanochemically synthesised are explored.

Mechanochemical synthesis has been used to prepare MOF-74-Zn,  $Zn_2C_8O_6H_2$ , a porous metal-organic framework. Several novel crystalline intermediates,  $C_{14}H_{20}N_2O_8$ ,  $C_{14}H_{22}N_2O_{10}Zn(\alpha)$ ,  $C_{14}H_{22}N_2O_{10}Zn(\beta)$  were found to form during mechanochemical synthesis prior to MOF-74. Their structures have been characterised by powder and single-crystal X-ray diffraction. The properties of mechanochemically-synthesised MOF-74-Zn have been investigated using analytical, spectroscopic and powder X-ray diffraction methods to compare to conventionally synthesised MOF-74.

The potential of MOF-74-Zn as a vehicle for drug delivery applications has been investigated. Reported here is the drug loading and unloading of MOF-74-Zn with ibuprofen. The maximum ibuprofen loading of 0.29 g/g of ibuprofen per gram of MOF-74-Zn is reported and the ibuprofen-MOF interactions have been investigated using solid-state NMR (SS-NMR) and inelastic neutron spectroscopy (INS).

By adopting a similar synthetic approach to that used for MOF-74, a novel isorecticular framework based on MOF-74-Zn has been prepared (IR-MOF-74-Zn). This new

framework has the same topology and pore shape as MOF-74-Zn but is synthesised with a larger organic linker, 4,4'-oxalylbis(imino)]bis(2-hydroxybenzoic acid). The linker was used to produce a framework with significantly larger potential surface area than MOF-74 with estimated pore diameters of 22 Å. As with MOF-74, crystalline intermediates form during synthesis. Three IR-MOF-74-Zn intermediates have been found and partially characterised using X-ray diffraction methods.

The crystal structures of 2,5-dihydroxyterephthalic acid ( $C_8H_6O_6$ ) and its potassium salt ( $C_8H_6O_6K(H_2O)$ ) are also reported. Additionally, the crystal structure of the DMF solvate of 4,4'-oxalylbis(imino)]bis(2-hydroxybenzoic acid ( $C_{16}H_{12}N_2O_8(C_3H_7O)_2$ ) and its zinc paddlewheel coordination polymer, ( $Zn_2(C_2H_3O_2)_2C_{16}H_{12}N_2O_8(C_3H_7O)_2$ ), have also been characterised.

## **Acknowledgments**

I am extremely proud to have finished this PhD, which would have been entirely impossible without the support of my two supervisors, Kenneth Shankland and Paz Vaqueiro. I was incredibly lucky to find two supervisors who cared so much about my work and I can honestly say that there was no chance that this thesis would be anywhere near the quality it is without their guidance and corrections.

The work contained in this thesis would be incomplete without the help I received from people both inside and outside the university. I must thank Nick Spencer for maintaining the crystallography lab, Claire Murray for her help on DLS I11, and Sebastian Rochart for the experiments run as part of my research. Finally, I have to thank Radoslaw Kowalczyk for his help with collecting NMR data.

Throughout my time at the University of Reading, I have made a handful of extremely close friendships which I hope will last a lifetime. Alex, Will, Sam, Sandy, Tasha. I also hugely appreciate the support I received from the solid state materials group at the university from my cohorts. In particular I'm grateful to Sarah, John, and Seb.

I must thank give special thanks to my parents who nurtured me through my childhood and supported me through my undergraduate and doctoral years. Finally, I have to thank Lauren Moses for encouraging and supporting me through the long months of writing this thesis.

I would like to dedicate this thesis to my family and friends.



## **Declaration of original authorship**

Declaration: I confirm that this is my own work and the use of all material from other sources has been properly and fully acknowledged

Jethro Beamish-Cook

# Contents

Abstract.....	I
Acknowledgments .....	III
Declaration of original authorship .....	IV
1- Introduction .....	1
1.1 Background.....	1
1.2 Synthesis of MOFs.....	6
1.2.1 Mechanochemical synthesis .....	7
1.2.2 <i>In situ</i> mechanochemical reactions and their intermediates .....	8
1.3 Alternative synthesis methods .....	9
1.4 Applications of MOFs .....	11
1.4.1 MOFs as filters for heavy metals and radionuclides.....	11
1.4.2 MOFs for gas-storage .....	11
1.4.3 MOFs for drug delivery .....	12
1.5 Porous materials for drug delivery.....	21
1.5.1 Zeolites for drug delivery .....	21
1.5.2 Silicas and activated carbon for drug delivery.....	21
1.5.3 Polymers in drug delivery.....	21
1.6 Metal choice in MOF drug delivery .....	23
1.7 MOF-74 Family of frameworks.....	23
1.8 Aims of this work .....	28
2- Experimental Techniques .....	30

2.1 Introduction.....	30
2.1.1 Mechanochemical Synthesis.....	30
2.1.2 Activation and loading of frameworks .....	32
2.2 Thermogravimetric analysis .....	33
2.2.1 Experimental.....	33
2.3 Differential scanning calorimetry .....	34
Experimental.....	34
2.3 Elemental analysis .....	34
2.4 Spectroscopy.....	36
2.4 IR spectroscopy.....	36
2.5 UV-Vis spectroscopy.....	36
2.6 Inelastic neutron scattering .....	37
2.7 Optical Microscopy.....	37
2.8 Scanning electron microscopy .....	38
2.9 X-ray diffraction .....	38
2.9.1 Single-crystal X-ray diffraction.....	39
2.9.2 Powder X-ray Diffraction (PXRD).....	41
2.10 Particle-size analysis measurements.....	48
2.11 Nuclear Magnetic Resonance (NMR).....	49
2.11.1 Experimental.....	50
2.11.2 Solid-state NMR (SSNMR).....	50

2.12 BET gas sorption measurements.....	51
2.12.1 Experimental.....	52
Chapter 3- Mechanochemical synthesis and characterisation of MOF-74-Zn .....	53
3.1 Introduction.....	53
3.2 Experimental.....	56
3.2.1 Mechanochemical synthesis of MOF-74 using H <sub>2</sub> O .....	56
3.2.2 Mechanochemical synthesis of MOF-74 using DMF .....	56
3.2.3 Activation.....	57
3.2.4 MOF-74 stability in solvents .....	57
3.2.5 PXRD.....	58
3.2.6 Elemental analysis .....	58
3.2.7 IR spectroscopy.....	58
3.2.8 Gas adsorption measurements .....	58
3.2.9 Size distribution measurements .....	58
3.2.10 SEM of activated MOF-74-Zn sample .....	59
3.2.11 Investigation of the reaction mechanism .....	59
3.3 Results.....	63
3.3.1 Mechanochemical synthesis using water or DMF .....	63
3.3.2 Characterisation of MOF-74 prepared using DMF.....	64
3.3.3 Optimised MOF-74-Zn synthesis using DMF as milling solvent.....	65
3.3.4 Activation of MOF-74-Zn .....	72

3.3.5 Stability of MOF-74.....	79
3.3.5.1 Methanol .....	81
3.3.6 Particle size of synthesised MOF-74-Zn samples.....	85
3.3.7 MOF-74-Zn reaction intermediates .....	87
3.3.8 Rietveld refinements of intermediates to calculate QPS .....	100
3.4 Discussion.....	102
3.4.1 mechanochemical synthesis and properties of MOF-74-Zn .....	102
3.4.2 intermediates formed in the mechanochemical synthesis of MOF-74-Zn...	103
3.5 Conclusion .....	106
Chapter 4- Loading ibuprofen into MOF-74-Zn.....	107
4.1 Introduction.....	107
4.2 Experimental.....	109
4.2.1 MOF-74 synthesis.....	109
4.2.2 MOF-74-Zn ibuprofen loading .....	109
4.2.3 Preparation of phosphate buffer solution.....	109
4.2.4 UV-Vis calibration curves .....	109
4.2.5 Unloading ibuprofen from MOF-74-Zn in phosphate buffer .....	110
4.2.6 Analysis of ibuprofen loaded MOF-74-Zn sample.....	111
4.3 Results.....	113
4.3.1 MOF-74 ibuprofen loading.....	113
4.3.2 CHN .....	117

4.3.3 IR spectra of loaded sample.....	118
4.3.4 INS of loaded MOF-74 samples .....	120
4.3.5 PXRD of loaded sample .....	124
4.3.6 SS-NMR of loaded and blank sample.....	126
4.3.7 DSC of loaded sample .....	127
4.3.8 SEM of loaded samples .....	129
4.4 Discussion.....	130
4.4.1 understanding ibuprofen loading in MOF-74 .....	130
4.4.2 MOF-74 family ibuprofen loading comparison.....	131
4.4.3 Further work and drug release experiments.....	132
4.5 Conclusion .....	134
Chapter 5- Mechanochemical synthesis and characterisation of an isoreticular MOF-74 framework.....	135
5.1 Introduction.....	135
5.2 Experimental.....	137
5.2.1 Synthesis of H <sub>4</sub> ODA.....	137
5.2.2 Synthesis of IR-MOF-74-Zn.....	138
5.2.3 Stability of IR-MOF-74-Zn in solvents .....	139
5.2.4 Attempted activation of IR-MOF-74-Zn .....	140
5.2.5 In-situ monitoring of IR-MOF-74-Zn synthesis .....	140
5.3 Results.....	142
5.3.1 Characterisation of the H <sub>4</sub> ODA linker.....	142

5.3.2 Synthesis of IR-MOF-74-Zn.....	148
5.3.3 Attempts to solve IR-MOF-74-Zn crystal structure .....	158
5.3.4 Stability of IR-MOF-74-Zn in solvents .....	160
5.3.5 Attempted Activation of IR-MOF-74-Zn .....	167
5.3.6 In-Situ monitoring of IR-MOF-74-Zn synthesis .....	168
5.4 Discussion.....	177
5.4.1 Discussion on the synthesis of IR-MOF-74-Zn.....	177
5.4.2 IR-MOF-74-Zn intermediates.....	178
5.5 Further work .....	180
5.6 Conclusion .....	181
Chapter 6- Miscellaneous crystal structures containing MOF linkers.....	182
6.1 Introduction.....	182
6.2 Experimental.....	183
6.2.1 Structure solution of H <sub>4</sub> DHTA .....	183
6.2.2 Structure solution of KH <sub>3</sub> DHTA·(H <sub>2</sub> O).....	183
6.2.3 Synthesis and Structure solution of Zn <sub>2</sub> H <sub>2</sub> ODA·DMF <sub>2</sub> (H <sub>2</sub> O) <sub>2</sub> .....	183
6.2.4 Synthesis of H <sub>4</sub> TDA .....	184
6.3 Results.....	186
6.3.1 H <sub>4</sub> DHTA .....	186
6.3.2 KH <sub>3</sub> DHTA(H <sub>2</sub> O) .....	194
6.3.3 ZnAcH <sub>2</sub> ODA(DMF) .....	202

6.3.4 H <sub>4</sub> TDA(DMF).....	211
6.4 Discussion.....	214
6.4.1 H <sub>4</sub> DHTA and KH <sub>3</sub> DHTA(H <sub>2</sub> O) .....	214
6.4.2 Zn <sub>2</sub> Ac <sub>2</sub> H <sub>2</sub> ODA(DMF) <sub>2</sub> .....	214
6.4.3 H <sub>4</sub> TDA(DMF).....	215
6.5 Conclusion .....	216
6.5.1 Structures of H <sub>4</sub> DHTA and KH <sub>3</sub> DHTA(H <sub>2</sub> O).....	216
6.5.2 Zn <sub>2</sub> Ac <sub>2</sub> H <sub>2</sub> ODA(DMF) <sub>2</sub> .....	216
Chapter 7- Conclusions and further work.....	218
7.1 Conclusions.....	218
7.2 Future work.....	221
References.....	i

CIF files of solved structures are given in Appendix which is found on the accompanying SD card to this thesis.



# 1- Introduction

## 1.1 Background

Over the last 25 years there has been much interest in the field of porous materials research, specifically in the class of compounds known as metal-organic frameworks or MOFs. Before MOFs, porous material research was focussed on activated carbons and zeolites.<sup>1</sup> Since interest increased dramatically in the late 1990s porous materials' research has been dominated by MOFs. As illustrated by Figure 1, the number of MOF structures published yearly exploded from 1990 to 2010. In the past, MOFs were called multiple names, including porous coordination polymers (PCP),<sup>2</sup> but the term MOF has been broadly adopted.

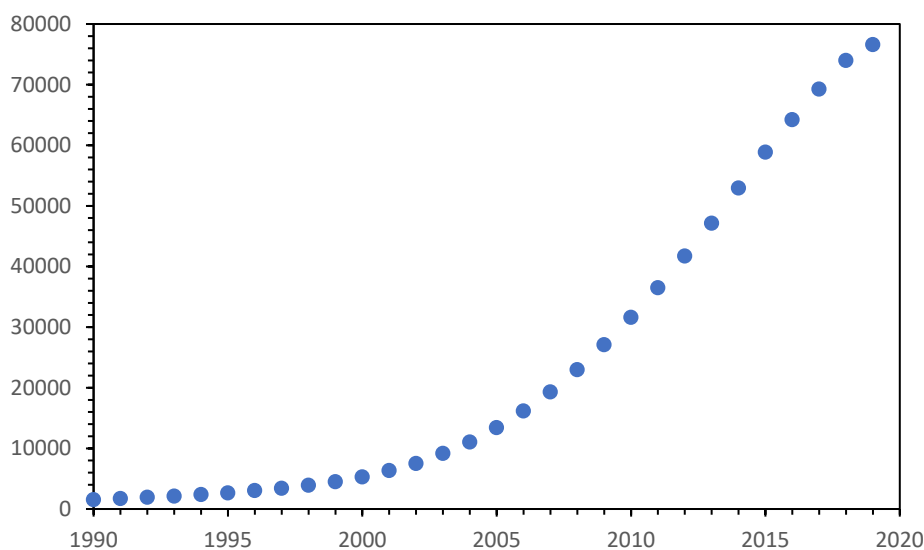


Figure 1 Number of MOF structures reported each year from 1970 to 2010. Source CCDC CSD.<sup>3</sup>

A MOF is constructed from metal-ions which act as nodes and organic ligands which act as bridges between nodes (Figure 2). This node and bridge connection can result in extended structures with a range of dimensionalities. A subset of MOFs have the potential to exhibit permanent porosity and large surface areas, which is the primary reason for the interest in the field.

The most important historical MOFs are those with very large surface areas; **MOF-5**,<sup>4</sup> **BioMOF-100**,<sup>5</sup> **HKUST-1**,<sup>6</sup> **MIL-100**,<sup>7</sup> and **UIO-66** <sup>8</sup> are well known examples. The largest reported surface area for a MOF is **DUT-60** <sup>9</sup> which has a surface area exceeding 7800 m<sup>2</sup> g<sup>-1</sup>.

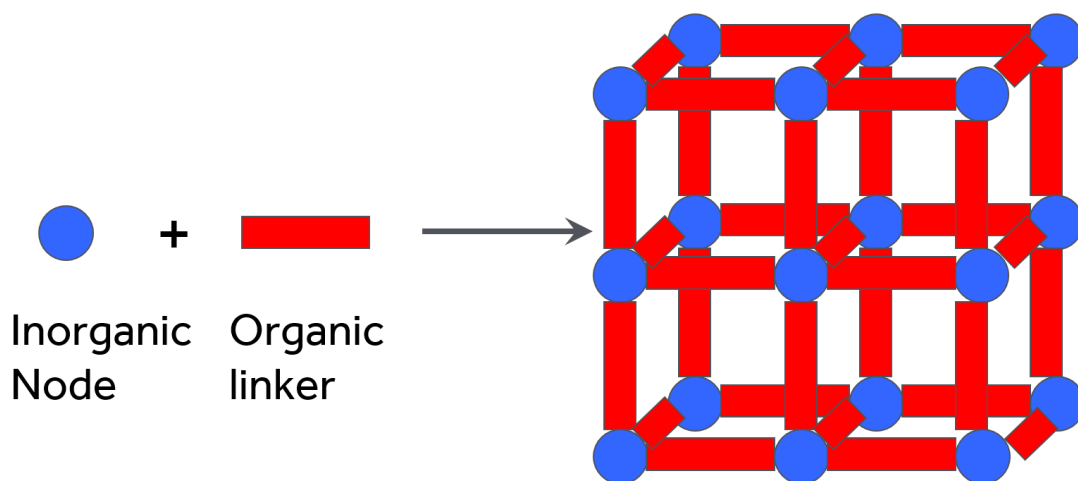


Figure 2 Schematic representation of a MOF.

MOFs nodes can be constructed from almost all cations, including all transition metals, and, when the possible variation in organic linkers is taken into account, an almost infinite number of MOFs can be generated. Linkers are primarily comprised of two categories: O donors and N donors. O donor linkers are most commonly polycarboxylic acid and alcohol groups. The most common N donor linkers have cyanide, pyridine, and imidazole groups. The combination of metal node choice, linker donor group, and linker geometry can produce a huge range of MOFs with differing properties. MOFs properties can be further tuned using post synthetic modification to functionalise organic linkers to further suit target applications.<sup>10</sup>

The inorganic nodes in MOFs can be single metal atoms with whichever coordination complexes are available to a metal; for example zinc commonly forms tetrahedral and octahedral complexes.<sup>11, 12</sup> In addition to single metal inorganic nodes, metal clusters can also form inorganic nodes; these are known as secondary building units (SBUs). An SBU is the spatial arrangement of multiple metal atoms coordinated to organic linkers to form metal clusters (Figure 3). The most common SBU is the paddlewheel (Figure 3a) which is a metal dimer connected by carboxylic groups, most commonly forming in synthesis using metal acetate sources. SBUs add further complexity to metal choice as both single metal choice and possible secondary building units need to be considered when designing a target framework. The example SBU (Figure 3) the “paddlewheel” is produced most notably by  $\text{Cu}^{2+}$  but also forms in  $\text{Zn}^{2+}$  and  $\text{Fe}^{2+}$  environments.<sup>13-15</sup>

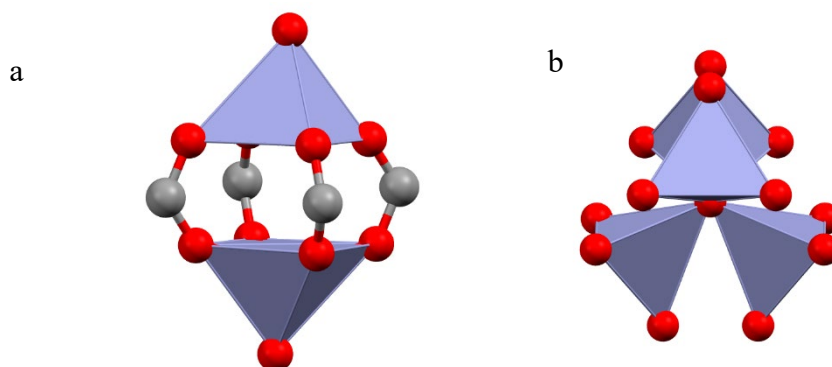


Figure 3 Two examples of common secondary building units found in MOFs . Figure 3a zinc paddlewheel SBU. Figure 3b edge-sharing tetrahedral zinc coordination. Elements: carbon (grey), oxygen (red), zinc (blue polyhedra).

The combination of organic linker properties and inorganic nodes coordination produce MOFs with specific spatial arrangements; the 3D structure of a MOF is more commonly known as a MOF topology. Using SBUs a whole new series of MOFs can be produced which have the same topology but different linker properties. A good example is the **IR-MOF-5** series created by Yaghi *et al.*, which produced frameworks of increasing linker length and surface area (Figure 4).<sup>16</sup>

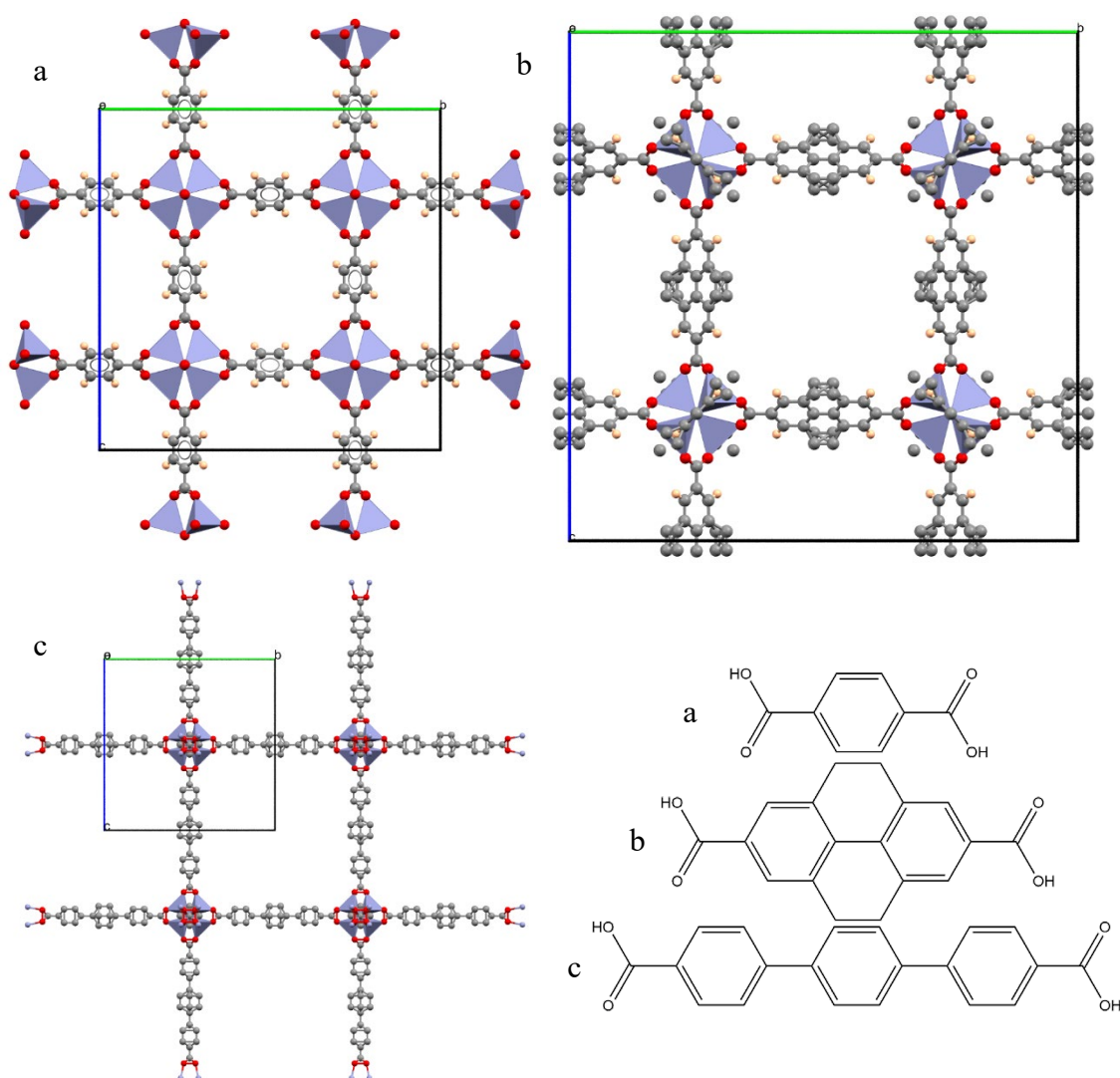
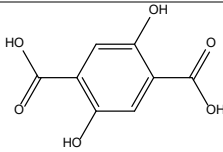
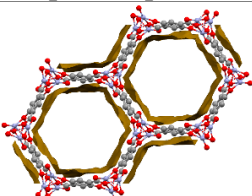
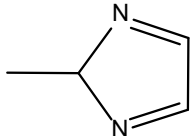
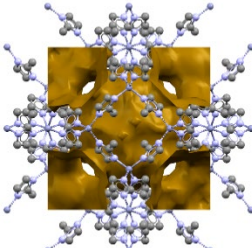
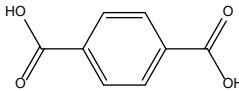
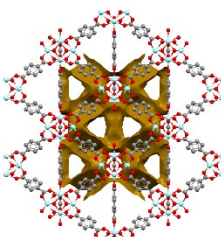
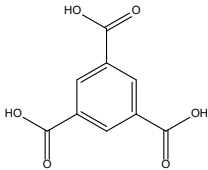
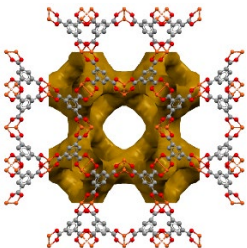
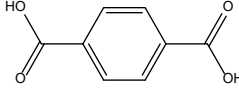
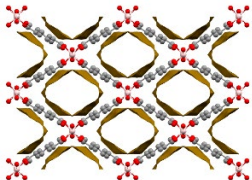
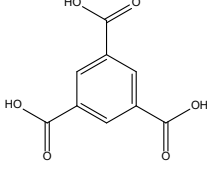
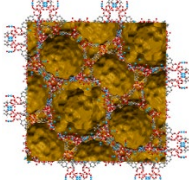


Figure 4 MOF-5 demonstrates ability to form isorecticular frameworks, each framework has the same topology, but pore size increases with linker length. Figure 4a MOF-5 packed and viewed down crystallographic  $a$ -axis.<sup>17</sup> Figure 4b IRMOF-5 packed and viewed down crystallographic  $a$ -axis.<sup>16</sup> Figure 4c IR-2MOF-5 packed and viewed down crystallographic  $a$ -axis.<sup>16</sup> Sketches at bottom right correspond to linkers used to synthesise frameworks. Elements Present: carbon (grey), oxygen (red), blue polyhedra (zinc).

Shown in Table 1 are the six most researched MOFs together with their theoretical BET surface areas. Surface area and pore shape is often used when considering which of the MOFs to use for a purpose, though other factors go into account for other applications; for example, linker and metal toxicity is a consideration for drug delivery applications.

Table 1 List of the most common MOFs including the linker used in synthesis and theoretical Chem BET surface area. Accessible surface area of the MOFs are shown as yellow surfaces. Accessible surfaces calculated using Mercury void space calculation.<sup>18</sup>

MOF	Linker sketch	View of pore & pore shape	surface area (m <sup>2</sup> g <sup>-1</sup> )
<b>MOF-74</b> <sup>19</sup>		 Hexagonal channels	1360 <sup>20</sup>
<b>ZIF-8</b> <sup>21</sup>		 Interconnected pores	1813 <sup>22</sup>
<b>UiO-66</b> <sup>8</sup>		 Triangular channels	1067 <sup>23</sup>
<b>HKUST-1</b> <sup>24</sup> <b>Fe-BTC</b> <sup>25</sup>		 Interconnected pores	1635 <sup>26</sup> 1600
<b>MIL-53</b> <sup>27-29</sup>		 Square channels	1946 <sup>30</sup>
<b>MIL-100</b> <sup>31</sup>		 Interconnected pores	2006 <sup>32</sup>

## 1.2 Synthesis of MOFs

Solvothermal synthesis is the most common synthesis method for producing MOFs. It is widely used as a synthetic method as it enables the synthesis of many otherwise unproducible products.<sup>33</sup> Solvothermal synthesis uses modest pressure (between 1 and 3 mPa) and high temperature (between 60 and 240 °C) to form products. In a standard solvothermal synthesis procedure, small quantities of reactants are dissolved in polar solvents such as water, DMF, and alcohols. The reactants are sealed in Teflon lined stainless steel autoclaves (Figure 5) and heated; typically for several days. The heating rate, max temperature, time at max temperature, and cooling rate all affect the products produced.

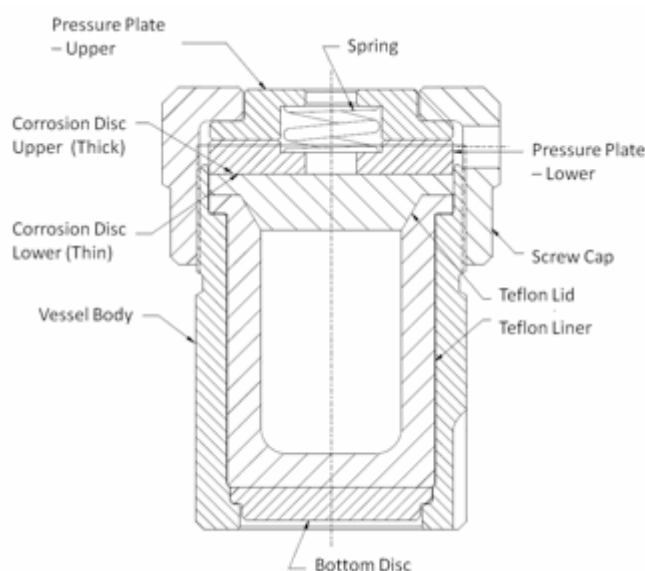


Figure 5 Schematic diagram of a Teflon lined autoclave used in solvothermal synthesis. Source: Oregon State University autoclave training course<sup>34</sup>

Solvothermal synthesis methods are very wasteful and difficult to take to industrial scale compared to alternative synthesis methods. It is quite common for 15 mL of solvent to be used to make only 100- 500 mg of product. For MOFs specifically, in recent years a range of alternative synthesis methods have been found including microwave synthesis,<sup>35</sup> room-temperature synthesis methods,<sup>36</sup> and mechanochemical synthesis methods.<sup>37</sup>

### 1.2.1 Mechanochemical synthesis

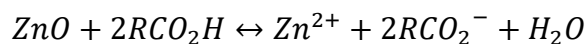
Mechanochemical synthesis is the use of mechanical force to stimulate chemical reactions. Mechanochemical synthesis is defined as a chemical reaction that is induced by the direct absorption of mechanical energy.<sup>38</sup> Mechanical energy manifests in several ways including: stress-strain effects, shear forces, friction, and cavitation effects. Unfortunately, the exact reaction mechanisms involved for many mechanochemical reactions are poorly understood.

It is widely accepted that the mechanism a mechanochemical reaction will follow is different from its corresponding thermal or photosynthetic reaction. Due to the differences in reaction pathways, materials can be produced very efficiently using mechanochemical synthesis.

A very common concept in mechanochemical synthesis is the addition of small volumes of solvent; this is known as liquid assisted grinding (LAG), and has been shown to change reaction intermediates and result in different products.<sup>39</sup> There are examples of reactions taking much longer to complete without solvent addition, or cases where target products do not form at all<sup>40</sup> when solvent is not added.

Mechanochemical reactions are most commonly carried out at room-temperature. It has recently been demonstrated that the temperature of both the starting materials and the milling jar can significantly influence the rates of mechanochemical reactions.<sup>41</sup> Temperature, starting material stoichiometry, solvent volume, reaction time, jar size, rate of vibration/rotation, and the number / mass of milling balls all have the potential to affect the resulting products. This means that a systematic approach to reaction optimisation is often the most appropriate.

All mechanochemical reactions discussed in this work involve the deprotonation of carboxylic acids. Zinc oxide reacts with carboxylic acids to produce coordination products, along with water as a by-product. The formation of water hydrates the reaction mixture, which pushes the reaction equilibria toward products.<sup>42</sup>



### 1.2.2 *In situ* mechanochemical reactions and their intermediates

A benefit of mechanochemical reactions is the ability to “pause” a reaction, at which point various analytical techniques can be carried out on the reaction mixture. This allows for *in situ* studying of the reaction with reaction progress monitored by analytical techniques.<sup>43</sup> The two most common techniques used to monitor reactions are: Raman spectroscopy<sup>44, 45</sup> and powder X-ray diffraction.<sup>42</sup> Raman spectroscopy allows for monitoring change in functional groups throughout a reaction; PXRD is used to study the crystalline intermediates and will be a focus of the mechanochemical reactions studied in this thesis.

Throughout mechanochemical reactions crystalline intermediates can, and often do, form. The phenomenon is widely reported in all fields of mechanochemical synthesis.<sup>46</sup> Working out the chemical composition of these intermediates is rather challenging; in the best case, the intermediate will correspond to an already solved crystal structure. These solved crystal structures can be searched through use of crystal structure databases, such as the CCDC CSD<sup>3</sup> and the ICSD.<sup>47</sup> Rietveld refinement can then be performed using the reported crystal structures. In the worst-case scenario, structure solution from PXRD is necessary and is considerably more complicated (see Section 2.9.2.2).



### 1.3 Alternative synthesis methods

In addition to mechanochemical synthesis and solvothermal synthesis several other synthetic routes have been reported. In particular, flow chemistry synthesis methods are the next most promising after mechanochemical and solvothermal methods. This synthesis method uses high-pressure heated coils, and a mixture of starting materials is pushed continuously through the coils to synthesise a MOF (Figure 6). Flow synthesis methods allow for high-throughput production of crystalline MOFs with controlled particles sizes. So far, the synthesis of several well-known MOFs have been reported, including **HKUST-1**,<sup>48</sup> **UiO-66**,<sup>49</sup> and **MIL-53**.<sup>50</sup>

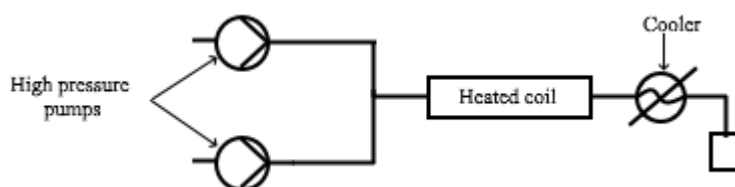


Figure 6 Simplified schematic of flow reaction used for continuous flow MOF synthesis method.

The final method worth mentioning is microwave synthesis.<sup>51</sup> Microwave synthesis is defined as the use of microwave radiation to heat reaction mixtures which produces chemical reactions.<sup>52</sup> Over the last few years, microwave synthesis has garnered a fair amount of academic interest as an alternative MOF synthesis method. The key benefit of microwave synthesis is the greatly reduced reaction times compared to solvothermal synthesis methods, taking reaction times of hours down to minutes. Microwave synthesis has been successful in synthesising several well-known MOFs including: **UiO-66**,<sup>53</sup> **MIL-101**,<sup>54</sup> and **MOF-74-Ni**.<sup>55</sup> Unfortunately, microwave synthesis is difficult to scale-up for industrial synthesis as the penetrative power of microwaves is quite shallow.<sup>56</sup>

A good metric for judging where MOF industrial interest lies is looking at what MOFs can be purchased from chemical suppliers. Presented in Table 2 are the commercially available MOFs which can be purchased from a variety of suppliers; also included are the methods of synthesis. It is clear that for industrial scale, currently, electrochemical

synthesis and mechanochemical synthesis are preferable to solvothermal and microwave synthesis due to the ease of scaling.

Table 2 List of commercially available MOFs sorted by synthesis method. Sources: Sigma-Aldrich.<sup>57</sup> MOF technologies,<sup>58</sup> Strem Chemicals,<sup>59</sup> Promethean Particles.<sup>60</sup>

<b>Synthesis technique</b>	<b>Available MOF</b>	<b>Scale for purchase</b>
Electrochemical (Sigma Aldrich)	ZIF-8	10 g – 500 g
	MIL-53	10 g – 500 g
	HKUST-1	10 g – 500 g
	Fe-BTC	10 g – 500 g
	MOF-177	10 g – 500 g
Mechanochemistry (MOF technologies)	MOF-74	25 g – 1000 kg
	HKUST-1	25 g – 1000 kg
	MIL-53	25 g – 1000 kg
	ZIF-8	25 g – 1000 kg
Solvothermal (Strem)	MIL-100	500 mg – 2 g
	UiO-66	500 mg – 2 g
	ZIF-8	1 g – 5 g
Continuous flow (Promethean particles)	MIL-53	50 g – 1 kg
	ZIF-8	50 g – 1 kg
	MOF-74	50 g – 1 kg
	HKUST-1	50 g – 1 kg

## 1.4 Applications of MOFs

MOFs have great potential for a range of applications due to their large surface areas and useful chemical properties. In particular, catalysis, molecular separation, and storage have all received much academic attention due to the large potential surface areas. Other potential uses have been highlighted in recent years including MOFs in radio imaging applications,<sup>61</sup> magnetism,<sup>62</sup> and light-emission.<sup>63,64</sup> The area this thesis focuses on is the potential use of MOFs for drug delivery applications.

### 1.4.1 MOFs as filters for heavy metals and radionuclides

In recent years, a potential use for water-stable MOFs has arisen as a filter for heavy metals.<sup>65</sup> MOFs are excellent candidates for these applications due to their large surface areas and porosity which allow MOFs to capture contaminants in both water and air. Certain MOFs are also able to catalytically remove heavy metals from aqueous solutions due to electron transfer effects.<sup>66,67</sup> A number of well-known MOFs including **MIL-100**,<sup>68</sup> **UiO-66(NH<sub>2</sub>)**,<sup>69</sup> and **MIL-125**<sup>70</sup> can catalytically reduce Cr(VI) to Cr(III) in less than 60 minutes. Radionuclide capture is also very promising with MOFs capable of capturing a range of radioactive elements from solution including uranium,<sup>71</sup> selenium,<sup>72</sup> and thorium.<sup>73</sup>

### 1.4.2 MOFs for gas-storage

Due to their exceptionally high surface area and porosity, the majority of MOF research focuses on gas-storage applications. Gas-storage research focuses on two applications: the use of MOFs as storage for hydrogen fuel cells,<sup>74-77</sup> and using MOFs to capture CO<sub>2</sub><sup>78-81</sup> to reduce greenhouse gas emissions.

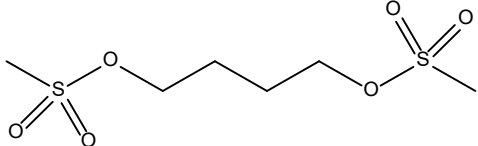
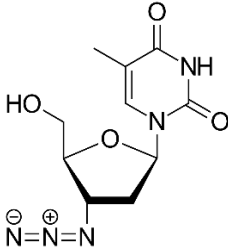
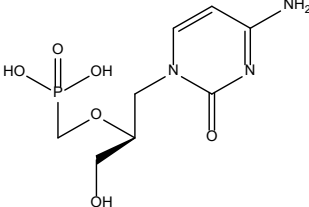
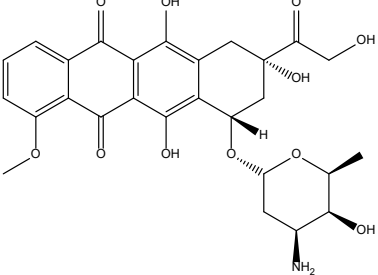
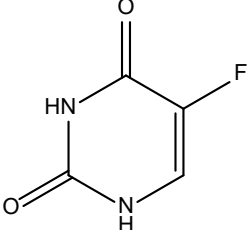
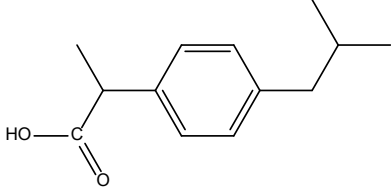
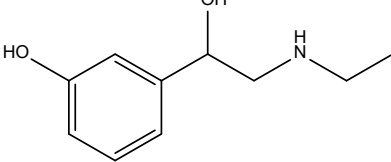
### **1.4.3 MOFs for drug delivery**

Most MOF research focuses on the pursuit of ever larger surface areas for gas-storage, but other potential applications for MOFs have been found. One potential application is the use of MOFs for drug delivery. MOFs could be used for drug delivery in two key areas. Firstly, many potential chemotherapy drugs cannot be directly administered for several reasons, including side effects, poor targeting, and poor body uptake.<sup>82</sup> Secondly, MOFs have the potential to give high drug loading with slow release meaning patients would need to take fewer doses of medication.<sup>83</sup> Due to their porosity and tuneability MOFs are ideal for these two applications.

Leveraging the porosity of MOFs for drug delivery applications has generated interest in recent years, with the simplest application involving the uptake and release of NO (see Section 1.4.3.3.); which can work for any framework with good CO<sub>2</sub> storage capacity. Zeolites have also been reported to be potential drug delivery candidates,<sup>84</sup> but due to their physical and chemical tuneability MOFs are more interesting candidates.

Table 3 presents the drugs that have been loaded into MOFs and their therapeutic applications.

Table 3 Drugs that have been loaded into frameworks, as discussed throughout Section 1.4.3.

Compound name	Molecular diagram	Application of drug
<b>Busulfan</b>		Anti-cancer
<b>Azidothymidine triphosphate</b>		HIV/AIDS medication
<b>Cidofovir</b>		HIV/AIDS medication
<b>Doxorubicin</b>		Chemotherapy
<b>5-Fluoruracil</b>		Chemotherapy
<b>Ibuprofen</b>		Pain relief
<b>Etilefrine</b>		Cardiac stimulant

#### 1.4.3.1 Using MOFs to encapsulate drug molecules

The current most common strategy for loading drugs into frameworks is via a post-synthetic modification method. In this method, MOFs are synthesised, activated (see Section 2.1.2), drugs are then incorporated into the framework via immersion in a concentrated drug solution. Table 4 shows a selection of existing drug loading studies using drug encapsulation techniques. Drug loading into MOFs is still in its infancy, so model drugs such as caffeine and ibuprofen are commonly used as model drugs as “proof of concept”. Reported studies of MOF drug loading studies suggest that MOFs perform competitively when compared with silica<sup>85</sup> and polymers<sup>86</sup> with “good” examples of drug loading percentages for MOFs around 20% (w/w) and in best cases towards 50% (weight of drug per weight of MOF).

Table 4 Representative examples of drug encapsulation using MOFs.

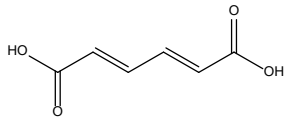
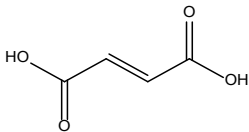
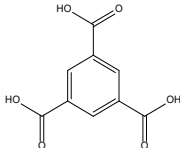
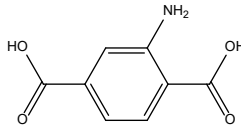
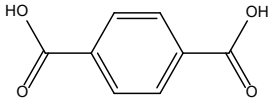
<b>MOF and inorganic node</b>	<b>Cargo</b>	<b>Maximum loading w/w (%)</b>	<b>Ref.</b>
<b>bioMOF-1 (Zn)</b>	Etilefrine	9	87
<b>bioMOF-100 (Zn)</b>	Etilefrine	10	87
<b>UiO-66 (Zr)</b>	Caffeine	22	88
<b>UiO-66 (Zr)</b>	5-Fluoruracil	1.5	89
<b>MIL-100 (Fe)</b>	Caffeine	50	88
<b>MOF-74 (Fe)</b>	Ibuprofen	21	90
<b>MOF-74 (Ni)</b>	Ibuprofen	25	91
<b>ZIF-8 (Zn)</b>	5-Fluorouracil	21.2	92

Three examples of drug loading studies are presented below. All three used encapsulation methods to load drugs into the MOFs studied. The studies take into account issues with initial MOF choice, loading technique, and MOF solvent stability.

#### 1.4.3.1.1 Drug encapsulation examples

Only a few biological studies of drug loading and release on MOFs have so far been performed (Table 5). One notable study is by Horcajada *et al.*,<sup>93</sup> who tested drug loading on a variety of MOFs including:  $\text{Fe}_3\text{O}(\text{CH}_3\text{OH})_3(\text{fumaric acid})_3$  (**MIL-89**),  $\text{Fe}_3\text{O}(\text{CH}_3\text{OH})_3(\text{fumaric acid})_3.(\text{CH}_3\text{CO}_2)$  (**MIL-88A**),  $\text{Fe}_3\text{FO}(\text{H}_2\text{O})_2(\text{BTC})_2$  (**MIL-100**),  $\text{Fe}_3\text{O}(\text{BDC-NH}_2)(\text{OH})(\text{H}_2\text{O})_2$  (**MIL-101\_NH<sub>2</sub>**), and  $\text{Fe}(\text{OH})(\text{BDC})$  (**MIL-53**). Results indicated that for many challenging drugs, rigid structures with large pore openings such as **MIL-100** and **MIL-102\_NH<sub>2</sub>** had larger uptakes than more flexible structures such as **MIL-89**. When studying the stability of the MOFs in water at 37 °C it was found that both **MIL-100** and **MIL-88A** degraded significantly after seven days.

Table 5 MOF loadings of a number of problematic drugs. The loading percentage is given as weight of drug as a fraction of total weight. Data taken data from ref <sup>93</sup>.

MOF	MIL-89	MIL-88A	MIL-100	MIL-101_NH <sub>2</sub>	MIL-53
<b>Organic Linker</b>	Muconic acid	Fumaric Acid	Trimesic Acid	Amino terephthalic acid	Terephthalic acid
<b>Molecular diagram of organic linker</b>					
<b>Flexible linker</b>	yes	yes	no	no	yes
<b>Pore size (Å)</b>	11	6	25 29	29 34	8.6
<b>Busulfan loading w/w (%)</b>	4.2	3.3	31.9		17.9
<b>Azidothymidine triphosphate loading (%)</b>	-	6.4	85.5	90.4	2.8
<b>Cidofovir loading (%)</b>	81	12	46.2	68.1	-
<b>Doxorubicin loading (%)</b>	-	-	11.2	-	-



The study tested the effect of the MOFs on rats. The lack of immune system response or inflammatory reactions suggested that the MOFs studied were non-toxic to the rats. This is a very positive factor for the viability of carboxylate-based MOFs.

More recently, the uptake of etilefrine (Figure 7) by  $Zn_8(\text{Adenine})_4(\text{BPDC})_6\text{O}$  (**bioMOF-1**), **bioMOF-4**,  $Zn_8(\text{Ad})_4(\text{BPDC})_6\text{O}_2$  (**bioMOF-100**), and  $Zn_8(\text{Ad})_4(\text{ABDC})_6\text{O}_2$  (**bioMOF-102**) was studied by Oh *et al.*<sup>87</sup>

Etilefrine is a cardiac stimulant, which increases cardiac output, stroke volume, and blood pressure. Etilefrine was chosen for drug loading due to the drug's cationic nature, which is ideal for incorporation into negatively charged MOFs. When testing the MOFs for their stability in water, it was found that **bioMOF-1** maintained its crystal structure in water for the longest period, with only small damage visible after eighty days. On the other hand, **bioMOFs 100** and **102** both decayed after relatively short periods. Loading of the MOFs were achieved by exchange in etilefrine solution.

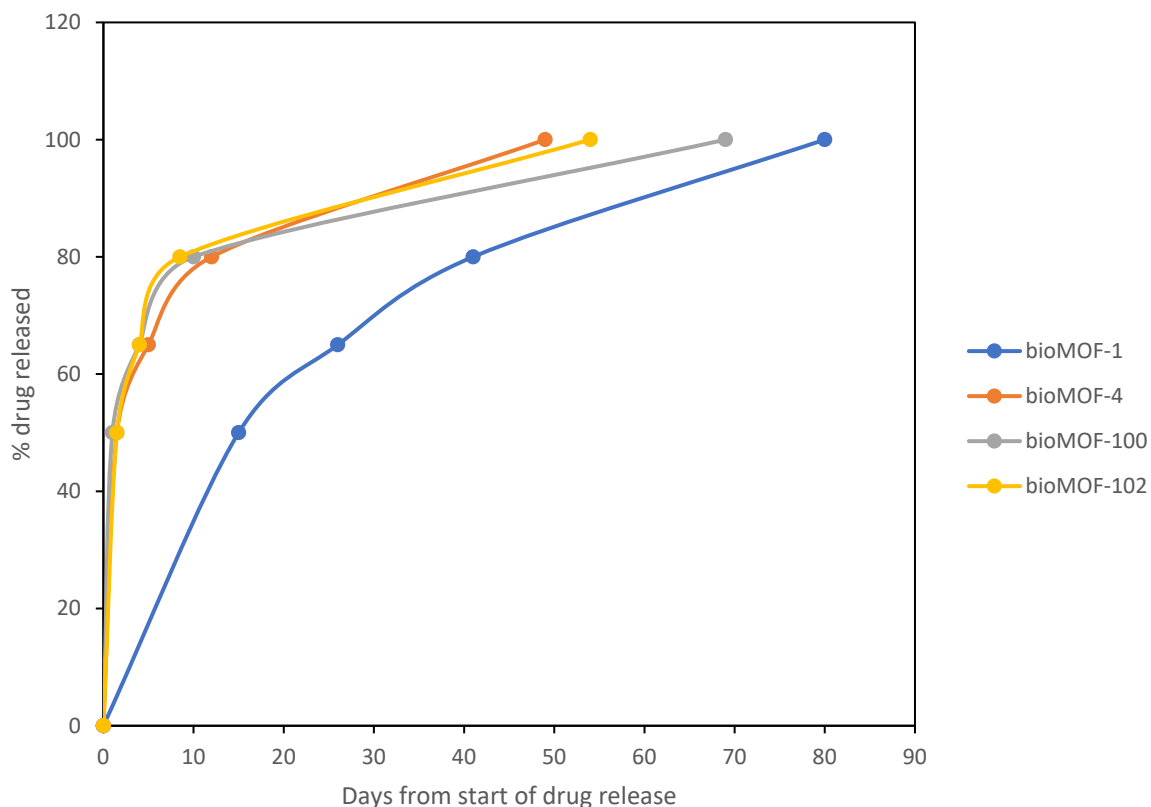


Figure 7 Etilefrine release from a selection of bioMOFs over the course of 3 months.

The etilefrine release data for the MOFs showed low maximum loading capacities, all close to 10% w/w. The release curve came from **bioMOF-1**, which released 50% of the loaded etilefrine over the course of 15 days, and the remaining etilefrine over 65 days (Fig 4). On the other hand, **bioMOFs 100** and **102** released 50% of their load in only 4 hours and the other 50% over 69 and 54 days respectively. This burst release could be attributed to the mesoporous nature of **bioMOF-100** and **bioMOF-102**, releasing all etilefrine in the middle of the pores very quickly. It was also of note that only **bioMOF-1** and **bioMOF-4** maintained crystallinity after drug release; however, such stability *in vitro* indicates both frameworks undergo a cation exchange process in simulated body fluid rather than framework destruction.

Cunha *et al.*<sup>88</sup> used a number of the more porous MOFs, **MIL-100(Fe)**, **MIL-127(Fe)**, **MIL-53(Fe)**, and **UiO-66(Zr)**, to encapsulate caffeine from an ethanol-caffeine solution.

It was found that all the materials adsorbed as much caffeine as it would be expected when taking into account the MOF's internal volume, with the exception of amine functionalised **MIL-53**. To establish that encapsulation has occurred, the FTIR vibration bands around 1770 and 1658  $\text{cm}^{-1}$ , which are characteristic of C=O bonds, were used. As with other studies, Monte Carlo simulations were used to predict the maximum drug adsorption inside a given framework, where most of the simulated uptakes matched closely to the experimental uptakes. The most interesting aspect of this study was the importance of solvent choice when designing the encapsulation scheme. In the case of this paper, both water and ethanol were both used as solvents, due to caffeine's high solubility in both solvents. It was found that the use of ethanol actually reduced the total amount of encapsulated drug. It was theorised that this was due to ethanol's preferential uptake into the frameworks over caffeine. For the most part, as expected, drug uptake correlated well to the total volume of each given framework, with **MIL-100(Fe)** giving far and away the highest at 50% w/w.

#### 1.4.3.2 Drugs as MOF linkers

Beyond directly loading MOFs with pharmaceutical payloads, an emerging technique is using pharmaceutically active molecules as the linker when synthesising MOFs. This allows for the delivery of two drugs concurrently; one as the payload loaded into the framework, and the other released as the MOF decomposes (Figure 8).<sup>94</sup> At the time of writing this thesis, there are only two examples of this MOF design: a modified MOF-74 structure (Figure 8), and a Hf framework for delivering anti-cancer drugs.<sup>95</sup>

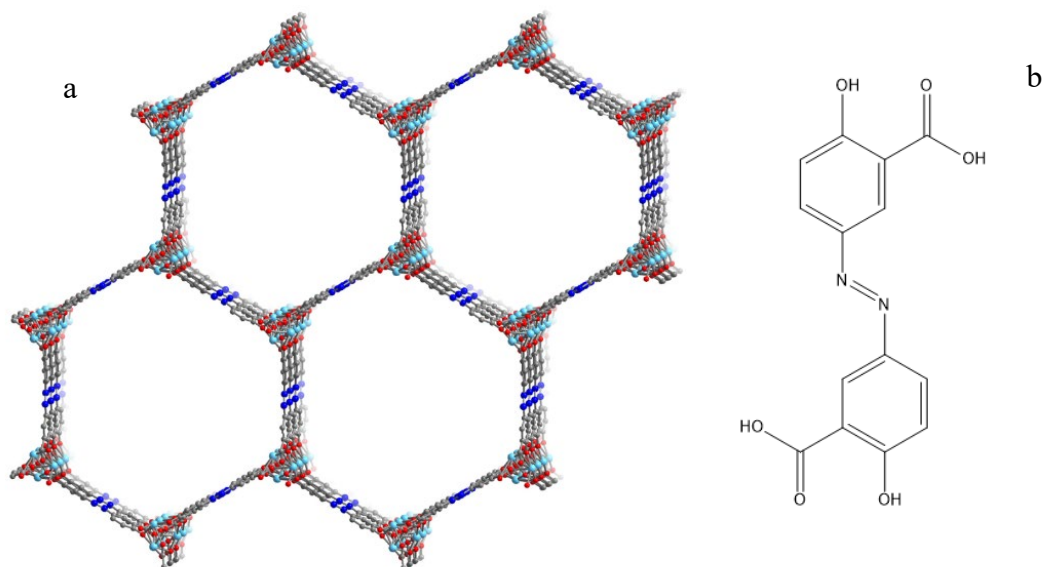


Figure 8 View along [001] of the Isoreticular MOF-74 synthesised by Levine *et al.* (a), which used olsalazine as linker. (b) Molecular diagram of the linker olsalazine, a pharmaceutical compound itself. Elements: carbon (grey), nitrogen (blue), oxygen (red), magnesium (light blue). Hydrogen omitted for clarity.

#### 1.4.3.3 NO loading in MOFs

Therapeutic uses of NO have been researched heavily since 1987, because this is a highly reactive radical species ( $\cdot\text{NO}$ ) which is key to a range of biological functions. A number of papers on the storage of NO in polymers<sup>96</sup> as well as in MOFs have been published. Examples include **MOF-74(Mg)**<sup>97</sup> and **HKUST-1**,<sup>77</sup> both of which exhibit very large adsorption capacities and hysteresis, with clear structural changes on gas adsorption. It has been theorised that any metal that forms coordinatively unsaturated frameworks should be capable of storing NO; meaning many MOFs with large surface areas are ideal NO storage candidates.

## **1.5 Porous materials for drug delivery**

In addition to MOFs, other porous materials have been explored for potential drug delivery applications. Porous material drug delivery has three material categories of interest: zeolites, polymers, porous silicas and activated carbons. Zeolites, porous silicas and activated carbons behave in a similar way to MOFs, they all have permanent porosity into which pharmaceutically active ingredients can penetrate.

### **1.5.1 Zeolites for drug delivery**

In terms of drug delivery potential zeolites are very similar to MOFs. Both can make use of the chemistry of their porous structures to deliver drugs to a target destination, and both MOFs and zeolites can be further chemically tuned to suit their application. Several zeolites have been had preliminary drug loading tests including ZSM-5,<sup>98</sup> Zeolite Y,<sup>99</sup> and Clinoptilolite.<sup>100</sup>

### **1.5.2 Silicas and activated carbon for drug delivery**

Beyond MOFs and zeolites other porous materials including activated carbons and porous silicas have been explored for their drug loading potential. Porous silicas have been used because of their large internal surface area.<sup>101</sup> As there are ongoing safety concerns on the effect of silicas on the human body activated carbons have been explored as a safe alternative.<sup>102-104</sup>

### **1.5.3 Polymers in drug delivery**

Polymers have been used for years as part of drug development research, mostly as a means to improve solubility in poorly water soluble drugs. However, ongoing studies on to the use of polymers as drug vehicles have been explored by several research groups.

Polymers can refer to either polymer dispersions, or for more complicated systems polymer gels with permanent porosity into which a drug might be loaded.<sup>86</sup> For a polymer

to be of any use in drug delivery the polymer must decompose in vivo, ideally inside the gastrointestinal tract. Polymer gels have attracted research interest recently for their stimulus sensitivity properties. These stimuli sensitive polymer systems are current focus of interest for polymer drug delivery; the stimuli a polymer might respond to range from pH sensitivity,<sup>105</sup> electrical potential,<sup>106</sup> and temperature differences.<sup>107</sup> As different organs have large differences in pH, it is the most suitable of the stimuli to use for drug delivery.<sup>108</sup>

These other drug delivery materials are all promising in their own right, but MOFs hold a few key advantages compared to each of them. Porous silicas can be toxic, while activated carbons do not have the chemical tuneability that MOFs possess. Polymer gels and zeolites are very promising and will likely work as a complement to MOFs as drug delivery materials, but both are much harder to tune and achieve desired properties.

## 1.6 Metal choice in MOF drug delivery

MOFs are in many ways' ideal candidates for drug delivery. Due to their porosity and tuneability, they have the potential to be used to deliver "difficult" drugs that cannot be administered directly due to reasons such as water instability or poor solubility. For a MOF to be useful, there are criteria that it must meet; it must be non-toxic, must be stable in air and water for extended periods, and it must have the ability to encapsulate drugs of interest. Obviously, any MOF used for drug delivery applications must be non-toxic to humans.

Table 6 Toxicity and daily recommended dose of the most common MOF metal sources. LD<sub>50</sub> corresponds to the dose required to kill 50% of specimens (usually rats) studied. Data taken from paper by Mellot-Draznieks et al.<sup>109</sup>.

<b>Metal-ion</b>	<b>LD<sub>50</sub> (g kg<sup>-1</sup>)</b>	<b>Daily Dose (mg)</b>
<b>Cu<sup>1+</sup>/Cu<sup>2+</sup></b>	0.025	0.8
<b>Mn<sup>2+</sup></b>	1.5	5
<b>Fe<sup>2+</sup>Fe<sup>3+</sup></b>	0.45	15
<b>Zn<sup>2+</sup></b>	0.35	15
<b>Mg<sup>2+</sup></b>	8.1	350
<b>Ca<sup>2+</sup></b>	1	1000

This non-toxic design starts with the choice of the metal for the nodes (Table 6). The toxicity of many metals limits the selection of useful metal-ions to magnesium, calcium, zinc, and iron.

## 1.7 MOF-74 Family of frameworks

The MOF family studied in this thesis is based on the archetypal MOF-74; which was previously known as **CPO-27**.<sup>110</sup> The MOF-74 framework is synthesised using 2,5-dihydroxyterephthalic acid (Figure 9) in mildly acidic conditions. The MOF has a chemical formula of M<sub>2</sub>(DHTA)(DMF)<sub>2</sub>(H<sub>2</sub>O)<sub>2</sub> where M = Zn,<sup>42</sup> Ni,<sup>111</sup> Mg,<sup>112</sup> Fe.<sup>113</sup>

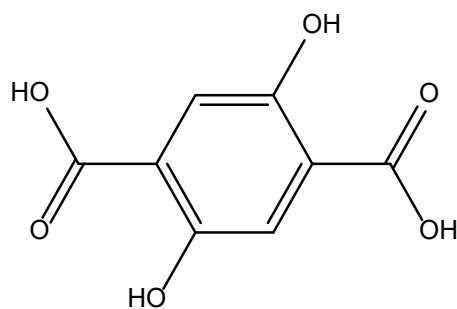


Figure 9 2,5-dihydroxyterephthalic acid (H<sub>4</sub>DHTA)

MOF-74 exhibits an octahedral geometry around metal centres. **MOF-74** can be synthesised with a range of metals including magnesium, nickel and zinc.<sup>110</sup> So far ibuprofen loading studies have been carried out using the nickel and iron analogues of the framework,<sup>90, 91</sup> but not **MOF-74-Zn**. It was recently reported that **MOF-74-Zn** can be synthesised using a mechanochemical synthesis method.<sup>42</sup> To the best of my knowledge, no drug loading studies have been performed on mechanochemically synthesised MOFs or **MOF-74-Zn**.

The MOF-74 first synthesised by Dietzel *et al.* in 2005 was a cobalt MOF with formula  $\text{Co}(\text{C}_8\text{H}_2\text{O}_6)(\text{H}_2\text{O})_2 \cdot (\text{H}_2\text{O})_8$ .<sup>114</sup> Dietzel discovered that the structure maintained its crystallinity even after solvent removal, a structural feature known as permanent porosity, and a key MOF property. Later, it was found that MOF-74 could be synthesised using a range of metals including Fe,<sup>115</sup> Ni,<sup>19</sup> Zn,<sup>110</sup> Mn,<sup>75</sup> Mg,<sup>81</sup> and mixed-metal variations (Figure 10).<sup>116</sup>



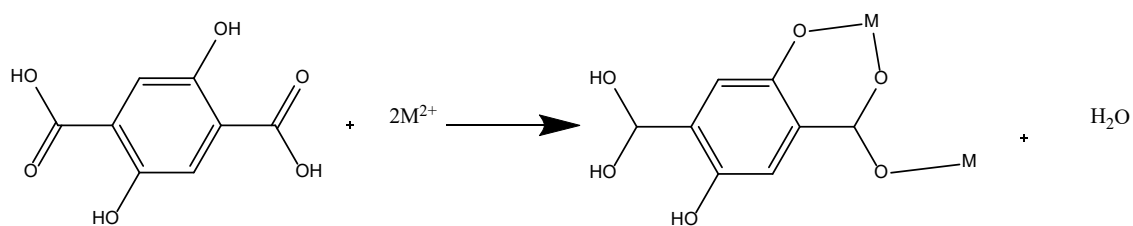


Figure 10 Schematic diagram of the general synthesis of MOF-74.  $M = \text{Fe, Mg, Mn, Ni, Zn}$ , with water as byproduct. Also shown is the fully protonated linker 2,5-Dihydroxyterephthalic acid ( $\text{H}_4\text{DHTA}$ ).

Discussed in this chapter is the mechanochemical synthesis of the metal-organic framework MOF-74-Zn, a 3D MOF with large pore size in relation to linker size and 11 Å diameter channels running through the structure (Figure 11).

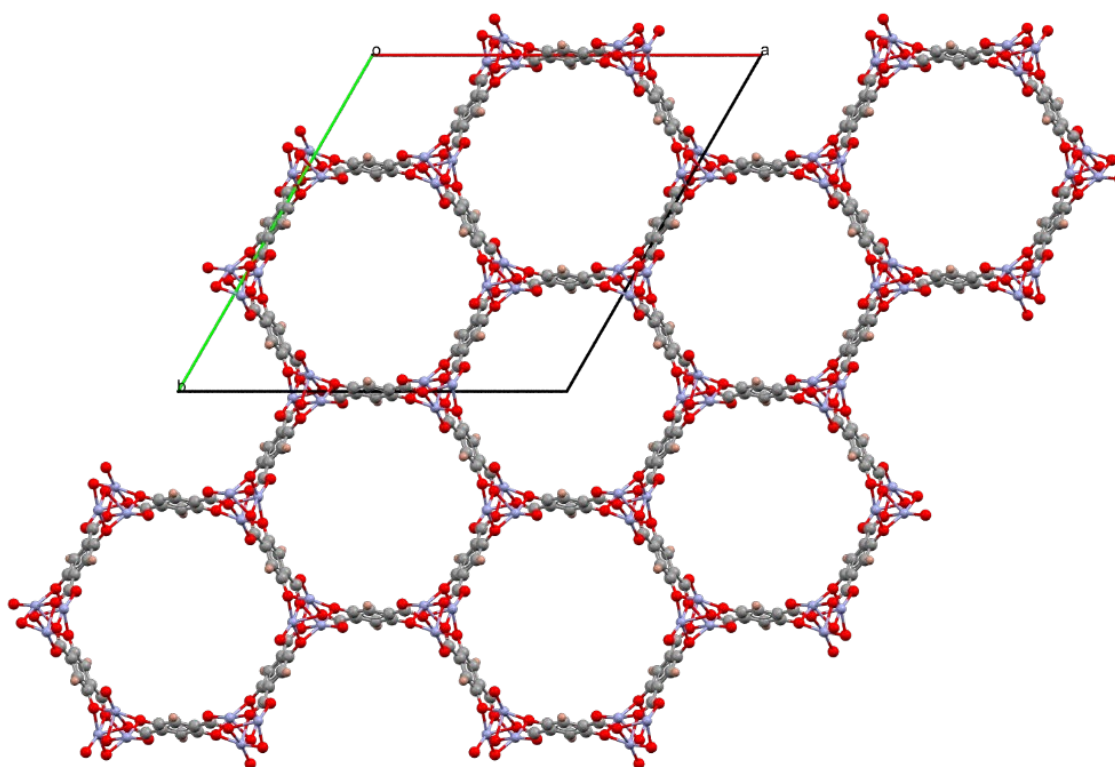


Figure 11 Structure of MOF-74 viewed down the  $c$ -axis showing the 11 nm diameter pores. Elements shown: carbon (grey), oxygen (red), zinc (blue), hydrogen (pink). Unit cell is shown .

In the synthesised MOF, each zinc is 6 coordinate in an octahedral configuration. Each of the zinc atoms face-share coordinated oxygens with their neighbours and align down the crystallographic  $c$ -axis.

In the activated porous structure, each zinc is 5 coordinated with an uncoordinated metal site. Each zinc is coordinated to three carboxyl groups and two hydroxyl groups from the DHTA linker <sup>116</sup>. The zinc atom's coordination environment is a coordinatively unsaturated octahedral arrangement (Figure 12). The crystallographic arrangement of the linker and metal centre remains unchanged in the activated structure with zinc atoms around a centre of inversion down the *c*-axis and the linker sitting on a crystallographic centre of inversion.

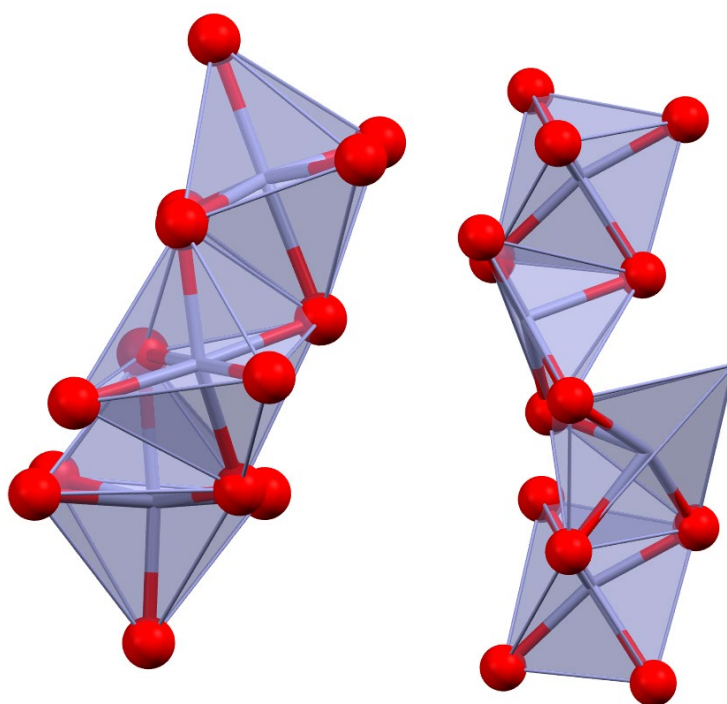


Figure 12 Coordination around zinc atoms in MOF-74. (left) coordination around synthesised MOF-74-Zn. (right) coordination around activated MOF-74. Both are distorted octahedra which edge share. Synthesised framework is 6 coordinate while activated framework is 5 coordinate.

Choosing which metal is used to make MOF-74 affects both its chemical and physical properties. The nickel and magnesium MOF-74 analogues are the most stable, but both have only been made to date via a solvothermal synthesis route and nickel is highly toxic. The zinc variant is only stable in water for around a week at room-temperature <sup>117</sup> but has a much more appealing mechanochemical synthesis route <sup>42</sup> than the traditional solvothermal synthesis route. The combination of reduced water stability and

mechanochemical synthesis route make studying the drug release properties of MOF-74-Zn interesting. While the mechanochemical synthesis of MOF-74-Zn has been reported previously, the exact mechanism by which the framework forms is poorly understood.

One of the interesting characteristics of the MOF-74 family is the range of isorecticular

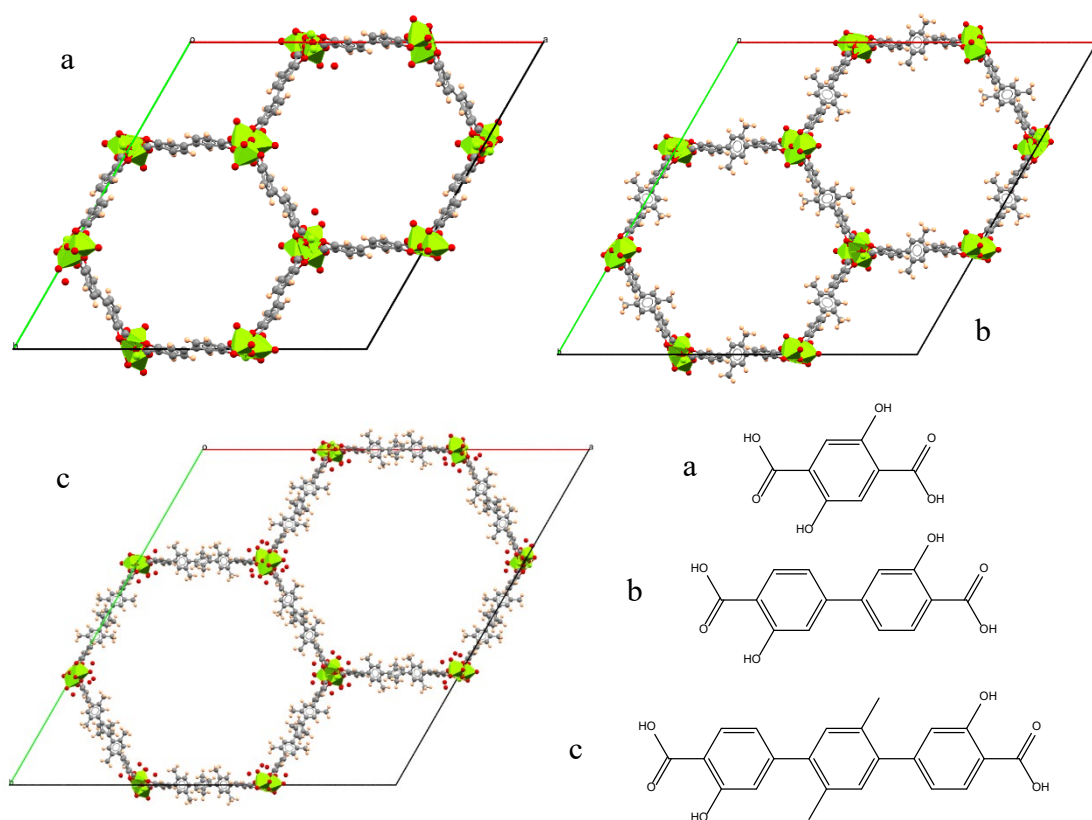


Figure 13 (top) Representative examples of series of isorecticular MOFs produced by Deng *et al* based on the MOF-74 framework. Each framework has the same SBU but differing linker length all as viewed down the *c*-axis. a: MOF-74-Mg b: IR-MOF-74-Mg c: IR-MOF-74-Mg-III. (bottom): Example of Linker extension used to synthesise larger rigid structures. Letters a,b,c correspond between top and bottom. Used by Deng, ref 35.

MOFs that can be synthesised. An extended family of MOF-74 structures has been synthesised by Deng *et al.* which increased the size of the linking terephthalic acid (Figure 13) to increase pore size. It was found that as long as rigid linkers were used the chains could be extended up to 11 phenyl rings long. It was found that the effect on chain

lengthening produced an almost entirely linear scaling of pore dimensions scaling from 10 by 14 Å up to 85 by 98 Å. As the pore size increased so too did the maximum internal surface area, which greatly increased the total volume of gas adsorbed by the framework.

118

In addition to the isoreticular MOF-74 frameworks, alternative MOF-74 frameworks also exist, namely, HIMS-74<sup>119</sup> and UTSA-74.<sup>120</sup> These frameworks are synthesised using the same starting materials as MOF-74, but under different reaction conditions. Both HIMS-74 and UTSA-74 have smaller pore diameters and surface areas than MOF-74.

The large MOF-74 family of structures has the potential to be very useful for drug delivery. It is also worth investigating if the isoreticular MOF-74 frameworks can be synthesised via a mechanochemical method.

## **1.8 Aims of this work**

The aim of this work is to study the mechanochemical synthesis of metal-organic frameworks with special interest in the crystalline intermediates that form during synthesis. The frameworks studied will ideally be suitable for use in drug loading studies, meaning both metals used in synthesis and linkers are non-toxic. As studied MOFs must be synthesised mechanochemically and be non-toxic, the best MOF candidates are the MOF-74 family of frameworks. As described earlier, the MOF-74 family of frameworks have large channels that run through the framework which can be easily tuned by modifying the organic linker used in synthesis. Currently, drug loading studies have been performed on the nickel and iron analogues of MOF-74, but not the zinc analogue. MOF-74-Zn will be synthesised using a mechanochemical method, then loaded with ibuprofen. Maximum ibuprofen loading will be studied along with analytical techniques

including solid-state NMR and inelastic neutron spectroscopy to investigate the interaction between ibuprofen and the MOF.

Mechanochemical synthesis of isoreticular MOF-74 frameworks will also be attempted by modifying the MOF-74 mechanochemical synthesis method, with mechanochemical intermediates expected; these intermediates will be studied using PXRD methods.

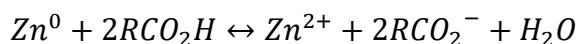
## 2- Experimental Techniques

### 2.1 Introduction

The most common way of synthesising metal-organic frameworks involves the use of solvothermal methods. Solvothermal synthesis uses a sealed jar containing a solvent and reactants which are then heated above the solvent's boiling point and then (often) slowly cooled <sup>121</sup>. The reaction stoichiometry, solvent volume used, and heating and cooling rates all affect the range of products that can be synthesised. This means that solvothermal synthesis can produce many different phases based on the above inputs, and some of these phases can be porous. The solvothermal synthesis approach has not been used in this work and is therefore not discussed further.

#### 2.1.1 Mechanochemical Synthesis

Mechanochemical synthesis is the use of mechanical force to stimulate chemical reactions. The mechanical effects involved in mechanochemistry are wide ranging, including stress-strain effects, shear forces, friction, and cavitation effects. It is widely accepted that the mechanism that a mechanochemical reaction will follow is different from that of a typical thermal or photosynthetic reaction. Due to the differences in reaction intermediates, materials can be produced very efficiently using mechanochemical synthesis.



##### 2.1.1.1 Experimental

Two different mills were used in this work. One is a shaker-type mill (Retsch MM400), equipped with a 25 mL cryo-rated stainless-steel milling jar, along with several stainless-steel milling balls. The shaker-type mill adds energy to the reaction mixture by shaking back and forth at a user-configurable rate, typically 30 Hz in this work. (Figure 14).

Shaker ball mills are ideal for testing mechanochemical synthesis with smaller reaction batch sizes, with reaction mixtures total mass less than 0.5 g.

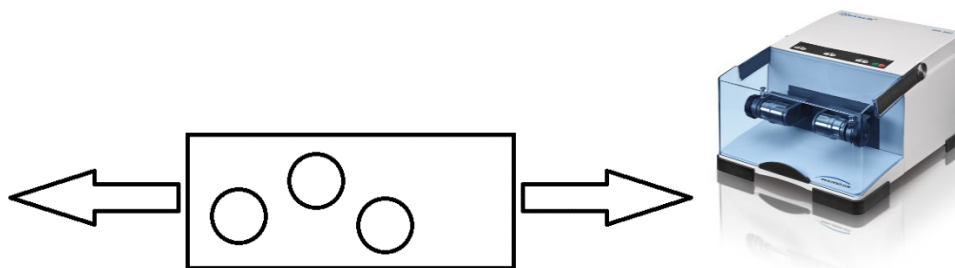


Figure 14 Schematic diagram of shaker type mill, with circles representing milling balls (left), Retsch MM400 shaker mill which was used in this project (right).

The other type of mill used was a planetary mill (Retsch PM 200) equipped a 50 mL stainless-steel milling jar, and several small stainless-steel milling balls. Planetary milling was used to scale up reaction mixtures in order to be able to synthesise 2 g batches of MOF. A planetary mill works by rotating a milling jar around two axes simultaneously. A large sun disk rotates in one direction, while the milling jar rotates in the opposite direction. The compounding effect of the rotation very efficiently adds kinetic energy into a system(Figure 15).

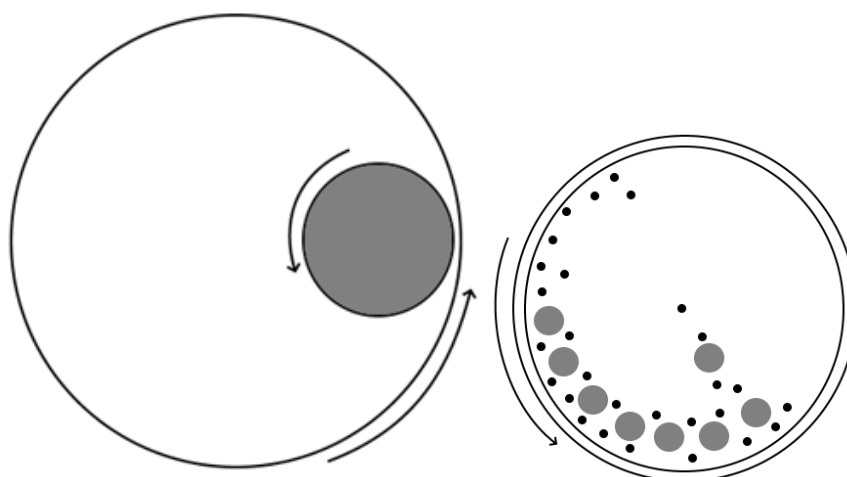


Figure 15 Schematic diagram of planetary mill showing the sundial and jar rotating in opposite directions (left). Schematic of contents of milling jar being affected by of both rotations (right).

## **2.1.2 Activation and loading of frameworks**

After synthesis, the pores of a MOF are inaccessible due to the presence of unreacted materials and solvent used in reaction. To remove these molecules and make the pore space accessible, a step known as “activation” is required. Activation is a process which involves removal of solvent and unreacted starting material molecules. There are several methods of activating a MOF, the simplest of which is heating in an oven under dynamic vacuum <sup>122</sup>. Depending upon the solvent present in the framework pores, additional solvent exchange steps are sometimes necessary. Solvent exchange is a process in which solvent molecules present inside the pores of a synthesised framework are swapped for more volatile solvent molecules <sup>123</sup> that are easier to remove.

### 2.1.2.1 Experimental

#### 2.1.2.1.1 Solvent exchange

Solvent exchange was performed on all materials that had been synthesised using DMF as a reaction solvent. Dry methanol was exchanged in to pores of frameworks in order to remove DMF. The framework material was added to a stirred volume of methanol, in the ratio of 1 g framework to 40 ml methanol. The solvent exchange procedure was carried out for three days, replacing the methanol solvent once every 24 hours.

#### 2.1.2.1.2 Activation

Samples were activated by placing them in a vacuum oven, then holding under vacuum for three hours. The temperature was then raised to 433 K and held for 24 hours. Finally, the sample was cooled to room-temperature under vacuum for at least 7 hours.



## **2.2 Thermogravimetric analysis**

Thermogravimetric analysis (TGA) is a technique which allows measurement of the thermal properties of materials. A sample of known weight is heated on a precise balance under gas flow and the sample mass is recorded as a function of temperature. Changes in weight correspond to a number of possible events, including desolvation, decomposition and oxidation as temperature increases <sup>124</sup>. TGA is particularly useful for MOF-type structures, as they typically exhibit multistep decompositions as solvent and guest molecules leave the pores of the framework at a lower temperature than that at which the framework collapses.

### **2.2.1 Experimental**

TGA measurements were performed on a TA Instruments TGA Q50 under air flowing at a rate of 60 mL min<sup>-1</sup>. The standard ramp rate was 5 K min<sup>-1</sup> with a collection range of 293-773 K. Each measurement used approximately 10 mg of ground sample in an alumina sample crucible. Data were analysed, and weight versus temperature plots constructed, using TA Universal analysis software.<sup>125</sup>

### **2.3 Differential scanning calorimetry**

Differential scanning calorimetry (DSC) is a method for analysing the thermal behaviour of materials. DSC uses a dual aluminium pan system with a sample pan and a reference pan. Roughly 10 mg of sample is loaded into the sample pan which is then sealed for measurement. A second aluminium reference pan is included in each measurement in order to allow background subtraction. Both the sample and the reference pan are simultaneously subjected to the same temperature programme. The difference in heat flow between the reference pan and the sample pan is measured by the instrument. Changes in heat flow correspond to changes in the sample such as melting, decomposition, and solidification, and are clearly visible as differences from the background curve.

#### **Experimental**

DSC data were collected using a TA Instruments DSC Q 2000 running from 273 K to 423 K at a rate of 10 K min<sup>-1</sup> under nitrogen with a flow rate of 20 mL min<sup>-1</sup>. Traces were analysed using TA universal analysis software,<sup>125</sup> which plotted heat flow against temperature.

The DSC's use of sealed aluminium sample pans can be problematic for MOF samples. Before activation, MOFs contain a considerable amount of solvent and this solvent becomes vapour when heated, breaking the seal on the sample pans and ruining data collection. This means that only solvent-free MOF samples can be analysed by DSC.

### **2.3 Elemental analysis**

Elemental analysis is a destructive analytical technique which can be used to measure calculate the quantitative mass fractions of carbon, nitrogen, and hydrogen in solid samples. Typically referred to by the acronym "CHN", it works by combusting organic

samples at 1273 K in oxygen in order to decompose them to CO<sub>2</sub>, H<sub>2</sub>O, and N<sub>2</sub>. The combusted gases are passed through a gas chromatography column in order to separate, and this followed by thermal conductivity measurements for calculating the volume of each gas. This quantitative measurement directly corresponds to the elemental percentages of the input material independent of its mass (Figure 16).

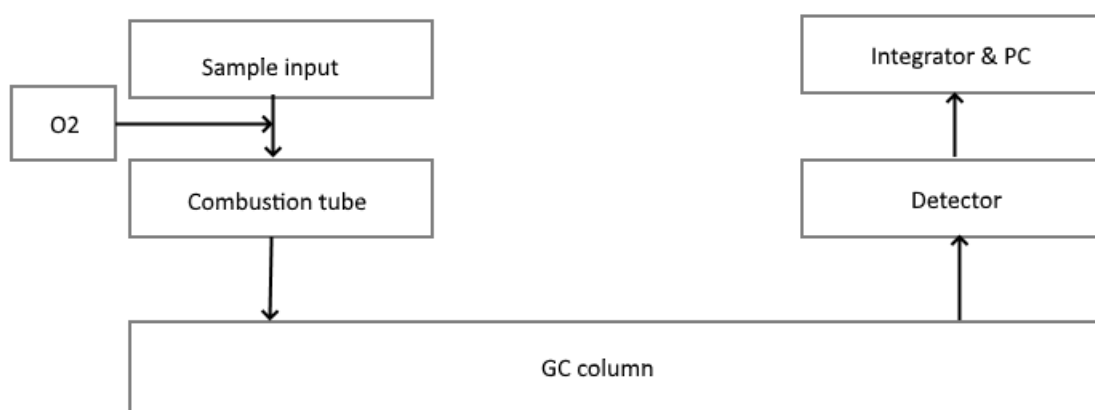


Figure 16 Schematic of CHN analyser layout

Duplicate CHN measurements were carried out by Medac Ltd. using a FlashEA 1112 series CHNS-O analyser. Each measurement was performed in duplicate to check sample homogeneity. Data were tabulated and compared to theoretical C, H, N compositions.

## 2.4 Spectroscopy

### 2.4 IR spectroscopy

Infrared spectroscopy measures the absorption of infrared radiation (wavelength 600-4000  $\text{cm}^{-1}$ ) by molecules. Each functional group in a molecule has a characteristic absorption frequency which can be used to determine which chemical groups are present in a sample <sup>126</sup>. This technique is used to determine the functional groups present in samples both in the framework, and which organic molecules are present in the framework pores.

IR spectra were collected on a PerkinElmer Spectrum 100 FT-IR spectrometer equipped with a diamond attenuated total reflectance (ATR) attachment. An ATR allows for collection of accurate IR spectra of solid samples without further processing, unlike the more traditional KBr disc method. Powdered samples were placed on the ATR and pressure was applied with the attached tool. Data were collected and analysed using Spectrum software. Spectra were collected between 600 and 4000  $\text{cm}^{-1}$  using a total of 12 accumulations.

### 2.5 UV-Vis spectroscopy

UV-Vis spectroscopy utilises molecular absorption of radiation in the visible and ultraviolet regions (750-190 nm). UV-Vis spectroscopy uses similar principles to those in IR spectroscopy, but rather than measure molecular excitation motions, UV-Vis instead measures electronic excitations in samples in the solution state. The extent of absorption at a given wavelength is directly proportional to the concentration of the sample in solution, and so the concentration of an unknown solution can be calculated. The relationship between absorption and concentration is given by the Beer-Lambert Law.

$$A = \epsilon cl$$

UV-Vis spectra were collected on a Cary 300 Bio UV-Visible Spectrophotometer running with an empty reference cell. Background for a given solvent was subtracted using a blank solvent sample. Unless otherwise specified, the data were collected in UV region 400-200 nm measuring absorbance between 0 and 1. Data were processed using Cary scan software.<sup>127</sup>

## **2.6 Inelastic neutron scattering**

Inelastic neutron scattering (INS) is a spectroscopic method which is particularly sensitive to the molecular environment of hydrogen atoms. In standard spectroscopic methods, photons are used to excite molecules and probe their structural properties; INS, on the other hand, uses neutrons as the structural probe. Consequently, INS spectra are significantly different from those produced by IR and Raman spectroscopy due to the lack of selection rules in INS.<sup>128</sup> INS is much more sensitive to hydrogen than any other element, making INS an ideal tool for probing the internal surfaces of framework structures that contain very little hydrogen. Due to the requirement for a source of neutrons, INS instruments are most often located at large-scale facilities (such as nuclear reactors or spallation sources) which can generate neutrons with a large enough flux for spectra collection on reasonable timescales.<sup>129</sup>

INS spectra were collected by Dr Jeff Armstrong, instrument scientist for the TOSCA instrument at ISIS spallation neutron source.<sup>130</sup> 5 g of each sample were loaded into vanadium cans and data collected on the instrument at 20 K. Data were reduced using Mantid<sup>131</sup> INS spectra were plotted using Origin.<sup>132</sup>

## **2.7 Optical Microscopy**

All bulk samples were checked after milling for any signs of single-crystals using a Fuji optical microscope in reflectance and transmission mode. In cases where single-crystals

were found, they were isolated and set aside for analysis on the single-crystal X-ray diffractometer.

## **2.8 Scanning electron microscopy**

Scanning electron microscopy (SEM) is a method for visualising objects as small as ~1 nm. SEM uses a focussed beam of high-energy electrons to view solid samples. Electrons are accelerated to large kinetic energies, which are then used to bombard a sample.<sup>133</sup> Electron kinetic energy is dissipated upon hitting a sample which produces many different types of secondary electrons which are collected and used to map out an image of the sample being studied. Backscattered electrons are used to produce images of samples. Due to the volume of electrons hitting a sample it must be conductive, consequently samples are prepped beforehand by coating in a thin layer of gold to increase sample conductivity.

SEM images of samples were collected on a Cambridge 360 Stereoscan electron microscope, which operates under high vacuum. Approximately 3 mg of each sample were placed on the head of a sample holder, which were then coated in gold to provide conductivity. Images were collected down to 2 nm over with a collection time of approximately 3 minutes per sample.

## **2.9 X-ray diffraction**

X-ray diffraction is a method which is used heavily in materials chemistry and solid-state chemistry in order to investigate the atomic-level structure of crystalline solids. X-rays produce diffraction patterns when they interact with evenly spaced atoms which are between 1 and 100 Å apart. X-rays are generated by bombarding a metal target with electrons, which are produced by a tungsten filament. The metal target used determines the wavelength of X-rays produced; in laboratory-based diffractometers, both copper and

molybdenum sources are commonly used. Each metal source produces X-rays at multiple wavelengths, but typically a monochromator is used to filter out all but the desired radiation e.g.  $K_{\alpha}$ .

Evenly spaced arrays of atoms act as three-dimensional diffraction gratings which create constructive and destructive interference for the X-ray beams producing spots of intensity at particular locations in space, which are then detected and processed. Constructive interference occurs when Bragg's law is satisfied (Figure 17); this relationship is defined by the distance  $d$  between layers of atoms and the angle  $\theta$  at which these reflections are observed. <sup>134</sup>

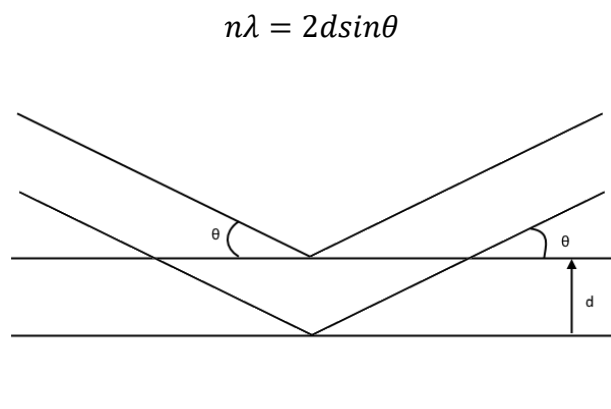


Figure 17 Bragg reflection ( $\theta$ ) from crystal planes with a  $d$ -spacing  $d$ .

### 2.9.1 Single-crystal X-ray diffraction

As described above, a single-crystal in an X-ray beam behaves like a 3-dimensional diffraction grating. In single-crystal X-ray diffraction, a detector is placed directly behind a crystal in the X-ray beam and diffracted intensities are collected (Figure 18). These intensities correspond to the  $hkl$  reflections associated with the unit-cell of the crystal. The raw intensity data must be processed to correct for several factors, including instrument geometry, detector efficiency and X-ray absorption. Using this reduced data,

one can work out the size and shape of the crystal's unit-cell and then begin the process of determining atom types and positions within the unit-cell.

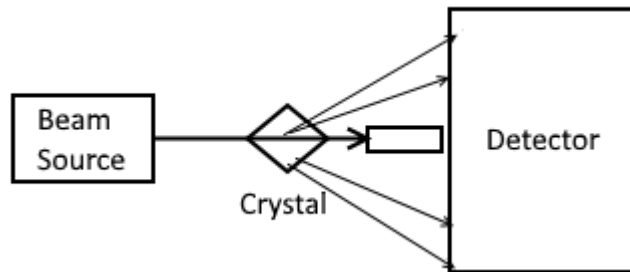


Figure 18 Schematic of single-crystal diffractometer.

The diffracted intensities are proportional to the structure factor magnitudes, where the structure factor is defined as shown in the equation below:

$$F(hkl) = \sum_{j=1}^n f_j e^{2\pi i[hx+ky+lz]}$$

$$I \propto F^2$$

Structure factors are important as they allow us to accurately map out the electron density of a crystal in order to be able to solve its structure. The position of the  $j^{\text{th}}$  atom is broken down into its fractional coordinates (x, y, z). Each element has its atomic scattering factor  $f_i$ , the equation works over the whole unit-cell with n atoms. Each diffracted beam has an amplitude  $|F_{hkl}|$ , and a phase angle  $\phi(hkl)$  so the equation can be expressed as below.

$$F(hkl) = |F_{hkl}| e^{i\phi(hkl)}$$

As measuring the sign of F is impossible, and the phase angle cannot be directly measured calculating electron density is impossible directly from an experiment, this is known as the phase problem.

$$\rho(xyz) = \frac{1}{V} \sum_{\substack{hkl \\ -\infty \\ +\infty}} |F(hkl)| \cdot e^{-2\pi i[hx+ky+lz-\phi(hkl)]}$$



The diffractometer permits measurement of any given structure factor magnitude  $|F(hkl)|$ , but the corresponding phase angle  $\phi(hkl)$  cannot be measured experimentally. Fortunately, the so-called “direct methods” of structure solution allow phase angles to be determined on a probabilistic basis using relationships between diffracted intensities, thus allowing electron density maps  $\rho(xyz)$  to be constructed and interpreted.

#### 2.9.1.1 Experimental

Single-crystal X-ray diffraction data were collected at 150 K on an Oxford Diffraction Gemini instrument equipped with a liquid-N<sub>2</sub>-based Cryojet cooling device, using a K $\alpha$  monochromated molybdenum source,  $\lambda=0.71073$  Å. Suitable crystal samples were mounted on the diffractometer using Paratone oil and a polymer loop, with the crystal being held in place when the oil froze in the nitrogen gas stream, prior to centring of the crystal on the diffractometer. Pre-experiments of duration ca. 5 -20 minutes were performed in order to determine the crystal’s lattice parameters and calculate a data collection strategy. Crystals were rejected if they diffracted poorly, or if a reasonable unit-cell could not be found; candidate crystals were checked until such time as one which passed both these checks was found. Data were collected and reduced using CrysAlisPro<sup>135</sup> software package . Structures were solved using SHELXT<sup>136</sup> and refined using SHELXL,<sup>137</sup> operating within the Olex2<sup>138</sup> software package. Visualisation of crystal structures were performed using the Mercury<sup>18</sup> and Crystal Maker<sup>139</sup> software packages.

#### 2.9.2 Powder X-ray Diffraction (PXRD)

Powder X-ray diffraction (PXRD) differs from single-crystal X-ray diffraction only in that diffraction is measured from a polycrystalline sample containing a vast number of (ideally) randomly oriented crystallites of size the order of a few microns. The random orientation of the crystallites means that instead of obtaining spots of intensity in 3D

space, the observed diffracted intensity is the sum of total intensity from all Bragg peaks scattering at a given diffraction angle in a 1D projection of 3D space. This means that overlapping Bragg peaks can be present in powder X-ray diffraction, reducing the diffracted intensity information content of the pattern relative to its single-crystal equivalent; this makes the process of solving crystal structures much more challenging. Despite this, there are several advantages of powder X-ray diffraction over single-crystal; PXRD sample preparation is significantly more straightforward, as provided a solid can be crushed into a powder it can be run on the diffractometer. The PXRD pattern is representative of the bulk, whereas an isolated single-crystal may not be. Another key advantage is the ability to quantitatively analyse the weight percentages of mixtures of crystalline phases. Finally, there are many situations where growing single-crystals large enough for single-crystal X-ray diffraction is unfeasible; in such cases, structure determination from powder data can be the only viable option.

#### 2.9.2.1 Refining structural models

The initial analysis of PXRD data collected in this work fits broadly into three stages. The first stage was powder indexing in order to determine the unit-cell of the structure. This was performed using multiple approaches, including DICVOL (as implemented in DASH) and SVD (as implemented in TOPAS). The lattice parameters of any indexed cell were then used to search the ICSD<sup>47</sup> and the CCDC CSD<sup>3</sup> crystallographic databases for possible crystal structure matches. As a second stage, to test the ability of the determined cell to explain the observed data, a so-called Pawley refinement was performed. The Pawley refinement parameters were typically: polynomial background, zero-point error, lattice parameters, peak shape parameters and reflections intensities. Pawley refinements were performed for all X-ray diffraction data collections to search for new phases and confirm presence of expected phases.

The final stage of PXRD data analysis was Rietveld refinement. Rietveld refinement is similar to Pawley refinement, except that it requires atomic coordinates (i.e. a crystal structure) in order to generate reflection intensities. A good Rietveld fit to the data is strong evidence that the crystal structure under study has been correctly determined.

$$y_i = I_k \exp \left[ \frac{-4 \ln(2)}{H_k^2} (2\theta_i - 2\theta_k)^2 \right]$$

Peak shape and intensity are calculated by the equation above. Where  $I_k$  is the intensity calculated using the structure factors from the CIF.  $H_k$  is the full width half maximum of a peak.  $\theta_k$  corresponds to the centre of the peak. This equation assumes that each peak has a Gaussian shape. Peaks are often asymmetrical at low angle; a modified equation is used in that case. <sup>140</sup>

The parameters used in all Rietveld refinements were polynomial background, zero-point error, lattice parameters, peak shape parameters, scale factor, overall temperature factor and atomic coordinates. In some cases, samples displayed preferred orientation, where crystallites in the sample are not randomly oriented; this has an adverse effect on observed diffracted intensities. In such cases, a 4<sup>th</sup> order spherical harmonics correction for preferred orientation was used.

PXRD data were indexed using DASH <sup>141</sup> software, and TOPAS 4.2 <sup>142</sup> software suites. Pawley and Rietveld refinements were performed using TOPAS 4.2. PXRD patterns were plotted using TOPAS 4.2 and EVA software. <sup>143</sup> Details about TOPAS input files and how to operate the software were obtained from the TOPAS wiki. <sup>144</sup>

#### 2.9.2.2 Crystal structure solution from PXRD data

There are a number of different methods for solving crystal structures using powder diffraction data which have been developed over the last 20 years. Each method has its

own set of pros and cons, and situations where it can be best applied. The majority of PXRD structure solution methods use a global-optimisation algorithm known as simulated annealing as their basis. Simulated annealing is a computational technique which is very effective at finding the “global minimum” of a multidimensional function. In the case of PXRD structure solution, the multidimensional function is the  $\chi^2$  for the observed and calculated diffraction patterns as a function of atomic coordinates; the global minimum, where the calculated and observed powder patterns agree very well, equates to the solved crystal structure.<sup>145</sup> Simulated annealing algorithms work very well in situations where complexity is relatively low, but odds of finding global minimum decreases rapidly as complexity increases.

The other main method used for powder structure solution is direct methods. Direct methods use the same basic methodology that has been so successful for single-crystal data, but with significant modifications made in order to get around the problem of reflection overlap and limited resolution. Success with direct methods is been found where data quality is exceptional (e.g. synchrotron data to high spatial resolution) and where strongly-scattering atoms (such as Br, I) are present in the crystal.

The prototypical example of simulated annealing software designed for powder data is the DASH program,<sup>141</sup> which uses known molecular fragments along with unit-cells derived from Pawley refinement to generate model powder patterns which are compared to experimental data. The prototypical example of direct methods software is EXPO<sup>146</sup> which also uses lattice parameters from a Pawley refinement but has no requirement for pre-defined connectivity from molecular fragments. Note that EXPO is also capable of performing simulated annealing.

In this work, structure solution from PXRD was achieved using DASH, EXPO, and TOPAS simulated annealing packages. In cases where multiple crystalline phases were present in the data, individual crystalline phases were fitted with a mixture of Pawley (for unknown phases) and Rietveld (for known phases) refinements, allowing the unknown phase peak pattern to be extracted from the observed data. Contents of unit-cells were estimated using reaction input stoichiometry and prior examples found on the CCDC of similar volume unit-cell structures. Input models were adjusted based on prior series outputs; for example, if large voids were found in prior runs, more molecules of solvent would be added as input.

#### 2.9.2.3 DFT for powder diffraction solved structures

Density Functional Theory (DFT) is a quantum-chemical approach to calculating the energy of an input molecule/crystal structure by modelling electronic interactions. Coupled with local minimisation algorithms such as BFGS, it is a powerful approach to minimising the energy of system. DFT is a very complex topic, and even a brief discussion of its fundamentals lies well outside the scope of this work. However, modern software packages implementing DFT for periodic systems make it relatively easy to utilise for validating solved crystal structures; it is in this context that it has been employed in this work. For all structures that were solved from powder diffraction data, energy minimisation using periodic DFT was employed to help obtain the most accurate crystal structure that were consistent with the observed diffraction data. The general structure solution strategy was therefore: (1) use standard molecular fragments, usually obtained from the CSD, as input into DASH; (2) if DASH generated a promising solution, transfer it into TOPAS and perform Rietveld refinement, treating input fragments as rigid bodies wherever possible; (3) take the rigid-body refined structure and subject it to energy

minimisation using DFT; (4) take the minimised structure and fit it against the PXRD data in a Rietveld refinement, allowing some final rigid-body refinement if needed (to allow for the “temperature difference” between the PXRD data collection and the notional 0 K of the DFT calculation).

#### 2.9.2.3.1 DFT experimental procedure

DFT calculations were performed by Professor Kenneth Shankland using Quantum Espresso program PWSCF v6.3,<sup>147</sup> running under Ubuntu Linux or Linux subsystem for Windows 10, on Dell Precision Workstations equipped with typically 16 to 24 CPU cores and either 48 GB or 64 GB memory.

All pseudopotentials from the pslibrary of Quantum Espresso

Exchange correlation function = Perdew-Burke-Ernzerhof

Projector augmented wave method = Kresse-Joubert

Dispersion correction = Grimme D3

Energy convergence threshold = 0.00005 Ry

Force convergence threshold = 0.0005 Ry

Kinetic energy cutoff (Ry) for wavefunctions = 50

Kinetic energy cutoff (Ry) for charge density and potential = 400

Minimisation method for both atoms and cell = BFGS ( Broyden–Fletcher–Goldfarb–Shannon)

#### 2.9.2.4 Quantitative phase analysis

Quantitative phase analysis (QPA) is a technique which can be applied to PXRD data with known crystalline phases to calculate the weight percentage of each phase. Provided

that there are no amorphous phases present, the QPA can be considered to be quite accurate for estimating the composition of phase mixtures.<sup>148</sup>

Rietveld-based QPA was performed for powders with multiple phases using TOPAS<sup>142</sup> software.

#### 2.9.2.5 Experimental

PXRD data were collected in-house on a Bruker D8 Advance operating in transmission capillary mode at 293 K. Between 5 and 10 mg of dried powder was packed into 0.7 mm diameter borosilicate glass capillaries which were then mounted on a goniometer and aligned in the X-ray beam. The D8 Advance uses a monochromated copper source,  $K_{\alpha 1}$   $\lambda=1.54060$  Å. Data were collected using a number of different data collection schemes, depending on the quality of data required, but step size was always  $0.017^\circ$ . Samples with large unit-cells were collected over 14 hours between  $3.5$  and  $50^\circ 2\theta$ . Fast sample scans were collected over one hour in the range  $5$  to  $65^\circ 2\theta$ . Lastly, samples which would be taken forward for powder X-ray structure solution would be collected over 14 hours using a variable count time approach, with much longer collection times at large values of  $2\theta$ .

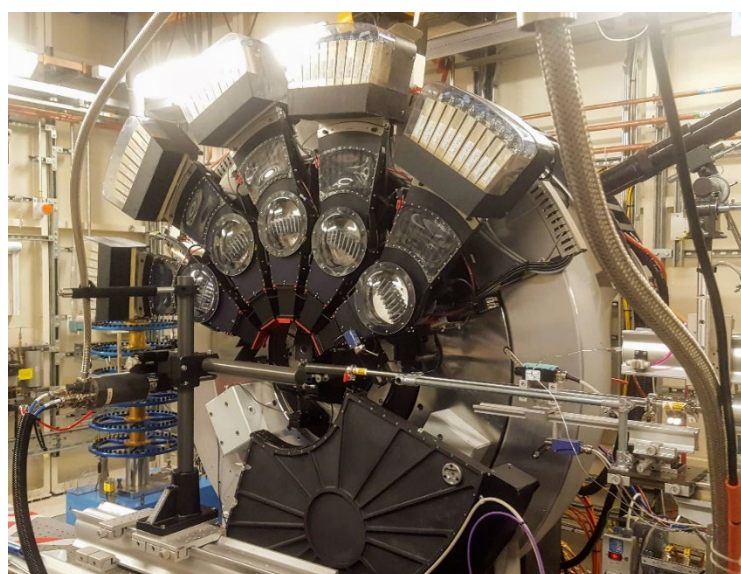


Figure 19 The detector array at Beamline I11 Diamond Light Source. MAC analysers arranged in semicircle around sample holder.

A series of experiments were run at the Diamond Light Source I11 high-resolution powder diffraction beamline (Figure 19).<sup>149</sup> 5-10 mg of dry powder sample were loaded in to 0.7 mm borosilicate capillaries which were mounted directly on the goniometer of the beamline. Unless otherwise stated, radiation of wavelength  $\lambda=1.38 \text{ \AA}$  was used. The detector used was the Multiple Analyser Crystal (MAC) detector, which uses five individual modules each containing nine analyser crystals. The detectors are oriented around the sample meaning each analyser collects a different portion of the diffractogram, which corresponds to much shorter than lab collection times.<sup>150</sup> Samples were rotated at 300 rpm during data collection. To reduce the possibility of radiation damage, samples were translated by 3 mm every five minutes, with total collection times of 30 minutes per sample. After collection, sample data were rebinned to a step size of  $0.003^\circ$ .

## **2.10 Particle-size analysis measurements**

Particle size analysis (PSA) is a broad term for techniques designed to measure the size distribution of particles. In this work, PSA is used as a term to describe the use of a 632.8 nm laser to measure particle scattering in solution and hence work out the particle size distribution. Scattering is measured as the amount of light which backscatters towards a detector. The angle through which light which is scattered back is inversely proportional to the particle size, with smaller particles scattering with larger angle (Figure 20). The measurement is based on the surface area of particles, which is then used to calculate particle radius. For this reason, all particles are treated as perfect spheres. For a good PSA measurement, particles are required to be completely monodisperse in solution, so a small amount of surfactant is added to aid in dispersion.



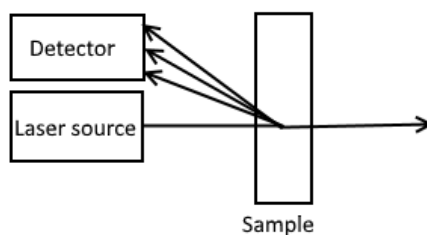


Figure 20 Schematic of backscattering particle-size analysis measurement is made.

PSA was measured using a Malvern Zetasizer Nano-ZS in backscatter configuration. Samples were prepared by dispersing 10 mg of powder in to 50 ml of ultrapure deionised water. 1 ml of this dispersion was added to a plastic cuvette for measurement. In cases where particles of less than 400 nm were measured, the dispersion was first filtered through a 0.4  $\mu\text{m}$  syringe filter. Each sample was measured three times with individual collection times of one minute each, with one minute before collection to allow particles to settle. Data were processed, and reports were made using Malvern Instruments report maker.<sup>151</sup>

## 2.11 Nuclear Magnetic Resonance (NMR)

NMR is an analytical technique for measuring chemical purity, and as a tool for solving molecular structure. NMR uses very strong magnets to excite nuclei to induce nuclear magnetic resonance with radio waves. For most common NMR nuclei, spin is  $\frac{1}{2}$ , which gives a single energy gap (Figure 21). The most common isotopes for NMR, proton  $^1\text{H}$ , carbon  $^{13}\text{C}$ , and  $^{15}\text{N}$  all have a spin of  $\frac{1}{2}$ . NMR is extremely useful for confirming the structure of organic compounds.

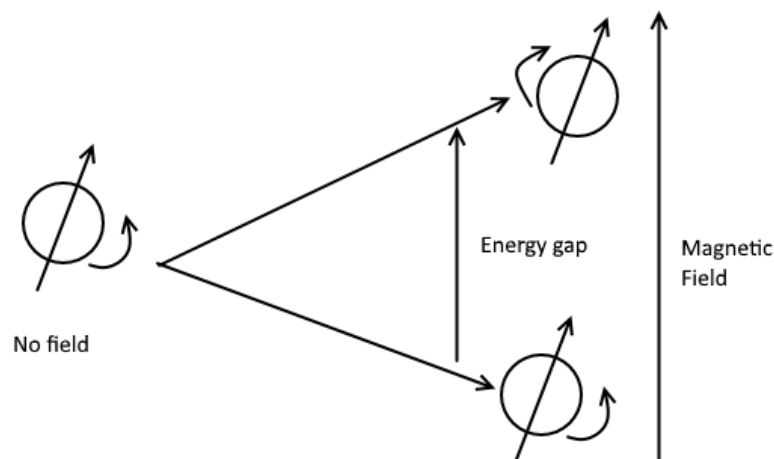


Figure 21 Energy gap between nuclei spins is produced when interacting with a magnetic field. The measurement of this energy gap between nuclei spins is the principle of NMR.

### 2.11.1 Experimental

5 mg of sample were dissolved in minimum volume deuterated DMSO, which was used to fill an NMR sample tube. Data were collected on a Bruker DPX spectrometer running at 400 MHz. Data were collected by Dr Radoslaw Kowalczyk at the University of Reading.  $^1\text{H}$  NMR and  $^{13}\text{C}$  NMR were collected for organic samples to confirm purity. Collection times were 10 minutes for  $^1\text{H}$  NMR and 30 minutes for  $^{13}\text{C}$  NMR. Data were processed and analysed using Bruker's Topspin software, graphics of spectrograms were also made using Topspin.<sup>152</sup>

### 2.11.2 Solid-state NMR (SSNMR)

Solid-state NMR is a spectroscopic technique for measuring NMR spectrums of solid materials. Getting high quality data is much more complicated in SSNMR than solution NMR as samples are anisotropic, this results in very broad peaks. The line broadening can be minimised by rapidly spinning a sample on the "magic-angle". The magic-angle is  $54.74^\circ$  which rotates all axis by the same amount effectively making the sample isotropic. Even with magic-angle spinning SSNMR spectra are more difficult to interpret than solution NMR.

### 2.11.2.1 Experimental

100 mg of powdered sample was loaded into a solid-state NMR rotor. Samples were compacted then run spectrometer. Data were collected by Dr Radoslaw Kowalczyk. The  $^{13}\text{C}$  solid-state cross-polarization magic angle spinning (CPMAS) NMR spectra were recorded on Bruker Advance III spectrometer operating at Larmor frequency of 125.76 MHz (11.75T). The standard bore 4 mm MAS probe was spun at 8 kHz rate. The standard Bruker CP pulse sequence was used with variable amplitude ramp 90 -100. The CP contact time was 3 ms, and the  $90^\circ$  pulse width was 3.7us at 38W power level. Totals of 256 (for pure ibuprofen) and 4096 (for MOFs) signal transients were accumulated with 12 s relaxation delays at ambient temperature. All spectra were referenced to external adamantane signal as a secondary reference (frequency peak at 38.0 ppm with respect to TMS). Data were processed, analysed, and graphical outputs made using Bruker's Topspin software suite.<sup>152</sup>

## 2.12 BET gas sorption measurements

BET (Brunauer-Emmett-Teller) gas sorption measurement is an analytical technique for calculating the internal surface area of a solid. It is commonly used to estimate the amount of accessible space inside porous materials.<sup>153</sup> BET is similar to Langmuir theory, as it measures the volume of gas taken up in to a solid, except in BET gases have multi-layered adsorption. Langmuir theory assumes that any gas absorbed forms a monolayer on the internal surface of a porous material,<sup>153</sup> while BET assumes that a proportion of the gas adsorbs in multiple layers. For this reason, Langmuir surface area calculations become inaccurate in solids with large internal surface areas. Total surface area is calculated using the equation below which relates the total surface area  $S_{\text{total}}$  to the volume of gas needed to form a monolayer  $v_m$ , Avogadro's number  $N$ ,  $s$  the cross-sectional area of a single

adsorbing molecule, and  $V$  the total volume of gas adsorbed. The specific surface area is calculated by dividing the surface area by the mass of sample measured.

$$S_{total} = \frac{(v_m N_s)}{V}$$

$$S_{BET} = \frac{S_{total}}{a}$$

In a typical BET adsorption experiment a sample is degassed, allowed to equilibrate at a low temperature, then gas is slowly added. After the gas is added, the volume of adsorbed gas is calculated, then the experiment is repeated at higher partial pressure. Partial pressure is plotted against adsorbed volume to obtain an adsorption isotherm. The shape of the isotherm is characteristic to the size and distribution of the internal surface of the solid being measured.<sup>153</sup>

### **2.12.1 Experimental**

BET adsorption measurements were conducted by Dr Sebastien Rochat at the University of Bath using a Micromeritics 3Flex surface characterisation analyser. Sorption measurements were conducted using nitrogen at 77 K. Data were analysed using included software package.

# Chapter 3- Mechanochemical synthesis and characterisation of MOF-74-Zn

## 3.1 Introduction

As described in chapter 1, there is a range of MOFs which can be synthesised with a huge range of properties under different synthesis conditions. This range of properties means that MOFs can be selected based on their required internal surface area, metal-ion choice, solvent stability, and synthesis method. As described in Section 1.6 MOF-74 can be considered a promising candidate for drug loading studies.

Discussed in this chapter is the mechanochemical synthesis of the metal-organic framework MOF-74-Zn, a 3D MOF with large pore size in relation to linker size and 11 Å diameter channels running through the structure (Figure 22).

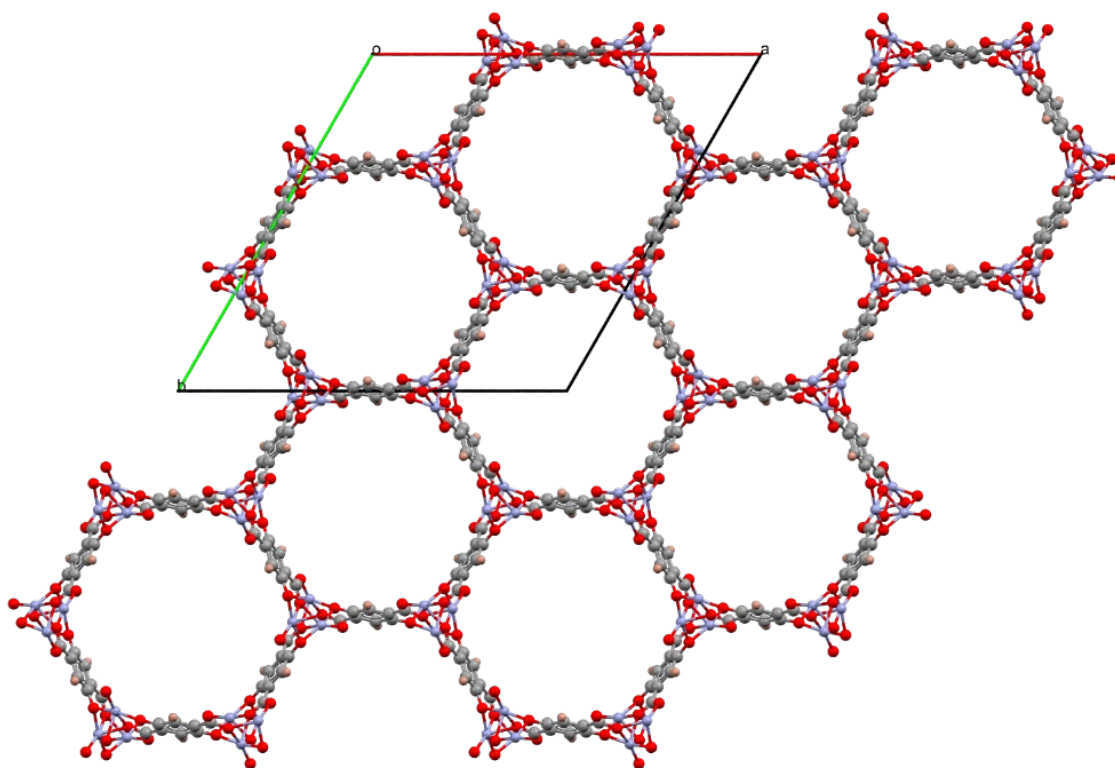


Figure 22 Structure of MOF-74 viewed down the *c*-axis showing the 11 nm diameter pores. Elements shown: carbon (grey), oxygen (red), zinc (blue), hydrogen (pink). Unit cell borders are shown in box, axis labels: a (red) b (green), c (blue).

In the synthesised MOF, each zinc is 6 coordinate in an octahedral configuration. Each of the zinc atoms face-share coordinated oxygens with their neighbours and align down the crystallographic *c*-axis.

In the activated porous structure, each zinc is 5 coordinated with an uncoordinated metal site. Each zinc is coordinated to three carboxyl groups and two hydroxyl groups from the DHTA linker. <sup>116</sup> The zinc atom's coordination environment is a coordinatively unsaturated octahedral arrangement (Figure 23). The crystallographic arrangement of the linker and metal centre remains unchanged in the activated structure with zinc atoms around a centre of inversion down the *c*-axis and the linker sitting on a crystallographic centre of inversion.

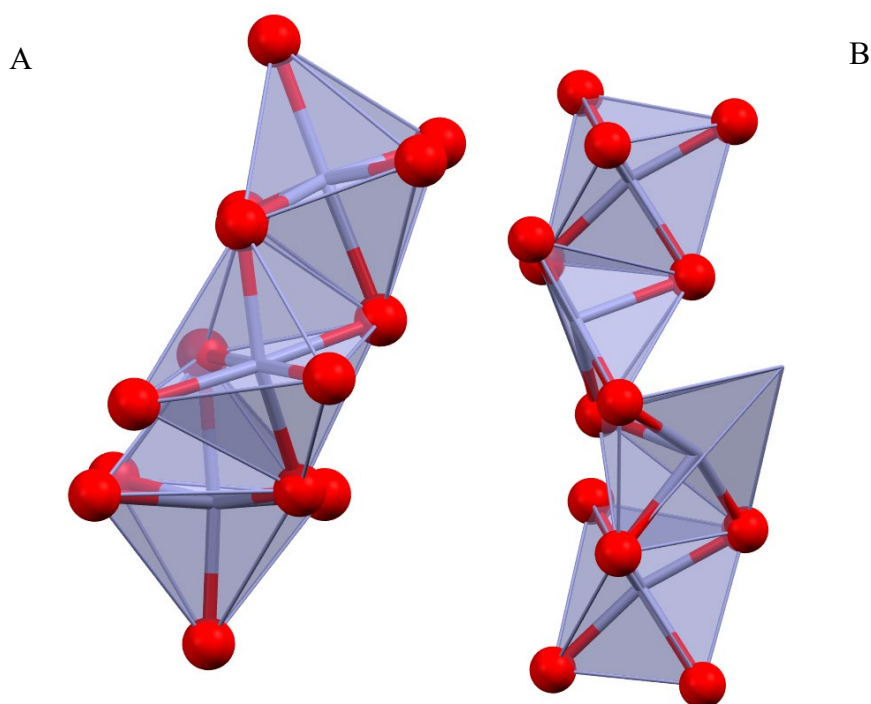


Figure 23a: coordination around synthesised MOF-74-Zn. Figure 23b: coordination around activated MOF-74. Both are distorted octahedra which edge share. Synthesised framework is 6 coordinate while activated framework is 5 coordinate. Coordination shown as see through polyhedra. Atoms present: Zinc (blue), Oxygen (red).

Choosing which metal is used to make MOF-74 affects both its chemical and physical properties. The nickel and magnesium MOF-74 analogues are the most stable, but both require a solvothermal synthesis route and nickel is highly toxic. The zinc variant is only stable in water for around a week at room-temperature<sup>117</sup> but has a much more appealing mechanochemical synthesis route<sup>42</sup> than the traditional solvothermal synthesis route. The combination of reduced water stability and mechanochemical synthesis route make studying the drug release properties of MOF-74-Zn interesting. While the mechanochemical synthesis of MOF-74-Zn has been reported previously, the exact mechanism by which the framework forms is poorly understood. Reported in this chapter are a number of intermediates which form during the mechanochemical synthesis of MOF-74 which help to give an understanding of what leads to the formation of the framework.

## 3.2 Experimental

### 3.2.1 Mechanochemical synthesis of MOF-74 using H<sub>2</sub>O

MOF-74 was synthesised using a Retsch 400MM ball mill. The synthesis method has been outlined in Section 2.1.1.1. 179 mg of ZnO (wurtzite polymorph) (2.2 mmol) and 220 mg of H<sub>4</sub>DHTA (1.1 mmol) were added to a 25 mL stainless steel milling jar to give a reaction ratio of Zn:H<sub>4</sub>DHTA 2:1. 300 µL of deionised water were added to the mixture along with a single 9 g stainless steel milling ball. The jar was sealed, and the materials milled for 90 minutes at a rate of 30 Hz. The resultant powder was washed with 5 mL water to remove left-over starting materials. PXRD of the powder was performed on the Bruker D8 Advance in capillary transmission, as described in Section 2.9.2.5. A Rietveld refinement using the PXRD data was carried out. Three phases, ZnO (wurtzite polymorph), Zn(H<sub>2</sub>DHTA)(H<sub>2</sub>O)<sub>2</sub>, and Zn<sub>2</sub>(DHTA)(H<sub>2</sub>O)<sub>2.8</sub>(H<sub>2</sub>O) were included in the refinement. Parameters refined were: phase fraction, thermal factors, background, zero-point, lattice parameters, and crystallite size and strain. Atomic coordinates were not refined.

### 3.2.2 Mechanochemical synthesis of MOF-74 using DMF

The reaction method was a modified version of the one first used by Julien *et al.*<sup>42</sup>. Milling jar size and solvent volume were changed. MOF-74 was synthesised using the Retsch 400MM ball mill synthesis method outlined in Section 2.1.1.1. 179 mg of ZnO (wurtzite polymorph) (2.2 mmol) and 220 mg of H<sub>4</sub>DHTA (1.1 mmol) were added to a 25 mL stainless steel milling jar to give a reaction ratio of Zn:H<sub>4</sub>DHTA 2:1. 300 µL of DMF were added to the mixture along with a single 9 g stainless steel milling ball. The jar was sealed, and the materials milled for 90 minutes at a rate of 30 Hz. The resultant powder was washed with 5 mL DMF to remove starting materials.



### 3.2.2.1 Optimising Mechanochemical reaction

The method described by Julien *et al.*<sup>42</sup> was first attempted before the conditions in 3.2.2 were found. 180 mg of ZnO (wurtzite polymorph) and 220 mg of H<sub>4</sub>DHTA were added together with 250  $\mu$ L DMF along with two 9 g stainless steel milling balls in a 25 mL jar. The jar was sealed and milled for 90 mins at a rate of 30 Hz. PXRD of the resultant powder was performed.

### 3.2.3 Activation

MOF-74 was activated as outlined in Section 2.1.2.1. Specifically, MOF-74 was first solvent exchanged using methanol by soaking in 40 mL methanol for three days. The methanol was replaced with fresh methanol every day. The MOF sample was then activated by putting the sample under vacuum in a vacuum oven for 3 hours. The sample was then heated to 453 K, still under vacuum, and held at temperature for 24 hours. The oven was then allowed to cool at a rate of 25 K per hour. After the MOF had cooled it was stored in a desiccator.

### 3.2.4 MOF-74 stability in solvents

The stability of MOF-74 in hexane, methanol and a phosphate buffer were assessed. The buffer was prepared as follows: 19 mL of 0.1 M NaH<sub>2</sub>PO<sub>4</sub>·H<sub>2</sub>O were added to 81 mL of 0.1 M Na<sub>2</sub>HPO<sub>4</sub>·7H<sub>2</sub>O. The solution was then diluted to 200 mL and the pH adjusted to 7.4 using drop-wise addition of HCl and NaOH.

In each case, 50 mg of activated MOF-74 were added to 20 mL of solvent. Over time, between 5 and 10 mg of powder were extracted from the solution and PXRD of the powder was performed.

### **3.2.5 PXRD**

Powder patterns of the products of the reactions described above were collected using procedure described in Section 2.9.2.5. Data were collected on the Bruker D8 Advance in capillary configuration with a total scan time of one hour.

### **3.2.6 Elemental analysis**

Elemental CHN analysis was carried out according to method described in Section 2.3. Samples were dried at 60 °C for 24 hours before sending to MEDAC for CHN analysis.

### **3.2.7 IR spectroscopy**

IR spectroscopy was carried out according to procedure outlined in Section 2.4.

### **3.2.8 Gas adsorption measurements**

Gas adsorption measurements were collected according to the procedure outlined in Section 2.12.1.

The “as synthesised” sample was heated to 363 K in an attempt to remove solvent from the pores. The heat was too low to activate the sample; however, the measurement was included to show the properties of non-porous, not-activated MOF-74-Zn.

The activated gas uptake sample was heated to 393 K for 6 hours prior to gas adsorption measurements.

### **3.2.9 Size distribution measurements**

Particle size distribution of synthesised MOF-74-Zn samples were collected according to Section 2.10.

3.2.9.1 Synthesis of MOF-74-Zn using 1  $\mu\text{m}$  particle size zinc oxide and size distribution measurement preparation

180 mg of 1  $\mu\text{m}$  particle size ZnO (wurtzite polymorph) and 220 mg H<sub>4</sub>DHTA were added along with 400  $\mu\text{L}$  of DMF in to a 25 mL stainless steel milling jar along with a single 9 g stainless-steel milling ball. The jar was sealed and milled for 90 minutes at 30 Hz. 10 mg of the MOF-74--Zn sample were dispersed in 100 mL of hexane and sonicated for 20 minutes before size distribution measurement.

3.2.9.2 Synthesis of MOF-74-Zn using 100 nm particle size zinc oxide and size distribution measurement preparation.

180 mg of 100 nm particle size ZnO (wurtzite polymorph) and 220 mg H<sub>4</sub>DHTA were added along with 400  $\mu\text{L}$  of DMF in to a 25 mL stainless steel milling jar along with a single stainless-steel milling ball. The jar was sealed and milled for 90 minutes at 30 Hz. 10 mg of the MOF-74-Zn sample were dispersed in 100 mL of deionised water along with two drops of TWEEN 20. The solution was sonicated for 30 mins to ensure full dispersion before size distribution measurement.

### **3.2.10 SEM of activated MOF-74-Zn sample**

An SEM picture of MOF-74-Zn was collected according to Section 2.8. 3 mg of activated MOF-74-Zn (Section 3.2.2 and Section 3.2.3) were added to the head of a sample pin. The sample was gold sputtered prior to image collection.

### **3.2.11 Investigation of the reaction mechanism**

3.2.11.1 Monitoring the mechanochemical synthesis of MOF-74

H<sub>4</sub>DHTA(DMF)<sub>2</sub> (1): Zinc oxide (0.043 g, 0.53 mmol) and H<sub>4</sub>DHTA (0.100 g, 0.5 mmol) were added to a 5 mL stainless steel grinding jar along with a single 7 g stainless steel

grinding ball and 150  $\mu\text{L}$  of DMF. The jar was sealed and milled at a rate of 30 Hz using a Retsch MM400 shaker type mixer mill. PXRD data were collected at beamline I11 of the DLS according to procedure in Section 2.9.2.5. Samples were taken at 2 mins, 4 mins, 6 mins, 8 mins, 10 mins, 12 mins, 14 mins, 20 mins, 30 mins, 40 mins, 50 mins, 60 mins, 70 mins, 80 mins, and 90 mins. Timings for samples were based on prior experimental work using laboratory X-ray data.

#### 3.2.11.2 Synthesis and structural determination of Intermediate 1

Zinc oxide (0.043 g, 0.53 mmol) and  $\text{H}_4\text{DHTA}$  (0.100 g, 0.5 mmol) were added to a 5 mL stainless steel grinding jar along with a single 7 g stainless steel grinding ball and 150  $\mu\text{L}$  of DMF. The jar was sealed and milled for 2 minutes at a rate of 30 Hz using a Retsch MM400 shaker type mixer mill. PXRD data were collected at beamline I11 of the DLS according to procedure in Section 2.9.2.5, and the powder pattern was confirmed to be a mixture of ZnO (wurtzite polymorph), and **(1)**.

The crystal structure of **(1)** was solved using DASH and EXPO. DASH was used for final structure solution. Input Half  $\text{H}_4\text{DHTA}$  molecule, DMF molecule. Run length: 1 million steps per run over 25 runs. The Structure was further refined using DFT energy minimisation before final rigid body Rietveld refinement in Topas 4.2.<sup>142</sup>

#### 3.2.11.3 Synthesis and structural determination of Intermediate 2

$\text{Zn}(\text{H}_2\text{DHTA})\text{DMF}_2(\text{H}_2\text{O})_2$  (**(2)**): 180 mg ZnO (wurtzite polymorph) (2.2 mmol) and 220 mg DHTA (1.1 mmol) were added to a 25 mL milling jar along with 450  $\mu\text{L}$  DMF and a single 9 g milling ball. The jar was sealed and milled for 15 minutes and left sealed for 4 days. At the end of the four days the jar was opened, and small single-crystals of **(2)** were found. A suitable small plate crystal was found, on which single-crystal X-ray diffraction

was carried out according to Section 2.7 for optical microscopy and Section 2.9.1.1 for single-crystal X-ray diffraction.

It was later found that intermediate 2 can also be synthesised by milling 180 mg ZnO (2.2 mmol) and 220 mg H<sub>4</sub>DHTA (1.1 mmol) in a milling jar with 300 µL DMF and a single 9 g milling ball for 5 minutes at 30 Hz. This reaction results in a mixture of ZnO and (1).

#### 3.2.11.4 Synthesis and characterisation of Intermediate 3

Zn(H<sub>2</sub>DHTA)DMF<sub>2</sub>(H<sub>2</sub>O)<sub>2</sub>: (3) Zinc acetate dihydrate (137.9 mg, 0.75 mmol) and H<sub>4</sub>DHTA (144.584 mg, 0.73 mmol) were added to a 25 mL stainless steel grinding jar along with two 4 g stainless steel grinding balls and 150 µL DMF. The jar was sealed and milled for 60 minutes at a rate of 30 Hz. Data were collected on Diamond I11 according to procedure in Section 2.9.2.5. The resulting powder was determined to be a mixture of Zn(H<sub>2</sub>DHTA)(H<sub>2</sub>O)<sub>2</sub> CCDC refcode ODIPOH, along with Zn(H<sub>2</sub>DHTA)DMF<sub>2</sub>(H<sub>2</sub>O)<sub>2</sub> (2).

The crystal structure of 3 was solved using EXPO. EXPO input

Zn<sub>2</sub>(C<sub>8</sub>O<sub>6</sub>H<sub>4</sub>)<sub>2</sub>(C<sub>3</sub>NOH<sub>7</sub>)<sub>4</sub>(H<sub>2</sub>O)<sub>4</sub>. The input formula matches to two zinc atoms, two H<sub>2</sub>DHTA molecules, four DMF, and four water molecules. Twenty-five trials were each fully refined using EXPO software, with the best solution taken forward. The best EXPO solution was further refined using DFT energy minimisation and final rigid-body Rietveld refinement.

#### 3.2.11.5 Synthesis of Intermediate 4

Synthesis of Intermediate 4 (4): Zinc oxide (178.8 mg, 2.11 mmol) and H<sub>4</sub>DHTA (220.1 mg, 1.05 mmol) were added to a 25 mL stainless steel milling jar along with a single 7 g stainless steel milling ball and 250 µl DMF. The jar was sealed and heated to 60 °C for

60 minutes. The heated sample was milled for 5 minutes at 30 Hz to produce a mixture of (4) and zinc oxide.

### 3.3 Results

#### 3.3.1 Mechanochemical synthesis using water or DMF

Powder X-ray diffraction analysis of data indicates that the nature of the solvent added to the reaction mixture has a major effect on the nature of the product. Figure 24 shows the collected PXRD pattern and Rietveld refined model of the product obtained using water to assist milling. Quantitative phase analysis suggests that after 90 minutes of milling, MOF-74-Zn makes up only 12 % of the weight of the sample (formula  $\text{Zn}_2(\text{DHTA})(\text{H}_2\text{O})_2 \cdot 8(\text{H}_2\text{O})$ ). The presence of ZnO indicates that the reaction did not result in complete conversion of starting materials to MOF-74-Zn.

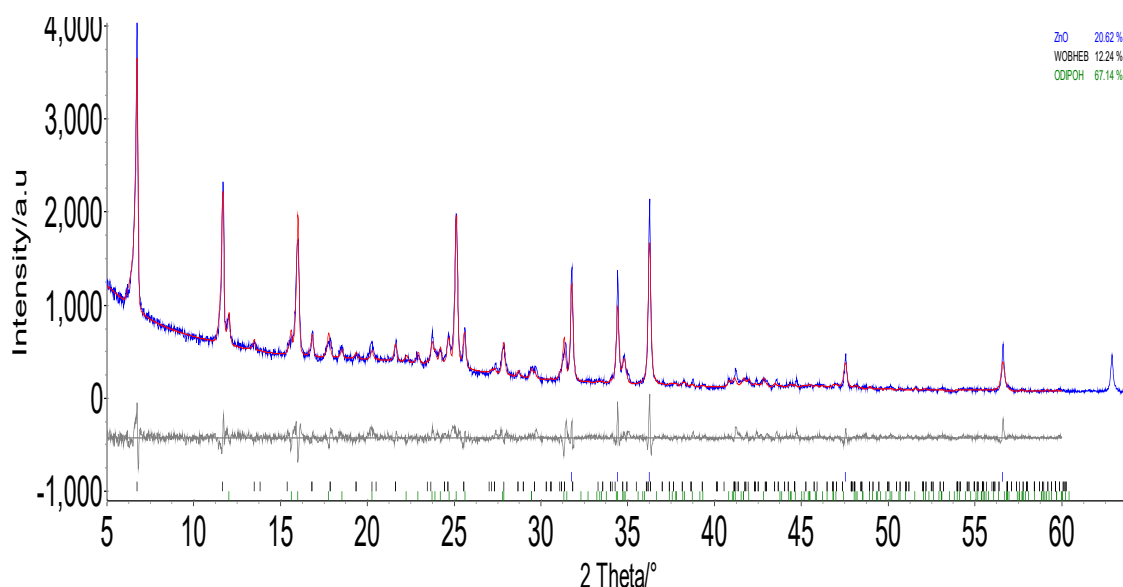


Figure 24 PXRD pattern and Rietveld refinement of attempts to synthesise MOF-74 using water to assist grinding. Phases modelled in Rietveld: ZnO,  $\text{Zn}(\text{H}_2\text{DHTA})(\text{H}_2\text{O})_2$ , and  $\text{Zn}_2(\text{DHTA})(\text{H}_2\text{O})_2 \cdot 8(\text{H}_2\text{O})$ . experimental PXRD (blue), calculated (red), difference curve (grey), hkl indices of phases used in refinement (tick marks).  $\text{Zn}(\text{H}_2\text{DHTA})(\text{H}_2\text{O})_2$  (green),  $\text{Zn}_2(\text{DHTA})(\text{H}_2\text{O})_2 \cdot 8(\text{H}_2\text{O})$  (black), ZnO (blue). Data were collected on Bruker D8 Advance.

Attempts to synthesise MOF-74-Zn using water to assist grinding were unsuccessful at fully converting starting materials to MOF-74. The reaction would quickly form  $\text{Zn}(\text{H}_2\text{DHTA})(\text{H}_2\text{O})_2$ , a reaction intermediate shown to form before MOF-74.<sup>42</sup>

Modifying reaction time, solvent volume, and milling balls had no effect on reaction completion. The synthetic procedure comes from a paper by Julien *et al.* with the only difference being milling jar size.<sup>42</sup> In contrast, reactions using DMF were successful, as shown in the following Section, and the remaining experiments of this chapter focuses on reactions assisted by DMF.

### 3.3.2 Characterisation of MOF-74 prepared using DMF

Shown in Figure 25 is the PXRD pattern and Rietveld model refinement of an attempt at synthesising MOF-74-Zn using the literature method described by Julien *et al.*<sup>42</sup>

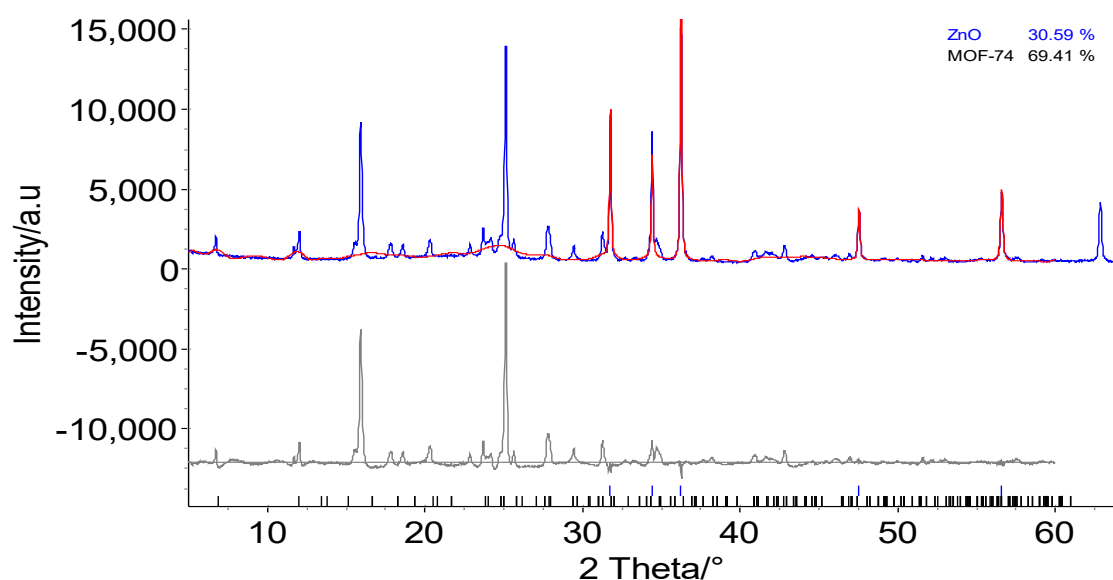


Figure 25 PXRD pattern and Rietveld refinement model of attempts at synthesising MOF-74-Zn using literature reaction conditions. experimental powder pattern (blue), calculated (red), difference curve (grey), hkl indices for two phases used in refinement (tick marks). MOF-74-Zn (black ticks), zinc oxide (blue ticks). Data were collected on Bruker D8 Advance.

The refinement shows that ZnO is still present, but no framework has formed after 90 minutes of milling. At least one crystalline intermediate phase is present. The intermediate phases crystal structures and pattern of formation is discussed further in Section 3.3.7. As MOF-74-Zn did not form using the literature procedure, a modified procedure was developed by changing milling ball mass and solvent volume used in the milling reaction.



### **3.3.3 Optimised MOF-74-Zn synthesis using DMF as milling solvent**

Shown in Figure 26 is the collected PXRD pattern and Rietveld refinement of a MOF-74-Zn sample synthesised using the optimised experimental procedure outlined in Section 3.2.2.1.

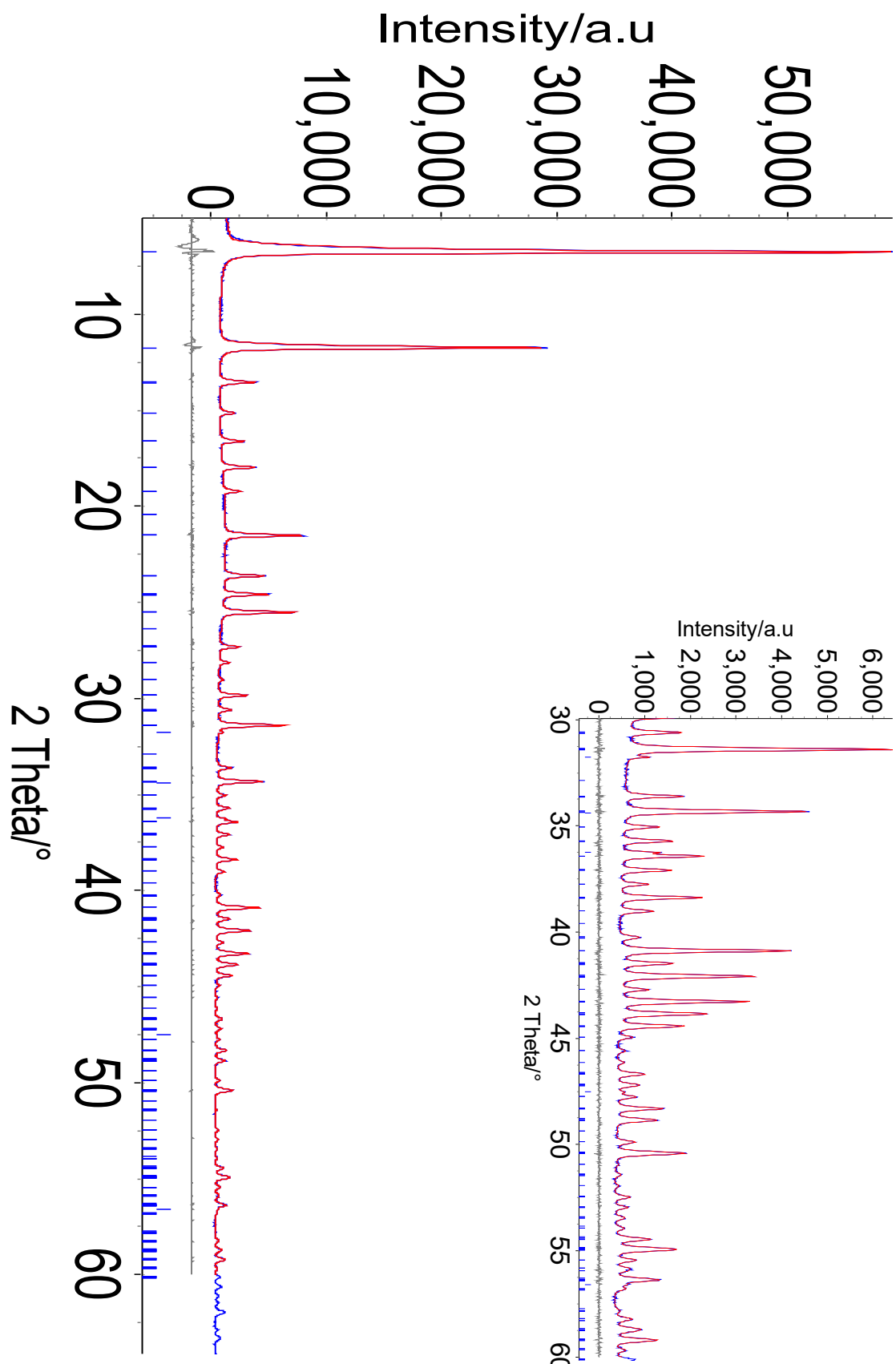


Figure 26 PXRD pattern of MOF-74 with DMF in the pores. Inset shows PXRD pattern at high  $2\theta$ . Experimental (Blue), simulated calculated PXRD (red), difference curve (grey), hkl tick markers for phase used in Rietveld refinement (blue ticks). Data were collected on Bruker D8 Advance.

Lattice parameters were refined initially using a Pawley refinement, in which background, lattice parameters, detector zero point, and crystallite size and strain were refined. The refined parameters were then fixed, and a Rietveld refinement was performed. Atom coordinates, which were not refined, were obtained from the cif CCDC refcode FIJDOS <sup>110</sup> with formula  $Zn_2(C_8O_6H_2).(C_3H_7N)_2(H_2O)_2$ , with DMF and water present in the pores and DMF coordinated to zinc. The parameters refined in the Rietveld were: scale, background, and thermal factors. Table 7 summarises the results of the Rietveld refinement.

Table 7 Results of the Pawley and Rietveld refinements of MOF-74-Zn. Formula:  $Zn_2(C_8O_6H_2).(C_3H_7N)_2(H_2O)_2$ .

<b>Crystal system</b>	<b>Trigonal</b>
<b>Space group</b>	$R\bar{3}$
<b><i>a</i> (Å)</b>	26.037(5)
<b><i>c</i> (Å)</b>	6.857(5)
<b>Volume (Å<sup>3</sup>)</b>	4025.5(5)
<b>R<sub>wp</sub>(%)</b>	6.003
<b>Pawley R<sub>wp</sub></b>	3.594
<b><math>\chi^2</math></b>	5.76

### 3.3.3.1 Elemental analysis

The C, H and N contents of the as-synthesised MOF-74 are shown in Table 8. The calculated elemental analysis on the basis of the composition  $Zn_2(DHTA)(DMF)_2(H_2O)_2$  is in poor agreement with experimental values. The experimental results are in good agreement with an elemental composition of  $Zn_2(DHTA)(DMF)_{0.5}(H_2O)_4$ , in which

most of the DMF has been replaced with water, the water having most likely come from the MOF samples contact with air.

Table 8 Elemental analysis of as-synthesised MOF-74 . (1) predicted formula:  $Zn_2(DHTA)(DMF)_2(H_2O)_2$ . (2) predicted formula  $Zn_2(DHTA)(DMF)_{0.5}(H_2O)_4$

	(1)	(2)	
<b>Element</b>	Predicted (%)	Predicted (%)	Experimental (%)
<b>C/%</b>	33.16	26.32	26.95
<b>H/%</b>	3.98	3.12	3.11
<b>N/%</b>	5.52	1.62	1.73

### 3.3.3.2 IR spectroscopy

The collected IR spectrum is shown in Figure 27. The broad peak at  $3242\text{ cm}^{-1}$  corresponds to the O-H stretch of water. The peak at  $2971\text{ cm}^{-1}$  corresponds to the C-H alkyl stretch from the DMF. The peak at  $1655\text{ cm}^{-1}$  corresponds to a C=O stretch. The peak at  $1545\text{ cm}^{-1}$  corresponds to the C-O stretch where the carboxyl group of DHTA has bonded to Zn. The feature seen at  $2158\text{ cm}^{-1}$  does not seem to correspond to any features in the structure, so is presumably an artefact of background subtraction.

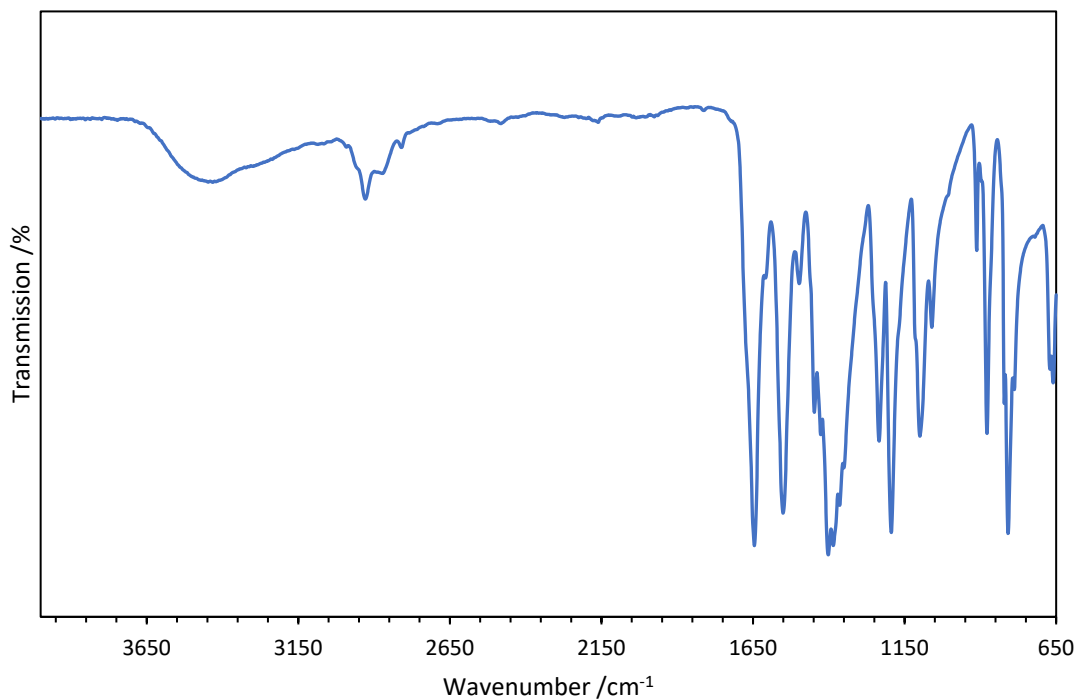


Figure 27 IR spectrum of synthesised MOF-74. Peaks ( $\text{cm}^{-1}$ ): 809 (s), 879 (m), 912 (w), 1044 (m), 1060 (w), 1100 (m), 1194 (s), 1234 (m), 1400 (s), 1497 (w), 1551 (s), 1646 (m), 2868 (w), 2930 (w), 34 (br).

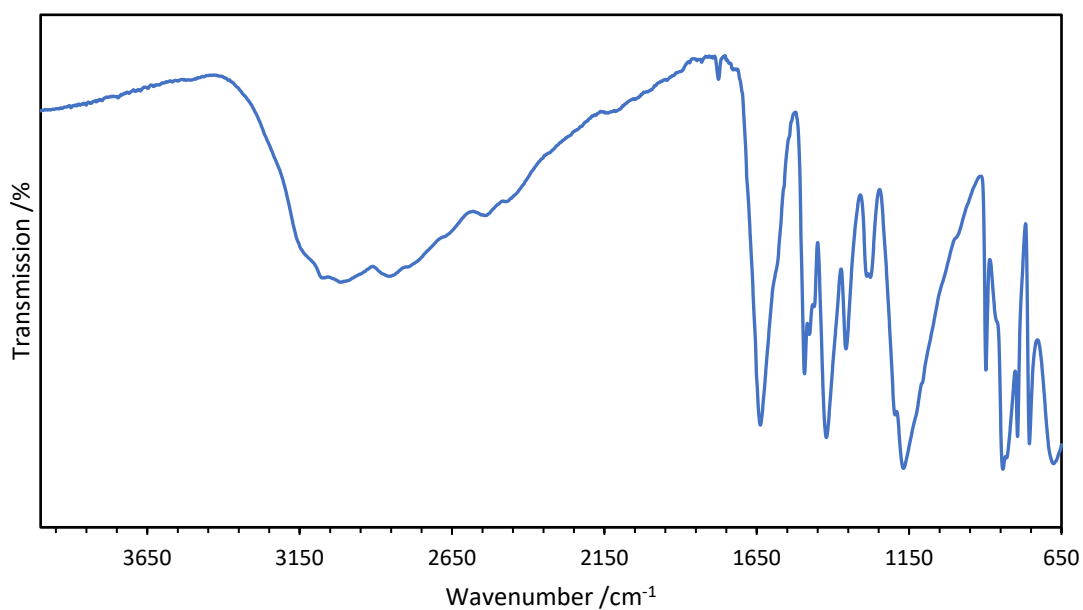


Figure 28 IR spectrum of  $\text{H}_4\text{DHTA}$ . Peaks ( $\text{cm}^{-1}$ ): 674 (br), 755 (s), 794 (s), 843 (s br), 899 (m), 1171 (s br), 1278 (m), 1423 (s), 1493 (m), 1639 (s), 3000 (m br).

Figure 28 shows the collected IR spectra of the  $\text{H}_4\text{DHTA}$  linker. By comparing the spectra's shown in Figure 27 and Figure 28 it is clear that there are significant IR

spectrum differences between the as-synthesised MOF-74-Zn sample and the starting material H<sub>4</sub>DHTA. In particular, the broad stretch at 3000 cm<sup>-1</sup> which corresponds to O-H stretches is completely absent from the MOF-74 sample; this is expected as the OH groups are deprotonated during formation of MOF-74.

### 3.3.3.3 TGA of synthesised MOF-74-Zn

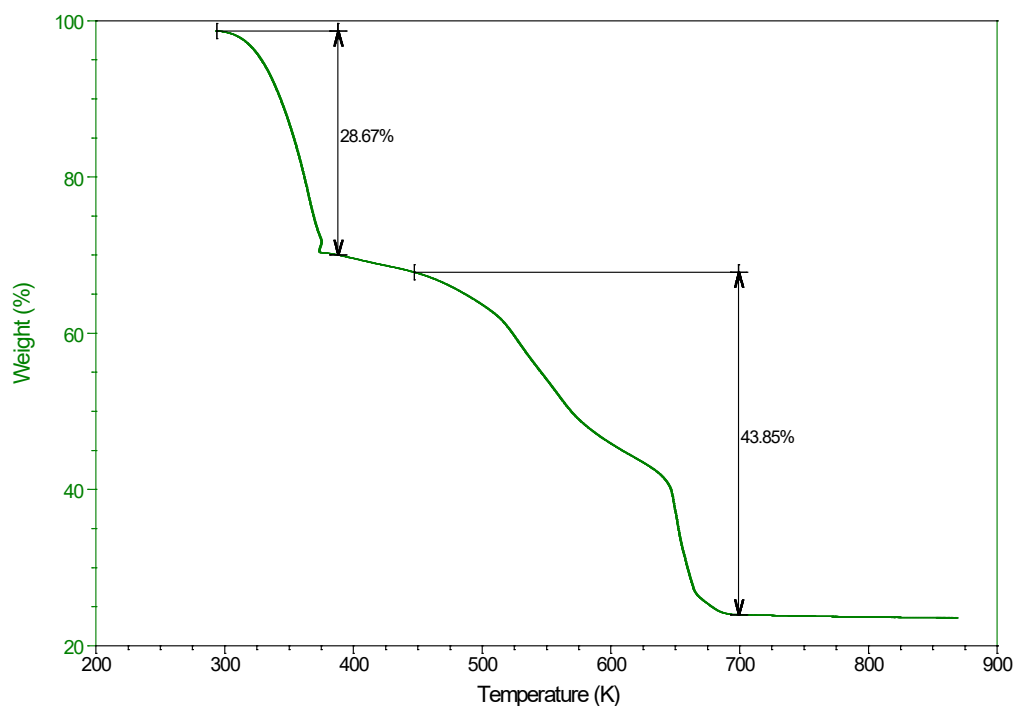


Figure 29 TGA of synthesised MOF-74-Zn in air. Temperature range of collection 293-893 K.

Figure 29 shows the TGA of the as-synthesised MOF-74-Zn sample. The first weight decrease of 28.67% corresponds to the loss of uncoordinated DMF and water from the MOF. The second weight decrease of 43.85% corresponds to the loss of coordinated DMF and the loss of the DHTA linker. The final 25% weight corresponds to the formation of zinc oxide as the sample was combusted in air.

### 3.3.3.4 Surface area analysis of synthesised MOF-74-Zn

Figure 30 shows the BET adsorption and desorption curves of an as-synthesised MOF-74-Zn sample. The adsorption curve is a typical Type II adsorption curve which indicates that the sample is either non-porous or macroporous. Type II adsorption curves are described by monolayer adsorption at low values of  $P/P_0$ , typically this monolayer forms at as low a pressure ratio as 0.05  $P/P_0$ .<sup>154</sup> The linear adsorption region between 0.05  $P/P_0$  and 0.7  $P/P_0$  corresponds to multilayer gas adsorption. The deviation between adsorption and desorption curves indicate that the sample is exhibiting an H3 hysteresis loop, where small irregular pores form from entrances to the porous network being partially blocked. This hysteresis loop is expected for a MOF sample which is not activated.

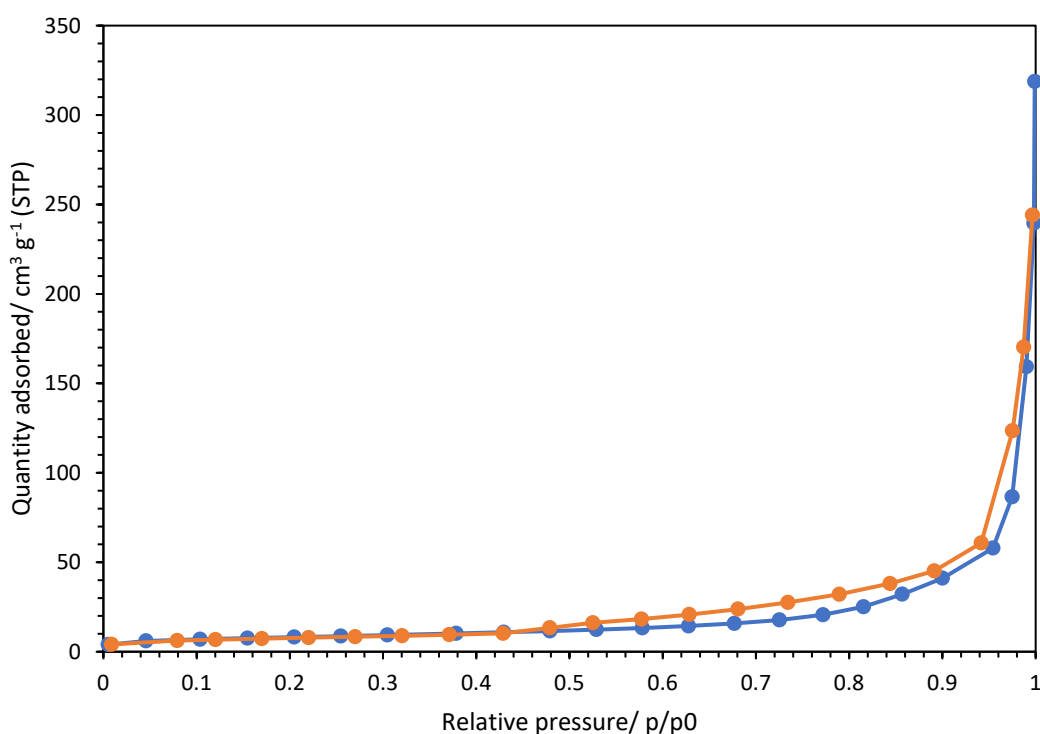


Figure 30 BET adsorption curve of synthesised MOF-74-Zn. (blue) adsorption curve, (orange) desorption curve.

BET surface area was calculated as part of the experiment. The total surface area showed by the sample was 29.2 m<sup>2</sup> g<sup>-1</sup>. This value is significantly smaller than the surface area previously reported for activated MOF-74-Zn samples.

### 3.3.4 Activation of MOF-74-Zn

#### 3.3.4.1 PXRD

The PXRD pattern of an activated MOF-74-Zn sample which was synthesised using the method outlined in 3.2.2 and activated using the method described in 3.2.3 is shown in Figure 31. Analysis shows that no new crystalline phases are present in the sample. The change in relative peak heights indicates that while the unit cell is the same as the unactivated MOF sample the contents of the cell (specifically the molecules in the pores) are different. A CIF based on the work of Dietzel *et al.*<sup>155</sup> which corresponds to MOF-74-Zn with empty pores, CCDC refcode WOBHIF was used as the basis for the Rietveld refinement (Figure 31).

Table 9 Refined Lattice parameters of activated MOF-74 including Pawley and Rietveld Rwp values.

<b>Crystal system</b>	<b>Trigonal</b>
<b>Space group</b>	R $\bar{3}$
<b><i>a</i> (Å)</b>	26.139(8)
<b><i>c</i> (Å)</b>	6.627(3)
<b>Volume (Å<sup>3</sup>)</b>	3921.2(3)
<b>Rietveld R<sub>wp</sub>(%)</b>	5.47
<b>Pawley Rwp (%)</b>	3.42



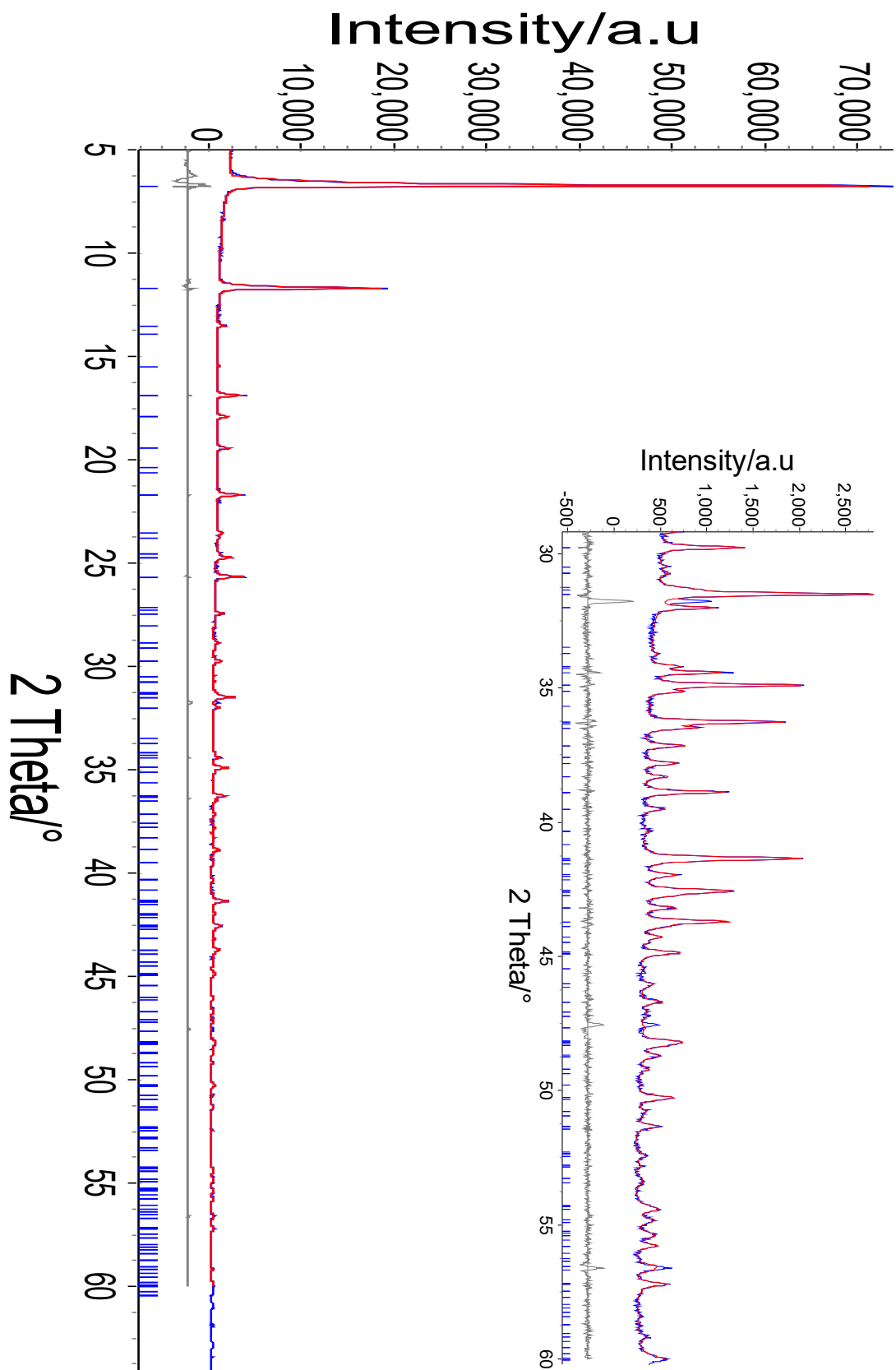


Figure 31 PXRD of activated MOF-74 showing Rietveld refinement. Showing experimental data (blue), model (red), difference curve (grey), hkl tick marks (blue under curve). Inset shows fit between 30 and  $60^\circ 2\theta$ . Inset shows two miss fit peaks at 32 and  $48^\circ 2\theta$  which correspond to a very small amount of unreacted zinc oxide.

The model used in the Rietveld refinement shows good agreement with the experimental data. Two unfitted features are present at 32 and 48 °2 $\theta$ , correspond to ZnO, but in total makes up less than 1% in the refined mass weight percentage of the Rietveld model.

#### 3.3.4.1 Surface area of activated MOF-74-Zn

The adsorption isotherm of the activated MOF collected at 77 K under N<sub>2</sub> is shown in Figure 32. The adsorption curve shown is typical of a Type I adsorption isotherm which corresponds to a microporous structure.

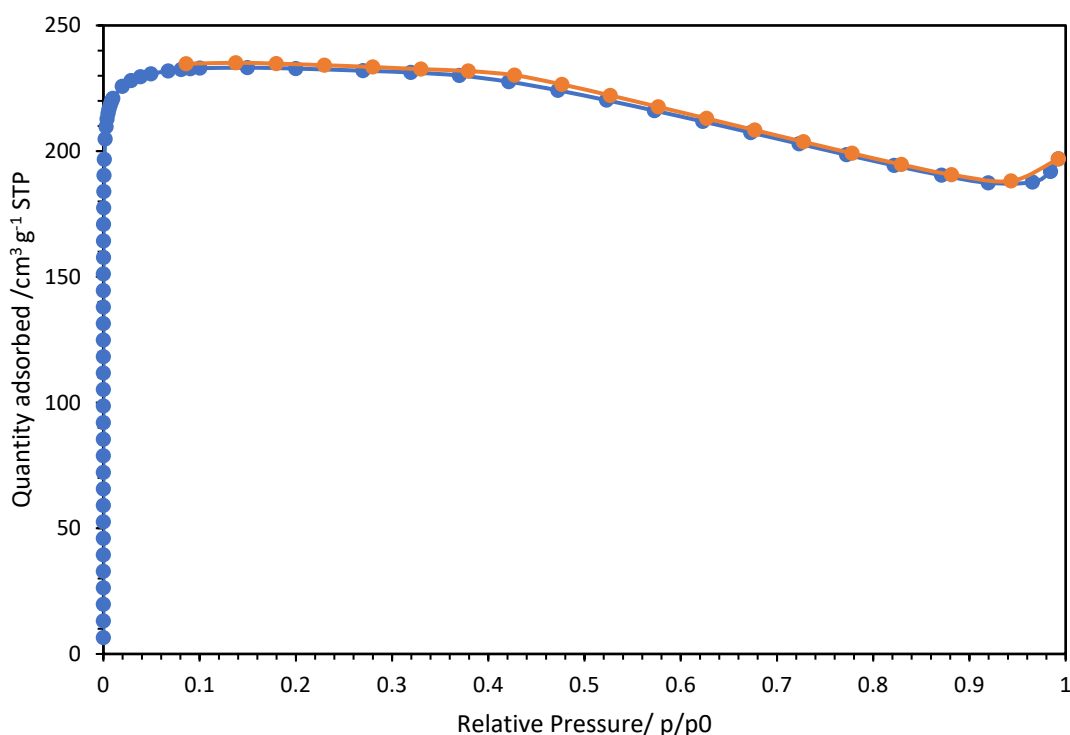


Figure 32 BET adsorption curve of activated MOF-74 at 77K. Plot shows type 1 adsorption isotherm. Adsorption shown as blue dots, desorption shown as orange dots.

The BET surface area was calculated to be 975 m<sup>2</sup>/g, a value smaller than the *theoretical* maximum surface area of 1300 m<sup>2</sup> g<sup>-1</sup>.<sup>156</sup> However, the largest *experimental* surface area measured for MOF-74-Zn is 1100 m<sup>2</sup> g<sup>-1</sup>.<sup>42</sup>

The adsorption and desorption curves are identical, showing that the MOF had not decayed during loading, and that the gas had not become trapped during loading. This lack of hysteresis loop is seen in microporous materials.<sup>157</sup>

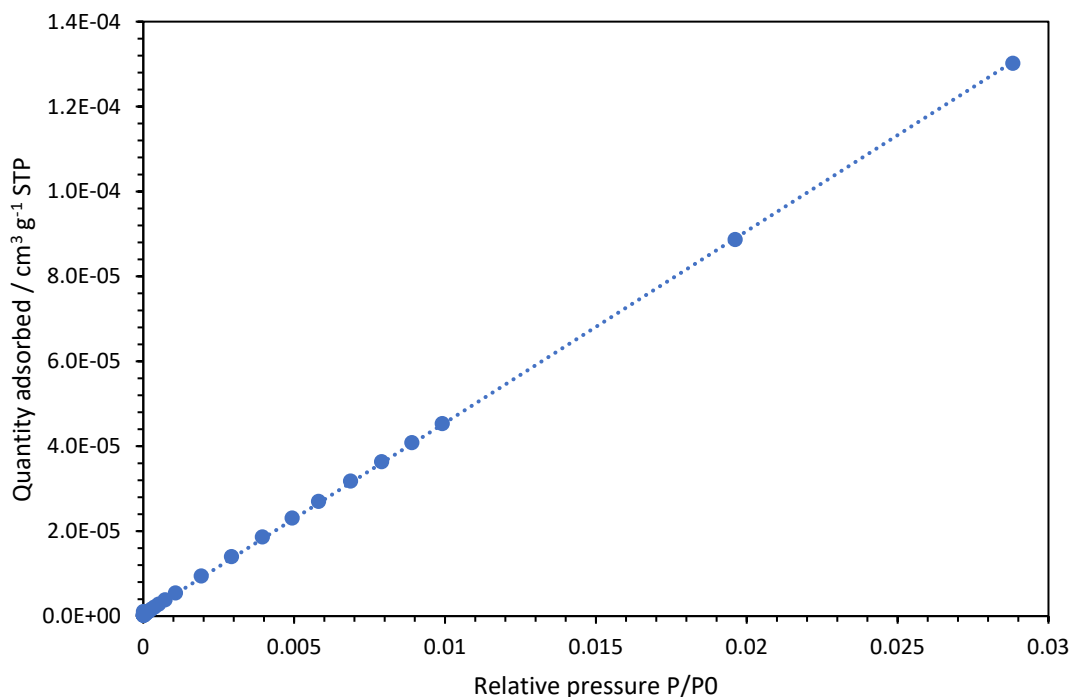


Figure 33 BET surface area change with increasing relative pressure. Trend is linear at low relative pressures.

Figure 33 shows the BET surface area as it changes with increasing relative pressure. The plot is focused on small relative pressures where the BET gas uptake is linear. This linear trend at small relative pressure is common in type 1 isotherms, which further confirms the sample has a microporous structure.

#### 3.3.4.2 IR spectra of activated MOF-74-Zn

The IR spectrum of activated MOF-74-Zn is presented in Figure 34. The IR spectrum has many of the same features as the as-synthesised MOF-74-Zn sample. The lack of peaks at  $2900\text{ cm}^{-1}$  corresponding to secondary amines confirms that DMF has been removed from the sample. However, a broad peak at  $3393\text{ cm}^{-1}$  corresponds to the O-H stretch of water. The strong peak at  $1549\text{ cm}^{-1}$  corresponds to the carboxylic salt C=O stretch. There

is no sign of unreacted H<sub>4</sub>DHTA in the sample which would be visible as a strong broad peak at 1190 cm<sup>-1</sup>. The broad stretch around 3400 cm<sup>-1</sup> corresponds to moisture picked up by the sample during data collection.

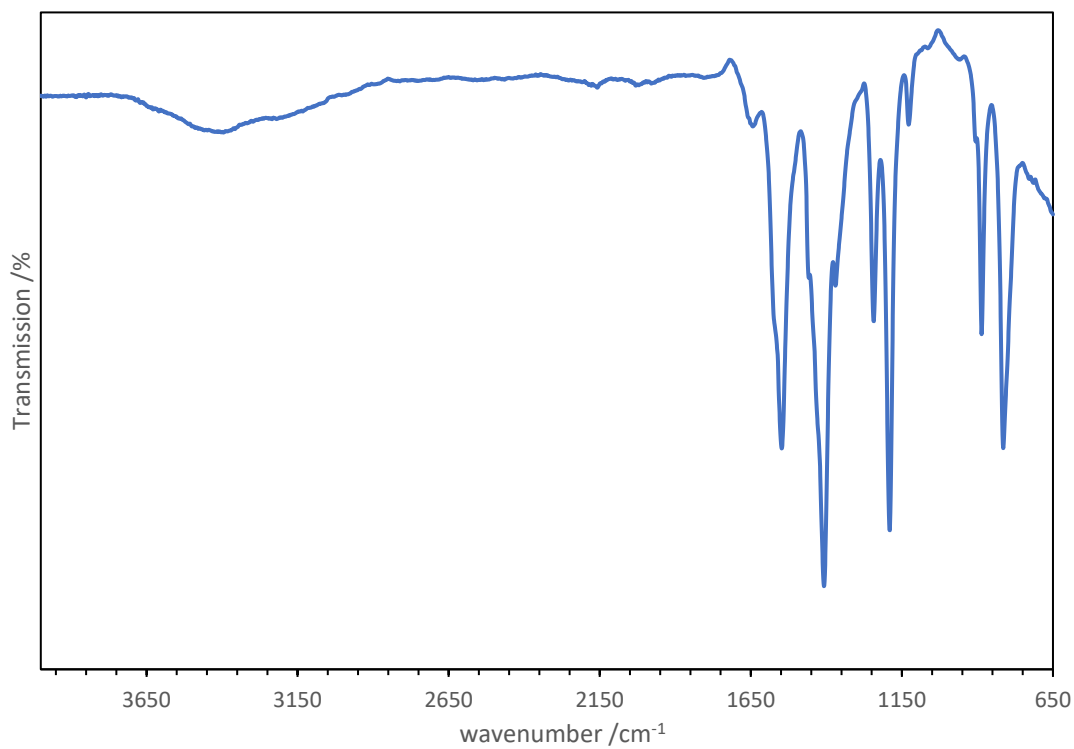


Figure 34 IR spectrum of activated MOF. Peaks 815 (m), 886 (m), 898 (w), 1128 (w), 1191 (s), 1124 (m), 1368 (w), 1408 (s), 1549 (m), 1644 (w), 3393 (wbr).

### 3.3.4.3 TGA of activated MOF-74-Zn

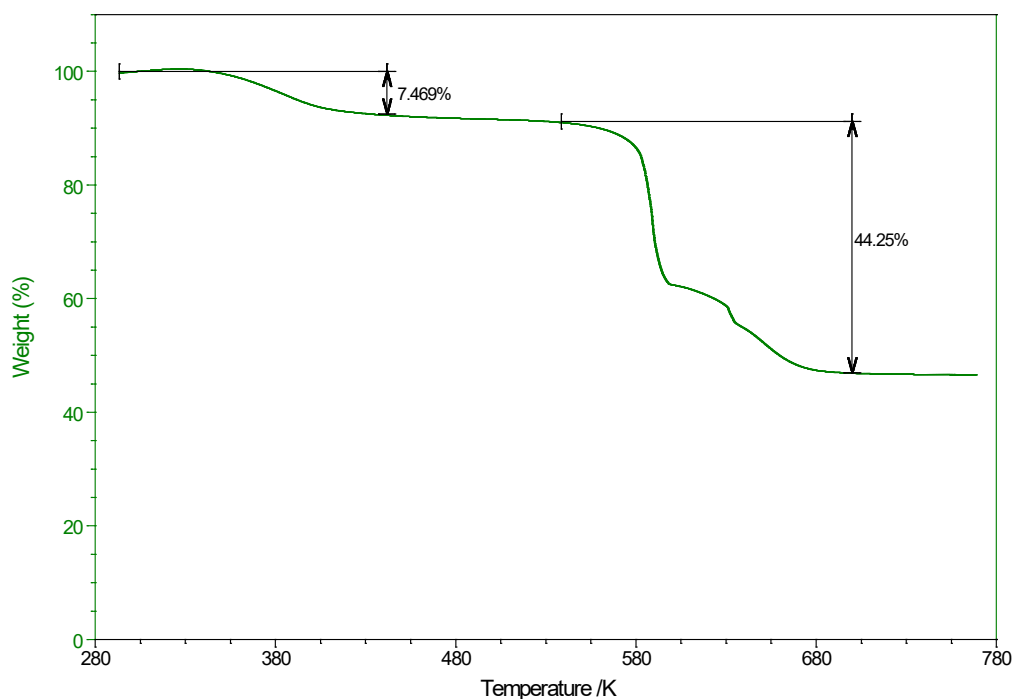


Figure 35 TGA curve of activated MOF-74 sample. The 7% weight drop between 290 and 390 K corresponds to moisture picked up by the sample over the course of 30 mins.

Figure 35 shows the TGA decomposition of the activated MOF-74-Zn sample there is an observable weight increase of roughly 1% between 290 K and 300 K which corresponds to moisture in the air pumped over the sample. The weight decrease shown between 300 K and 450 K corresponds to moisture picked up by the sample during the mounting of the sample on the TGA. The weight drop between 550 K and 700 K can be attributed to the decomposition of the DHTA linker along with the formation of the final product, zinc oxide (Figure 36). One formula unit of DHTA is lost which corresponds to 46% of the total weight, and two formula units of ZnO are formed which leaves the resultant 44% final weight.

A collected PXRD pattern of the sample after TGA leaves only ZnO (Figure 36) showing full decomposition of the framework and the loss of all organic groups by 1053 K leaving only the wurtzite ZnO polymorph present in the sample.

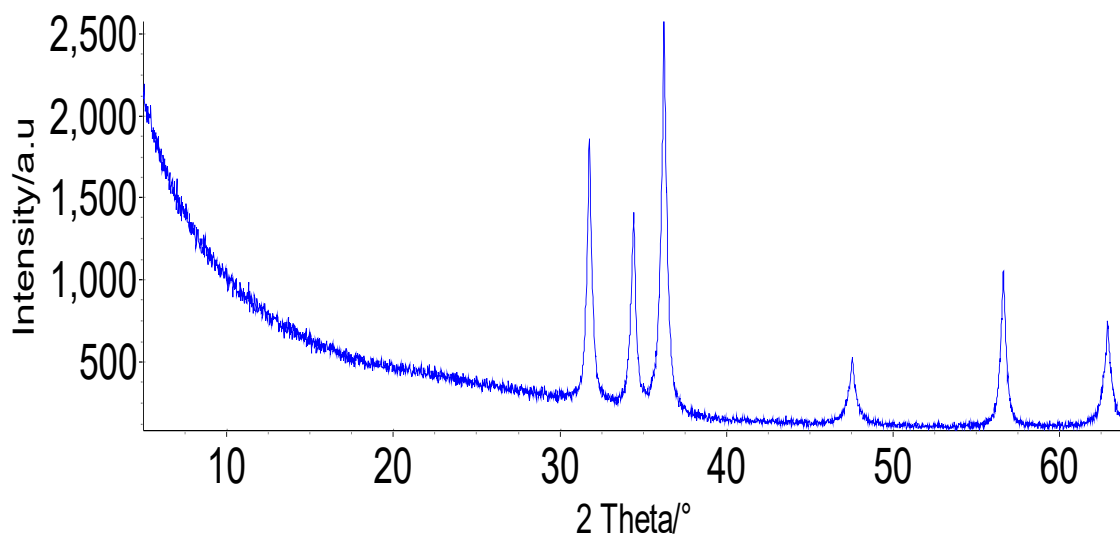


Figure 36 PXRD pattern of activated MOF-74 sample after TGA showing only ZnO phase.

#### 3.3.4.4 Elemental analysis of activated MOF-74

CHN analysis of an activated MOF-74-Zn sample was collected and compared to the predicted formula of  $\text{Zn}_2(\text{C}_8\text{O}_6\text{H}_2)$ , which gives a molecular weight of  $326 \text{ g mol}^{-1}$ . This comparison is presented in Table 10 which indicates that the solvent has successfully been removed from the pores of the framework. There is no evidence of DMF in the pores as there is no nitrogen present in the sample. The results show a small increase in hydrogen content compared to the predicted structure. It can be assumed that the sample took up a small amount of water when sent for analysis. Also presented is the predicted formula if the MOF had only been solvent exchanged, which corresponds to a formula of  $\text{Zn}(\text{C}_8\text{O}_6\text{H}_2)(\text{H}_2\text{O})_8$ . The clearest difference between the activated sample and the water filled sample is the carbon content, with a difference of 10%. As the sample contains 29% carbon and not 20% it can be inferred that the sample has taken up very little water.

Table 10 CHN analysis results of activated MOF-74-Zn sample. Predicted composition  $Zn_2(C_8O_6H_2)$ . Water filled sample uses composition  $Zn(C_8O_6H_2)(H_2O)_8$  and corresponds to MOF-74-Zn after the pores have absorbed a significant amount of water.

Element	Predicted (%)	Experimental (%)	Water filled (%)
C	29.58	29.2	20.40
H	0.62	0.98	4.28
N	0	0	0

### 3.3.5 Stability of MOF-74

#### 3.3.5.1 Stability in air

Exposing activated MOF-74 samples to moist air for prolonged periods affects this material, as illustrated in Figure 37. There are significant differences between the fresh material and activated MOF-74 aged for one month. The relative peak intensities change significantly, partially due to water uptake, but peak intensities also decrease significantly, suggesting degradation of the framework. In addition, a new peak appears at  $10.7^\circ 2\theta$ , which could be attributed to the formation of  $Zn(H_2DHTA)(H_2O)_2$ .<sup>158</sup> However, Pawley refinements using MOF-74-Zn and  $Zn(H_2DHTA)(H_2O)_2$  did not fit well to the experimental diffractogram. The best fit to the experimental pattern comes from a three-component simultaneous Pawley and Rietveld refinement using ZnO, MOF-74-Zn, and lattice parameters of intermediate 4 (see Section 3.3.7.7.). The refinement model fit well to the data with an  $R_{wp}$  of 2.75% (Figure 37). This result indicates that MOF-74-Zn decomposes to a mixture of ZnO and an intermediate structure.

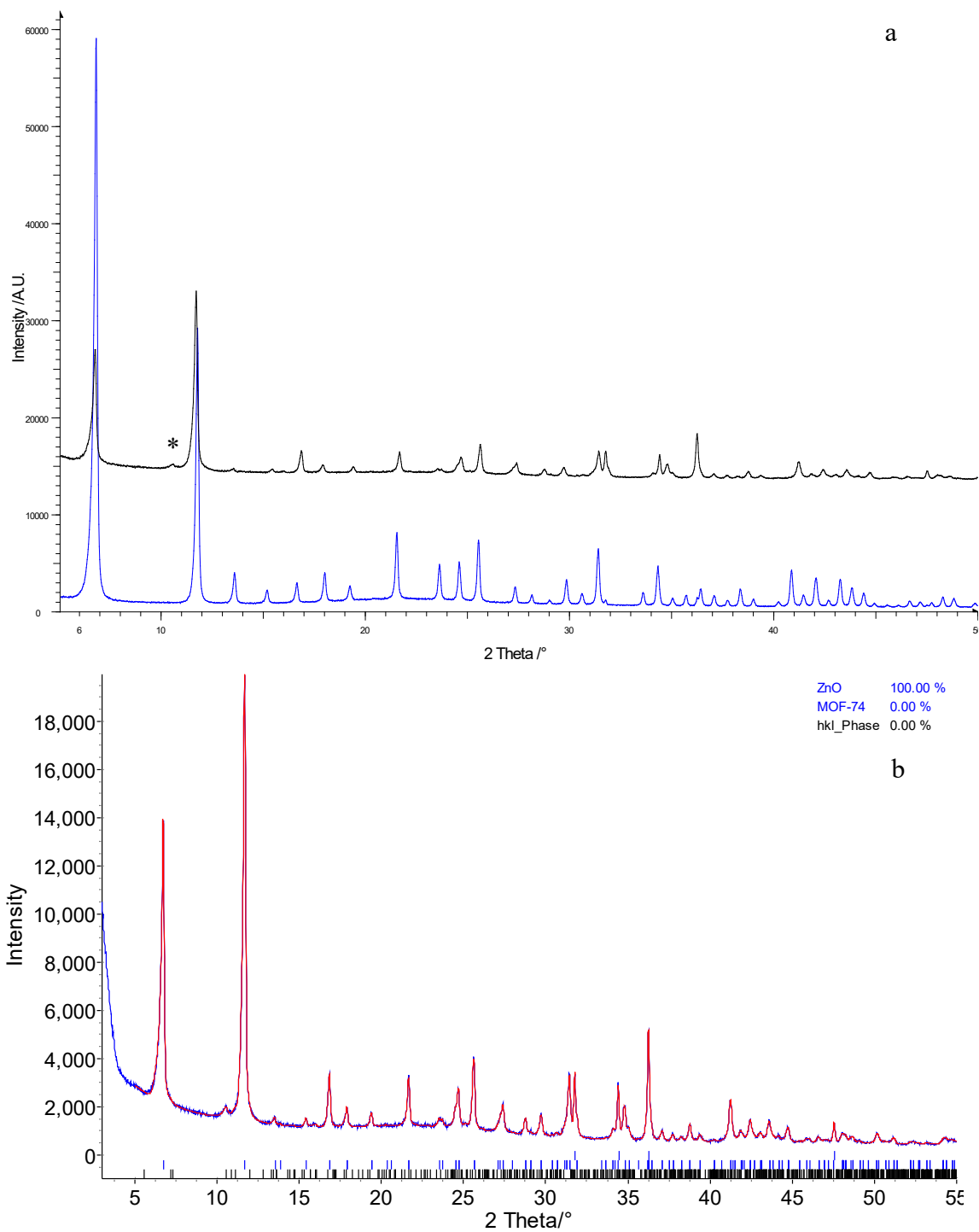


Figure 37 PXRD of activated MOF-74 (blue line) and MOF-74 aged for one month in air (black line). Starred peak corresponds to the most obvious peak of the intermediate phase (a). Simultaneous Pawley and Rietveld refinement of air decomposed MOF-74-Zn. Experimental (blue), calculated (red). Refinement used following phases: zinc oxide, MOF-74-Zn, and 4 (b).



### 3.3.5.1 Methanol

By contrast, powder X-ray diffraction data (Figure 38) collected on a sample soaked in methanol indicates that this material does not change upon exposure to methanol. This is confirmed by Pawley refinements of both datasets, which result in almost identical lattice parameters (Table 11), with comparable Pawley  $R_{wp}$  values of 4.22 and 4.30% for the initial addition and after one week, respectively.

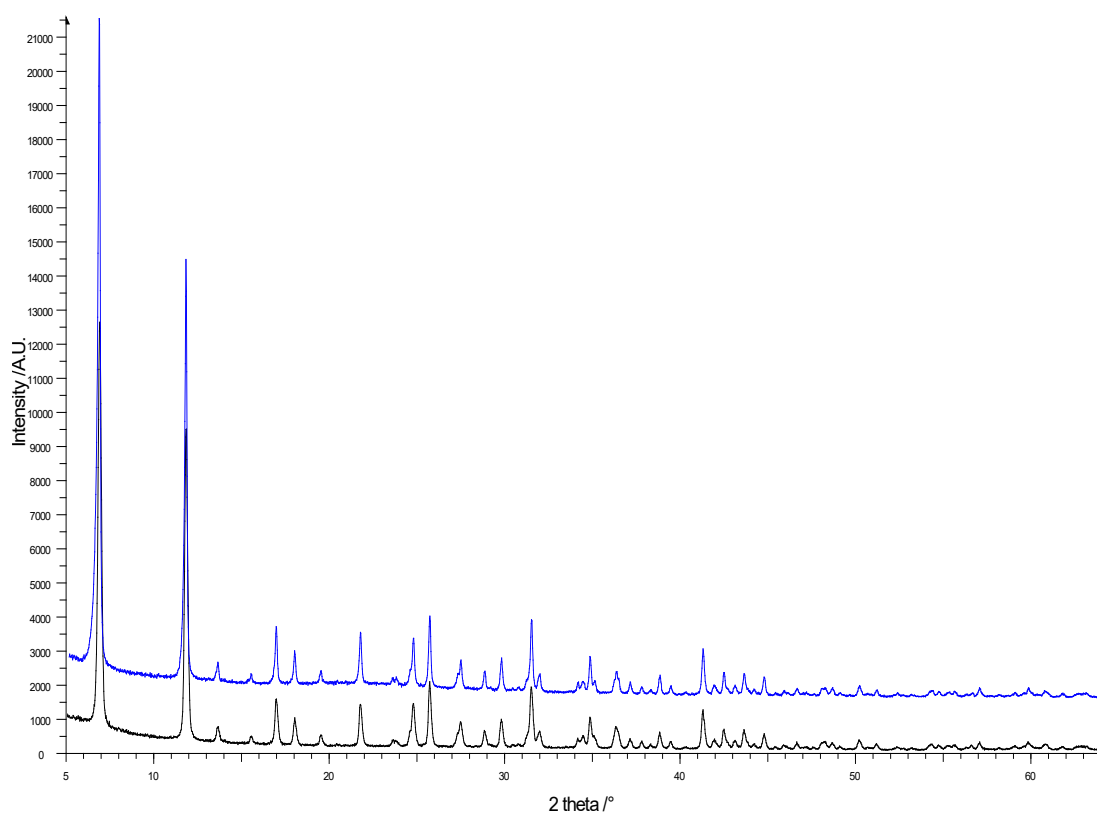


Figure 38 PXRD pattern showing stability of MOF-74 in methanol. PXRD pattern collected straight after adding to methanol (black). sample after one week in methanol (blue).

Table 11 Comparison of lattice parameters of MOF-74 samples in methanol. MOF-74 initial addition after immersion in methanol, and MOF-74 after 1 week in methanol.

	<b>MOF-74 initial addition</b>	<b>MOF-74 after 1 week</b>
<b>Crystal system</b>	Trigonal	Trigonal
<b>Space group</b>	<i>R</i> -3	<i>R</i> -3
<b><i>a</i> (Å)</b>	26.16(4)	26.37(5)
<b><i>c</i> (Å)</b>	6.64(3)	6.85(5)
<b>Volume (Å<sup>3</sup>)</b>	3941.3(4)	4025.5(5)

### 3.3.5.2 Stability in phosphate buffer.

When the MOF is exposed to a phosphate buffer (Figure 39) the framework decays. This can be most clearly seen in the PXRD pattern as peak intensities of MOF-74 decrease over time and the amorphous background increases. As the MOF peak intensities decrease, new peaks appear, most clearly seen after two months (starred peak in Figure 39).

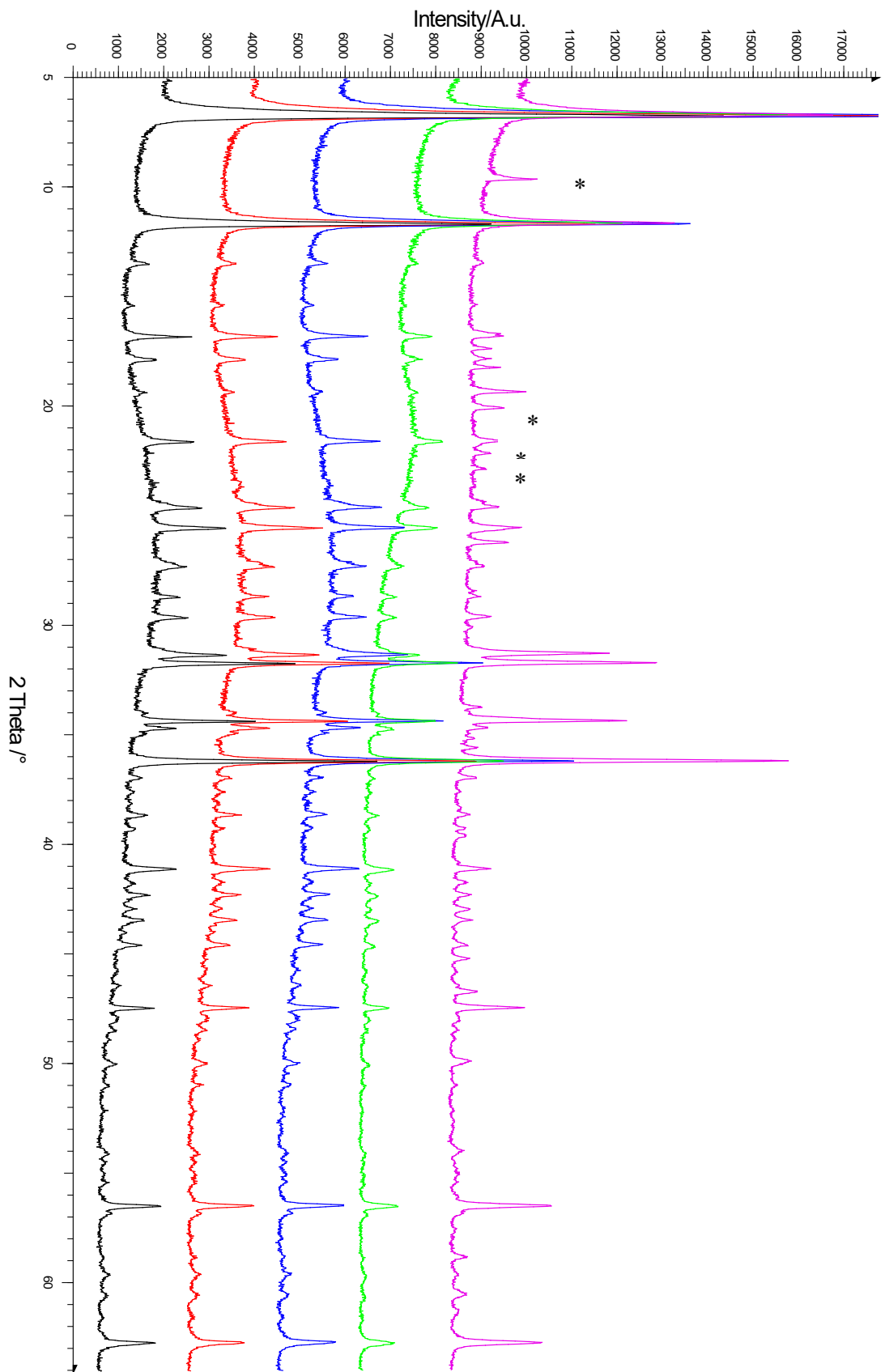


Figure 39 Powder patterns of MOF-74 exposed to a phosphate buffer for increasing amounts of time. Key: initial material (black). 1-hour exposure (red). 2 hours (blue). 48 hours (green). 2 months (pink). Stars show first three peaks of a new phase that forms as the MOF decomposes.

After two months the appearance of a new phase is evident (stars on Figure 39). This new phase was indexed (Table 12) using TOPAS with determined lattice parameters used in a simultaneous Pawley and Rietveld refinement along with ZnO and MOF-74-Zn phases (Figure 40).

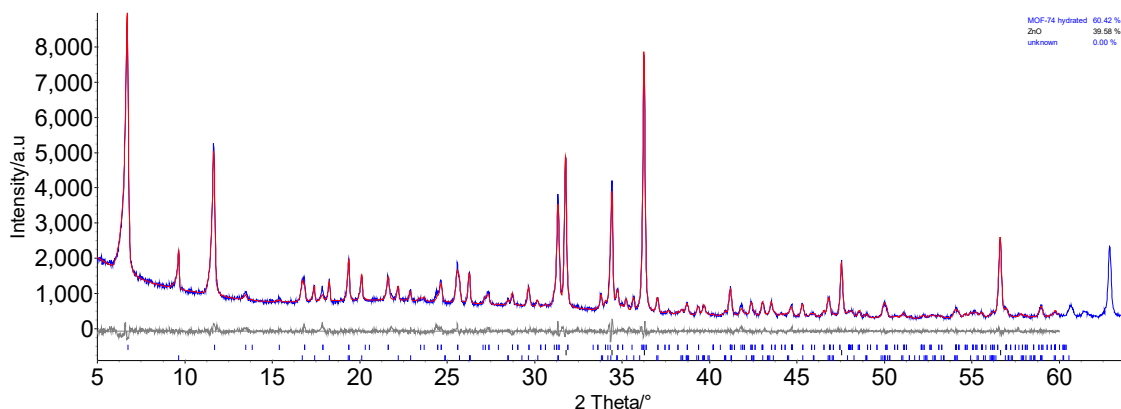


Figure 40 Simultaneous Pawley and Rietveld refinement using the powder diffraction pattern of MOF-74 exposed to a phosphate buffer for 2 months. Rietveld component: ZnO, MOF-74-Zn ( $\text{Zn}_2(\text{DHTA})(\text{H}_2\text{O})_2 \cdot (\text{H}_2\text{O})_8$ )

Searches on crystallographic databases have been carried out to identify this phase, but no matches have been found, indicating that this phase is most likely novel. The volume of the unit cell is very similar to the structure discussed in Section 6.3.2, which is a hydrated potassium salt of  $\text{H}_2\text{DHTA}$ . It is possible that this phase is a sodium salt of  $\text{DHTA}$ , or a new polymorph of the  $\text{H}_4\text{DHTA}$  hydrate.<sup>159</sup>

Table 12 Lattice parameters of new phase found from MOF-74-Zn decomposition in phosphate buffer.

<b>Crystal system</b>	<b>Monoclinic</b>
<b>Space group</b>	<i>P2<sub>1</sub>/c</i>
<b><i>a</i> (Å)</b>	5.296(4)
<b><i>b</i> (Å)</b>	18.291(2)
<b><i>c</i> (Å)</b>	5.030(2)
<b><math>\beta</math> (°)</b>	89.91(2)
<b>Volume (Å<sup>3</sup>)</b>	487.320(9)
<b>Pawley R<sub>wp</sub></b>	4.698

### 3.3.6 Particle size of synthesised MOF-74-Zn samples

The particle size of MOF-74-Zn samples was measured using size distribution analysis and SEM with results presented below.

#### 3.3.6.1 Size distribution

Figure 41 presents the particle size distribution of MOF-74-Zn samples. Figure 41a presents the particle size of MOF-74-Zn samples synthesised using 1  $\mu\text{m}$  particle diameter ZnO. The synthesised MOF-74-Zn samples have a diameter range between 4 and 8  $\mu\text{m}$ . Using smaller particle diameter ZnO results in smaller MOF-74-Zn particle size as seen in Figure 41b. The MOF sample in Figure 41b was synthesised using 100 nm diameter ZnO which resulted in significantly smaller MOF particles with a size range between 100 nm and 400 nm.

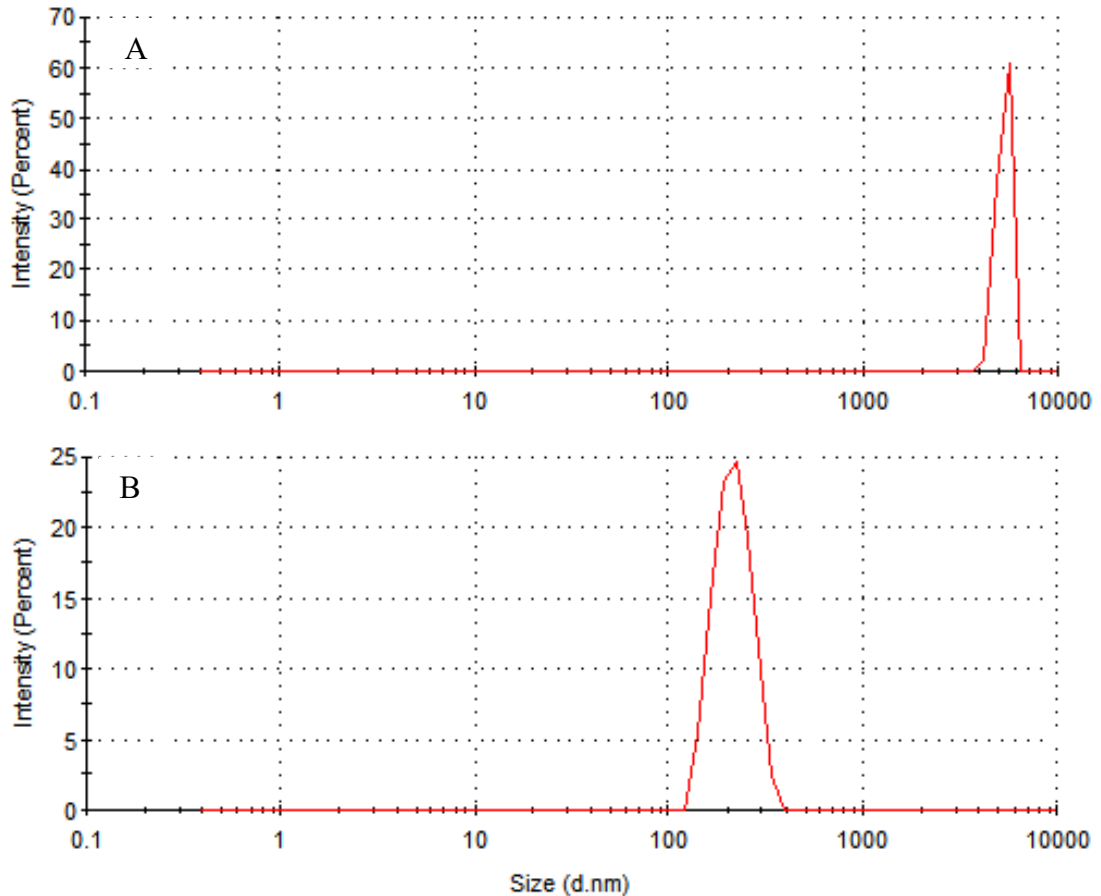


Figure 41 Particle size distribution of MOF-74-Zn samples. (A) size distribution using 1  $\mu\text{m}$  particle size ZnO. (B) Particle size using 100 nm particle size ZnO.

### 3.3.6.2 SEM

SEM of the activated MOF-74-Zn sample synthesised using 1  $\mu\text{m}$  zinc oxide (Figure 42) which confirms that the MOF-74-Zn particles are smaller than 1  $\mu\text{m}$ . The entire image spans roughly 80  $\mu\text{m}$  x 80  $\mu\text{m}$  with the MOF-74-Zn sample still appearing as a powder. During the image collection the MOF was found to charge significantly even after coating with gold preventing higher resolution images from being collected.

Overall this measurement agrees with the size distribution method, but collection on a higher resolution electron microscope would be required to more accurately confirm the framework particle size.

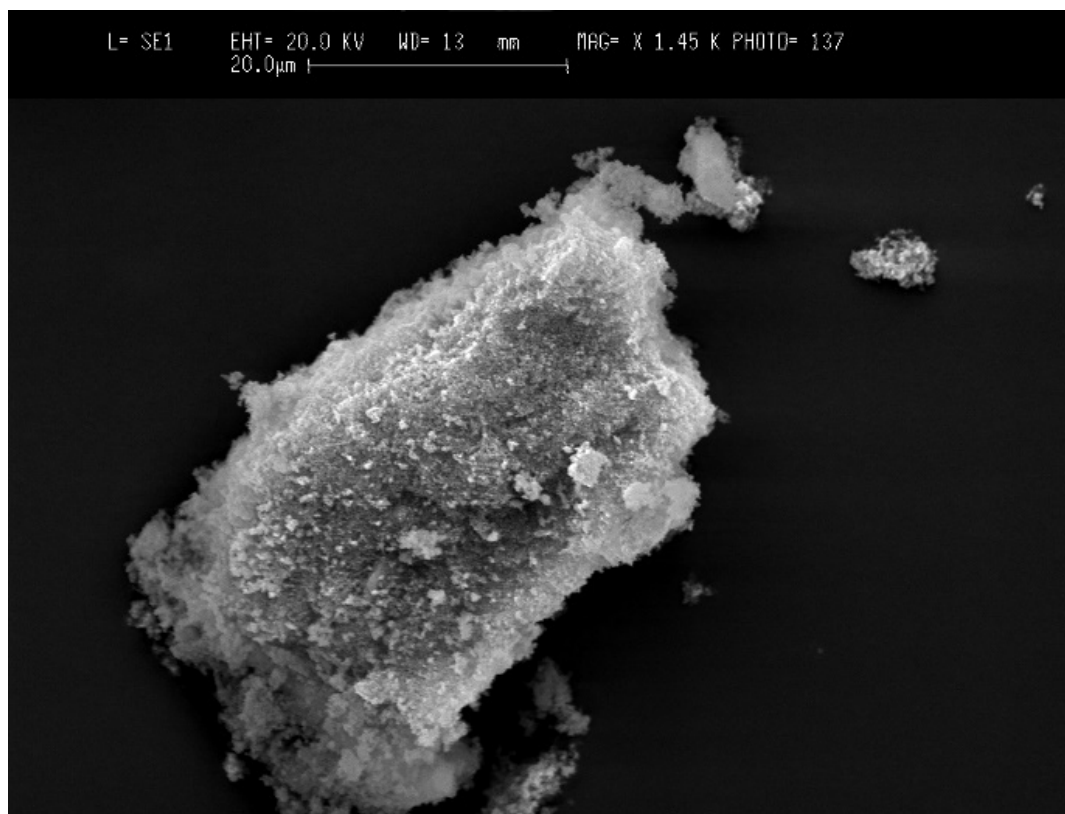


Figure 42 SEM of MOF-74-Zn sample. Scale of image 80  $\mu\text{m}$  x 80  $\mu\text{m}$ . Sample coated in gold monolayer to increase conductivity.

### 3.3.7 MOF-74-Zn reaction intermediates

While experimenting with the MOF-74 mechanochemical synthesis method, several semi-stable reaction intermediates were identified. Due to the short-term stability of these phases, approximately 24 hours before complete disappearance, high quality PXRD data were required, as only one of the intermediate structures grew crystals large enough for single-crystal X-ray diffraction. All other data were collected on Diamond I11 high-resolution powder diffraction beamline. Figure 43 shows the time resolved PXRD datasets collected during the mechanochemical reaction to form MOF-74-Zn. As can be

seen, there are large changes as phases form and disappear early in the milling reaction with a number of strong peaks appearing and disappearing throughout the reaction.

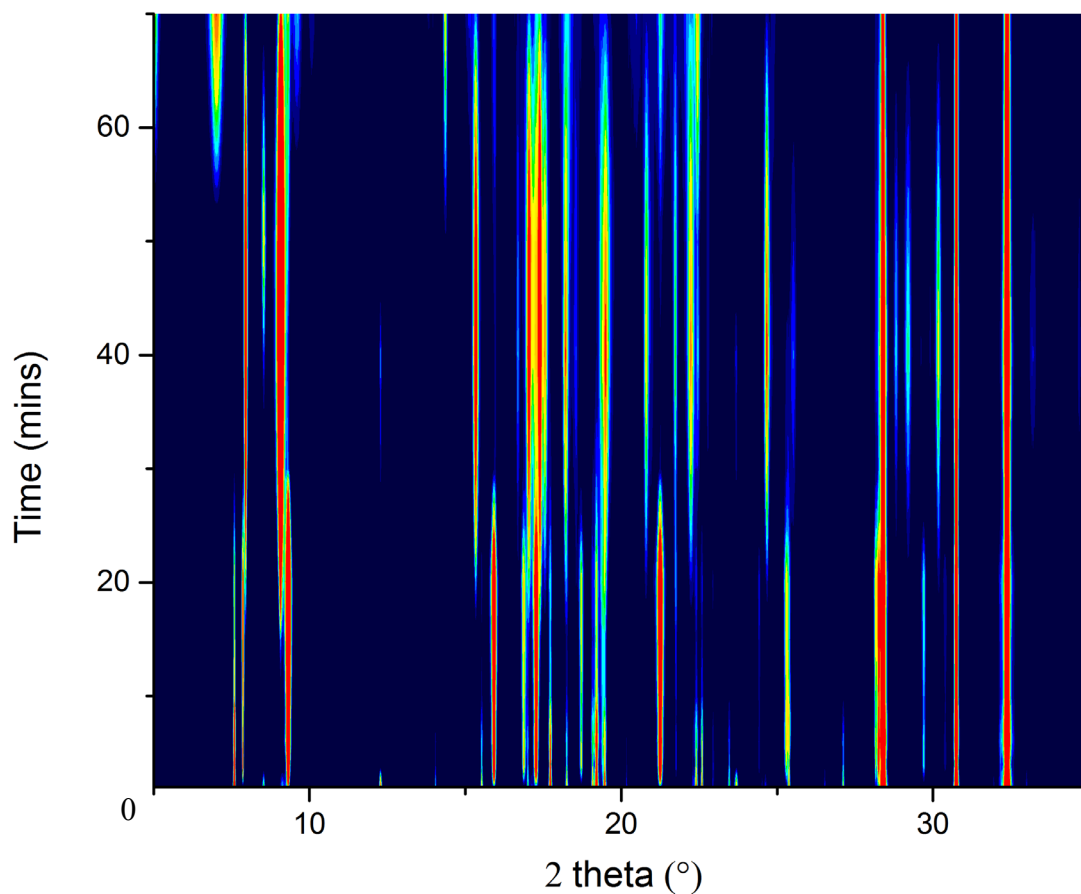


Figure 43 Time-resolved PXRD pattern of the mechanochemical synthesis of MOF-74. Colour scale indicating intensities with blue, lowest intensity, red highest intensity.

Table 13 shows the lattice parameters of the MOF-74-Zn intermediates along with refinement information where information is known.



Table 13 Lattice parameters and refinement values for intermediates formed in the mechanochemical synthesis of MOF-74 along with MOF-74 lattice parameters. 4 corresponds to a currently only indexed intermediate. MOF-74 is included in table to compare lattice parameters of intermediates to lattice parameters of final product. Data/restraints/parameters field used for number of parameters in powder structure solution data.

Identifier	1	2	3	4	MOF-74
<b>Solution method</b>	Powder diffraction	Single-crystal	Powder diffraction	Powder diffraction	CIF from paper <sup>110</sup>
<b>Empirical formula</b>	C <sub>14</sub> H <sub>20</sub> N <sub>2</sub> O <sub>8</sub>	C <sub>14</sub> H <sub>22</sub> N <sub>2</sub> O <sub>10</sub> Zn	C <sub>14</sub> H <sub>22</sub> N <sub>2</sub> O <sub>10</sub> Zn		Zn <sub>2</sub> C <sub>11</sub> O <sub>8</sub> H <sub>20</sub> N
<b>Formula weight</b>	344.32	443.73	443.73		424
<b>Temperature (K)</b>	293	250(3)	293	293	153(3)
<b>Crystal system</b>	Monoclinic	Triclinic	Monoclinic	Triclinic	Trigonal
<b>Space group</b>	<i>P</i> 2 <sub>1</sub> / <i>n</i>	<i>P</i> -1	<i>P</i> 2 <sub>1</sub> / <i>c</i>	<i>P</i> -1	<i>R</i> -3
<b><i>a</i> (Å)</b>	5.92029(5)	5.415(5)	10.01162(6)	17.201(5)	26.037(5)
<b><i>b</i> (Å)</b>	20.8177(2)	8.709(5)	5.41376(3)	14.317(6)	26.037(5)
<b><i>c</i> (Å)</b>	6.87864(8)	10.118(5)	17.55111(11)	7.423(7)	6.857(5)
<b><i>α</i> (°)</b>	90	82.786(5)	90	114.87(3)	90
<b><i>β</i> (°)</b>	98.0970(7)	89.035(5)	96.8507(7)	88.88(9)	90
<b><i>γ</i> (°)</b>	90	78.215(5)	90	110.31(5)	120
<b>Volume (Å<sup>3</sup>)</b>	839.319(15)	463.4(6)	944.487(10)	1538.06(4)	4025.5(5)
<b>Z</b>	2	1	2		18
<b>ρ<sub>calc</sub> g (cm<sup>3</sup>)</b>		1.590			
<b>μ (mm<sup>-1</sup>)</b>		2.363			
<b>F(000)</b>		230.0			
<b>Crystal size/mm</b>		0.1 × 0.1 × 0.05			
<b>Radiation (Å)</b>	1.381246	CuKα (λ = 1.54184)	1.381246		
<b>2Θ range for data collection (°)</b>		8.81 to 138.938			
<b>Index ranges</b>		-6 ≤ h ≤ 5, -10 ≤ k ≤ 10, -10 ≤ l ≤ 12			
<b>Reflections collected</b>					
<b>Independent reflections</b>	744		381		
<b>Data/restraints/parameters</b>	62	1689/0/148	53		
<b>Goodness-of-fit on F<sup>2</sup></b>		1.047			
<b>Final R indexes [I ≥ 2σ (I)]</b>		R <sub>1</sub> = 0.0344, wR <sub>2</sub> = 0.0803			
<b>Final R indexes [all data]</b>		R <sub>1</sub> = 0.0391, wR <sub>2</sub> = 0.0829			
<b>Largest diff. peak/hole (e Å<sup>-3</sup>)</b>		0.25/-0.36			
<b>R factors(Pawley, Rietveld) (%)</b>	1.62, 2.84	4.53	8.01, 9.93		6.003, 6.55

### 3.3.7.1 Structure determination of intermediate 1

Intermediate 1 forms after only 2 mins of milling. The powder diffraction pattern of intermediate 1 was collected at beamline I11 of the DLS. Intermediate 1's lattice parameters were indexed using DICVOL as implemented in DASH. As multiple phases were present in the powder pattern, the intensities corresponding to intermediate 1 needed to be extracted. A Pawley refinement was used to model the intermediate 1 phase and extract peak intensities. As the peaks corresponding to zinc oxide were unchanged from a starting mixture it was inferred that the new phase did not contain Zn, which meant that intermediate 1 was most likely a solvate of the H<sub>4</sub>DHTA linker. The only known solvate structure was that of C<sub>8</sub>O<sub>6</sub>H<sub>6</sub>(H<sub>2</sub>O)<sub>2</sub>, which is a water solvate of H<sub>4</sub>DHTA.<sup>160</sup>

The structure of intermediate 1 was solved from powder diffraction data using a mixture of DASH and EXPO. A partial structure solution was found by using EXPO direct methods. It was assumed that no zinc was present in the crystal structure. Taking into account the Hoffmann volumes (crystallographic volumes of individual atoms) of the predicted formula, it was possible to estimate and compare the possible formulae of intermediate 1.<sup>161</sup>

Table 14 shows the calculated unit-cell volume of intermediate 1 which was calculated using atomic volumes corresponding to C<sub>28</sub>H<sub>36</sub>N<sub>4</sub>O<sub>16</sub> (four DMF molecules and two H<sub>4</sub>DHTA molecules). Table 14 also shows the unit-cell volume calculated from a Pawley refinement of intermediate 1. The close agreement in unit-cell volume between the predicted cell volume and Pawley cell volume led to the use of the predicted formula as a structure solution input. This resulted in the partial structure shown in Figure 44, which provided useful information with regards to the nature of this intermediate.

Table 14 Comparison of predicted cell volume and Pawley unit-cell volume in intermediate 1. Predicted cell was calculated using 7 carbons, 10 hydrogens, 1 nitrogen, and 4 oxygens.

Element	Volume of single atom	Number of atoms	Volume of sum of atom	Total volumes
C	13.87	28	388.36	Predicted cell volume
H	5.08	36	182.88	800.2
N	11.8	4	47.2	Pawley cell volume
O	11.39	16	181.76	839

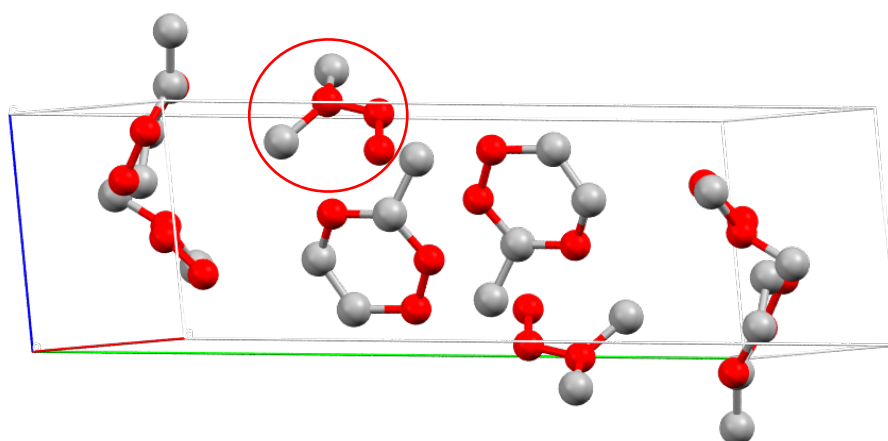


Figure 44 EXPO best solution for solving intermediate 1, atoms are incorrectly assigned. Elements: C (grey), oxygen (red).

Figure 44 shows the best solution found using EXPO, while some parts of the structure look reasonable the structure is clearly incorrect. The DMF molecule sitting on general positions (red circle in Figure 44), can be identified. The fact that benzene rings formed at all was strong evidence that the input atomic composition was correct. The terephthalic acid is incomplete and, although sitting on a general position, sits very close to a special position. In almost all other cases of crystal structures containing DHTA the centre of the molecule sits on a special position.<sup>160 162 163 164</sup> Using this information DASH was then used to solve the structure of intermediate 1 using the following fragments: 1xDMF molecule, 0.5xH<sub>4</sub>DHTA (Figure 45). The half H<sub>4</sub>DHTA molecule was anchored to a special position.

DASH uses Z-matrixes as inputs for solving crystal structures from powder diffraction data (Figure 45). The inputs used in the Z-matrixes correspond to the asymmetric unit of the crystal structure. To give the best chance of success, the molecular structures of the input Z-matrixes were taken from existing crystal structures found in the CSD<sup>3</sup>. The half H<sub>4</sub>DHTA molecule was obtained from refcode DUSJUX,<sup>159</sup> and the DMF molecule was obtained from the DMF solvate of terephthalic acid published by Dale *et al.*<sup>165</sup> refcode EVOVUG .

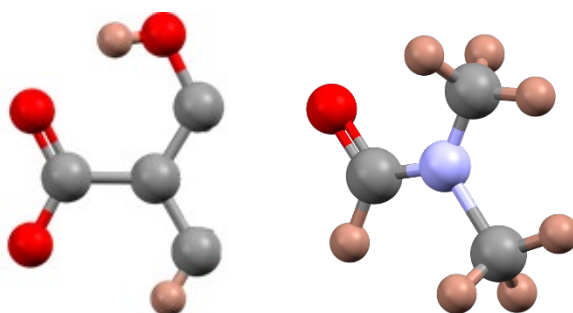


Figure 45 Z-Matrix inputs used to solve intermediate 1. (left) half of one H<sub>4</sub>DHTA molecule. (right) DMF molecule. Atoms are coloured as follows: carbon (grey), oxygen (red), hydrogen (pink), and nitrogen (light blue).

Based on the partial EXPO solution, it was most likely that the H<sub>4</sub>DHTA molecule would sit on a centre of inversion, while the DMF molecule would sit on a general position. The input for the Z-matrixes was half an H<sub>4</sub>DHTA molecule and one DMF molecule. The arrangement of the atoms in the H<sub>4</sub>DHTA were locked and the centre of the molecule was fixed at ( $\frac{1}{2}$   $\frac{1}{2}$   $\frac{1}{2}$ ). A DASH simulated annealing run was performed using these parameters using 25 trial runs with 1 million steps each.

The resultant crystal structure was further improved by DFT energy minimisation (Section 2.9.2.3) to give a final crystal structure. In order to calculate ESDs for lattice parameters, a rigid body Rietveld refinement was performed using TOPAS.

### 3.3.7.2 Crystal structure of intermediate 1

**(1)** (formula  $(C_8O_6H_6)(C_3H_7NO)_2$ ) crystallises in a monoclinic  $P2_1/n$  space group (Table 13) with CIF available in supplementary information. Each asymmetric unit contains a single  $H_4DHTA$  molecule and two DMF molecules. Both the  $H_4DHTA$  and DMF molecules pack down the  $a$ -axis.  $H_4DHTA$  molecules exhibit Intermolecular and intramolecular H bonding throughout the crystal structure. Short distances of 1.598 Å between the hydroxyl and carboxyl groups of the linker are consistent with intramolecular H bonding, while intermolecular H bonding occurs between carboxyl groups and DMF.

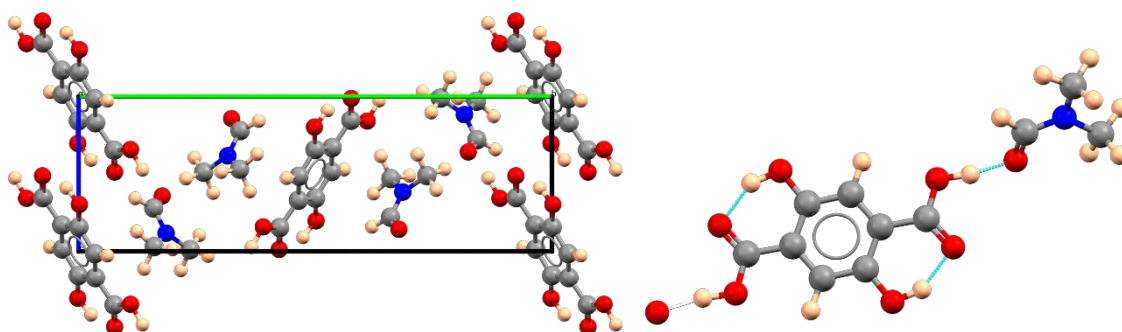


Figure 46 Crystal structure of **1**. (Left) packing along  $a$ -axis. (right) asymmetric unit showing internal and external H-bonding between neighbouring  $H_4DHTA$  and DMF molecules (blue dashed lines). Element colours: carbon (grey), oxygen (red), nitrogen (blue), hydrogen (orange), zinc (light blue). Unit-cell axis colours: green ( $b$ -axis), blue ( $c$ -axis),

### 3.3.7.3 Structural determination of intermediate 2

Intermediate 2 was first found when a MOF-74-Zn milling reaction was milled for only 15 minutes and a white powder was found. It was known that mechanochemical MOF synthesis routes produce crystalline intermediate phases, so a PXRD pattern was collected on the powder. The crystal structure solution is described in Section 3.2.11.3, the CIF of intermediate 2 is available in supplementary information.

### 3.3.7.4 Crystal structure of intermediate 2

**2** (formula  $Zn(C_8H_4O_6)(H_2O)_2(C_3H_7NO)$ ) crystallises in the triclinic space group  $P-1$  (Table 13). Each asymmetric unit contains one zinc atom, one DMF molecule, one water molecule, and half an DHTA linker (Figure 47a). Each zinc is octahedrally coordinated

to two water molecules, two DMF molecules, and two H<sub>2</sub>DHTA linkers with Zn-O bond lengths of 2.063 Å forming 1 D chains.

Each chain packs directly aligns with all other chains with no offset between

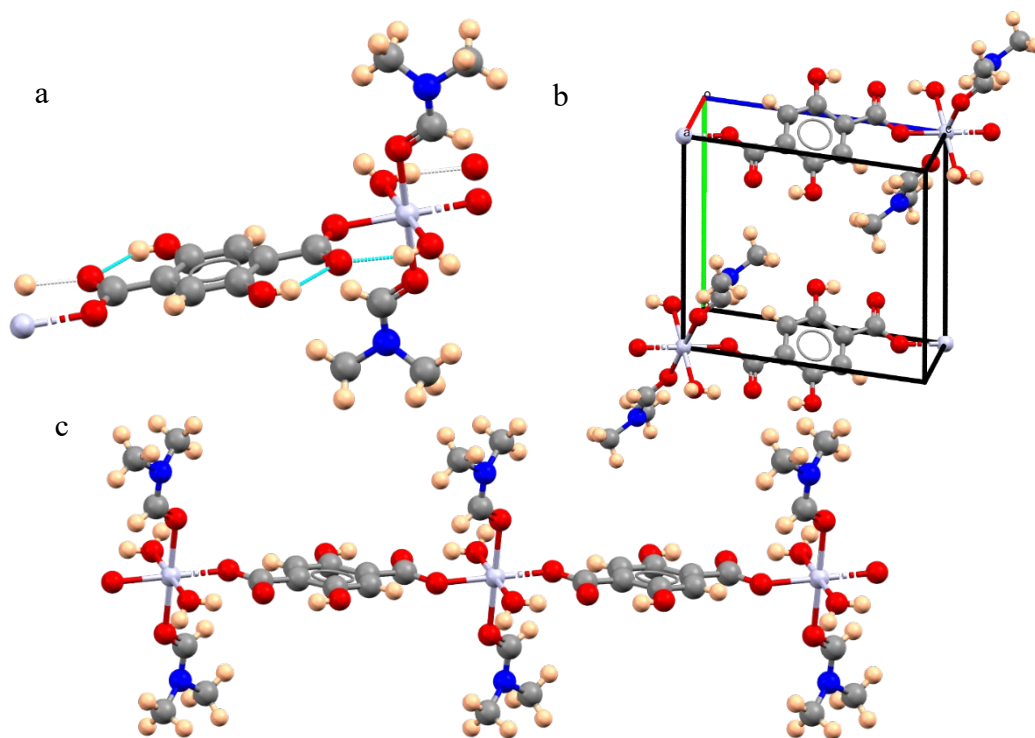


Figure 47 Structure of **2**. Single asymmetric unit showing H-bonding (a), packing of unit-cell (b), and example of coordination polymer chains (c). Element colours: carbon (grey), oxygen (red), nitrogen (blue), hydrogen (orange), zinc (light blue). Unit-cell axis colours: red (*a*-axis), green (*b*-axis), blue (*c*-axis),

neighbouring zinc atoms, and a zinc-zinc distance of 8.709 Å (Figure 47b). Hydrogen bonding stabilises the structure connecting the uncoordinated hydroxyl group to the carboxylic acid keeping the linker planar. No hydrogen bonding occurs between the chains, with packing due to the overlapping  $\pi$  stacking from the benzene rings in the structure.

A Rietveld refinement was performed to confirm bulk agreement of the crystal structure of **2** (Figure 48). Results indicated strong agreement (Rwp= 4.53%), no additional phases were present in the bulk powder.

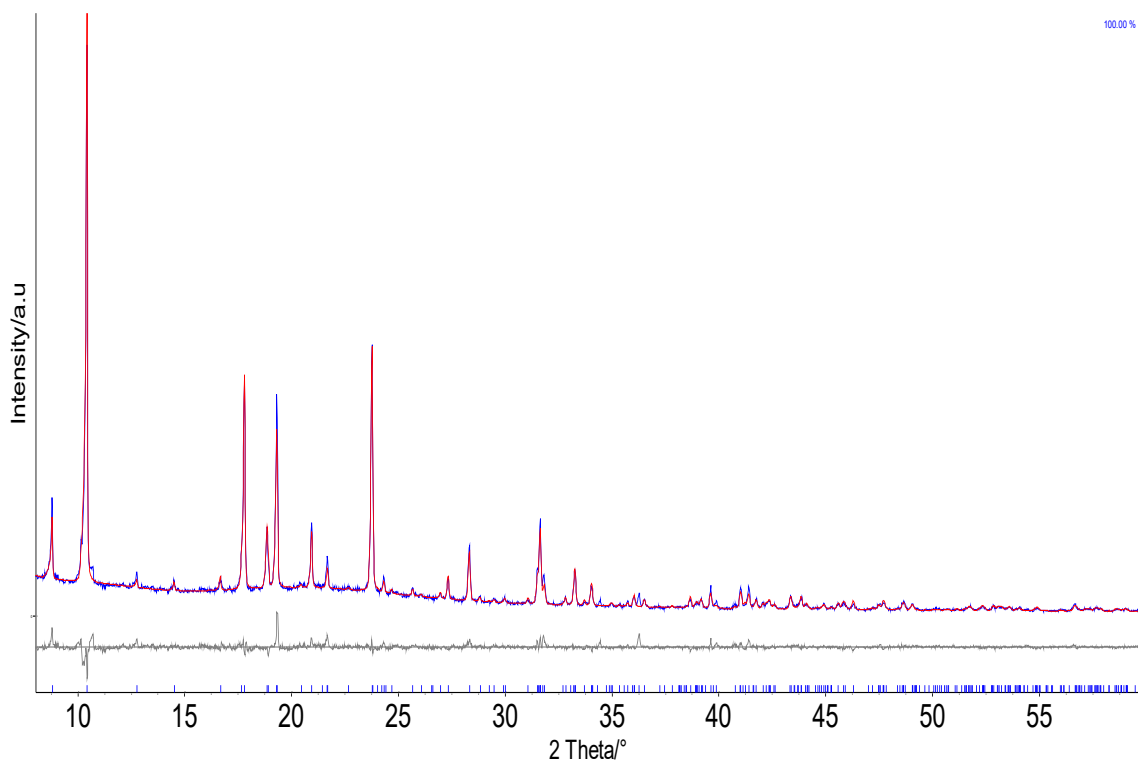


Figure 48 Rietveld Refinement of Intermediate 2. CIF used in refinement:  $\text{Zn}(\text{H}_2\text{DHTA})(\text{DMF})_2(\text{H}_2\text{O})_2$ . experimental dataset (Blue), calculated (red), difference curve (grey), hkl indices (tick marks).

### 3.3.7.5 Synthesis and structure solution of intermediate 3

Intermediate 3 was solved using powder diffraction data. Lattice parameters were first found by visually inspecting multiple powder patterns and grouping peaks which increased and decreased in intensity concurrently. The set of peaks was then used to find a set of lattice parameters using DICVOL as implemented in DASH. A Pawley refinement was performed using the found lattice parameters, then the phase was extracted using TOPAS. The extracted peak phase was used as an input for EXPO direct methods. The elemental composition was difficult to determine, and multiple different compositions were tried. The unit-cell of intermediate 3 is exactly double that of intermediate 2, so the total input used was  $Zn_2(C_8O_6H_4)_2(C_3NOH_7)_4(H_2O)_4$ . The input corresponded to two zinc atoms, four DMF molecules and 4 water molecules. Many EXPO runs were required to give a feasible crystal structure (Figure 49). Figure 49 shows the best structure result from EXPO which is clearly incorrect, as some elements are incorrectly assigned and no hydrogen atoms are present; however, the structure was close enough to correct to move forward with refinement. The structure was further refined using DFT energy minimisation.

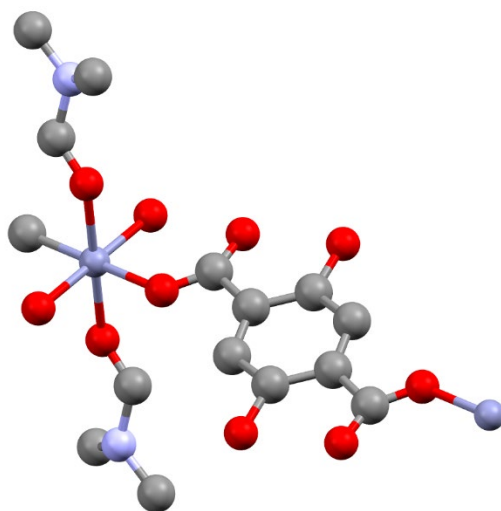


Figure 49 EXPO solution of intermediate 3 showing incorrectly assigned elements and no hydrogen atoms. Elements: Zinc (dark blue), carbon (grey), oxygen (red), zinc (light blue).



### 3.3.7.6 Crystal structure of intermediate 3

**3** (formula  $\text{Zn}(\text{C}_8\text{H}_4\text{O}_6)(\text{H}_2\text{O})_2(\text{C}_3\text{H}_7\text{NO})$ ) crystallise in monoclinic space group  $P2_1/a$  (Table 13) as a polymorph of intermediate **2**, which forms upon further milling of **2**, or by milling of zinc acetate dihydrate with DHTA for 90 minutes in a 1:1 ratio. Each zinc is octahedrally coordinated to two water molecules, two DMF molecules and two DHTA molecules forming 1 D chains (Figure 50a). Each zinc is located on a centre of inversion at  $(\frac{1}{2}, \frac{1}{2}, 0)$  whilst the centre of the DHTA linker sits on a centre of inversion at  $(\frac{1}{2}, \frac{1}{2}, \frac{1}{2})$  (Figure 50b). As a result, each chain zig zags down the  $a$ -axis in offset chains, as opposed to intermediate **2** where each DHTA stacks on top of each other.

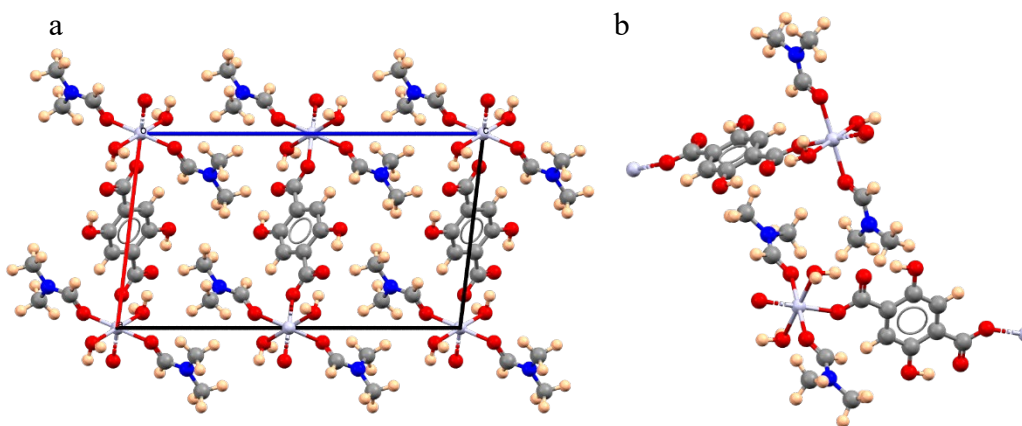


Figure 50 structure of **3**. 23(a) packing of unit-cell viewed down  $b$ -axis (left), 23(b) and example of chains packing in zig zag configuration (c). Element colours: carbon (grey), oxygen (red), nitrogen (blue), hydrogen (orange), zinc (light blue). Unit-cell axis colours: red ( $a$ -axis), blue ( $c$ -axis).

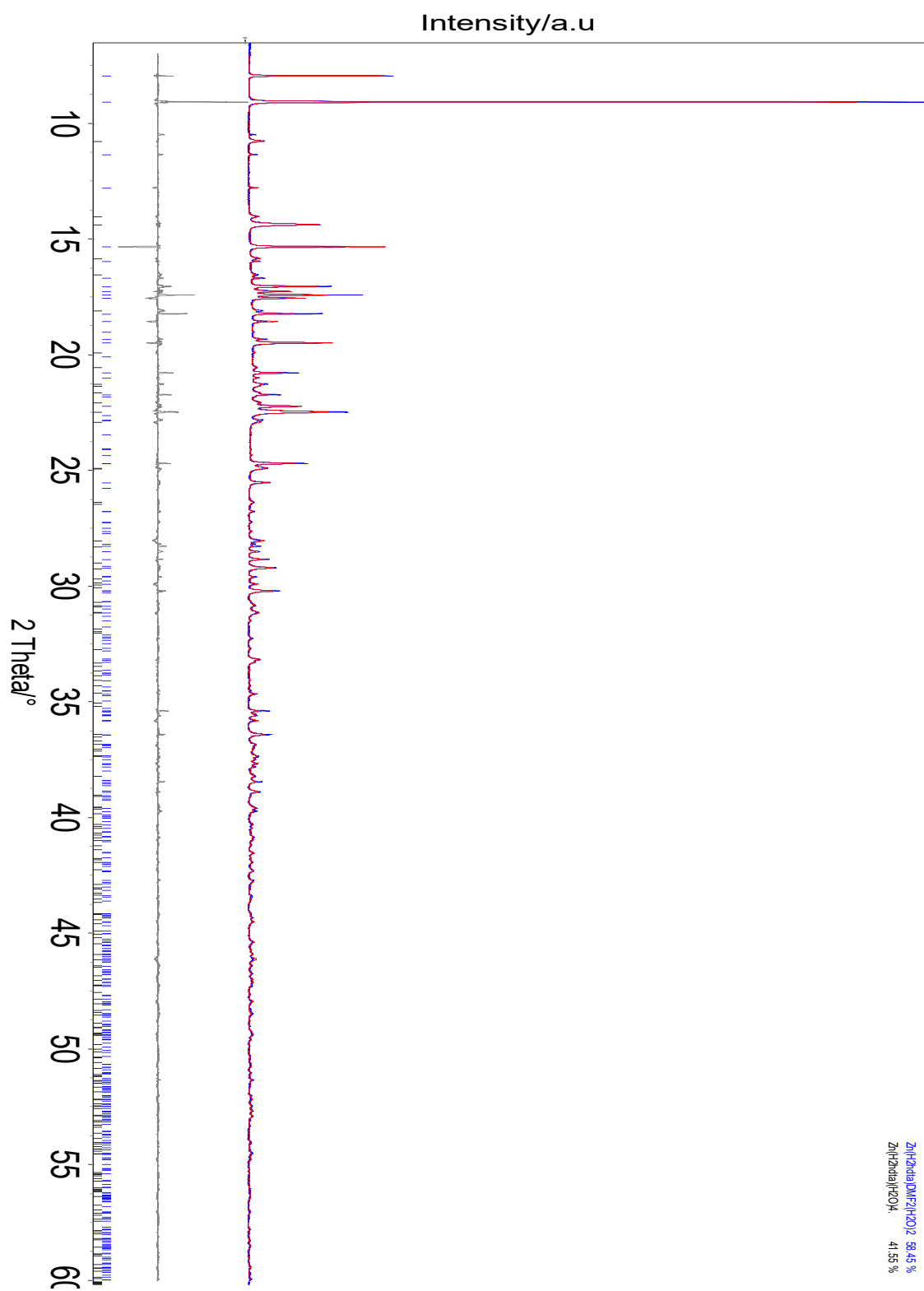


Figure 51 PXRd and Rietveld refinement of intermediate 3. Refinement is a mixture of  $\text{Zn}(\text{H}_2\text{DHTA})(\text{DMF})_2(\text{H}_2\text{O})_2$  (intermediate 3), and  $\text{Zn}(\text{H}_2\text{DHTA})(\text{H}_2\text{O})_2$  (MOF-74 water intermediate). experimental PXRd (Blue), calculated (red), difference curve (grey), blue tick marks correspond to intermediate 3, while black tick marks correspond to  $\text{Zn}(\text{H}_2\text{DHTA})(\text{H}_2\text{O})_2$

### 3.3.7.7 Synthesis and attempts to solve intermediate 4

Intermediate **4** was found to form after 70 minutes of milling a MOF-74 sample and is the last intermediate before the formation of the MOF-74 framework. Attempts to solve the crystal structure from powder diffraction data or growing single crystals were both unsuccessful.

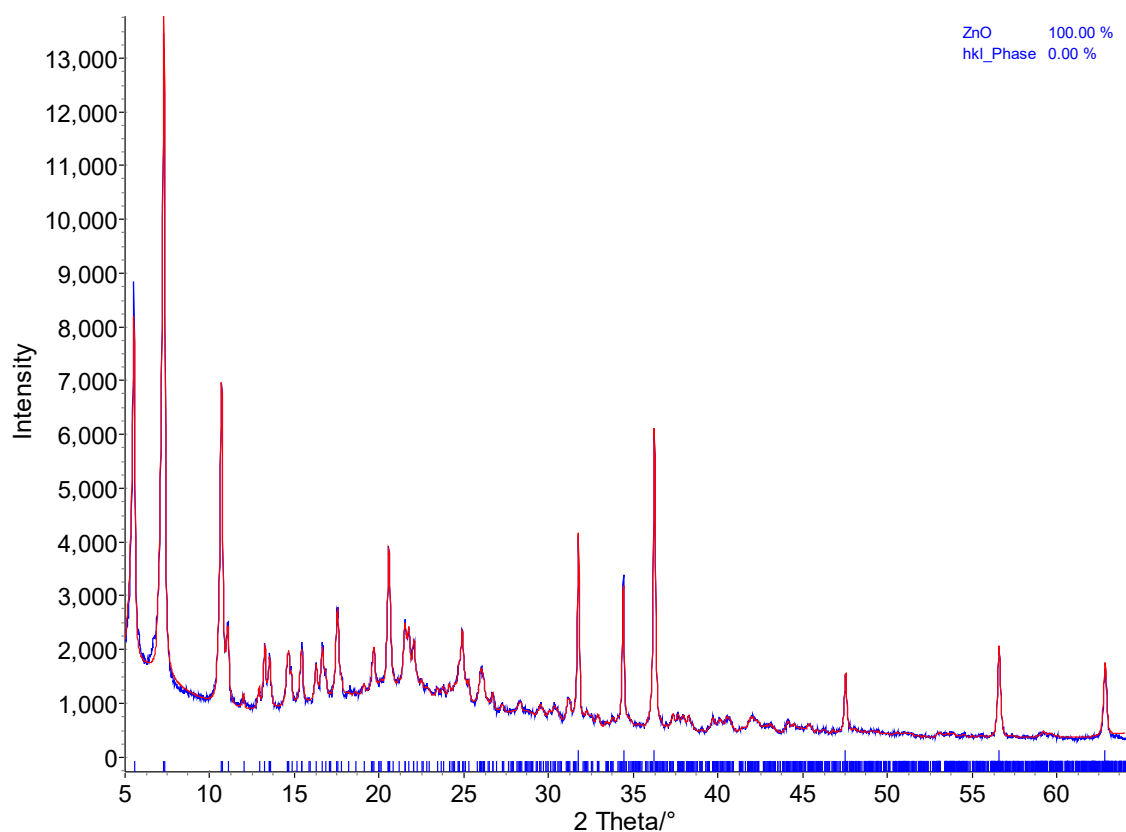


Figure 52 Powder pattern and Pawley refinement of MOF-74-Zn intermediate 4. Experimental (blue), calculated (red).

Figure 52 shows a simultaneous Rietveld and Pawley refinement of ZnO and lattice parameters of intermediate **4**.

### 3.3.8 Rietveld refinements of intermediates to calculate QPS

Using the solved crystal structures a series of multi-phase Rietveld refinements were carried out using the experimental data obtained from the milling experiment on Diamond I11. The weight percentage of each phase as a function of time was used to map out crystallographic changes throughout the reaction (Figure 53). The resultant plot clearly shows the changes in crystallographic phases as the reaction progresses.

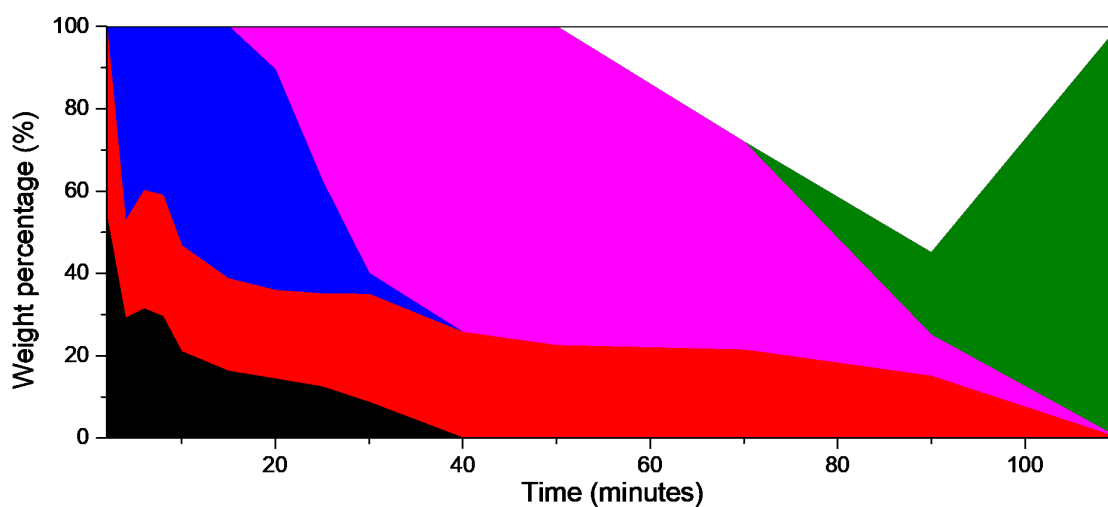


Figure 53 Plot showing changes of Rietveld weight percentages with time during the mechanochemical synthesis of MOF-74-Zn. Area under each colour represents weight percentage of each phase. Phases present and associated colours: black **1** ( $\text{H}_4\text{DHTA DMF}_2$ ), red (zinc oxide), blue **2** ( $\text{ZnH}_2\text{DHTA}(\text{DMF})_2(\text{H}_2\text{O})_2$ ), pink **3** ( $\text{ZnH}_2\text{DHTA}(\text{DMF})_2(\text{H}_2\text{O})_2$ ), green (MOF-74-Zn). White space indicates **4**.

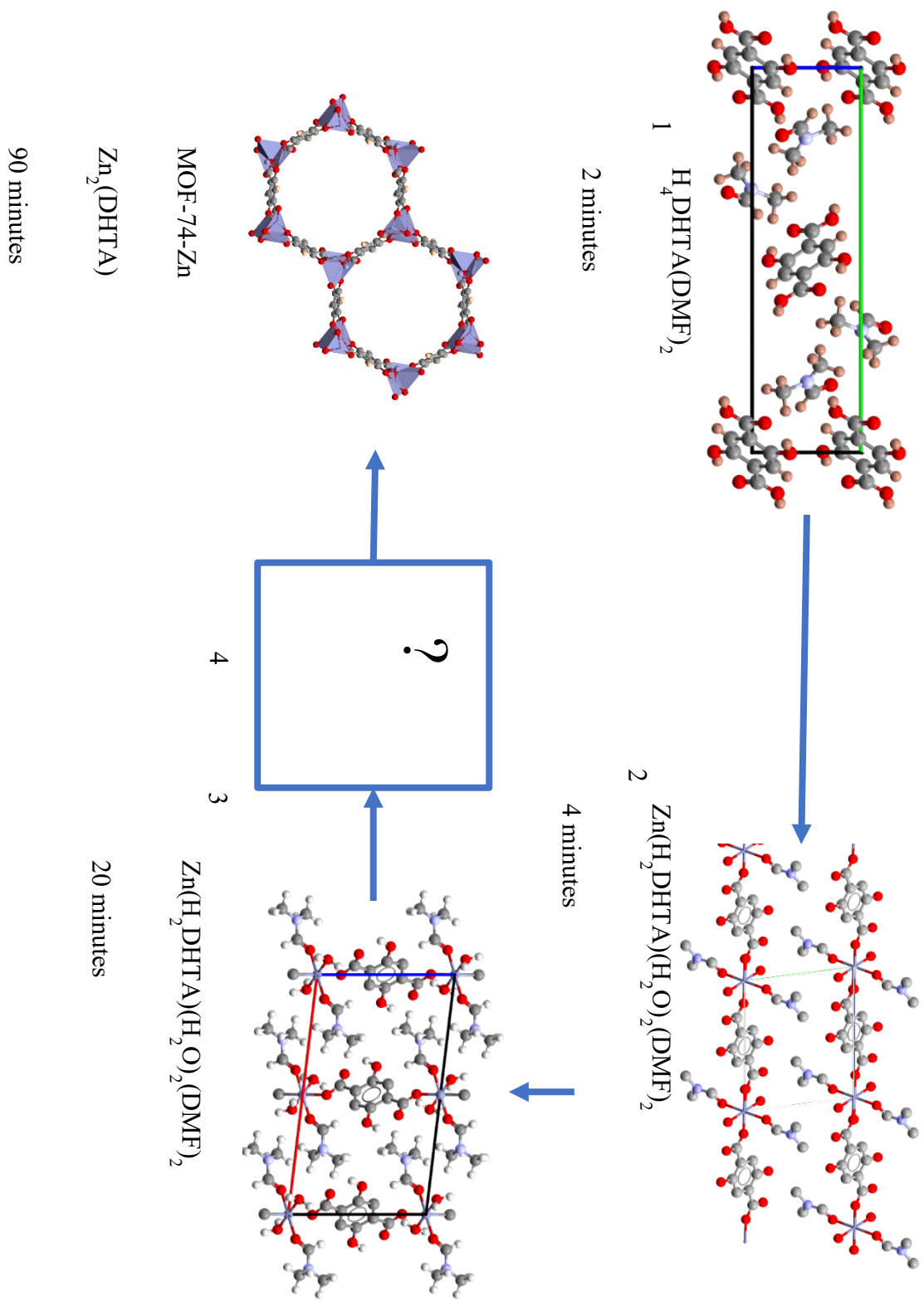


Figure 54 Intermediates formed during the mechanochemical synthesis of MOF-74-Zn, including times of formation.

### 3.4 Discussion

#### 3.4.1 mechanochemical synthesis and properties of MOF-74-Zn

This work demonstrates that MOF-74 can be synthesised via mechanochemical means, which facilitates large scale synthesis of this material for use in multiple drug delivery applications (Chapter 4). Although the mechanochemical synthesis method has been reported previously,<sup>42</sup> the work reported here is a significant improvement, leading to MOF-74 synthesis using DMF which fully forms MOF-74, a direct advancement of the work published by Julien *et al.* In the previously reported synthesis, MOF-74 never fully forms when DMF is used to assist grinding. DMF has advantages over water when used to synthesis MOF-74 including increased surface area,<sup>42</sup> and better stability, at least until the solvent is replaced in the MOF with water.<sup>117</sup> Using DMF also improved the BET surface area compared to using water during milling. Using water liquid assisted grinding reportedly gives BET surface areas of around  $500 \text{ m}^2 \text{ g}^{-1}$ ,<sup>42</sup> while the samples synthesised here had a BET surface area of  $975 \text{ m}^2 \text{ g}^{-1}$  and a Langmuir surface area of  $1000 \text{ m}^2 \text{ g}^{-1}$ . This value is smaller than the highest previously reported Langmuir surface area of  $1187 \text{ m}^2 \text{ g}^{-1}$ .<sup>166</sup> This decrease is most likely due to differences in sample particle size, and air contact time for the activated sample.

As part of this work, the stability of MOF-74-Zn was assessed in moist air, methanol, and phosphate buffer. The framework is entirely stable in methanol showing no changes in the PXRD pattern. This stability was measured because methanol is used in the solvent exchange step of the MOF synthesis. The stability of the activated MOF was measured in air over the course of two months. During the two months, the MOF decayed noticeably as judged by changes in the PXRD, with the decrease in peak intensities and the formation of  $\text{Zn}(\text{H}_2\text{DHTA})(\text{H}_2\text{O})_2$ ,<sup>158</sup> which is an intermediate in the formation of the MOF when water is used to assist grinding. Finally, the MOF stability was studied using

a pH 7.4 phosphate buffer. The activated MOF decayed steadily over two months as the MOF decayed and formed ZnO and a new phase. Weighted Rietveld analysis<sup>148</sup> indicates that roughly 50% of the MOF-74-Zn decomposes in two months, but that the framework decays initially very quickly.

Finding optimal synthesis conditions took a lot of iteration, with changes including: milling ball total weight, number of milling balls, size of milling jar, volume of DMF used, and total starting material weight used in the mill. The conditions arrived at in Section 3.3.3 are the culmination of this experimentation. One of the largest hurdles found with synthesising MOFs using DMF was the decomposition of DMF. DMF slowly decomposes forming dimethyl amine.<sup>167</sup> It was observed that DMF purity massively impacted on the rate of mechanochemical reaction, up to whether a framework would form at all. It was found that DMF would become unusable within 3 months of opening a bottle, and after that point the mechanochemical reaction would be very inconsistent, often not forming MOF-74-Zn at all.

As described in 3.3.6, the particle size of zinc oxide used to synthesise the MOF affects the particle size of the framework formed. While this may seem obvious, it is the first reported example of using starting material particle size to influence the particle size of a mechanochemically synthesised framework. In this case, it was found that using 100 nm particle size ZnO produced MOF-74-Zn of around 200 nm, while using ZnO of particle size 1  $\mu\text{m}$  would make MOF-74-Zn with particle sizes of close to 1  $\mu\text{m}$ .

### **3.4.2 intermediates formed in the mechanochemical synthesis of MOF-74-Zn**

Several MOF-74-Zn intermediate structures were found and characterised in this work. Of these intermediate phases only the existence intermediate 4 has been previously reported, though without lattice parameters.<sup>42</sup>

This work demonstrates that the reaction route taken during a mechanochemical synthesis is highly dependent on which solvent is used to assist grinding. When MOF-74 is synthesised using water to assist grinding only a single intermediate forms. This intermediate is a zinc H<sub>2</sub>DHTA coordination polymer with a Zn:DHTA ratio of 1:1. The structure of the water route intermediate is similar to intermediates 2, and 3, and was first reported by Ghermani *et al.*<sup>158</sup> and then confirmed as MOF intermediate by Julien *et al.*<sup>42</sup>

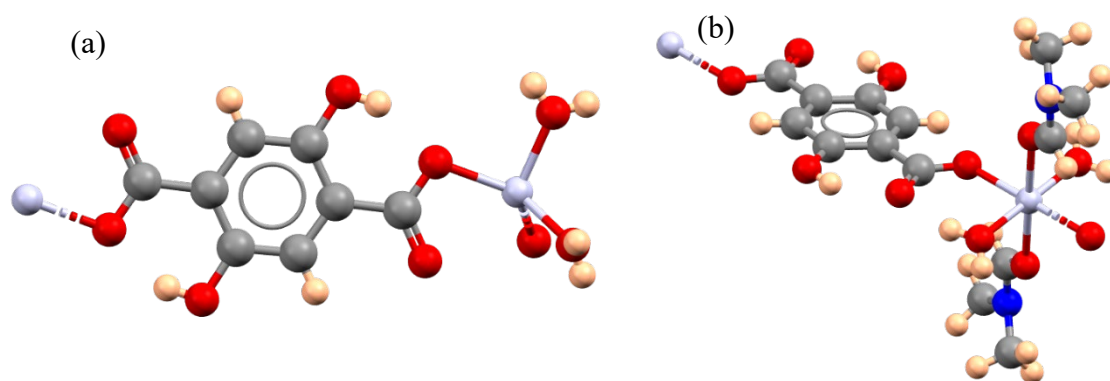


Figure 55 Formula unit of two MOF-74 mechanochemical intermediates. (a) Intermediate formed using water to assist grinding Formula: Zn(H<sub>2</sub>DHTA)(H<sub>2</sub>O)<sub>2</sub>. (b) intermediate formed using DMF to assist grinding formula: Zn(H<sub>2</sub>DHTA)(DMF)<sub>2</sub>(H<sub>2</sub>O)<sub>2</sub>. Element colours: carbon (grey), oxygen (red), nitrogen (blue), hydrogen (orange), zinc (light blue).

The intermediate formed using water has a tetrahedral coordination around the zinc centre which compared to the octahedral coordination found in the DMF intermediates as well as the MOF-74-Zn framework.

Although finding the crystal structures of intermediates 1-3 meaningfully pushes forward the understanding of intermediates forming in mechanochemical reactions, an important question remains. Intermediates 1-3 all exhibit close packed crystal structures, while the final framework has its open pored structure. It is expected that the structure of intermediate 4 is also porous due to the size of the unit-cell and knowing the structure will hopefully give the complete picture of the synthesis. Unfortunately, it does not seem possible to solve the structure using powder structure solution methods with the unit-cell



contents remaining uncertain. A method was found to synthesise intermediate 4 using only a short mill time by heating the sealed milling jar to 60 °C for an hour before milling for five minutes, meaning it might be possible to grow single-crystals of intermediate 4 in a similar way to how single-crystals were grown for intermediate 2.

### 3.5 Conclusion

The findings shown in this chapter can be summarised to a few key points. Firstly, the synthesis of MOF-74-Zn via mechanochemical methods has properties which are comparable to the synthesis of MOF-74-Zn via traditional solvothermal methods. Most importantly the surface area of the framework is very close to the highest previously reported for MOF-74-Zn.

Secondly, there are many more crystalline intermediate structures which form in the mechanochemical synthesis of MOF-74-Zn. These new intermediates are comparable to the previously reported mechanochemical intermediate which was synthesised using a water LAG synthesis method.

Finally, the ability to control particle size of MOF-74-Zn via zinc oxide particle size could have important ramifications to both the applications of MOF-74-Zn in drug delivery, as particle size of MOFs has previously been demonstrated to affect areas of accumulation in a body.<sup>168</sup> This ability to control where the MOF would accumulate in the body could be useful in drug delivery applications. In a wider context the ability to control framework particle size could potentially be applied to many other mechanochemical synthesis methods.

These points together both build upon the current understanding of the mechanochemical synthesis of framework structures.

## Chapter 4- Loading ibuprofen into MOF-74-Zn

### 4.1 Introduction

As discussed earlier, there are a few examples of loading drugs into MOFs for use in drug delivery, but only to the initial steps of testing with model drugs. So far, the most notable examples are MIL-53,<sup>93</sup> MIL-100,<sup>169</sup> and MOF-74. It is worth noting that all examples of MOFs being studied for drug delivery have used solvothermally synthesised MOFs, which are of larger particle size than those produced mechanochemically.

The open-pore structure of MOF-74 makes it an ideal candidate for loading small molecules. Before this work, the iron<sup>90</sup> and nickel<sup>91</sup> variants of MOF-74 were loaded using ibuprofen. The zinc MOF-74 has benefits over the other MOF-74 forms including slow framework decomposition in water, and low toxicity and high bioavailability. As discussed in Chapter 3, MOF-74-Zn can be synthesised in a number of different ways, and just as in Chapter 3 it was synthesised using the previously described mechanochemical method.

Ibuprofen was loaded into the framework for a few reasons. Firstly, it is cheap and easy to obtain. Secondly, no special precautions are needed when working with it. Finally, ibuprofen has low solubility in water, a property common to many existing and potential drugs. These factors together make ibuprofen an ideal model drug to test a delivery system.

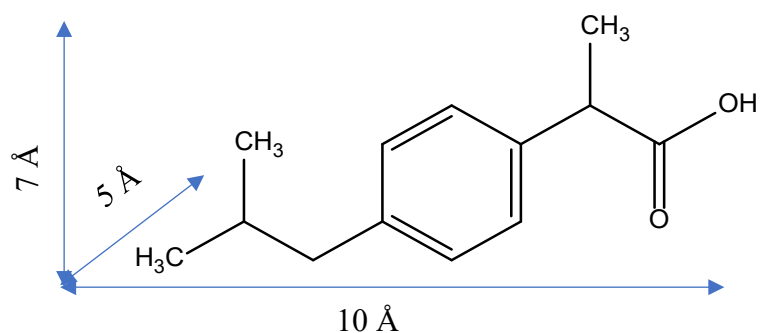


Figure 56 2D structure of ibuprofen

Comparison of the crystal structures of ibuprofen and MOF-74 suggest that the pores of the framework and ibuprofen are similarly sized. ibuprofen fits within a 10 Å x 7 Å x 5 Å box if the molecule is treated as rigid, these dimensions have been used in prior work to justify ibuprofen fitting in to porous materials.<sup>85</sup> The pores of MOF-74 are measured as circle of diameter 11 Å using the void space calculation as implemented in Mercury.<sup>18</sup> This similarity in size meant that initially there was uncertainty as to whether during loading ibuprofen would move inside the pores of the framework or adsorb to the surface of the framework. Consequently, this chapter investigates the surface interactions of ibuprofen and MOF-74-Zn.

## **4.2 Experimental**

### **4.2.1 MOF-74 synthesis**

MOF-74-Zn was synthesised via the previously described mechanochemical method (Section 3.2.2) using the Retsch MM400 mill method unless otherwise stated. Activation of MOF-74 was conducted using the method outlined in Section 3.2.3.

### **4.2.2 MOF-74-Zn ibuprofen loading**

Ibuprofen was loaded into MOF-74-Zn by soaking the activated MOF in a concentrated solution of ibuprofen in hexane. The concentrated ibuprofen solution was made by dissolving 3.75 g of ibuprofen in 250 ml of hexane to give a solution of 15 mg / mL ibuprofen in hexane. 1 g of activated MOF-74-Zn was added to the solution.

In order to monitor the rate of ibuprofen loading, 1 mL aliquots were extracted from the solution during the experiment. The aliquots were then diluted to make 100 mL hexane solutions. 5 mL of the diluted solution was filtered using 0.45  $\mu\text{m}$  PES syringe filters for UV-Vis analysis.

### **4.2.3 Preparation of phosphate buffer solution**

Phosphate buffer was prepared by dissolving 13.6 g of sodium phosphate dihydrate and 6.7 g of sodium phosphate monohydrate to deionised water to make a 1 L solution. This solution was brought to pH 7.4 by adding HCl and NaOH dropwise.

### **4.2.4 UV-Vis calibration curves**

#### **4.2.4.1 UV-Vis hexane calibration curve**

100 mg was dissolved in 250 mL of hexane to make a 0.4 mg mL<sup>-1</sup> solution. The 0.4 mg mL<sup>-1</sup> solution was used to make three other solutions of concentrations 0.025 mg mL<sup>-1</sup>, 0.05 mg mL<sup>-1</sup>, 0.1 mg mL<sup>-1</sup>, and 0.2 mg mL<sup>-1</sup>. The absorbance at each concentration was

measured according to the procedure outlined in Section 2.5. absorbance at 273 nm was used to measure ibuprofen concentration.

#### 4.2.4.2 UV-Vis phosphate buffer calibration curve

1 L of the phosphate buffer described in Section 4.2.3 was used along with 20 mg of ibuprofen to make an initial 20 mg L<sup>-1</sup> concentration solution. This solution was diluted to make solutions of concentrations 10 mg L<sup>-1</sup>, 5 mg L<sup>-1</sup>, 2.5 mg L<sup>-1</sup>, and 1 mg L<sup>-1</sup>. UV-Vis adsorption experiments were carried out in accordance with procedure outlined in Section 2.5. Absorbance at 223 nm was used to measure concentration.

#### **4.2.5 Unloading ibuprofen from MOF-74-Zn in phosphate buffer**

In order to measure the mass and timescale of ibuprofen release from the framework, a dissolution experiment was conducted. Ibuprofen has very low solubility in water, roughly 20 mg L<sup>-1</sup>, so a large volume of buffer was made. 1 L of phosphate buffer was made by dissolving 13.6 g of sodium phosphate dihydrate and 6.7 g of sodium phosphate monohydrate in deionised water to make a 1 L solution. This solution was brought to pH 7.4 by adding HCl and NaOH dropwise. 100 mg of loaded MOF-74 was added to 12000 MW dialysis tubing along with 30 mL of the buffer solution. The solution was stirred, and samples taken at regular intervals for two days. 5 mL samples were removed from the bulk solution and filtered through a 0.45 µm satorius syringe filter. UV-Vis spectra of samples were collected using the method described in Section 2.5 using a phosphate buffer blank to subtract background.

## **4.2.6 Analysis of ibuprofen loaded MOF-74-Zn sample**

### 4.2.6.1 CHN analysis

CHN elemental analysis of a loaded MOF-74-Zn sample was carried out according to Section 2.3. The CHN values for the activated MOF-74-Zn sample are described in Section 3.2.3.

The loaded sample was taken directly from the loading experiment. The loaded sample was then washed with hexane to remove ibuprofen from the surface of the MOF. In order to remove hexane, the solvent used in the loading experiment, the sample was heated at 100 °C in a vacuum oven for 3 hours. The dried sample was then sent for elemental analysis.

### 4.2.6.2 IR spectroscopy

IR spectra were collected according to the procedure outlined in Section 2.4. Loaded sample was prepared with the same method as described in 4.2.6.1. The activated MOF-74-Zn sample was prepared according to procedure outlined in 3.2.3.

### 4.2.6.3 Inelastic neutron spectroscopy

INS data were collected according to the procedure outlined in Section 2.6. Data for three samples were collected: an activated MOF-74-Zn sample (1), a pure ibuprofen sample (2), and an ibuprofen loaded MOF-74-Zn sample (3).

#### 4.2.6.3.1 Ibuprofen INS

Ibuprofen was used as purchased from BASF without modification. 5 g of ibuprofen was used to collect the INS data.

#### 4.2.6.3.2 Blank MOF-74-Zn sample

5 g of MOF-74-Zn were synthesised by 12 repetitions of the procedure described in Section 3.2.3. All batches were combined and then activated according to the procedure described in Section 3.2.3.

#### 4.2.6.3.3 Ibuprofen loaded MOF-74-Zn sample

5 g of MOF-74-Zn were synthesised by another 12 repetitions of the prior described MOF-74-Zn mechanochemical synthesis method. The samples were combined and then activated and loaded using the prior described method.

#### 4.2.6.4 PXRD pattern of MOF-74-Zn

PXRD data of ibuprofen-loaded MOF-74-Zn were collected using the procedure outlined in Section 2.9.2. The phases present in the sample were investigated using a Pawley refinement. Initial lattice parameters were obtained from a CIF of MOF-74-Zn.<sup>155</sup> Lattice parameters were initially set to a: 26.26 Å, c: 6.70 Å but allowed to refine. Detector zero-point, background, crystallite size, and crystallite strain were all refined.

PXRD diffractogram of activated MOF-74-Zn was collected and a Rietveld model was refined using the previously described method in Section 3.3.4.1.

PXRD was conducted on a physical mixture of ibuprofen and activated MOF-74-Zn. The physical mixture was made by combining 20 mg of ibuprofen with 80 mg of activated MOF-74-Zn. The mixture was milled for 3 minutes at 15 Hz in a 5 mL milling jar with a single 1.4g stainless steel milling ball in the Retsch MM 400 mill. PXRD of the resultant powder was conducted and a Pawley refinement performed. The lattice parameters for ibuprofen were obtained from CCDC CSD refcode IBPRAC;<sup>170</sup> and the lattice parameters for MOF-74-Zn were taken from a CIF of MOF-74-Zn.<sup>155</sup> Pawley refined parameters: detector zero-point, background, crystallite size, and crystallite strain.



#### 4.2.6.5 DSC of MOF-74-Zn samples

DSC data were collected for activated MOF-74-Zn and ibuprofen-loaded MOF-74-Zn. Samples were prepared by heating in a vacuum oven at 100 °C for 6 hours to ensure that all moisture was removed. Samples were prepared and experiments run according to the procedure in Section 2.3.

#### 4.2.6.6 SS-NMR of MOF-74-Zn samples

Solid-state NMR data were collected from three samples: A blank MOF-74-Zn sample (1), an ibuprofen sample (2), and an ibuprofen-loaded MOF-74-Zn sample (3). Samples were heated to 100 °C in a vacuum oven to remove moisture before data collection.

#### 4.2.6.7 SEM of MOF-74-Zn samples

SEM pictures of activated and loaded MOF-74-Zn were collected using the procedure explained in Section 2.8. Samples were heated to remove moisture in a vacuum oven at 100 ° before measurement. Samples gold sputtered to increase surface conductivity.

### **4.3 Results**

#### **4.3.1 MOF-74 ibuprofen loading**

Ibuprofen was loaded into MOF-74-Zn by soaking activated MOF in a concentrated solution of ibuprofen in hexane. Hexane is a non-polar solvent and has no ability to coordinate with the unsaturated site on the zinc of the framework, and conveniently ibuprofen has very good hexane solubility. After loading, samples were heated at 373 K for 12 hours in a vacuum oven to remove hexane. Samples were then weighed to estimate the total mass of ibuprofen taken into the sample. Sample weight increased by 25% compared to the starting activated sample mass. It is worth nothing that MOF-74 samples very quickly take up water, so moisture can be assumed to be a component of the mass increase. To further prove that ibuprofen had been taken into the framework more

analysis was required. The most important analytical technique used was UV-VIS which revealed the rate of uptake as well as the total mass taken into a MOF sample.

#### 4.3.1.1 UV-Vis calibration curve

In order to measure the rate at which ibuprofen was adsorbed into MOF-74 by UV-Vis adsorption a calibration curve was needed. Ibuprofen has a number of peaks in the UV range, a very strong peak at 225 nm and three smaller peaks at 255, 264, and 273 nm (Figure 57). Due to the concentration of ibuprofen in the loading solution the peak at 225 nm was not useable so the peak at 273 nm was instead used for the calibration curve.

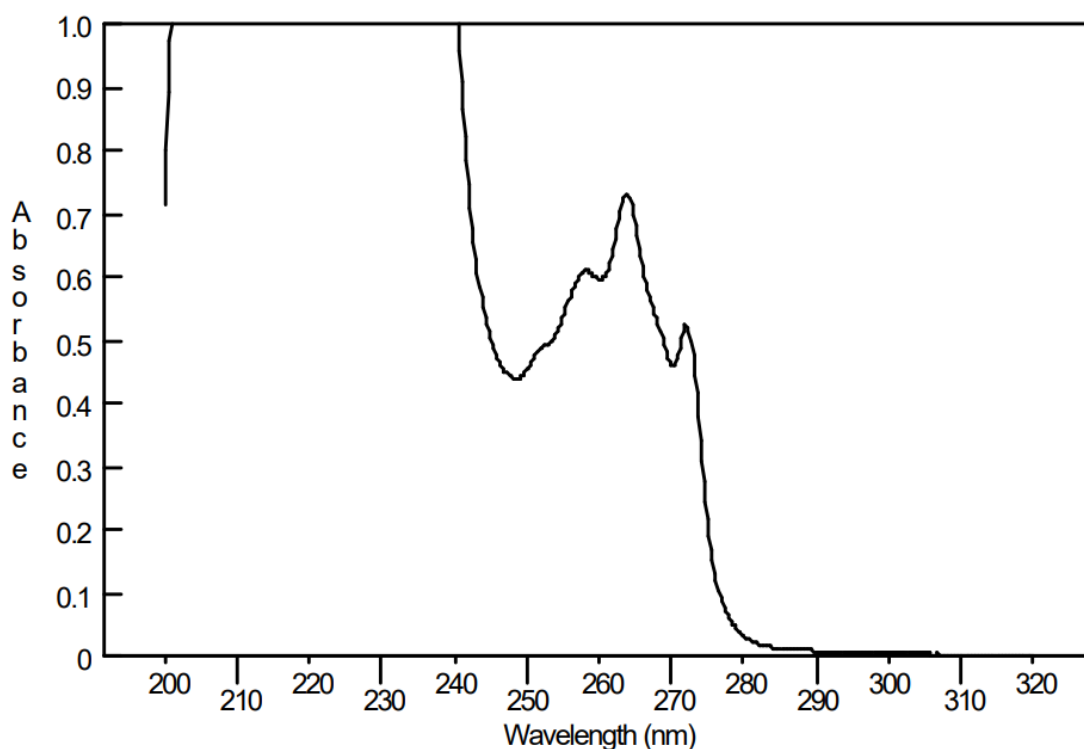


Figure 57 UV vis spectrum of ibuprofen in hexane. Peak at 225 nm is so large it is out of range.

Using the 273 nm UV-Vis adsorption peak, an ibuprofen concentration calibration curve was made (Figure 58). 0, 0 was included as a datapoint as background was subtracted

from hexane. The linear regression line describes the observed data very well ( $R^2=0.9991$ ).

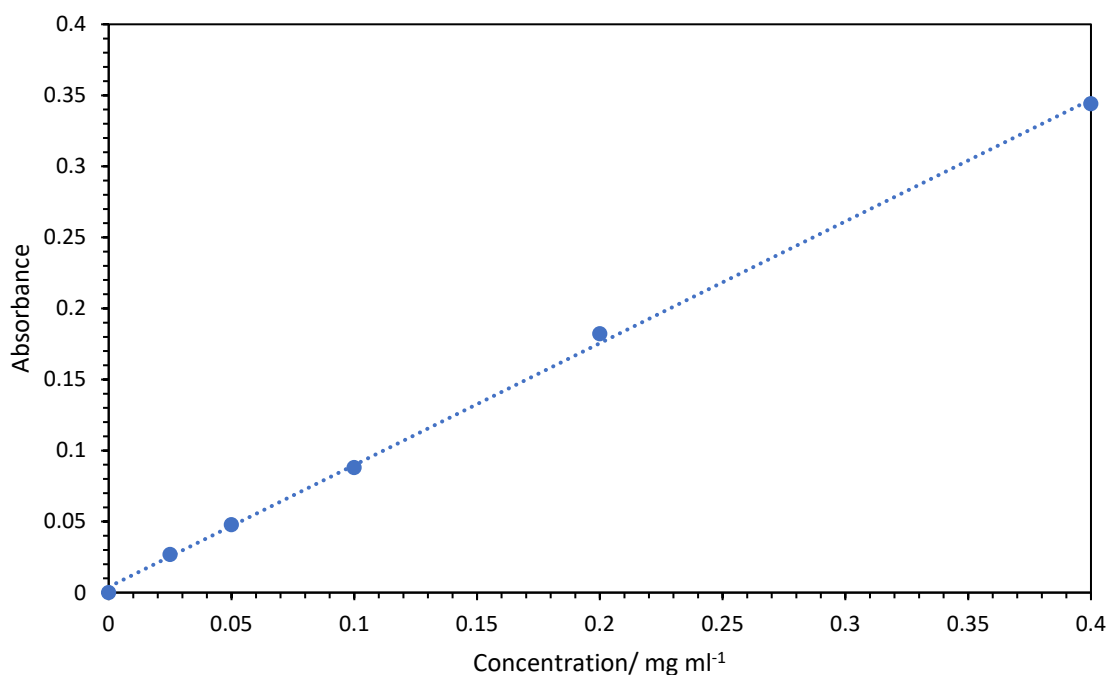


Figure 58 Calibration curve of ibuprofen in hexane. Equation of line of best fit:  $y=0.8577x + 0.004$

#### 4.3.1.2 Uptake of ibuprofen during loading

In order to measure the rate of ibuprofen uptake into a MOF-74 sample, UV-vis spectroscopy was used. In order to measure change in ibuprofen concentration aliquots were taken from the loading solution. The solution was sampled frequently during loading, 1mL samples were taken from the loading solution and diluted 100x before being filtered for UV-Vis analysis. The ibuprofen concentration was determined using the 273 nm peak used in calibration curve (Figure 58). The difference in absorbance between the first sample and the last indicated that across the experiment ibuprofen concentration had decreased (Figure 59). As no extra solvent was added to the loading solution during the experiment, any decrease in concentration must be due to the uptake of ibuprofen into the framework.

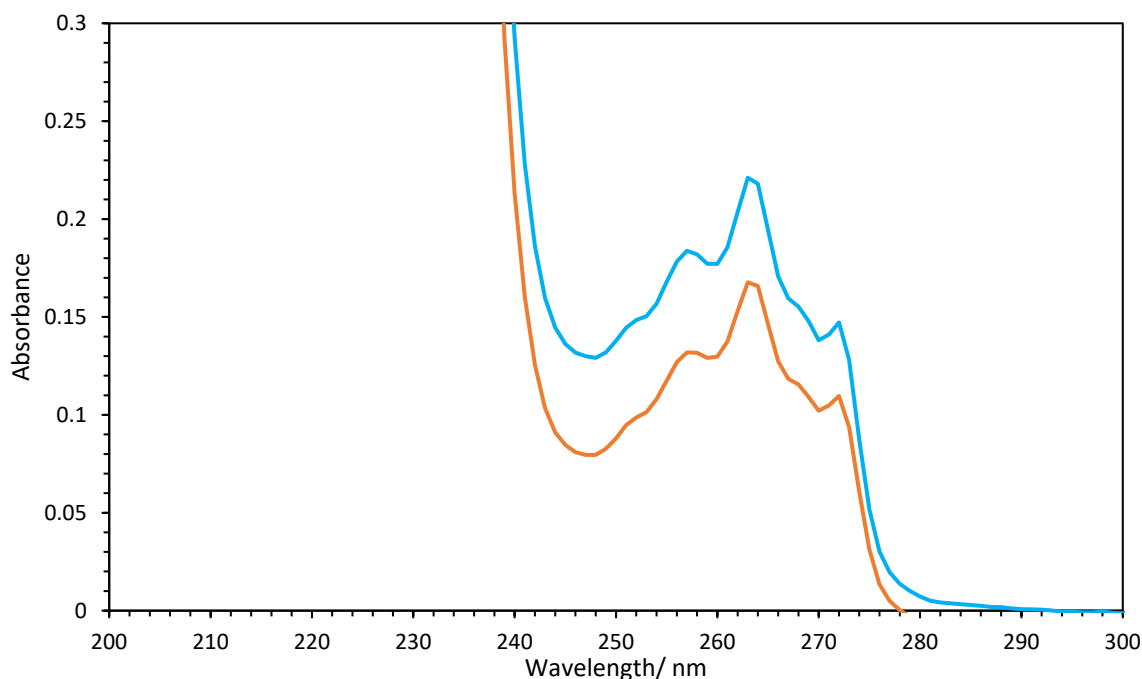


Figure 59 Ibuprofen absorption change with time during loading using 273 nm peak. Plot shows the difference between initial UV spectra (blue) and final UV spectra (orange) during the loading experiment.

Loading was carried out over the span of 100 hours by measuring the UV absorption of the aliquots. By plotting the intensity of the 273 nm absorption peak against time the progress of the loading was measured (Figure 60). The results indicate that 80% of the total loaded mass was taken into the sample in the first three hours. The initial absorbance of 0.116 corresponds to a concentration of  $0.13058 \text{ mg mL}^{-1}$  of the diluted solution (Equation 1a). The final absorbance of 1.106 corresponds to a final diluted concentration of  $0.1189 \text{ mg mL}^{-1}$  (Equation 1b).

Equation 1 (a) Calculation of initial ibuprofen concentration in loading experiment. (b) Calculation of the final ibuprofen concentration in the loading experiment

$$\text{a} \quad \textit{initial Conc} = \frac{0.116 - 0.004}{0.8577}$$

$$\text{b} \quad \textit{Final Conc} = \frac{0.106 - 0.004}{0.8577}$$

The absorbance difference between initial absorbance of 1.116 to the end absorbance of 0.106 corresponds to a bulk concentration difference of  $0.01168 \text{ mg mL}^{-1}$  of diluted solution. As the solution was diluted 100 x this change in concentration corresponds to a decrease of ibuprofen in solution of 292 mg. This mass change corresponds to a total loaded weight of 0.29 g/g, meaning total mass of 0.29 grams of ibuprofen incorporated into each 1 gram of MOF-74.

Equation 2 Calculation of ibuprofen mass change during loading experiment.

$$\text{Ibuprofen mass (g)} = 0.01168 \text{ mg ml}^{-1} \times 250 \text{ ml} \times 100$$

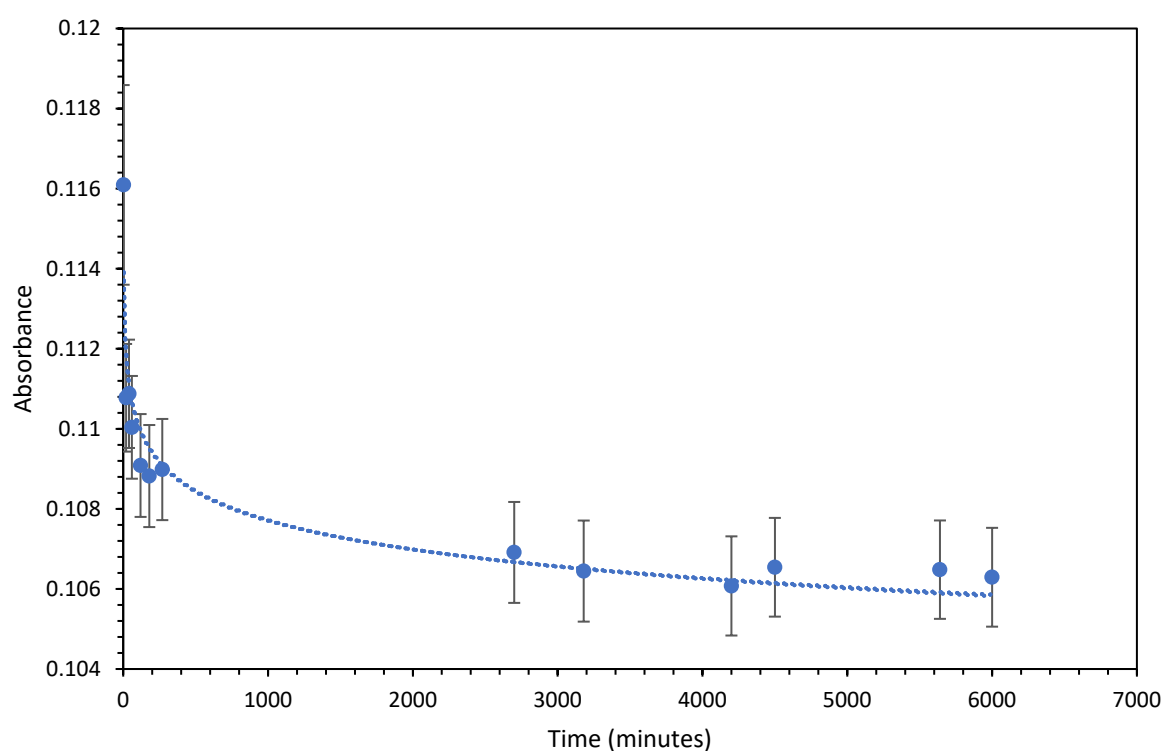


Figure 60 Change in UV-Vis absorption over time during MOF-74-Zn ibuprofen loading. Equation of line of best fit:  $y=0.1151x^{-0.01}$ .

#### 4.3.2 CHN

CHN analysis is a much more accurate weighing method to ensure that sample composition is as expected. In Table 15, two different CHN analysis results are presented.

The blank MOF-74 predicted composition was calculated using the formula of

$Zn_2(C_8H_4O_6)$ , which corresponds to the formula of MOF-74 with an uncoordinated zinc site and nothing present in framework pores. The ibuprofen loaded framework predicted composition was calculated using the formula of  $(Zn_2(C_8H_4O_6)) \cdot (C_{13}H_{18}O_2)_{0.36}$ . This ratio corresponds to a loaded mass of 0.25 g/g of ibuprofen per gram of activated MOF-74. This value is lower than the amount of ibuprofen taken up during the loading experiment. This reduction in ibuprofen mass could be due to the sample being washed with a small amount of hexane prior to the CHN measurement.

Table 15 Elemental compositions established by CHN analysis of MOF-74 samples. CHN analysis of activated and empty pored MOF-74 (left), elemental composition of ibuprofen loaded MOF-74(right)

<b>Empty MOF-74</b>			<b>Ibuprofen loaded MOF-74</b>		
<b>Element</b>	Predicted	Experimental	<b>Element</b>	Predicted	Experimental
<b>C</b>	29.58	29.2	<b>C</b>	38.1	37.8
<b>H</b>	0.62	0.98	<b>H</b>	0.2	0.7
<b>N</b>	0	0	<b>N</b>	0	0

There is an observable increase in H% in both of the CHN results displayed in Table 15. This is most likely due to an uptake of water on to the surface of the MOF which is extremely hydroscopic.

#### 4.3.3 IR spectra of loaded sample

IR spectra of MOF-74 samples were collected before and after loading (Figure 61). Samples were heated at 100 °C for three hours in a vacuum oven to remove solvent molecules from samples.

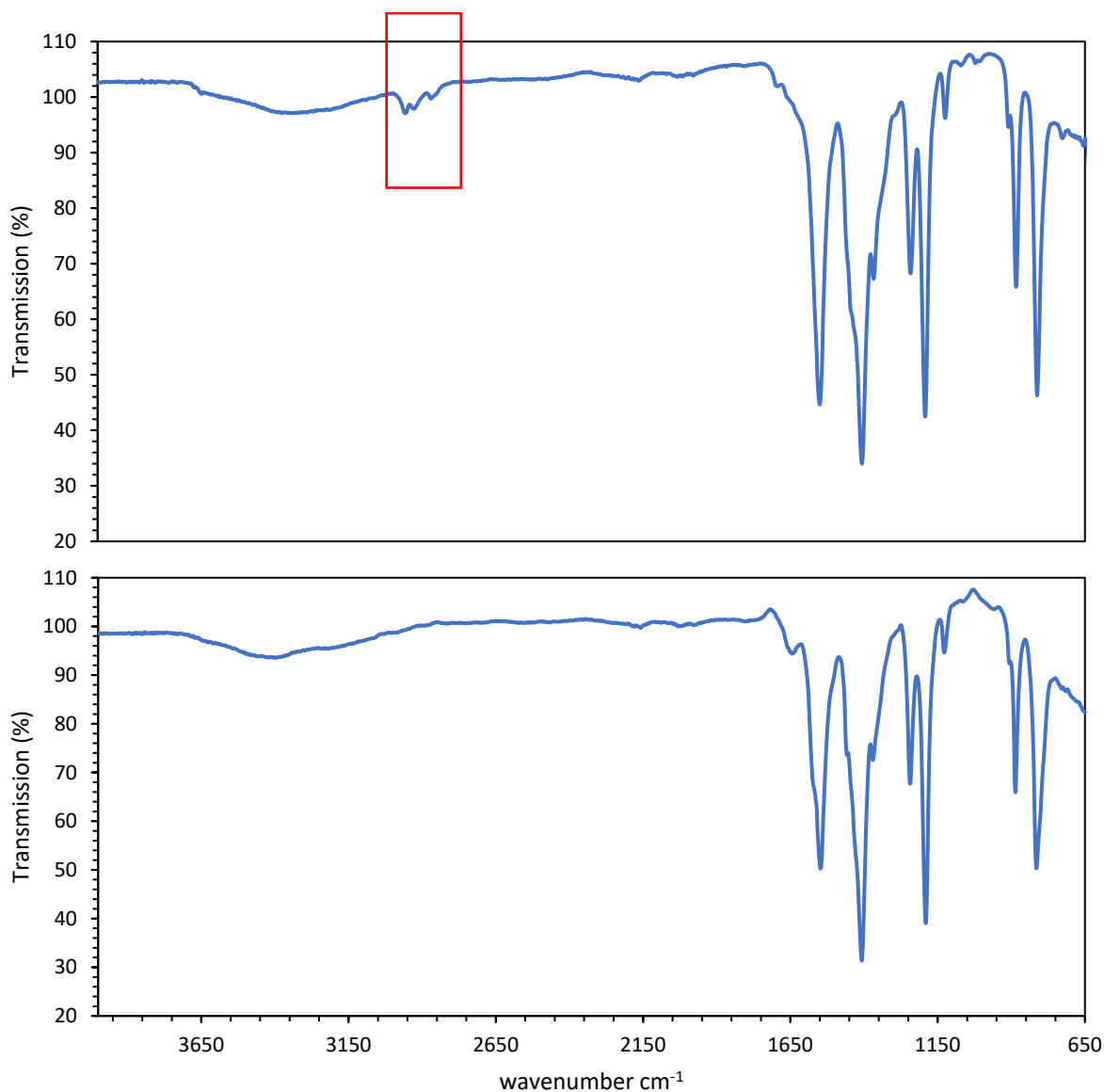


Figure 61 IR spectra of MOF-74. (bottom) MOF-74 with empty pores, (top) ibuprofen loaded MOF-74, area boxed in red corresponds to aromatic C-H ibuprofen vibrations. Peak assignments: (top) 812 (s), 884 (m), 1125 (w), 1192 (s), 1243 (m), 1366 (m), 1408 (s), 1551 (s), 2858 (w), 2922 (w), 2958 (w), 3352 (w br). (bottom): 815 (s), 886 (m), 1128 (w), 1192 (s), 1245 (m), 1372 (m), 1408 (s), 1548 (s), 1647 (w), 3381 (w br).

The IR spectrum indicate that ibuprofen is at the very least present in the loaded sample.

The bands at  $3000\text{ cm}^{-1}$  correspond to the  $\nu_{\text{Ar}}(\text{C-H})$  of the aromatic groups on the ibuprofen. The ibuprofen peak  $\nu(\text{C=O})$  is not visible in the sample, which may be due to similarity to the carboxylic groups present in the linker.

#### 4.3.4 INS of loaded MOF-74 samples

After initial attempts to prove ibuprofen loading using IR spectroscopy were unsuccessful, inelastic neutron spectroscopy was explored. INS is a much more sensitive spectroscopic method than IR spectroscopy, hydrogen sensitivity in particular. Activated MOF-74 contains very little hydrogen by percentage mass, with only one hydrogen environment present in samples, on the other hand ibuprofen has a much higher hydrogen percentage and eight hydrogen environments.

Spectra for three samples were collected, an empty MOF-74 spectrum, a loaded MOF-74 spectrum, and a spectrum of pure ibuprofen (Figure 62). As expected, the activated MOF-74 sample has very few peaks present. The loaded MOF-74 sample has many more peaks. In order to determine which peaks were due to ibuprofen the spectrum from the empty MOF-74 sample was subtracted from the loaded sample to produce a “residual” spectrum.

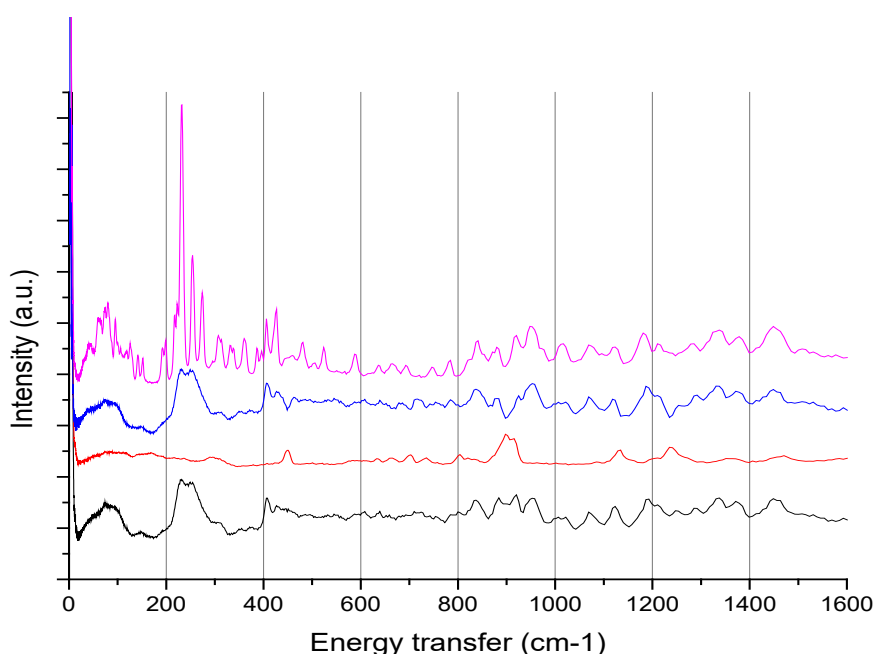


Figure 62 INS spectrum of MOF-74 and ibuprofen samples. ibuprofen loaded MOF-74 sample (black, bottom), activated MOF-74 sample (red second from bottom), subtracted spectrum removing empty MOF peaks from loaded spectrum (blue second from top), ibuprofen (magenta top).



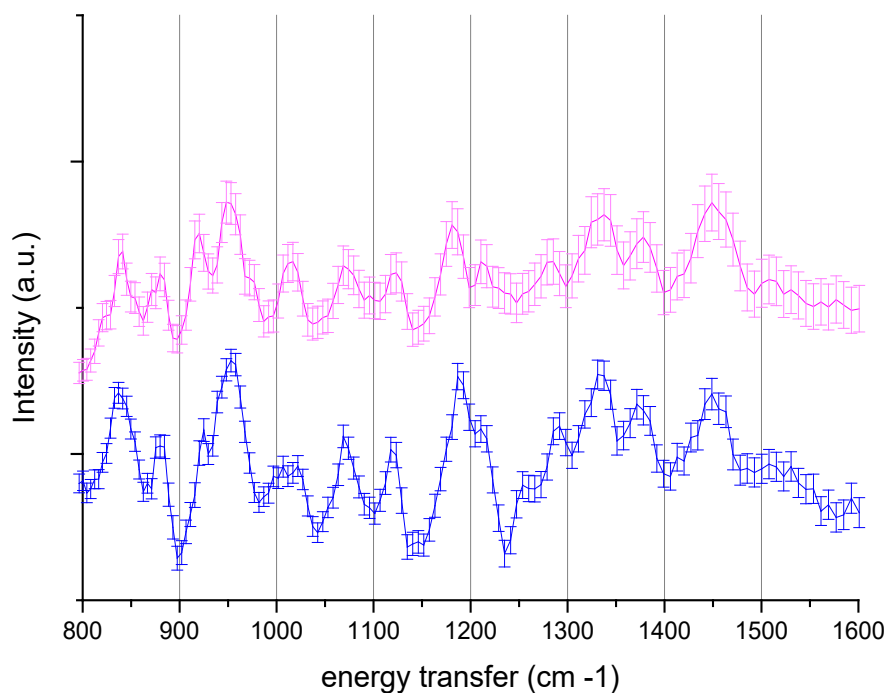


Figure 63 INS comparison of ibuprofen (magenta), and ibuprofen inside MOF-74 sample (blue) between 800 – 1600  $\text{cm}^{-1}$ , which correspond to the ibuprofen aromatic stretches.

Predicting stretches in INS intuitively can be very difficult, so stretches are calculated using DFT<sup>171</sup>. Table 16 shows the INS stretches of ibuprofen as calculated by a plane wave DFT calculation by Qian et al.<sup>85</sup>

Using the spectrum along with Table 16 and Figure 64, we can begin to understand the interaction between the ibuprofen and the MOF. Comparing INS in the region between 800-1600  $\text{cm}^{-1}$  shows two almost identical spectrum (Figure 63). This region corresponds to the hydrogens around the aromatic ring (hydrogens on carbons 6,7, 9, and 10) on the ibuprofen showing very little change between the loaded and ibuprofen reference. This means that the aromatic regions of the ibuprofen are not interacting in any significant way with the framework. On the other hand, in the region of 0-500  $\text{cm}^{-1}$  (Figure 62) peaks have become much broader with very little definition; this region corresponds to the

motions of the ibuprofen carboxyl group and the carbons numbered 1 and 2. This effect has been previously reported when loading ibuprofen, and has been used by Qian et al,<sup>85</sup> to suggest that ibuprofen has become amorphous and is interacting with the surface of the framework rather than forming independent crystallites. However; it does not confirm whether ibuprofen is inside the pores of the framework, or just coating the outside of the framework particles.

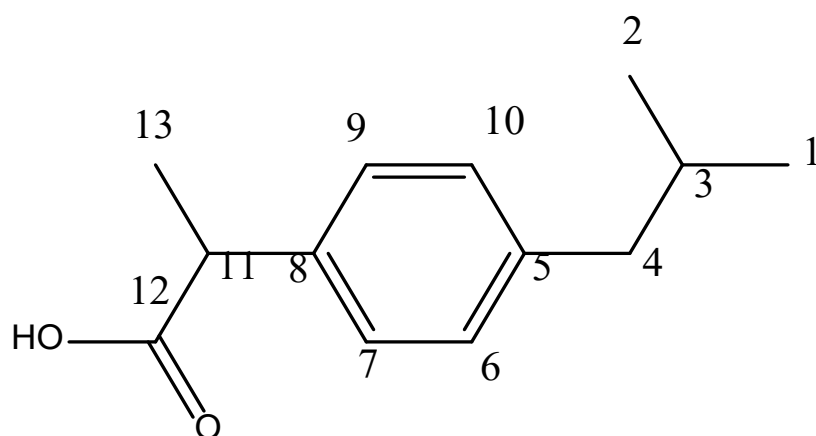


Figure 64 Structure of ibuprofen. Numbering relates to those in Table 16

Table 16 INS spectroscopy peak assignments for ibuprofen. atom labelling same as Figure 64

<b>Wavenumber (cm<sup>-1</sup>)</b>	<b>Approximate Description of Motions</b>
<b>223</b>	Torsional motion of C3-C1-H3, C3-C2-H3, and C11-C13-H3
<b>255</b>	Torsional motion of C3-C1-H3, C3-C2-H3, and C11-C13-H3
<b>276</b>	Bending motions of C4-C3-C1-H3, C4-C3-C2-H3, and C11-C13
<b>336</b>	Torsional motion of C3-C1-H3, C3-C2-H3, and C11-C13-H3
<b>425</b>	Benzene ring deformation
<b>481</b>	Rocking motion of C11-C12-OH
<b>523</b>	Bending mode of C12-O-H
<b>589</b>	Bending mode of C11-C12-OH
<b>691</b>	Stretching mode of C12-OH
<b>838</b>	Benzene ring deformation
<b>951</b>	Bending modes of C6-H, C7-H, C9-H and C10-H
<b>1008</b>	Bending mode of C11-H
<b>1063</b>	Benzene ring deformation
<b>1070</b>	Rocking motion of C11-C13-H3
<b>1331</b>	Bending mode of C4-H
<b>1446</b>	Bending mode of C4-H

### 4.3.5 PXRD of loaded sample

A PXRD of a loaded MOF-74 sample was collected according to the method outlined in Section 2.9.2.5, using the Bruker D8 in capillary configuration. Figure 65 shows the collected diffractogram along with a Pawley refinement.

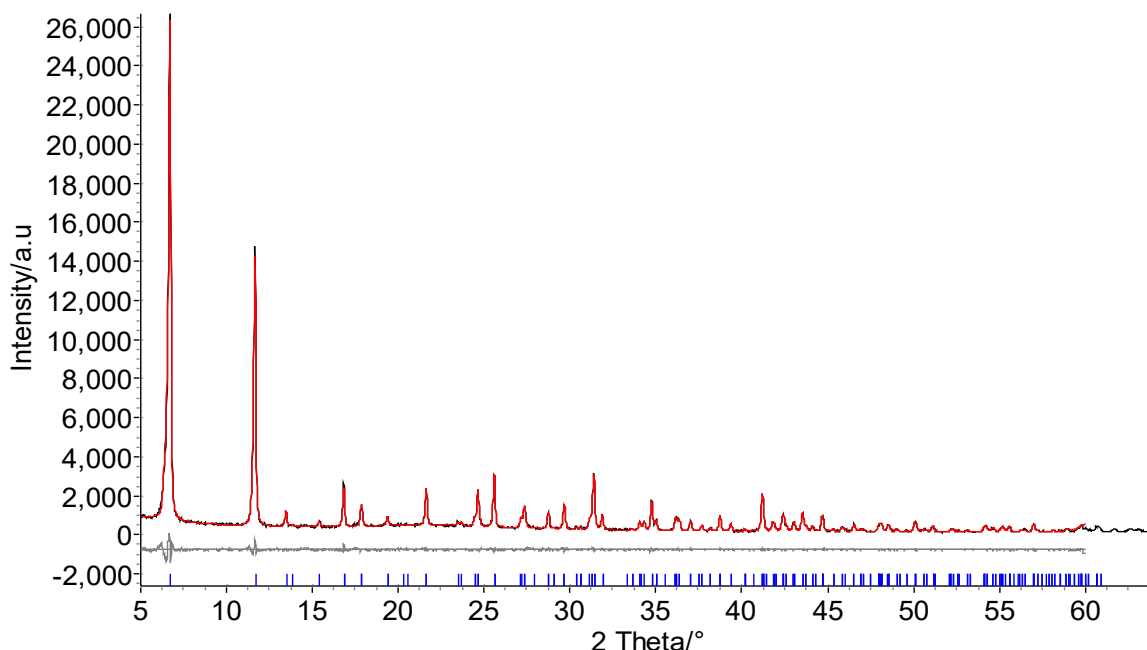


Figure 65 PXRD pattern of loaded MOF-74-Zn sample. Pawley refinement shown. Observed (blue), calculated (red), hkl indices (tick marks), and difference curve (grey).

The loaded MOF-74 sample shows no signs of the crystalline ibuprofen phase, or any evidence of framework decomposition in the hexane ibuprofen solution. After loading ibuprofen into the framework, the relative peak intensities of the MOF-74 phase have changed significantly and are different to the relative peak heights of either the hexane soaked or activated MOF-74 samples. Pawley refinements were used to compare lattice parameters of the MOF which are presented in Table 17. Pawley refinements were used instead of Rietveld refinements due to poor fit of the Rietveld model to the observed loaded MOF-74 sample, due to the change in relative peak heights in the PXRD pattern.

Table 17 Lattice parameters from Pawley refinements of empty MOF-74 and ibuprofen loaded MOF-74

Lattice parameter	Activated MOF-74	Ibuprofen loaded MOF-74
Space group	<i>R</i> -3	<i>R</i> -3
<i>a</i> (Å)	26.132(4)	26.093(6)
<i>b</i> (Å)	26.132(4)	26.093(6)
<i>c</i> (Å)	6.645(8)	6.713(8)
$\alpha$ (°)	90	90
$\beta$ (°)	90	90
$\gamma$ (°)	120	120
Volume (Å <sup>3</sup> )	3926.1(7)	3955.5(8)

Unit-cell volumes change by less than 1% between the empty pore framework and the ibuprofen loaded framework, this is consistent with past examples when changing molecules within the pores of MOF-74.<sup>80</sup>

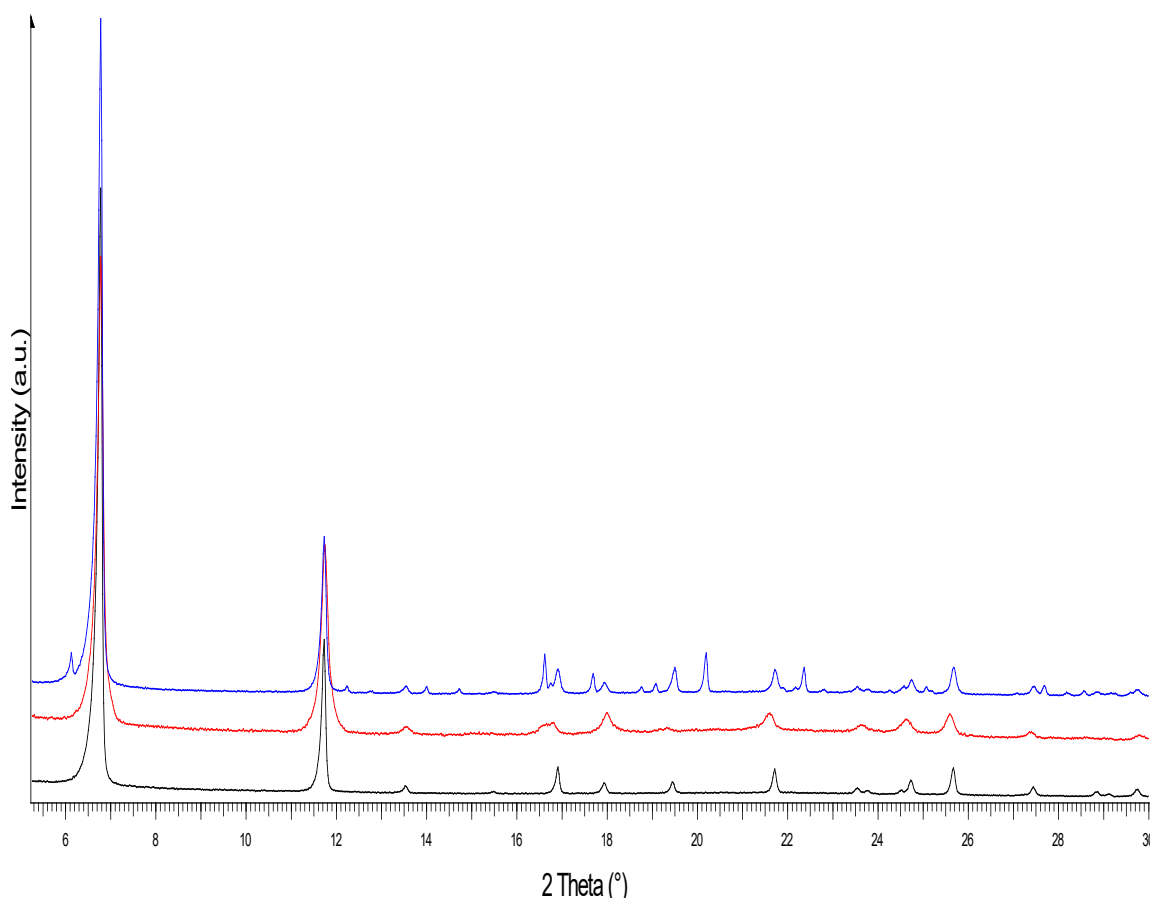


Figure 66 PXRD pattern of MOF-74. Activated MOF-74 (black), ibuprofen loaded MOF-74 (red), ibuprofen and MOF-74 physical mix (blue).

To give further evidence that the ibuprofen became amorphous, a mixture of ibuprofen and activated MOF-74-Zn was made. Figure 66 shows the difference in powder pattern between a loaded MOF-74-Zn sample and the corresponding powder pattern of a MOF-74-Zn and ibuprofen mixture. This mixture was made by combining together 20 mg of ibuprofen were mixed with 80 mg of activated MOF-74-Zn; the ratio used was the same as the ratio of ibuprofen to MOF in the loaded sample. There is no evidence of crystalline ibuprofen in the loaded sample, therefore the ibuprofen must be molecularly dispersed. Amorphous ibuprofen reverts to its crystalline form very quickly unless stabilised.<sup>172</sup> Therefore, ibuprofen's presence either on the surface of the MOF or inside the pores of the MOF are remaining in a dispersed state rather than returning to their crystalline form.

#### **4.3.6 SS-NMR of loaded and blank sample**

In order to further prove that ibuprofen had been incorporated into the framework <sup>13</sup>C SS-NMR data of two MOF-74 samples were collected (Figure 67). Interpreting SS-NMR is non-trivial, but fortunately interpretation was facilitated by the absence of peaks in the region between 0 and 60 ppm. The ibuprofen peaks are very visible in this region in the loaded sample. The peak positions and peak shapes have all shifted slightly, potentially indicating that the ibuprofen is interacting with the MOF. The most likely interaction site would be the uncoordinated metal site present in the MOF, so it is likely that is the interaction point.

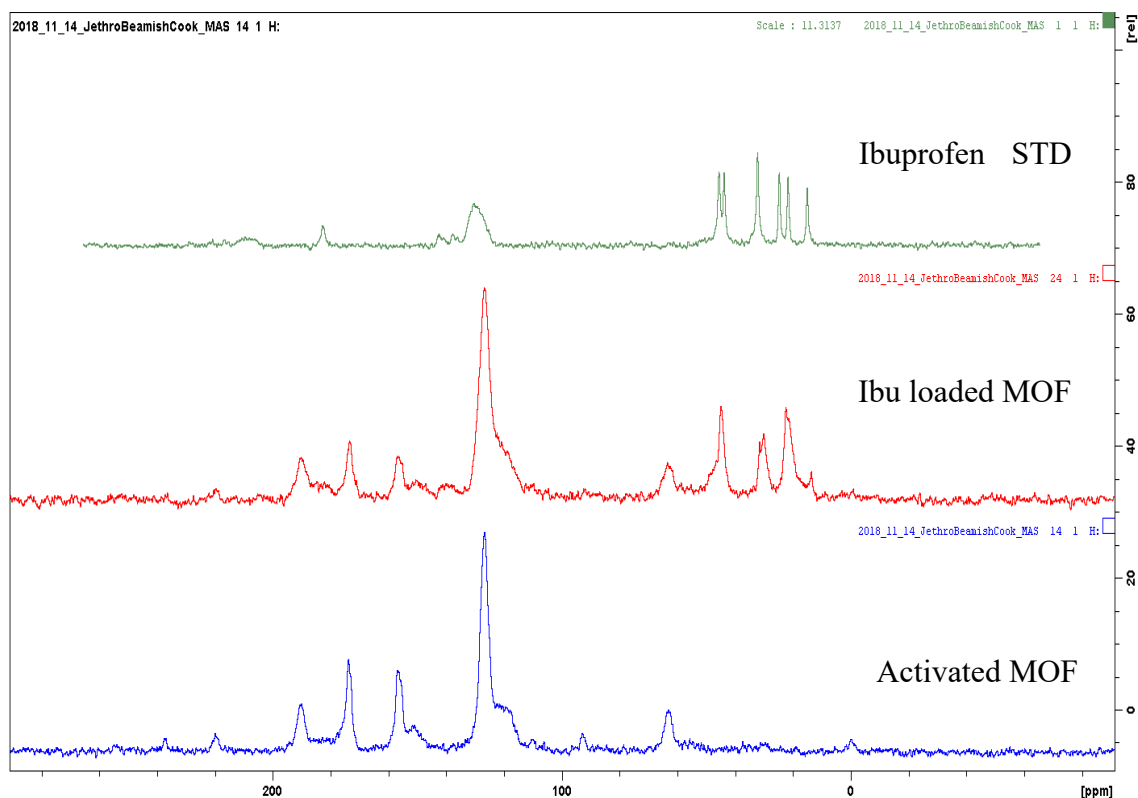


Figure 67  $^{13}\text{C}$  SS-NMR of MOF-74 samples. activated MOF-74 (blue), ibuprofen loaded MOF-74 (red), ibuprofen standard (green).

Blank MOF peaks (ppm): 81 (w), 120 (m br), 125 (s), 150 (w), 155 (m), 175 (m), 190 (w), 220 (v w).

Loaded MOF peaks (ppm): 14 (w), 23 (m doublet), 35 (m doublet), 44 (m), 50 (w br), 81 (w), 120 (w br), 125 (s), 150 (w), 155 (m), 175 (m), 183 (w), 190 (w)

Ibuprofen peaks (ppm): 14 (w), 21 (m), 25 (m), 35 (m), 44 (m doublet), 130 (m br), 183 (w)

#### 4.3.7 DSC of loaded sample

DSC runs of activated and loaded MOF-74 samples were collected according to the procedure outlined in Section 2.3. Samples were heated in a vacuum oven for six hours

at 373 K before data collection in order to remove any solvent present either in pores or on surface of samples.

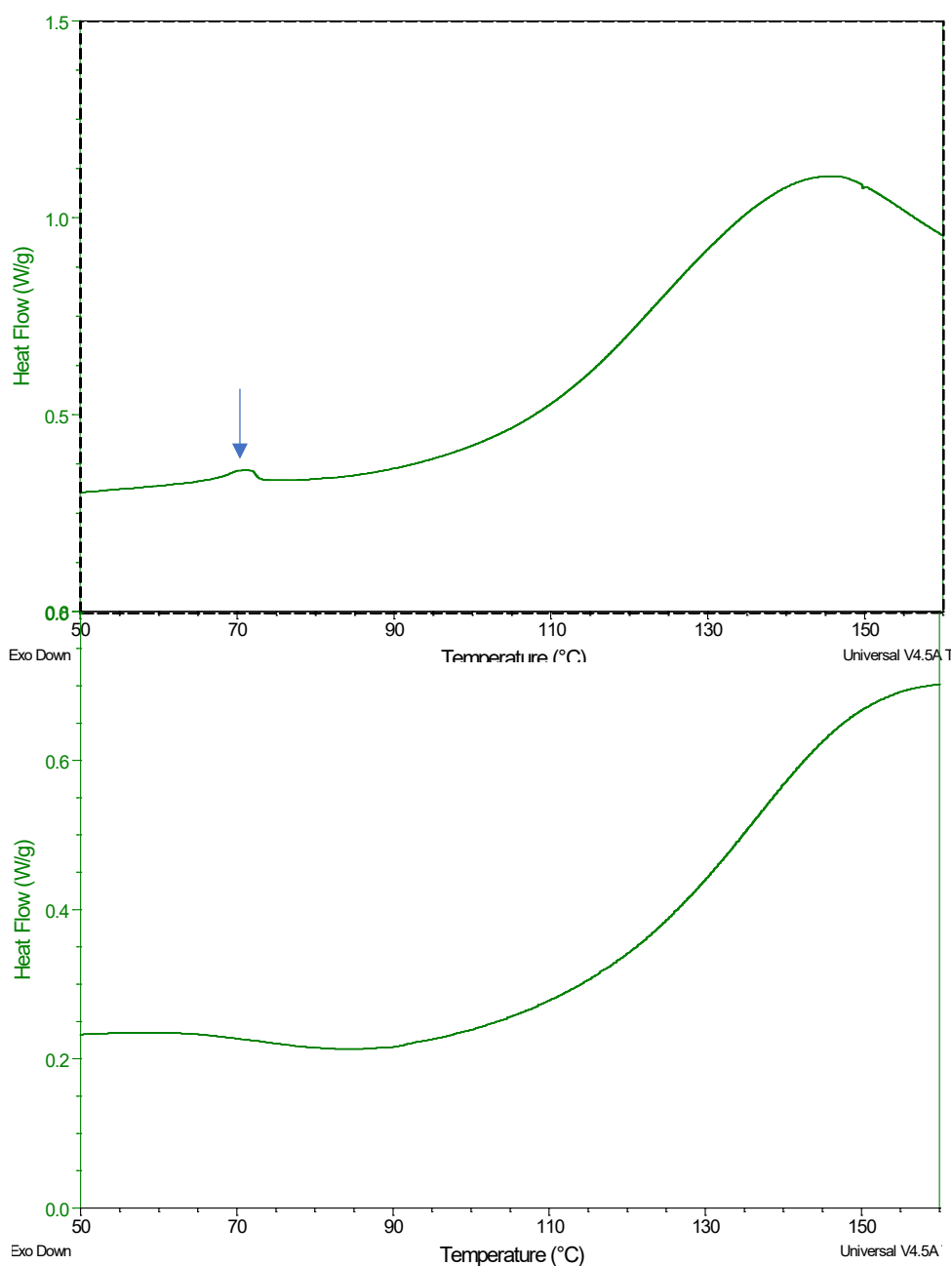


Figure 68 DSC of MOF-74 samples. ibuprofen loaded MOF-74 sample (top), activated MOF-74-Zn (right). Endothermic signals are shown as increases in heat flow. Arrow points to ibuprofen melting.

The collected DSC data is shown in Figure 68. Comparison of the two samples shows two main differences, a small peak at 70 °C and a shift of the broad peak at 170 °C to 140 °C. The peak at 70 °C, an exothermic change, can be attributed to a loss of



crystallinity in ibuprofen. Typically the ibuprofen temperature at which ibuprofen melts is 78 °C<sup>173</sup> but a shift in melting temperature is often observed when the ibuprofen is encapsulated in a drug release medium.<sup>174</sup>

#### 4.3.8 SEM of loaded samples

SEM photographs of activated and loaded samples were collected according to the method outlined in Section 2.8.

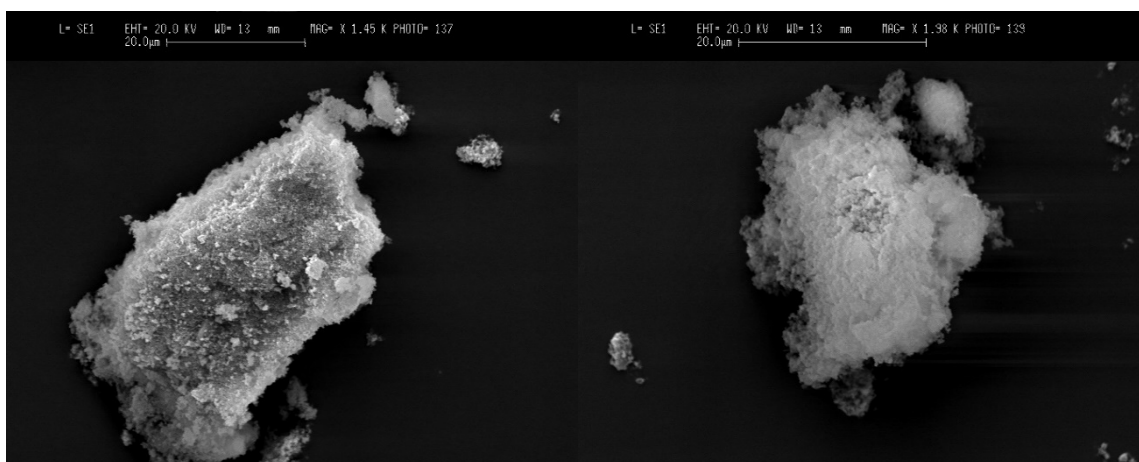


Figure 69 SEM of MOF-74 samples. (left) activated MOF-74 with empty pores, (right) ibuprofen loaded MOF-74 sample.

The SEM show very similar pictures between the activated MOF-74-Zn sample and the ibuprofen loaded MOF-74 sample. The SEM pictures that both MOF samples are very fine powders, where each particle is hard to resolve. Looking at the images there is no sign of ibuprofen crystallising on the surface of the MOF particles. The images were hard to collect as the MOF is an insulator and was charging even though both samples were gold sputtered to increase conductivity. Due to the insulating nature of the MOF samples collection of higher resolution images was not possible without modifying the image collection procedure; a potential improvement could be a thicker gold coating than the 7 nm coating used in the image collection.

## 4.4 Discussion

### 4.4.1 understanding ibuprofen loading in MOF-74

Presented in this chapter is both the loading of ibuprofen into MOF-74 and analysis of ibuprofen loaded MOF-74 samples to try to understand how ibuprofen interacts with MOF-74-Zn. The ibuprofen was loaded into the MOF using an immersion method. An activated MOF-74-Zn sample was added to a highly concentrated ibuprofen solution. This method was chosen over the other potential methods as it was the loading method used in many other MOF drug loading experiments.<sup>90 175 93</sup>

In the handful of other MOF drug loading experiments, the location of ibuprofen molecules has not been explored. Instead, all the other existing reports only study the viability of using MOFs for drug delivery. The other existing publications measure the maximum ibuprofen loadable into a MOF framework and the rate of release in a simulated body fluid.

While measuring the maximum loading of ibuprofen into MOF-74-Zn, it became abundantly clear that understanding the MOF-ibuprofen interaction was extremely important. To this end, SS-NMR and TOSCA INS were used in conjunction with PXRD to measure the properties of loaded MOF-74 in relation to activated MOF-74. SS-NMR and INS data both strongly suggested that the ibuprofen was interacting with the surface of the MOF. The measured PXRD pattern showed a large difference between a loaded MOF sample and an ibuprofen MOF mixture, with the crystalline ibuprofen phase being completely absent from the loaded sample. All evidence pointed towards ibuprofen becoming molecularly disperse as it fit in to the pores of the MOF.

INS studies of MOF-74 are not entirely new; neutron spectroscopy has been used by Pham et al,<sup>176</sup> to find the H<sub>2</sub> binding sites of the MOF-74 series, but the INS of a drug

loaded MOF sample has not been previously reported (INS has been used for drug loaded samples with other materials). In particular, INS studies have been conducted on silica particles which have similar pore structures to MOF structures explored in this chapter.<sup>85</sup> The INS results explored by Quian *et al.* are very similar to the results presented in this chapter. In both cases INS peaks corresponding to ibuprofen's carboxylic group broaden significantly. This suggests that the carboxylic groups are interacting with the surfaces of the MOF. The broadening of peaks in INS can be attributed to molecules functional groups existing in multiple spatial arrangements, in this case, where the ibuprofen is interacting with the surface of the MOF. These surface interactions lead to a number of slightly different ibuprofen configurations, mostly around the ends of the molecules, where the ibuprofen is interacting with the MOF surface.

A paper published by Erucar *et al.*<sup>177</sup> simulated the MOF interactions with ibuprofen via DFT which also showed ibuprofen interacting with MOF surfaces and coordinating to metal centres. This evidence corroborates with the INS data suggesting that ibuprofen interacts with the framework surface in multiple ways. Together, this mixture of experimental evidence and theoretical understanding strongly supports the loading of ibuprofen into the framework and interacting with the framework surfaces.

#### **4.4.2 MOF-74 family ibuprofen loading comparison**

Ibuprofen was successfully loaded into MOF-74-Zn via immersion in a concentrated solution. This work presents an advancement in the field of MOF drug delivery applications. Drug loading studies of other MOF-74 analogues have been previously reported, specifically ibuprofen loading into the Fe<sup>90</sup> and Ni<sup>91</sup> analogues. Additionally, the maximum possible methotrexate loading mass for the MOF-74 series was calculated using DFT.<sup>178</sup> Methotrexate does not have exactly the same dimensions as ibuprofen but offers a good comparison of maximum possible theoretical loading compared to

experimental values. The maximum ibuprofen loading values have been tabulated in Table 18. As all the MOF-74 analogues have very similar pore sizes, the maximum ibuprofen loadings can be compared. Both the nickel analogue and the iron analogue appear to have a smaller max loading mass compared to the zinc analogue. It is worth noting that all studies so far reported exhibit experimental drug loading values significantly below the theoretical max loading of ibuprofen into MOF-74-Zn .

Table 18 Maximum ibuprofen loadings of MOF-74 analogues. \* calculated using methotrexate not ibuprofen, but molecule dimensions very similar.

<b>MOF-74 analogue</b>	<b>Maximum ibuprofen loading (g/g)</b>
<b>MOF-74-Ni</b>	0.25
<b>MOF-74-Fe</b>	0.21
<b>MOF-74-Zn</b>	0.25-0.29
<b>Theoretical max loading</b>	0.35*

It is worth noting that particle size was not taken into account when comparing the ibuprofen loadings of the MOF-74 analogues. As demonstrated in Section 3.3.6.1, the particle sizes of mechanochemically synthesised MOF-74 are in the micrometre range. The particle sizes of the other MOF-74 analogues are not reported in their respective publications.

#### **4.4.3 Further work and drug release experiments**

##### **4.4.3.1 Unloading ibuprofen from MOF-74**

Initial attempts to measure the rate at which ibuprofen leaves MOF-74 in buffer solution were unsuccessful due to a range of reasons covered in Section 4.4.3.2. Not knowing the rate at which ibuprofen leaves the framework makes it very difficult to truly evaluate the differences between the different MOF-74 analogues for drug delivery. In theory using HPLC followed by UV-Vis it will be possible to measure the release rate.

#### 4.4.3.2 Issues with unloading experiments

The dissolution experiment method was refined across many runs, due to a number of different factors. As described in Section 3.3.6 the particle size of synthesised MOF-74 is dependent on the particle size of ZnO used as a reactant. Smaller particle size ZnO was found to speed up milling reaction time; however, the 0.1  $\mu\text{m}$  particle size ZnO, which was used as a reactant for MOF-74 synthesis produced MOF-74 with particle sizes around 0.2  $\mu\text{m}$ . The 0.2  $\mu\text{m}$  MOF particles were not filtered by the 0.45  $\mu\text{m}$  syringe filters producing a “noisy” UV-Vis spectrum which made determining the concentration of ibuprofen in solution impossible.

The other setback was the decomposition of MOF-74 in the phosphate buffer. MOF-74 decomposes in phosphate buffer in a week timescale, this decomposition released 2,5-dihydroxyterephthalic acid into the solution along with ibuprofen. 2,5-dihydroxyterephthalic acid has peaks in the UV-Vis region at 215 nm and 250 nm, while ibuprofen has a peak at 225 nm. Due to the peaks being so close together isolating the ibuprofen peaks was impossible, hence the need for HPLC.

## 4.5 Conclusion

In summary it has been shown in this chapter that MOF-74-Zn is a strong candidate for further research for medicinal applications. All evidence suggests that MOF-74 incorporates ibuprofen into its pores. No single piece of evidence definitively proves that the ibuprofen has moved into the pores of the framework rather than the surface of the MOF. That said the INS, and SS-NMR indicate that the ibuprofen is interacting extensively with the MOF which points more towards its presence in the pores. It is of particular note that MOF-74-Zn matches the ibuprofen uptake of MOF-74-Ni and exceeds that of MOF-74-Fe. It is very promising that mechanochemically synthesised MOFs are equally useful as their solvothermally synthesised analogues, while offering huge advantages in terms of synthesis times and solvent volumes required.

The next steps would be to measure the cytotoxicity of MOF-74-Zn. In theory MOF-74-Zn would be unlikely to destroy cell lines, but it would still be worth investigating. Thinking beyond ibuprofen, there are many potential drugs which could be loaded into MOF-74 which not yet been studied. There is still huge potential in MOFs for use in drug delivery, but much more research needs to be conducted in this field, namely finding MOFs which are very acid stable, with large surface areas and non-toxic components which could be further studied. In addition, studying the maximum capacity of other drugs inside MOF-74-Zn would be very useful, with 5-fluorouracil and methotrexate as potentially interesting drugs to study.

## Chapter 5- Mechanochemical synthesis and characterisation of an isorecticular MOF-74 framework

### 5.1 Introduction

The structure of MOF-74 has been discussed thoroughly in Chapters 1, 3, and 4. A yet undiscussed feature of the MOF is the ability to functionalise the linker in order to change the properties of resultant MOFs. This property has been used to optimise MOFs for catalysis, gas adsorption, and to drastically increase surface area.

A remarkable feature of MOFs, first discussed by Yaghi,<sup>16</sup> is that it is possible to vary the length of the linker while retaining the underlying topology of the MOF. This is often described as isorecticular chemistry. In the case of MOF-74, this approach results in the isorecticular MOF-74 series, more commonly known as the IR-MOF-74 series.<sup>118</sup> This series of MOFs has the same functionality when coordinating to a metal centre, and so produces frameworks with the same topology. The IR-MOF-74 series uses extended terephthalic acid linkers (Figure 70) to produce frameworks with much larger pores than MOF-74.

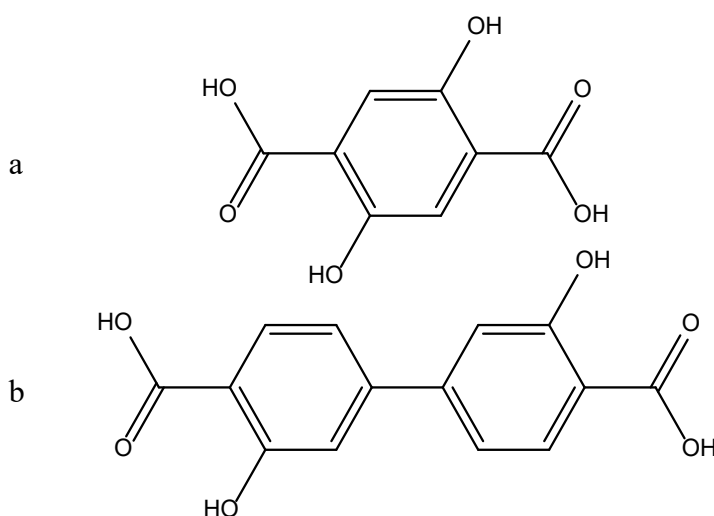


Figure 70 Comparison of the H<sub>4</sub>DHTA linker found in MOF-74 (a) with IR-H<sub>4</sub>DHTA which is used to synthesise IR-MOF-74-II (b).

So far only a couple of publications have explored the synthesis of isorecticular MOF-74 structures.<sup>94, 118, 179</sup> The main limiting factor for exploring isorecticular MOFs is the time-consuming organic synthesis required to produce the required linkers. Deng *et al.*<sup>118</sup> synthesised a series of IR-MOF-74 structures using the chemical structure motif shown in Figure 71. While these linkers seem ideal candidates to explore, their synthesis requires long multistep reaction procedures. Luckily Nguyen *et al.* synthesised a series of alternative linkers which were used to make a new IR-MOF-74 series, called VNU-74.<sup>180</sup> The linker used is 4,4'-oxalylbis(imino)]bis(2-hydroxybenzoic acid) (abbreviated as H<sub>4</sub>ODA for the protonated linker, Figure 71) is significantly easier to synthesise than those used to prepare IR-MOF-74; requiring a single-step one-pot synthesis method. Magnesium, nickel, cobalt analogues of VNU-74 have already been reported,<sup>180</sup> but the zinc analogue is not known. This chapter explores the synthesis of a new VNU-74 zinc analogue, and its synthesis by mechanochemical methods. To make the relationship between VNU-74 and MOF-74 clearer the isorecticular structure will be described as IR-MOF-74-Zn throughout the chapter.

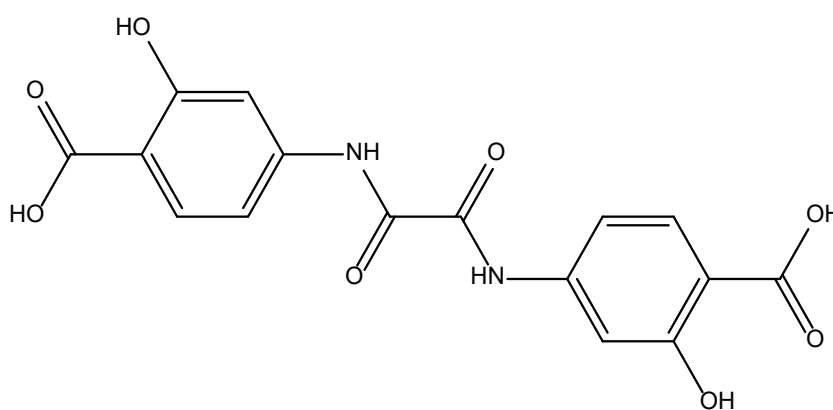


Figure 71 H<sub>4</sub>ODA, a linker which can be used to synthesise IR-MOF-74 frameworks.



## 5.2 Experimental

### 5.2.1 Synthesis of H<sub>4</sub>ODA

H<sub>4</sub>ODA was synthesised using the route outlined by Nguyen *et al.*<sup>180</sup> 6.121g 4-amino salicylic acid was mixed with 50 mL diethyl ether. The solution was cooled to 5 °C using an ice bath. 1.6 mL oxalyl chloride was added dropwise over the course of one hour to the solution. The mixture was stirred for four hours, still in an ice bath. The mixture was then removed from the ice bath and stirred for a further 20 hours. 100 mL deionised water was then added to the mixture. The product was filtered and washed with 100 mL DMF, 750 mL deionised water, and 200 mL methanol. The final product was dried at 65 °C for 24 hours to give H<sub>4</sub>ODA. H<sub>4</sub>ODA was characterised using NMR by dissolution of 5 mg of H<sub>4</sub>ODA in 5 mL of DMSO-d<sub>6</sub>. The IR spectrum of H<sub>4</sub>ODA was collected according to Section 2.4. PXRD data of H<sub>4</sub>ODA were collected both on Bruker D8 and on Diamond I11 according to Section 2.9.2.5.

#### 5.2.1.1 H<sub>4</sub>ODA DMF solvate

50 mg H<sub>4</sub>ODA (**1**) was dissolved in 20 ml of hot DMF which was heated to 70 °C. The solution was hot filtered and stored in a semi-sealed vessel. The vessel was left to cool to room-temperature, then for a further 4 days until crystals suitable for single-crystal X-ray diffraction were found. Single-crystal X-ray diffraction was performed on a small needle crystal at 150 K according to the procedure outlined in Section 2.9.1.1. Roughly 10 mg of the produced crystals were ground and PXRD was performed. A Rietveld refinement was carried out to confirm that the bulk powder exhibits the crystal structure determined using single-crystal data.

## 5.2.2 Synthesis of IR-MOF-74-Zn

### 5.2.2.1 Initial Reaction parameters

ZnO (0.178 g, 2.2 mmol) and H<sub>4</sub>ODA (0.378 g, 1.1 mmol) along with 400  $\mu$ L DMF were loaded in a 25 mL milling jar along with two 7 g stainless steel milling balls. The jar was sealed and milled for 90-minute intervals in the Retsch MM 400 mill. Small amounts of powder were removed every 90 minutes and PXRD data were collected.

### 5.2.2.2 Optimised Reaction parameters

ZnO (0.1227 g, 0.15 mmol) and H<sub>4</sub>ODA (0.278 g, 0.077 mmol) along with 260  $\mu$ L DMF were added to a 25 mL milling jar along with 6 x 1.4 g milling balls. The jar was sealed and milled for a total of 600 minutes at 30 Hz in the Retsch MM 400 mill.

### 5.2.2.3 Attempts at synthesis using H<sub>2</sub>O as milling liquid

ZnO (0.179 g, 2.2 mmol) and H<sub>4</sub>ODA (0.377 g, 1.1 mmol) along with 350  $\mu$ L H<sub>2</sub>O were added to a 25 mL milling jar along with 2 x 7 g stainless steel milling balls. The jar was sealed and milled in the Retsch MM 400 mill for a total of 360 minutes, with small powder samples collected every 90 minutes. PXRD data were collected of these powder samples.

### 5.2.2.4 Scaled up reaction parameters

ZnO (0.312 g, 3.83 mmol) and H<sub>4</sub>ODA (0.73 g, 2 mmol) along with 1 mL DMF were added to a 25 mL planetary milling jar. In addition, 30 x 0.7 g stainless steel milling balls were added. The jar was sealed and milled for a total of 3000 minutes in the Retsch PM 200 planetary ball mill. PXRD data were collected.

### **5.2.3 Stability of IR-MOF-74-Zn in solvents**

#### 5.2.3.1 Stability in DMF

10 mg of IR-MOF-74-Zn were added to 15 mL of DMF. The MOF was left in DMF for 3 days. The sample was removed from the DMF and PXRD was performed on the Bruker D8 Advance according to the procedure outlined in Section 2.9.2.5.

#### 5.2.3.2 Stability in chloroform

10 mg of IR-MOF-74-Zn were added to 15 mL of chloroform. The MOF was left in chloroform for 3 days, after which the sample was removed from the chloroform and PXRD was performed on the Bruker D8 Advance according to the procedure outlined in Section 2.9.2.5.

#### 5.2.3.3 Stability in hexane

11 mg of IR-MOF-74-Zn were added to 13 mL of hexane. The MOF was left in hexane for 3 days, then removed from the hexane. PXRD was then performed using the Bruker D8 Advance according to the procedure outlined in Section 2.9.2.5.

#### 5.2.3.4 Stability in methanol

9.5 mg of IR-MOF-74-Zn were added to 14 mL of methanol. The MOF was soaked in methanol for 3 days, then removed from the solvent. PXRD was performed using the Bruker D8 Advance according to the procedure outlined in Section 2.9.2.5.

#### 5.2.3.5 Stability in water

10 mg of IR-MOF-74-Zn were added to 15 mL of water. The MOF was soaked in water for 3 days, after which the MOF was removed from the solvent. PXRD was performed using the Bruker D8 Advance according to the procedure outlined in Section 2.9.2.5.

#### 5.2.3.6 Stability under vacuum

15 mg of IR-MOF-74-Zn brought to vacuum in a vacuum oven then heated to 60 °C and held at temperature for 12 hours. The oven was cooled to room temperature over 3 hours, then the vacuum was released. PXRD was performed using the Bruker D8 Advance according to the procedure outlined in Section 2.9.2.5.

#### 5.2.4 Attempted activation of IR-MOF-74-Zn

50 mg of IR-MOF-74-Zn was washed in 3x 5 mL DMF then immersed in 50 mL hexane. The hexane was decanted and replaced every 24 hours four times. The MOF was then held under vacuum in a vacuum oven for three hours, after which the MOF was heated to 100 °C for 12 hours. After heating, the sample was cooled over 8 hours and the vacuum released. PXRD was performed on Bruker D8 Advance according to Section 2.9.2.5 and surface area analysis was performed according to procedure outlined in Section 2.12.1.

#### 5.2.5 In-situ monitoring of IR-MOF-74-Zn synthesis

##### 5.2.5.1 In-house monitoring of synthesis

ZnO (0.1228 g, 0.15 mmol particle size 1 µm) and H<sub>4</sub>ODA (0.280 g, 0.077 mmol) along with 270 µL DMF were added to a 25 mL milling jar along with 6 x 1.4 g stainless steel milling balls. The jar was sealed and milled for 6 hours, after which a small sample was taken for PXRD analysis. Further samples were taken for every 30 minutes of milling for a total milling time of 10 hours. PXRD was performed on the Bruker D8 Advance according to the procedure outlined in Section 2.9.2.5.

##### 5.2.5.1 First synchrotron experiment

ZnO (0.1227 g, 0.15 mmol particle size 100 nm) and H<sub>4</sub>ODA (0.278 g, 0.077 mmol) along with 260 µL DMF were added to a 25 mL milling jar along with 6 x 1.4 g milling balls. The jar was sealed and milled for a total of 9 hours at 30 Hz in the Retsch MM 400

mill. Small amounts of sample were removed every 30 minutes and PXRD was performed on DLS I11 according to Section 2.9.2.5.

#### 5.2.5.2 Second synchrotron experiment

ZnO (0.1227 g, 0.15 mmol particle size 100 nm) and H<sub>4</sub>ODA (0.278 g, 0.077 mmol) along with 260  $\mu$ L DMF were added to a 25 mL milling jar along with 6 x 1.4 g milling balls. The jar was sealed and milled for a total of 4 hours at 30 Hz in the Retsch MM 400 mill. Small amounts of sample were removed after 4, 5, 6, 7.5 hours and PXRD was performed on DLS I11 according to Section 2.9.2.5.

## 5.3 Results

### 5.3.1 Characterisation of the H<sub>4</sub>ODA linker

#### 5.3.1.1 IR

Figure 72 shows the collected IR spectrum of the as-synthesised H<sub>4</sub>ODA linker. The stretch at 3329 cm<sup>-1</sup> confirms the presence of the amide group of the H<sub>4</sub>ODA linker. As it appears as a single peak it shows that linker contains only a secondary amine (the amide group); if the peak were a multiplet it would correspond to a primary amine.

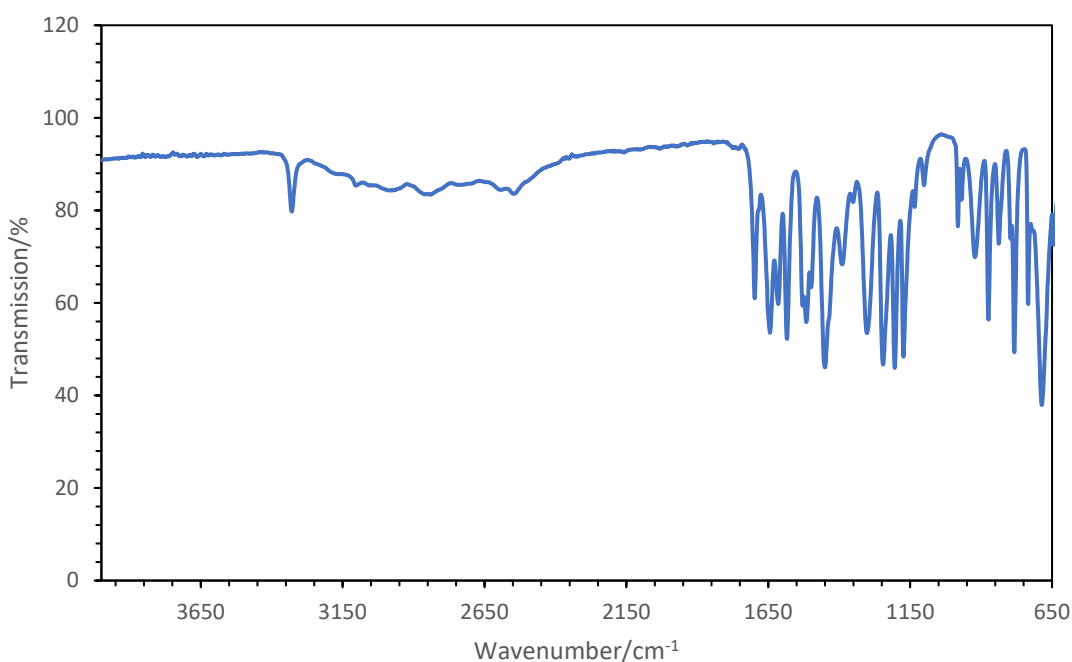


Figure 72 IR spectrum of as-synthesised H<sub>4</sub>ODA.

IR stretches: 686 (s), 734 (w), 783 (m), 795 (w), 839 (w), 874 (m), 922 (w), 935 (w), 982 (w), 1100 (w), 1135 (w), 1174 (m), 1204 (s), 1246 (s), 1302 (m), 1324 (w), 1390 (m), 1451 (s), 1509 (m), 1516 (m), 1585 (m), 1616 (m), 1644 (m), 1696 (m), 3329 (w).

#### 5.3.1.2 PXRD

##### 5.3.1.2.1 PXRD of the as-synthesised H<sub>4</sub>ODA linker

Figure 73 shows the collected PXRD pattern of the as-synthesised linker. The powder pattern has very few features making indexing the unit-cell and solving the crystal structure very difficult.

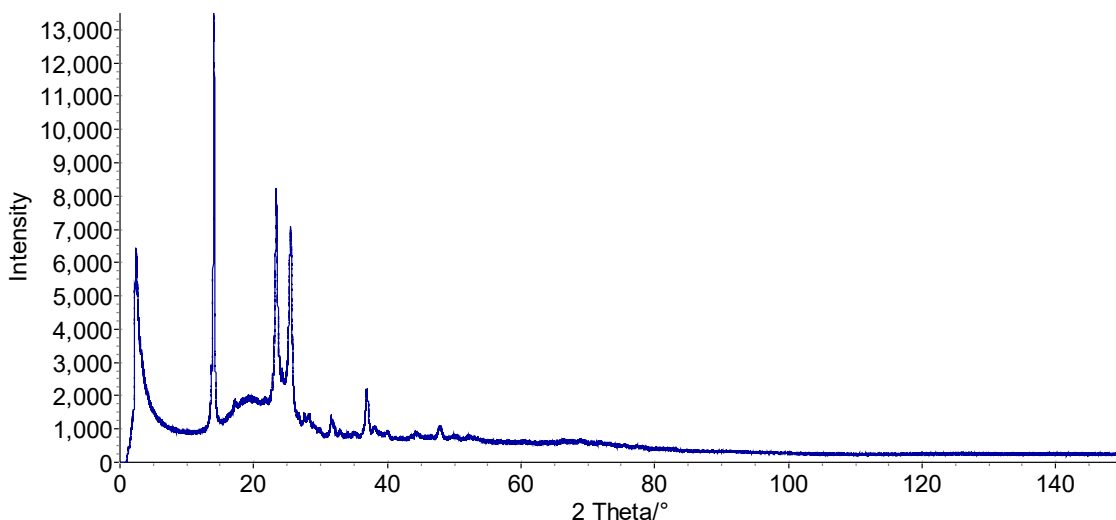


Figure 73 PXRD diffractogram of as-synthesised H<sub>4</sub>ODA linker. PXRD collected on Bruker D8 Advance.

As structure solution from powder was not feasible, structure determination via single-crystal X-ray diffraction was attempted. To this end, H<sub>4</sub>ODA solubility was measured using several common solvents including: water, methanol, diethyl ether, ethanol, acetone, hexane, and DMF. H<sub>4</sub>ODA was only found to be significantly soluble in DMF and single crystals were successfully grown (Section 5.2.1.1).

#### 5.3.1.2.2 Crystal structure of the H<sub>4</sub>ODA DMF solvate

Shown in Table 19 are the crystallographic details and refinement parameters used when solving and refining the structure of the H<sub>4</sub>ODA DMF solvate.

Table 19 Crystallographic details and refinement parameters used when solving H<sub>4</sub>ODA.2DMF.

<b>Identifier</b>	<b>5</b>
<b>Solution method</b>	Single-crystal
<b>Empirical formula</b>	C <sub>22</sub> H <sub>26</sub> N <sub>4</sub> O <sub>10</sub>
<b>Formula weight</b>	506.47
<b>Temperature (K)</b>	150.1(4)
<b>Crystal system</b>	Triclinic
<b>Space group</b>	<i>P</i> -1
<b><i>a</i> (Å)</b>	7.0516(16)
<b><i>b</i> (Å)</b>	8.154(2)
<b><i>c</i> (Å)</b>	10.483(2)
<b><math>\alpha</math> (°)</b>	72.31(2)
<b><math>\beta</math> (°)</b>	81.220(19)
<b><math>\gamma</math> (°)</b>	86.73(2)
<b>Volume (Å<sup>3</sup>)</b>	567.5(2)
<b>Z</b>	1
<b><math>\rho_{\text{calc}}</math> g (cm<sup>3</sup>)</b>	1.482
<b><math>\mu</math> (mm<sup>-1</sup>)</b>	1.009
<b>F(000)</b>	266.0
<b>Crystal size/mm</b>	0.2 × 0.1 × 0.07
<b>Radiation (Å)</b>	CuK $\alpha$ ( $\lambda$ = 1.54184)
<b>2<math>\Theta</math> range for data collection (°)</b>	8.946 to 123.746
<b>Index ranges</b>	-7 ≤ <i>h</i> ≤ 7, -9 ≤ <i>k</i> ≤ 4, -11 ≤ <i>l</i> ≤ 10
<b>Reflections collected</b>	2612
<b>Independent reflections</b>	1693 [ <i>R</i> <sub>int</sub> = 0.0474, <i>R</i> <sub>sigma</sub> = 0.0673]
<b>Data/restraints/parameters</b>	1693/0/167
<b>Goodness-of-fit on F<sup>2</sup></b>	1.044
<b>Final R indexes [<i>I</i> ≥ 2<math>\sigma</math> (<i>I</i>)]</b>	<i>R</i> <sub>1</sub> = 0.0589, <i>wR</i> <sub>2</sub> = 0.1556
<b>Final R indexes [all data]</b>	<i>R</i> <sub>1</sub> = 0.0858, <i>wR</i> <sub>2</sub> = 0.1864
<b>Largest diff. peak/hole (e Å<sup>-3</sup>)</b>	0.31/-0.33



The DMF solvate of H<sub>4</sub>ODA crystallises in a *P*-1 triclinic space group (Figure 74). (1) has a stoichiometric ratio of 1:2 H<sub>4</sub>ODA : DMF. H<sub>4</sub>ODA molecules pack in chains across crystallographic *b*-axis of the unit-cell along with DMF molecules which are hydrogen bonded at each end. The centre of the H<sub>4</sub>ODA molecule sits on the special position of the unit-cell ( $\frac{1}{2}$ ,  $\frac{1}{2}$ , 0) and the DMF molecules sit on general positions. The CIF of the structure is included in the appendix.

The structure exhibits both intra and intermolecular H-bonding similar to the H<sub>4</sub>DHTA

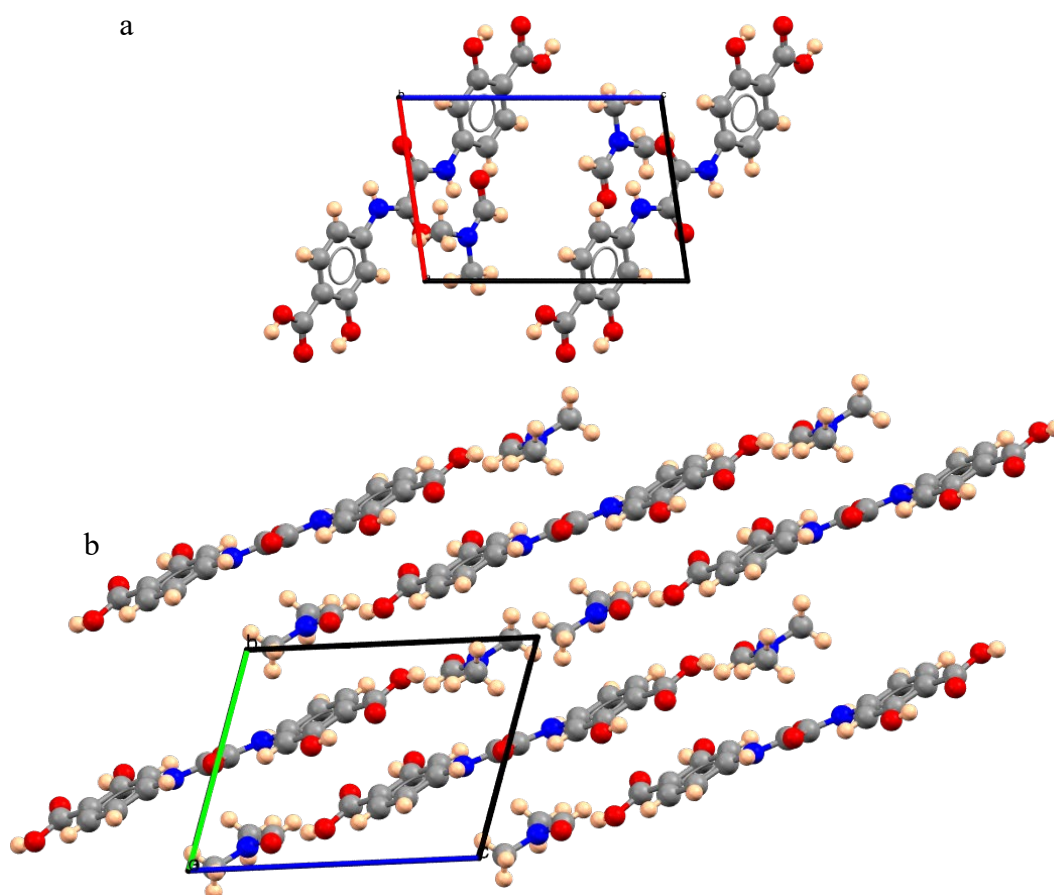


Figure 74 Crystal structure of H<sub>4</sub>ODA.DMF<sub>2</sub> viewed down the *b*-axis (a), as viewed down the *a*-axis (b).

Cell axis legend: *a* (red), *b* (green), *c* (blue). Elements present: carbon (grey), oxygen (red), nitrogen (blue), hydrogen (pink).

DMF solvate described in Section 3.3.7.2. Intermolecular H-bonding is present between the DMF molecules oxygen atom and the carboxylic acid groups at each end of the molecule; intramolecular H-bonding occurs between neighbouring hydroxyl and carboxyl groups in the molecule (Figure 75). The carboxylic hydrogen to DMF oxygen

has a very short H-bond distance of 1.713 Å indicating a strong covalent H-bond,<sup>181</sup> while the hydroxyl to carboxyl H-bond length is a more typical 1.876 Å.

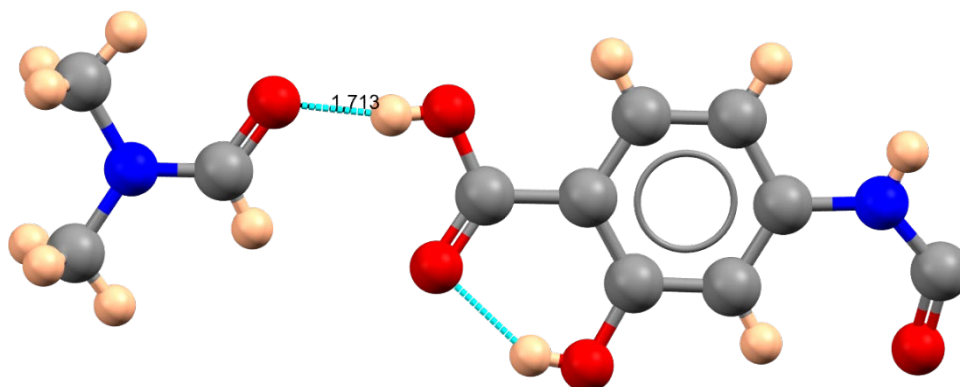


Figure 75 Detailed view of the hydrogen bonding found in H<sub>4</sub>ODA.2DMF showing half an H<sub>4</sub>ODA molecule. Blue dashed lines are from intramolecular H-bonding, red dashed lines correspond to intermolecular H-bonding. Elements: carbon (grey), oxygen (red), hydrogen (pink), nitrogen (blue).

The H<sub>4</sub>ODA molecule twists by ~4° across the long length of the molecule with a more extreme torsion between the molecule's benzene rings and amide groups (Figure 76). The torsion of 12 ° and amide angle of 128 ° are very typical angles for N-aryl amides; however, the N-Ar bond length is very short at 1.40 Å as compared to the more typical 1.42 Å bond length.<sup>182</sup>

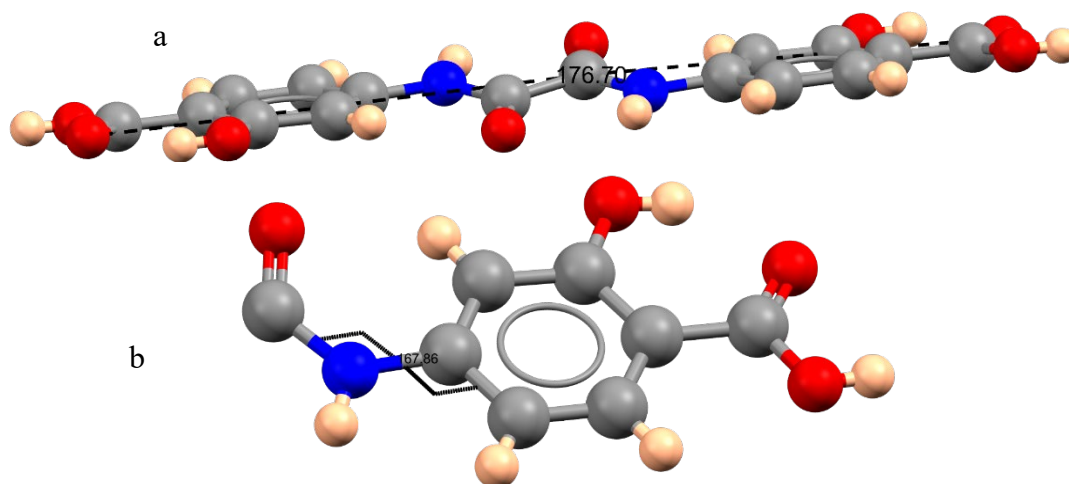


Figure 76 View of the torsion angles of H<sub>4</sub>ODA in DMF solvate structure. Twist across the molecules long length (a), torsion angle of amide functional group inside the H<sub>4</sub>ODA molecule (b). Elements: carbon (grey), oxygen (red), hydrogen (pink), nitrogen (blue).

Table 20 Refined lattice parameters for H<sub>4</sub> ODA.2(DMF) determined by single-crystal X-ray diffraction and by Rietveld refinement.

	Single-crystal	PXRD refinement
<b>Crystal system</b>	Triclinic	Triclinic
<b>Space group</b>	<i>P</i> -1	<i>P</i> -1
<b><i>a</i> (Å)</b>	7.0517(1)	7.069(5)
<b><i>b</i> (Å)</b>	8.154(2)	8.244(7)
<b><i>c</i> (Å)</b>	10.483(2)	10.583(7)
<b><math>\alpha</math> (°)</b>	72.31(2)	73.07(4)
<b><math>\beta</math> (°)</b>	81.22(2)	81.23(5)
<b><math>\gamma</math> (°)</b>	86.73(2)	85.90(5)
<b>Volume (Å<sup>3</sup>)</b>	567.46(1)	582.9(8)
<b>R<sub>wp</sub> (%)</b>	5.60	8.244
<b>R<sub>int</sub></b>		-
<b>collection temperature (K)</b>	150	298

#### 5.3.1.2.3 Rietveld refinement for H<sub>4</sub>ODA.2(DMF)

A Rietveld refinement was conducted using data collected on the ground powder of H<sub>4</sub>ODA.2(DMF) to confirm agreement with the structure determined by single-crystal X-ray diffraction. A CIF containing the parameters arising from the final refinement can be found in the Appendix. The Rietveld refinement profile is shown in Figure 77. In order to achieve good agreement between calculated and observed intensities, inclusion of preferred orientation was necessary, as crystals of H<sub>4</sub>ODA.2(DMF) were extremely long, thin plates. Some disagreement in intensities remains especially at high 2 $\theta$  angles; this is most likely due to the model not accounting for the preferred orientation correctly. Despite this, the refinement undeniably proves that the bulk powder exhibits the structure determined by single-crystal X-ray diffraction.

There is good agreement between the lattice parameters determined using Rietveld refinement and those of the structure determined by single-crystal X-ray diffraction (Table 20). The increase of unit-cell of volume from 567 Å<sup>3</sup> to 582 Å<sup>3</sup>, 2.5%, is due to the difference of collection temperature.

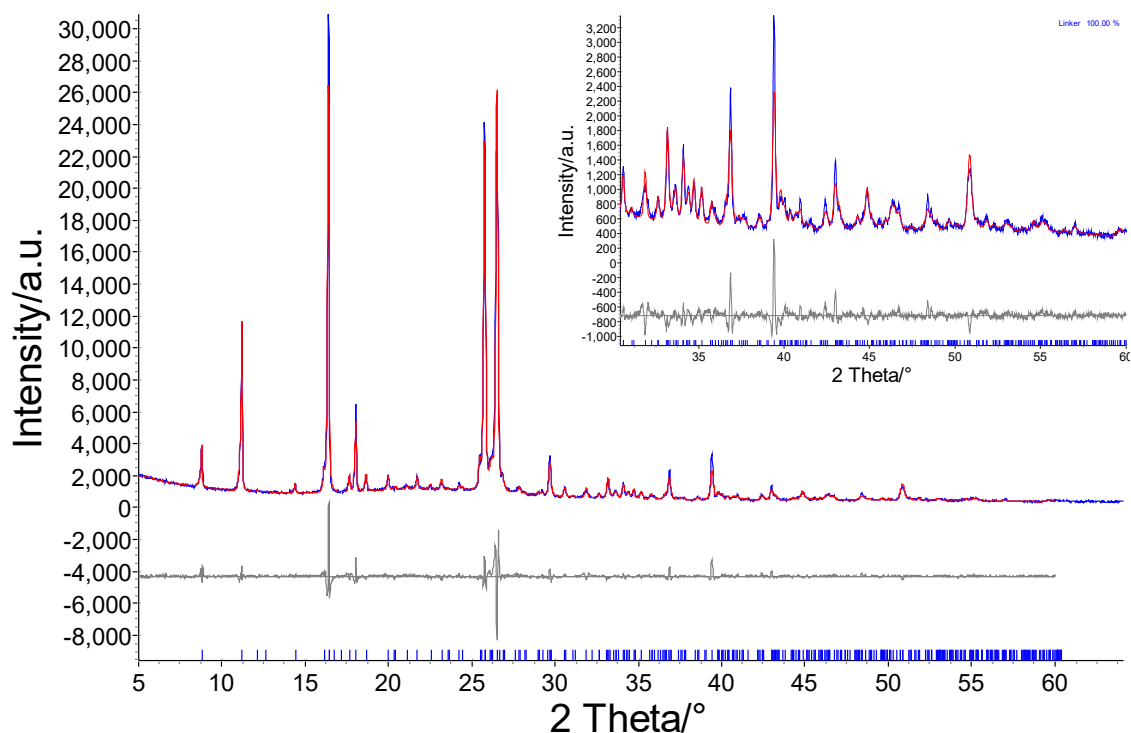


Figure 77 Rietveld refinement of H<sub>4</sub>ODA·DMF<sub>2</sub>. Experimental (blue), calculated (red), hkl indices (tick marks). Inset shows refinement at high angle. Data collected on Bruker D8 Advance.

### 5.3.2 Synthesis of IR-MOF-74-Zn

#### 5.3.2.1 Optimisation of the reaction conditions

The initial attempt to synthesise IR-MOF-74-Zn used a 2 mmol to 1 mmol Zn:H<sub>4</sub>ODA ratio (the same ratio as used to synthesise MOF-74-Zn), but it did not result in the formation of the target framework (Section 5.2.2.1). As the structure of this isorecticular MOF has not yet been determined, the published lattice parameters and powder pattern of the IR-MOF-74-Mg analogue were used for comparison purposes (Figure 78).

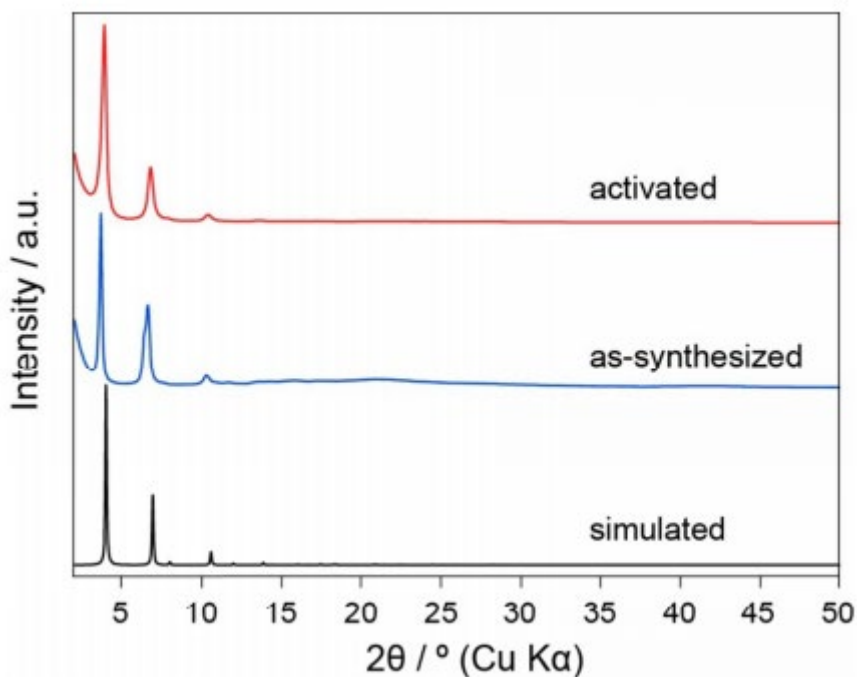


Figure 78 PXRD pattern of IR-MOF-74-Mg taken from paper by Nguyen et al.<sup>180</sup>

#### 5.3.2.1.1 PXRD

Figure 79 shows the collected PXRD diffractogram of the initial attempt to synthesise IR-MOF-74-Zn. The starred peaks on Figure 79 correspond to the zinc oxide phase which was still intense after 270 minutes milling. In addition to zinc oxide, there are clearly many more peaks indicating that at least one intermediate phase has formed (for more detail on IR-MOF-74-Zn intermediates see Section 5.3.6.1). To attempt to produce the desired phase, the effect of a range of variables on the nature of the product were explored, including: milling jar size, milling ball total mass, milling ball size, solvent volume, solvent, milling time, starting material particle size and starting material mass.

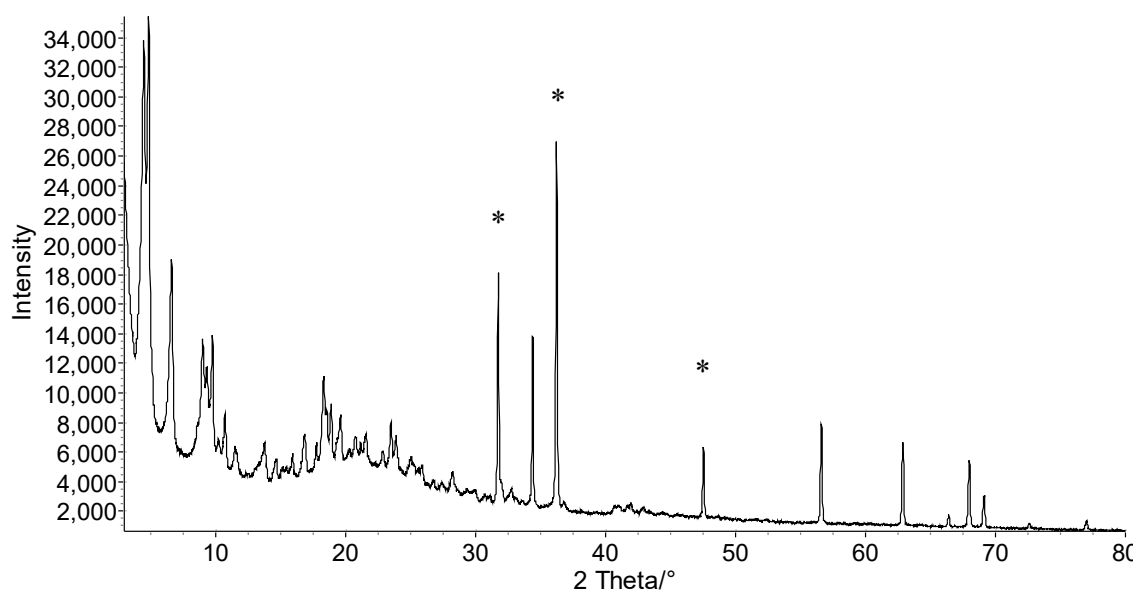


Figure 79 PXRD pattern of initial attempt to synthesise IR-MOF-74-Zn. Stars correspond to unreacted zinc oxide phase. Data collected on Bruker D8 Advance.

### 5.3.2.2 Synthesis using H<sub>2</sub>O

The effect of replacing DMF with water was investigated. Although incorporation of water in the initial reaction mixture did not produce IR-MOF-74-Zn, a different intermediate phase to the ones formed when using DMF, was produced.

#### 5.3.2.2.1 PXRD

Figure 80a shows the collected PXRD pattern of the attempted synthesis of IR-MOF-74-Zn using water to assist synthesis. As can be seen by the sharp peaks at 32 and 34 °2θ, zinc oxide is still present in the diffractogram; evidence that the reaction did not go to completion. Figure 80b shows the overlaid H<sub>4</sub>ODA diffractogram which indicates that the linker has been consumed to make a new crystallographic phase. This new phase was indexed using DICVOL as implemented in DASH. A Pawley refinement was then performed using the found lattice parameters (Table 21). Structure solution was attempted using EXPO and DASH, but due to peak broadness and lack of information of unit-cell contents the structure remains unsolved.

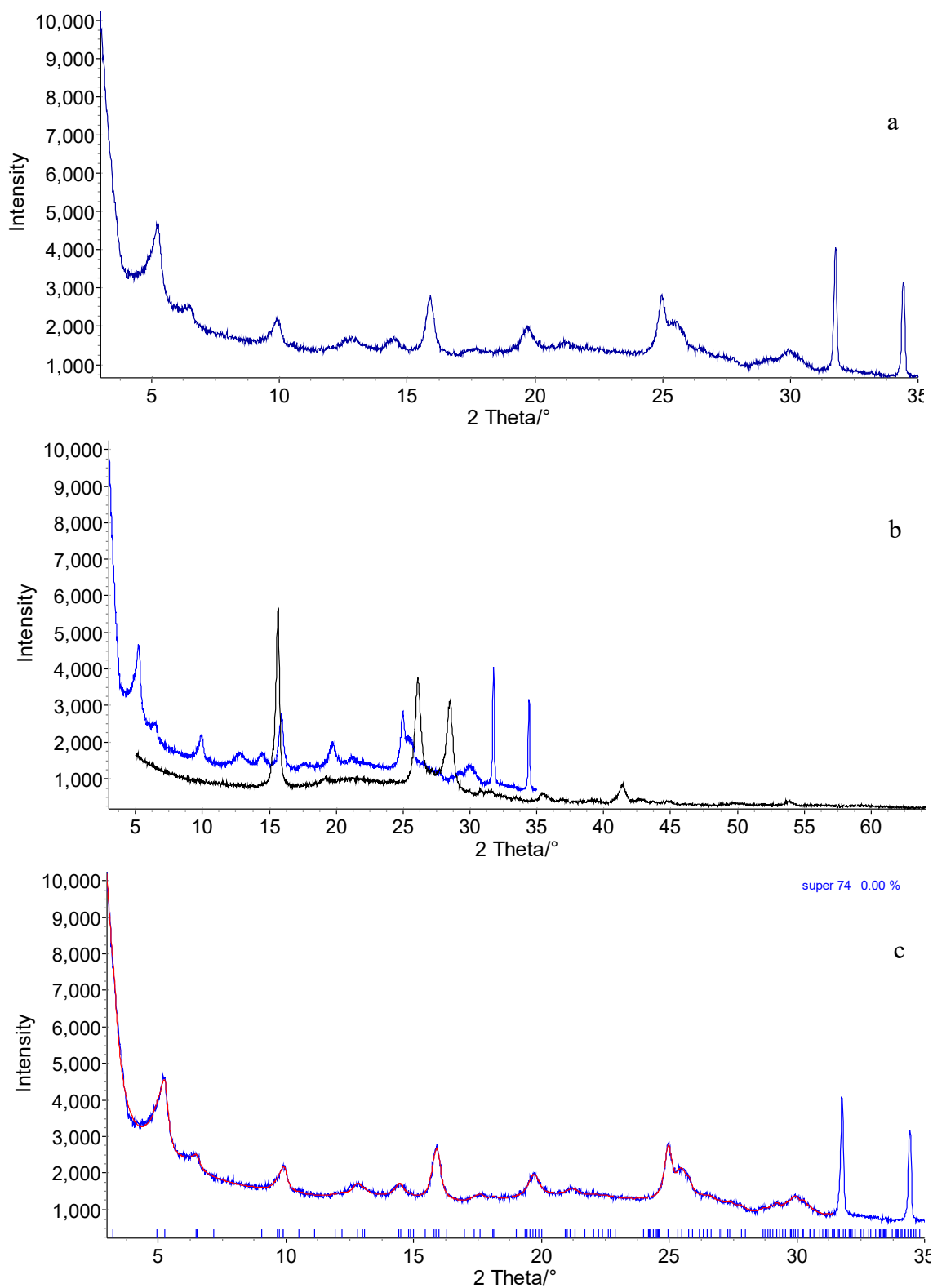


Figure 80 PXRD diffractogram of IR-MOF-74-Zn synthesis attempt using water (a). Overlaid diffractogram of H<sub>4</sub>ODA linker (b). Pawley refinement using lattice parameters from Table 21 (c). Experimental (blue), H<sub>4</sub>ODA diffractogram (black), calculated (red), hkl indices (tick marks). Data collected on Bruker D8 Advance.

Table 21 Lattice parameters of IR-MOF-74-Zn water LAG intermediate. Parameters are a result of Pawley refinement.

<b>Crystal system</b>	<b>Monoclinic</b>
<b>Space group</b>	P2
<b><i>a</i> (Å)</b>	29.6(3)
<b><i>b</i> (Å)</b>	3.0(9)
<b><i>c</i> (Å)</b>	18.3(1)
<b><math>\beta</math> (°)</b>	113.5(7)
<b>Volume (Å<sup>3</sup>)</b>	1490(5)
<b>Rwp (%)</b>	2.77

### 5.3.2.3 Optimised Reaction

Eventually a successful reaction method was found which produced IR-MOF-74-Zn in 10 hours of milling (Section 5.2.2.2). Reaction time, milling ball mass, solvent starting material ratio, total starting material mass were all permuted to find the optimised reaction. The milling time is a significant improvement over the previously reported Mg analogues two-day solvothermal reaction time.

#### 5.3.2.3.1 PXRD

Figure 81 shows the PXRD diffractogram of IR-MOF-74-Zn as collected at DLS I11. In the Pawley refinement, the presence of a small amount of a IR-MOF-74-Zn intermediate is evident at  $4^\circ 2\theta$ . In addition, zinc oxide peaks are also present, albeit the peaks are of low intensity.



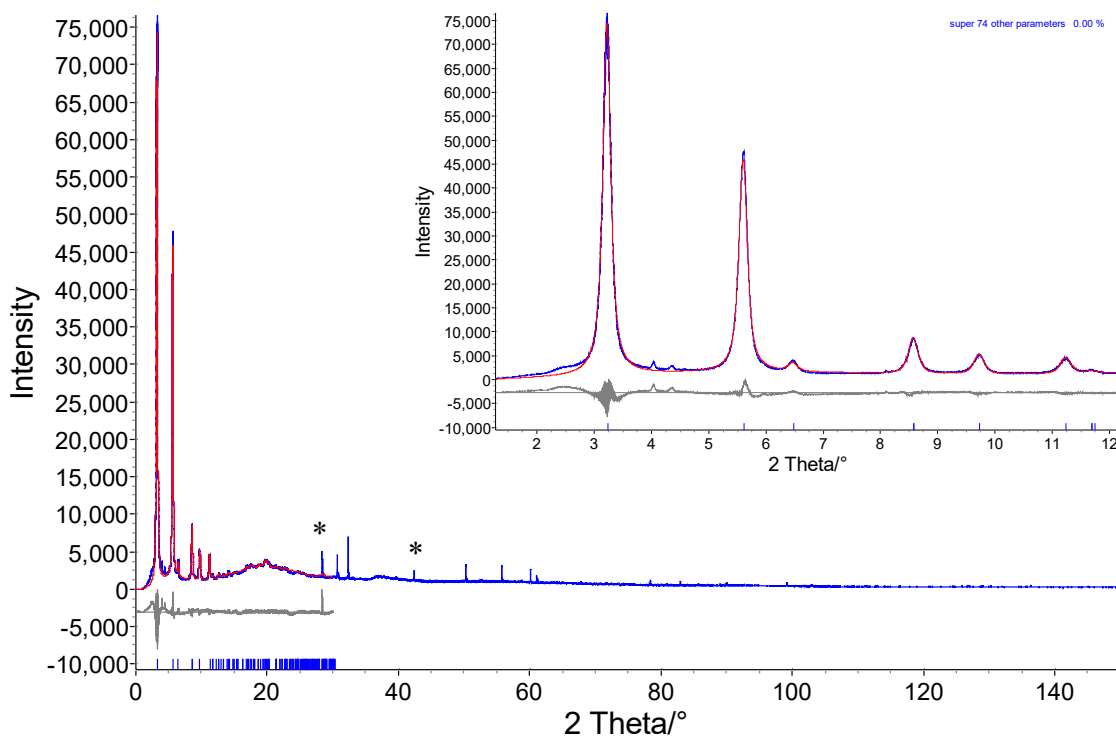


Figure 81 Powder X-ray diffraction pattern for IR-MOF-74-Zn and Pawley refinement. Sample contains unreacted zinc oxide (marked with \*). Inset shows refinement at low angle. Curves: experimental (blue), calculated (red), difference curve (grey), tick marks (calculated hkl indices for phase). Data collected on DLS I11.

The Pawley refinement was used to determine the lattice parameters of the IR-MOF-74-Zn phase. The lattice parameters of IR-MOF-74-Mg were used as a starting point (Figure 81).<sup>180</sup> Comparison of the lattice parameters determined here for IR-MOF-74-Zn with the previously reported Co, Ni and Mg analogues, reveals a significant enlargement of the  $c$  parameter. However, the first peak corresponding to the  $c$ -axis is not present until  $2\theta = 11.74^\circ$  with very little intensity so confidence in the refined value is low (Table 22). Given the similarity of the ionic radii of  $\text{Co}^{2+}$ ,  $\text{Ni}^{2+}$  and  $\text{Zn}^{2+}$  (0.72, 0.74 and 0.72 Å respectively), this would suggest the lattice parameters of the Zn analogue should be very similar.

Table 22 Comparison of lattice parameters between IR-MOF-74-Mg published lattice parameters<sup>180</sup> and IR-MOF-74-Zn Pawley refinement. IR-MOF-74-Mg refinement was performed on an activated sample. The Pawley refinement on the IR-MOF-74-Zn sample was performed on an as-synthesised sample.

IR-MOF-74 analogue	Mg	Zn
<b>Crystal system</b>	Trigonal	Trigonal
<b>Space group</b>	<i>R</i> -3	<i>R</i> -3
<b><i>a</i> (Å)</b>	44.4044(4)	48.87(3)
<b><i>c</i> (Å)</b>	6.38782(9)	6.84(4)
<b>Volume (Å<sup>3</sup>)</b>	11745.2(9)	14147(4)

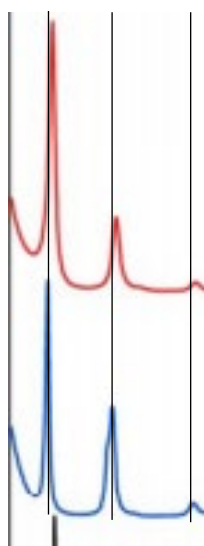


Figure 82 Comparison of first three peaks of IR-MOF-74-Mg between as synthesised and activated samples. Data taken from paper by Nguyen *et al.* As synthesised (Bottom), Activated (red), black lines to show peak shifts.

Figure 82 shows the difference in peak positions of IR-MOF-74-Mg as synthesised by Nguyen *et al.*<sup>180</sup> comparison of the peaks indicates that the as-synthesised samples have much larger *a* and *b* crystallographic axis than the activated samples as evidenced by the shifts in the peaks. The first two peaks correspond to the *hkl* indices 110 and 030 which both show a significant shift in  $2\theta$  between the as-synthesised and activated samples. This might suggest that IR-MOF-74 is flexible, it is possible that the framework swells

increasing unit-cell size when solvents are present in the pores. Flexible MOFs are not uncommon, in particular the MIL-53 family of MOFs all exhibit large changes in unit-cell volume when solvent is added or removed.<sup>183</sup>

As the Rietveld refinements for IR-MOF-74-Mg were performed on the activated sample which has smaller lattice parameters than the as-synthesised IR-MOF-74-Mg the comparison between IR-MOF-74-Mg and IR-MOF-74-Zn becomes poor.

#### 5.3.2.3.2 Elemental analysis

Table 23 shows the experimentally determined C, H and N content for an as-synthesised IR-MOF-74-Zn sample. The predicted formula used was

$Zn_2(ODA)(DMF)_2(NH_3)_{2.5}(H_2O)_2$  elemental formula  $Zn_2H_{32.5}N_{5.5}O_{12}C_{22}$ . There is a difference between the experimental formula and the predicted formula, which is most likely due to additional solvent on the surfaces/ in the pores of the structure which does not divide into neat ratios. Ammonia has been used as one of the solvents present in the sample. DMF is known to decompose to dimethylamine and eventually ammonia when in contact with metal-ions and moisture even at room temperature.<sup>184</sup> It is possible that the DMF decomposed during the extended milling reaction required to synthesise IR-MOF-74-Zn.

Table 23 CHN analysis results of as-synthesised IR-MOF-74-Zn.

<b>Element</b>	<b>Experimental (%)</b>	<b>Predicted (%)</b>
<b>C</b>	37.43	37.92
<b>H</b>	4.94	4.70
<b>N</b>	10.73	11.06

#### 5.3.2.4 Scaled up reaction

It was found that synthesis of IR-MOF-74-Zn was possible to scale-up to make 1 g batches of the framework, albeit with a significantly longer reaction time than the small-scale synthesis (Section 5.2.2.4).

##### 5.3.2.4.1 PXRD

Figure 83 shows the collected PXRD pattern of the scaled-up synthesis method (Section 5.2.2.4). The figure shows an improvement over the original synthesis method as no intermediate peaks are present in the sample; only small zinc oxide peaks ( $2\theta = 32^\circ$ ,  $34^\circ$ ,  $36^\circ$ ).

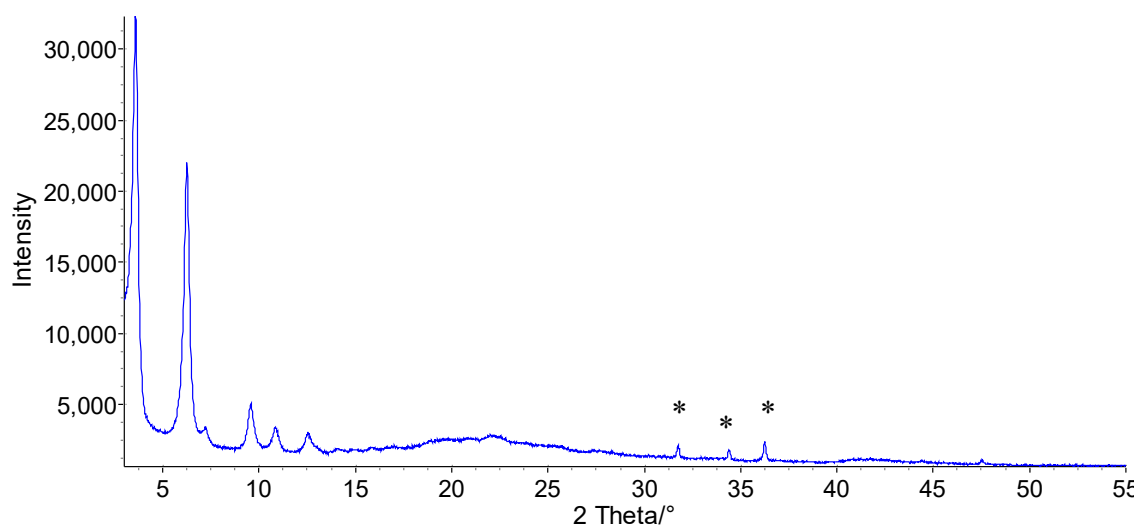


Figure 83 Collected PXRD pattern of scaled-up synthesis of IR-MOF-74-Zn. Collected on Bruker D8 Advance. Starred peaks correspond to unreacted zinc oxide in wurtzite polymorph.

A simultaneous Pawley and Rietveld refinement was carried out using the refined lattice parameters of IR-MOF-74 (Pawley) given in Table 24 and zinc oxide (Rietveld). This resulted in very good agreement with the experimental data, with an  $R_{wp}$  of 4.98 %, though only a few peaks are clear in the IR-MOF-74 phase (Figure 84).

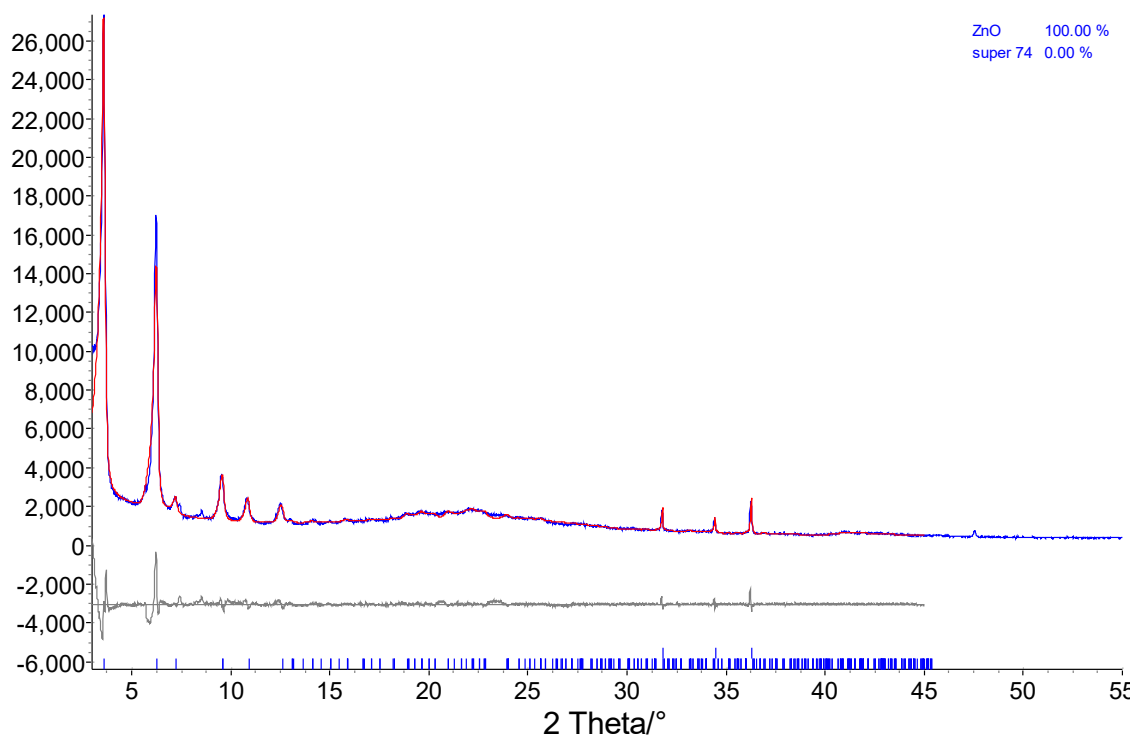


Figure 84 Simultaneous Pawley and Rietveld refinements of IR-MOF-74-Zn and ZnO phases. Experimental (blue), calculated (red), hkl indices for IR-MOF-74-Zn ( lower tick marks), hkl indices for ZnO (upper tick marks). Collected on Bruker D8 Advance.

Table 24 shows the comparison of the refined lattice parameters determined for IR-MOF-74-Zn produced by the standard synthesis (Retsch MM400 mill) and by the scaled-up synthesis methods (Retsch PM 100). Both synthesis methods produce samples with very similar lattice parameters with a variation of only 0.9% in the  $a$  parameter. The improvement in  $R_{wp}$  for the second refinement is probably related to two factors, the absence of IR-MOF-74-Zn intermediates in the pattern, and the modelling of the zinc-oxide phase in a simultaneous Rietveld refinement.

Table 24 Comparison of refined lattice parameters between IR-MOF-74-Zn synthesis methods. Shaker ball mill synthesis method described in Section 5.2.2.1; planetary ball mill synthesis method described in Section 5.2.2.4.

<b>Synthesis method</b>	<b>Shaker ball mill</b>	<b>Planetary ball mill</b>
<b>Crystal system</b>	Trigonal	Trigonal
<b>Space group</b>	<i>R</i> -3	<i>R</i> -3
<b><i>a</i> (Å)</b>	48.87(3)	48.4(12)
<b><i>c</i> (Å)</b>	6.84(4)	6.84(3)
<b>Volume (Å<sup>3</sup>)</b>	14147(4)	13890(6)
<b>Rwp (%)</b>	11.2	4.98

### 5.3.3 Attempts to solve IR-MOF-74-Zn crystal structure

Attempts were made to solve the crystal structure of IR-MOF-74-Zn from X-ray powder diffraction data. The IR-MOF-74-Zn sample was prepared using the reaction method described in Section 5.2.2.1 using the Retsch MM 400 mill. Peak intensities were extracted from the DLS I11 diffractogram using the refined Pawley lattice parameters (Figure 85). This extracted diffractogram was then used with DASH to create simulated annealing runs to attempt to solve the crystal structure. It was assumed that the atomic coordinates would be very similar to those of MOF-74-Zn with the linker sitting on a centre of inversion and zinc atoms sitting on general positions around a 3-fold rotation axis. To simplify the model, no solvent was included (the structure was treated as the activated structure).

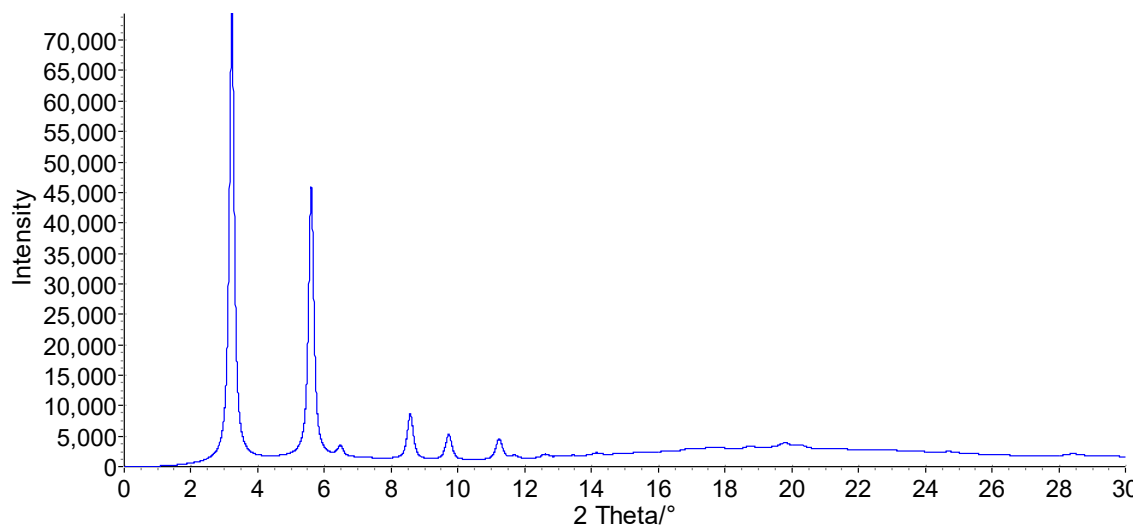


Figure 85 Extracted diffractogram of IR-MOF-74-Zn. Hkl indices are shown under the first few peaks.

Across 100 simulated annealing runs, the best structure is not entirely correct. The best result is shown in Figure 86 and Figure 87. While the linker is correctly placed in the unit-cell it is incorrectly oriented around the  $c$ -axis. This incorrect position is due to the lack information in the extracted peak phase. The largest issue is the lack of sharp peaks, only 7 peaks in the diffractogram have enough intensity to extract any information.

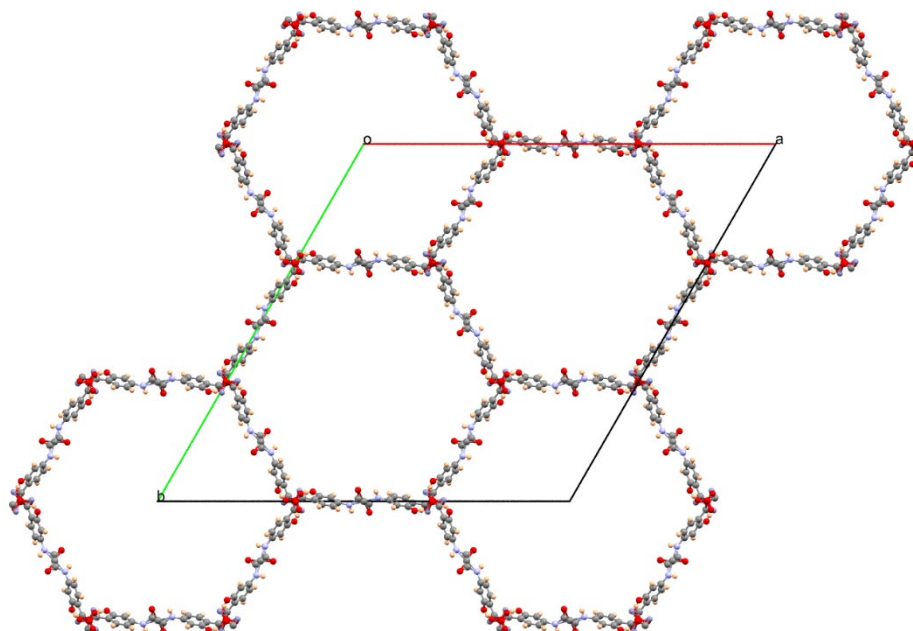


Figure 86 Best structure solution attempt from powder diffraction data of IR-MOF-74-Zn showing packing viewed down the  $c$ -axis.

In the simulated annealing runs, the zinc atoms were allowed to move freely while the linker was fixed to the centre of inversion. As can be seen in Figure 87, the Zn-O bond distances are incorrect as they are much too close together (expected 1.6-1.9 Å, some as short as 1.1 Å in the simulated annealing structure). This result ultimately shows that finding a definitive structure for IR-MOF-74-Zn will only be possible with single-crystal X-ray diffraction data requiring the growth of suitable single crystals; ultimately meaning a solvothermal synthesis method will need to be developed.

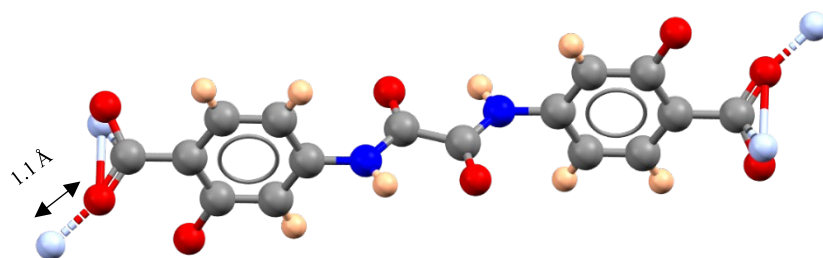


Figure 87 Formula unit of best crystal structure solution of IR-MOF-74-Zn. Elements colours as follows: carbon (grey), oxygen (red), hydrogen (yellow), nitrogen (blue), zinc (light blue).

#### 5.3.4 Stability of IR-MOF-74-Zn in solvents

In order to figure out the best activation method for IR-MOF-74-Zn it was first immersed in several solvents for multiple days to test stability (Section 5.2.3). These solvent stability tests were necessary as it was found that the previously reported activation methods for isorecticular MOF-74 analogues did not work. In addition to measuring the MOFs' direct solvent stability, a single step activation was also attempted (Section 5.3.4.1.5). Figure 88 shows the powder pattern of IR-MOF-74-Zn before soaking in any solvent.



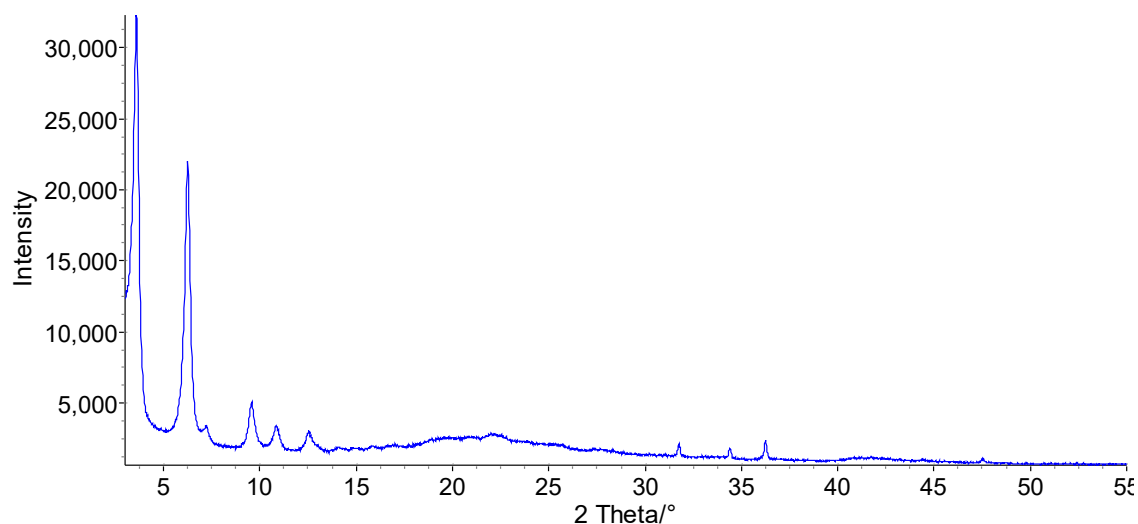


Figure 88 Initial PXRD pattern of IR-MOF-74-Zn before soaking in any solvent. Data collected on Bruker D8 Advance.

#### 5.3.4.1 PXRD

##### 5.3.4.1.1 DMF

Figure 89 shows the diffractogram of an IR-MOF-74-Zn sample after immersion for 3 days in DMF. The sample was stable in DMF with very little change in peak intensity; unsurprising as the framework was synthesised using DMF as a solvent. Unfortunately,

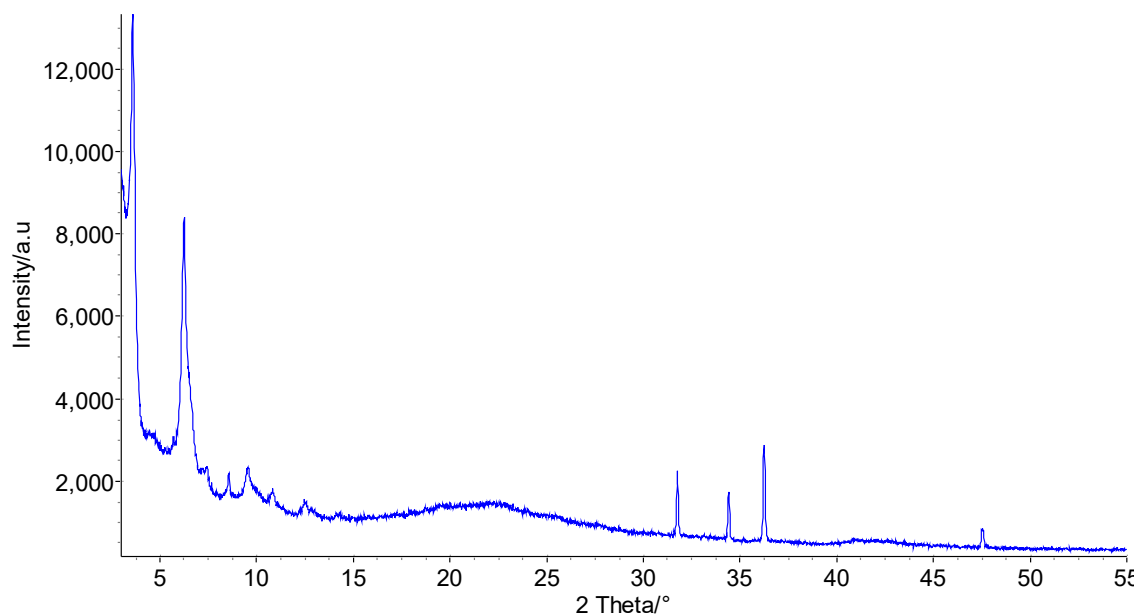


Figure 89 Diffractogram of IR-MOF-74-Zn after immersion in DMF for 3 days. Data collected on Bruker D8 Advance.

DMF is unsuitable for solvent exchange for activation as the boiling temperature is very high.

#### 5.3.4.1.2 Chloroform

Figure 90 shows the PXRD pattern of IR-MOF-74-Zn after being soaked in chloroform for 3 days. After soaking the IR-MOF-74-Zn phase has entirely disappeared indicating that the framework has entirely decomposed. The only crystalline phase visible in diffractogram is a wurtzite zinc oxide phase (starred peaks on Figure 90)

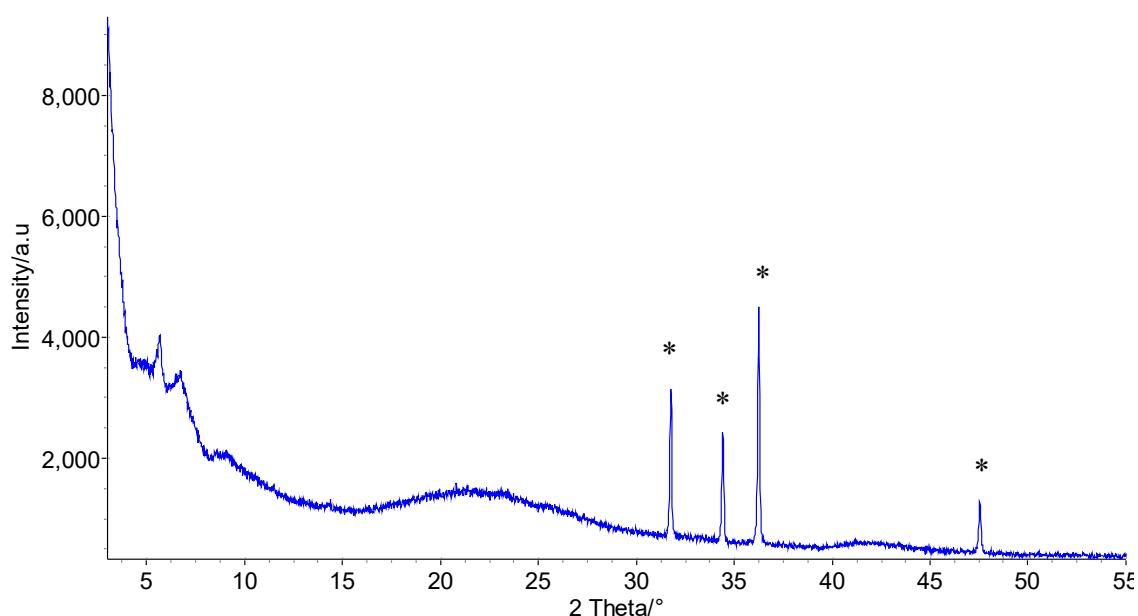


Figure 90 PXRD pattern of IR-MOF-74-Zn immersed in chloroform. Starred peaks correspond to zinc oxide wurtzite phase. Data collected on Bruker D8 Advance.

#### 5.3.4.1.3 Hexane

Figure 91 shows the PXRD pattern of IR-MOF-74-Zn after soaking in hexane for 3 days. The peaks attributed to the MOF phase have changed considerably, but the framework seems to remain partially intact. A Pawley refinement was performed (Figure 92) to compare the lattice parameters of the framework to prior to soaking (Table 25). Comparison of the lattice parameters suggests that the total unit-cell volume has changed by 2.8% meaning the framework unit-cell has not changed considerably after soaking;

however, the decrease in IR-MOF-74-Zn peak intensity suggests some amount of framework decay.

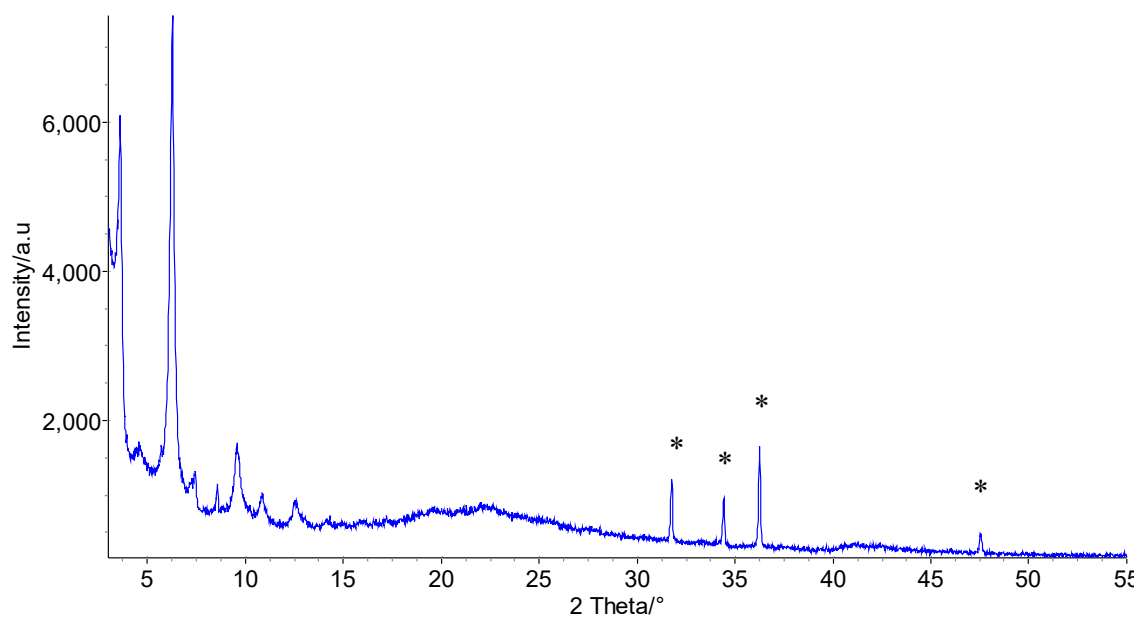


Figure 91 PXR D pattern of IR-MOF-74-Zn after soaking in hexane. Starred peaks correspond to zinc oxide Wurtzite phase. Data collected on Bruker D8 Advance.

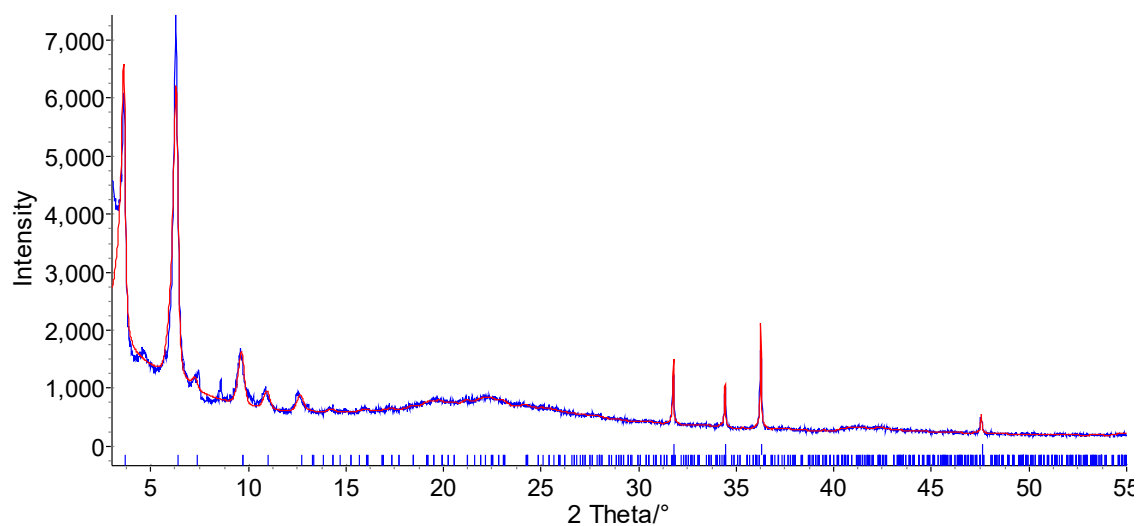


Figure 92 Pawley refinement of IR-MOF-74-Zn after soaking in hexane. Data collected on Bruker D8 Advance.

Table 25 Comparison of lattice parameters between IR-MOF-74-Zn before and after soaking in hexane for 3 days.

	Before hexane soaking	After hexane soaking
<b>Crystal system</b>	Trigonal	Trigonal
<b>Space group</b>	<i>R</i> -3	<i>R</i> -3
<b><i>a</i> (Å)</b>	48.4(12)	48.2(2)
<b><i>c</i> (Å)</b>	6.84(3)	6.7(5)
<b>Volume (Å<sup>3</sup>)</b>	13890(6)	13510(9)
<b>Rwp (%)</b>	4.99	9.5

#### 5.3.4.1.4 Methanol

Figure 93 suggests that IR-MOF-74-Zn also degrades in methanol as the peaks corresponding to the framework entirely disappeared after soaking in methanol for 3 days.

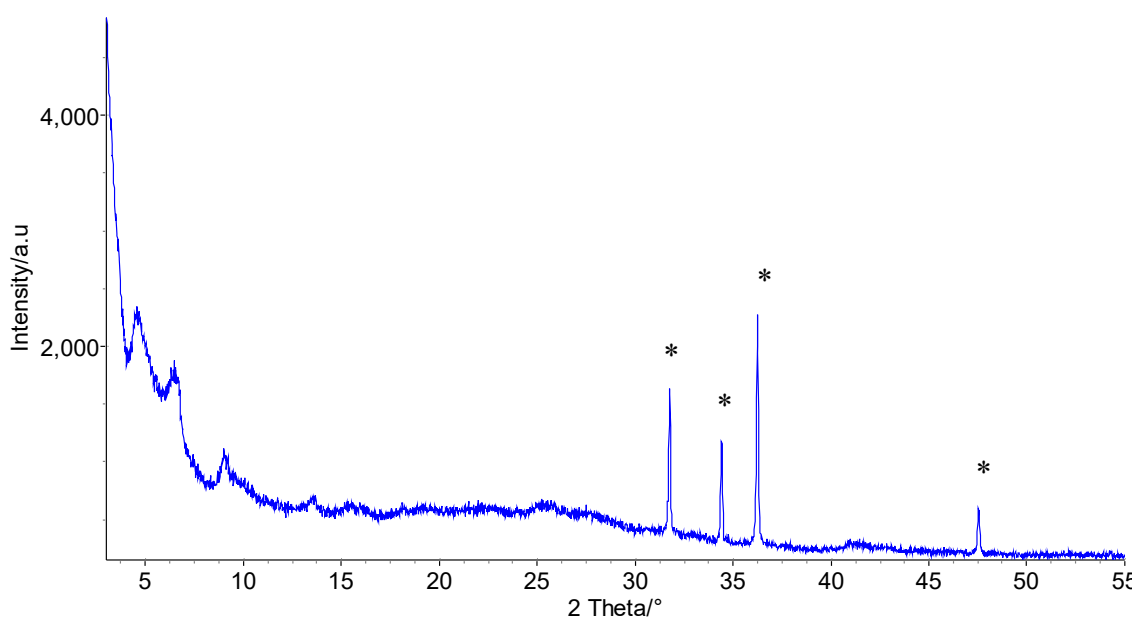


Figure 93 PXRD pattern of IR-MOF-74-Zn after soaking in methanol. Starred peaks correspond to zinc oxide phase. Data collected on Bruker D8 Advance.

#### 5.3.4.1.5 Vacuum

An IR-MOF-74-Zn sample was placed under vacuum and heated to 333 K and held at temperature for 12 hours. The collected PXRD pattern of the vacuum treated sample is shown in Figure 94 and shows the complete decomposition of the IR-MOF-74-Zn phase.

This is a consequence of attempting activation without first exchanging DMF from the pores. The direct activation of the framework was attempted to confirm that solvent exchange was in fact necessary as some MOFs can be activated straight after synthesis.

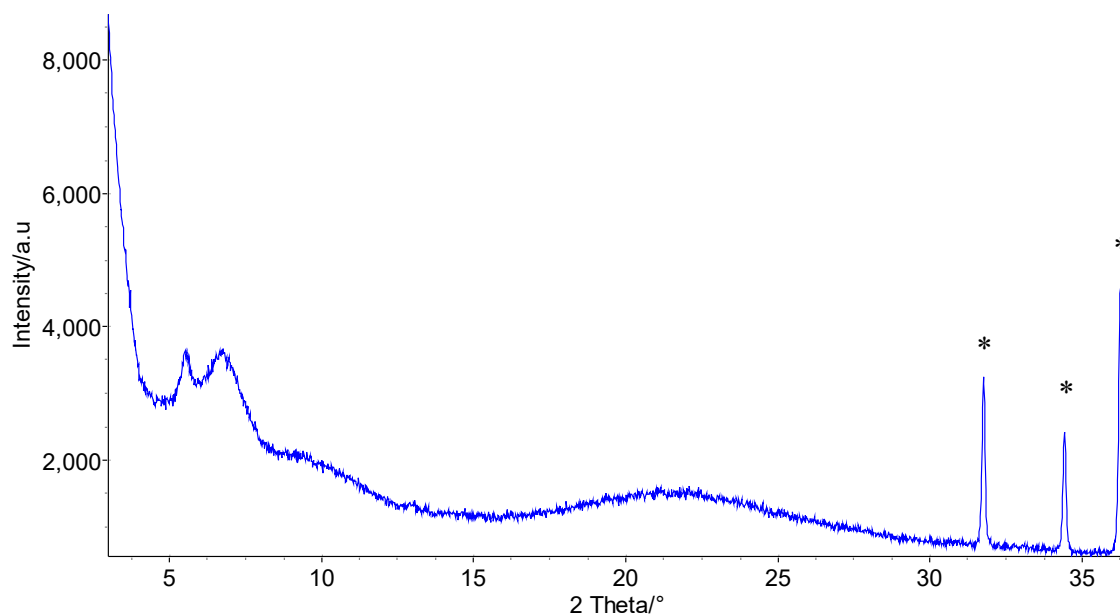


Figure 94 Collected PXRD pattern of IR-MOF-74-Zn after placing under vacuum for 12 hours. Starred peaks correspond to zinc oxide phase. Data collected on Bruker D8 Advance.

#### 5.3.4.1.6 Water

Soaking IR-MOF-74-Zn in water for 3 days produced a large change in powder pattern (Figure 95). The IR-MOF-74-Zn phase entirely disappeared and was replaced a new phase. This new phase was unknown and unreported. The lattice parameters of this phase were indexed using DICVOL as implemented in DASH<sup>141</sup>. A Pawley refinement was performed using the found lattice parameters.

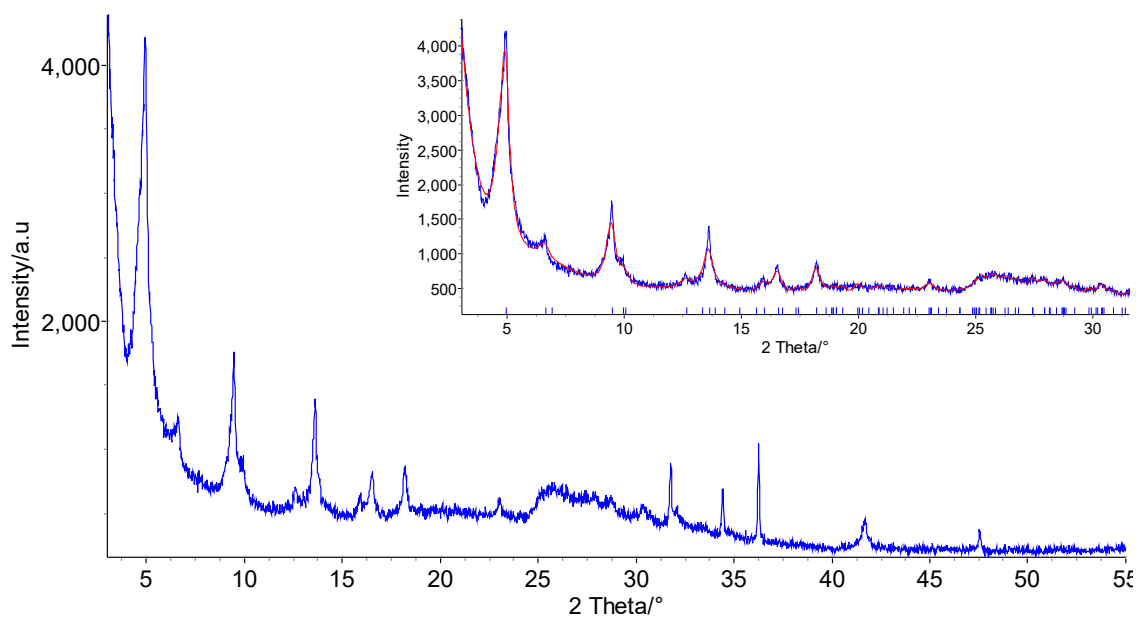


Figure 95 PXRD of IR-MOF-74-Zn after soaking in water for 3 days. Pawley refinement of water decomposition phase (inset). Curves: experimental (blue), calculated (red). Data collected on Bruker D8 Advance.

The new phase was compared to H<sub>4</sub>ODA, H<sub>4</sub>ODA.2(DMF), and 4-aminosalicylic acid.<sup>185</sup> It was found that there was no peak overlap indicating that this was, in fact, a new phase.

Table 26 Refined lattice parameters of IR-MOF-74-Zn water decomposition phase.

<b>Crystal system</b>	<b>Monoclinic</b>
<b>Space group</b>	<i>P</i> 2 <sub>1</sub>
<b><i>a</i> (Å)</b>	18.75(2)
<b><i>b</i> (Å)</b>	5.54(9)
<b><i>c</i> (Å)</b>	14.0(1)
<b><math>\beta</math> (°)</b>	108.6(6)
<b>Volume (Å<sup>3</sup>)</b>	1380(3)
<b>R<sub>wp</sub> (%)</b>	6.259

### 5.3.5 Attempted Activation of IR-MOF-74-Zn

The solvent stability experiments outlined in Section 5.3.4 revealed that IR-MOF-74-Zn decomposes quickly in methanol (the most common solvent used for solvent exchange), but that framework stability in hexane was reasonable. With this knowledge an activation method was designed which used hexane to first exchange the DMF from the pores of IR-MOF-74-Zn. After solvent exchange the IR-MOF-74-Zn sample was heated in a vacuum oven to remove hexane. PXRD and surface area analysis were used to measure remaining framework stability and test for permanent porosity.

#### 5.3.5.1 PXRD

Figure 96 shows the collected diffractogram of the activated IR-MOF-74-Zn sample. After activation the IR-MOF-74-Zn phase has almost entirely disappeared leaving only small very broad peaks (ZnO peaks are also visible as sharp peaks at 32, 34, 36 °2θ).

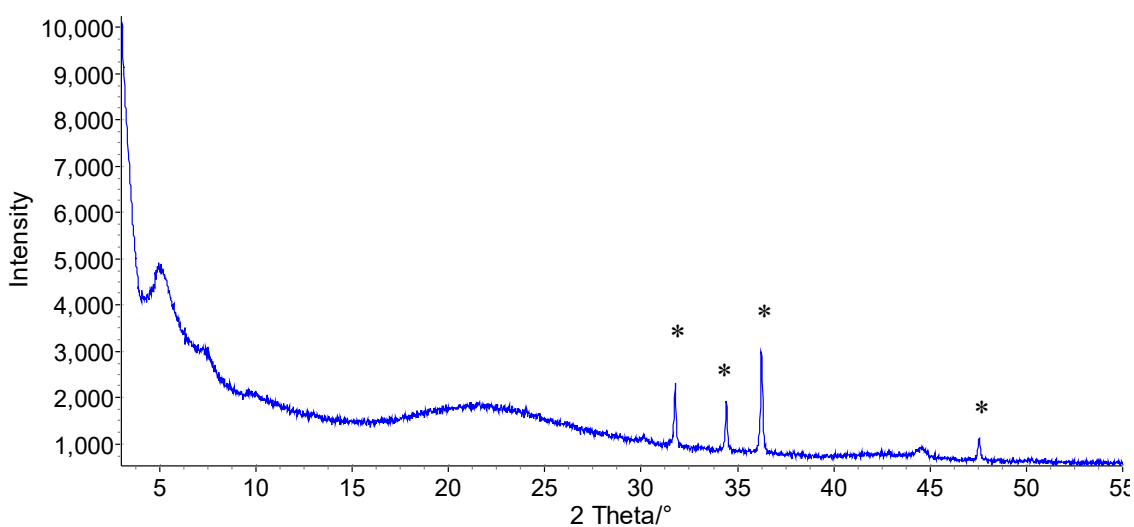


Figure 96 Powder X-ray diffraction pattern of "activated" IR-MOF-74-Zn sample. Starred peaks correspond to zinc oxide phase. Data collected on Bruker D8 Advance.

This degradation of the IR-MOF-74-Zn crystalline phase is a strong indicator that the framework has collapsed, but to further confirm ChemBET surface area analysis was performed on the sample.

### 5.3.5.2 ChemBET

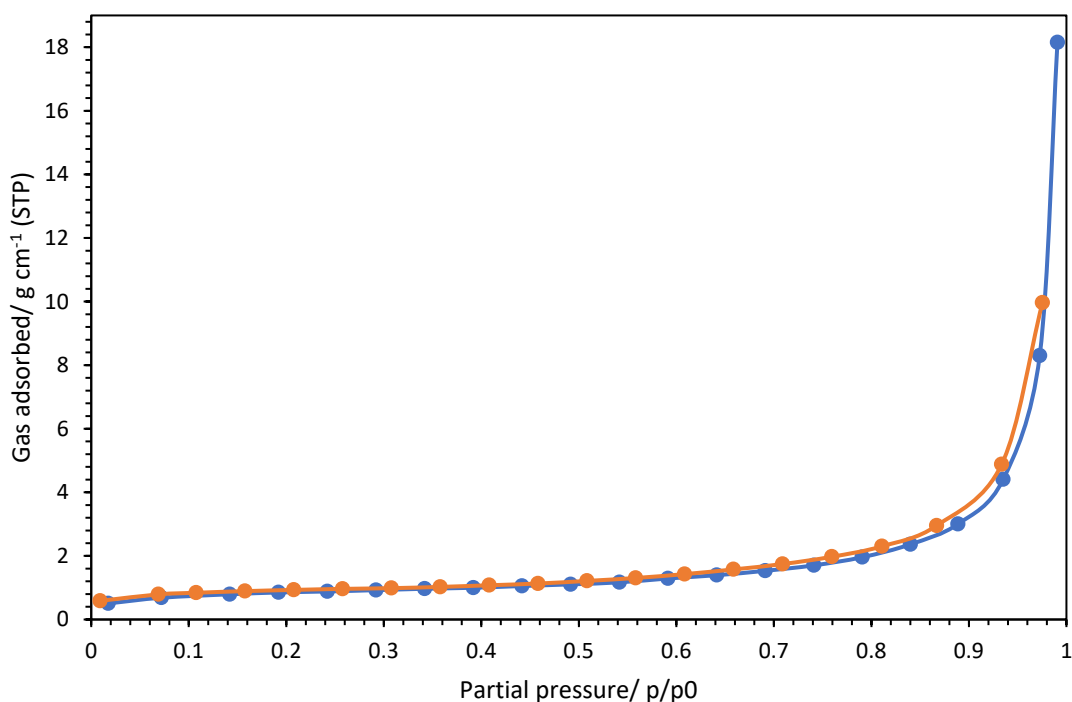


Figure 97 Chem BET surface area result for IR-MOF-74-Zn.

Figure 97 shows the surface area analysis of an “activated” IR-MOF-74-Zn sample. The total surface area of the sample is  $3.09 \text{ m}^2\text{g}^{-1}$  which is significantly smaller than the theoretical surface area of  $2200 \text{ m}^2 \text{g}^{-1}$ . The extremely small surface area result indicates an effectively “non-porous” sample; which gives further evidence that the sample decomposes using the attempted activation technique.

### 5.3.6 In-Situ monitoring of IR-MOF-74-Zn synthesis

Attempts were made to find if any crystalline reaction intermediates were formed during the mechanochemical synthesis of IR-MOF-74-Zn. As MOF-74-Zn formed crystalline intermediates (see Section 3.3.7), it seemed likely that IR-MOF-74-Zn would as well. To this end, an experiment was designed in which the reaction was paused part way through and PXRD collected on small amounts of the reaction mixture. This experiment was both



carried out in-house on the Bruker D8 Advance, as well as at DLS I11 to collect high-resolution powder diffraction data.

#### 5.3.6.1 PXRD on in-house data

In-house data were initially used to measure the appearance of the IR-MOF-74-Zn phase (most clearly seen in the low-angle region in Figure 98). Figure 98 shows the changes in PXRD during the formation of IR-MOF-74-Zn from 6 hours into the synthesis process. As can be seen, the IR-MOF-74-Zn phase does not begin to appear until the mixture has been milled for 8 hours.

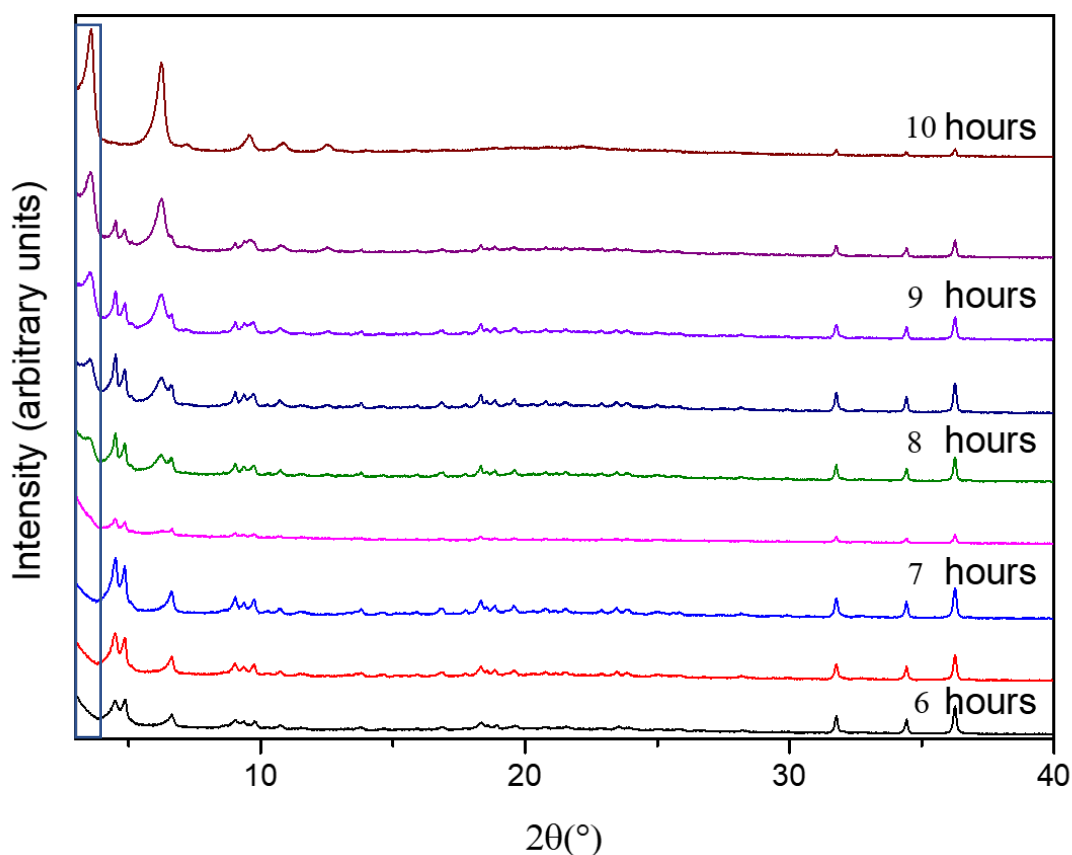


Figure 98 Powder diffraction patterns of IR-MOF-74-Zn synthesis as a function of time. Boxed region corresponds to the region of the first peak of IR-MOF-74-Zn phase.

Apart from the formation of IR-MOF-74-Zn (and the disappearance of an intermediate phase), the collection of powder patterns in Figure 98 show little change across the final 2 hours of synthesis; however, it was assumed that as with the synthesis of MOF-74-Zn

several intermediate phases would form and be consumed early in the reaction. To test this theory an experiment at DLS I11 was designed which would monitor the reaction process focussing on the early hours of the synthesis (due to time constraints of the experiment).

Figure 99 shows the change in powder diffraction pattern of the experiment with time. The changes in powder pattern show three intermediates forming throughout the reaction. The first intermediate to form is shown in (1), the intermediate forms in 60 minutes of milling. The second intermediate to form is (2); this intermediate forms in 240 minutes of milling, and the third intermediate (3) which forms in 540 minutes of milling is marked with an exclamation mark.

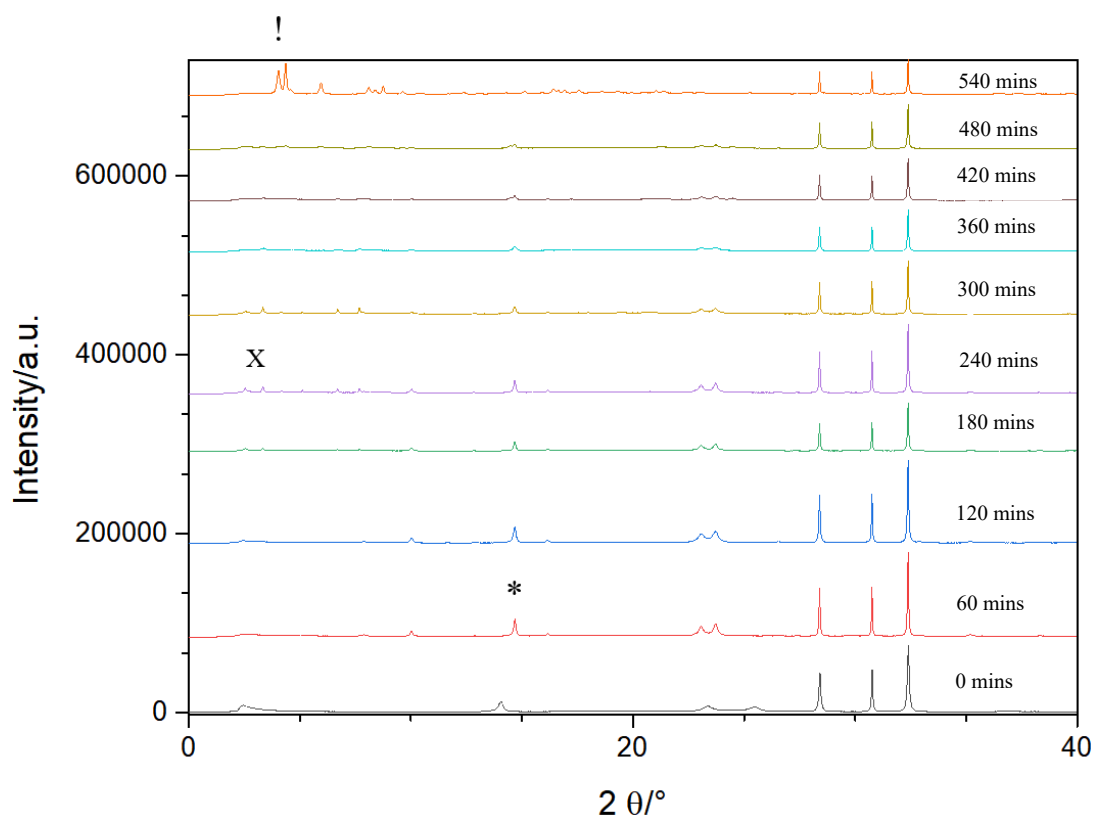


Figure 99 PXR pattern of IR-MOF-74-Zn milling reactions collected at Diamond I11  $\lambda=1.38 \text{ \AA}$ . Powder patterns were collected for every 60 minutes of milling, starting at zero minutes. The largest peak corresponding to (1) is starred (\*). The largest peak corresponding to (2) is marked with an X. The largest peak corresponding to (3) is marked with !.

After the formation of (3), no further changes were observed in the reaction. It is assumed that this lack of progress in the reaction is due to the continuous opening of the milling jar throughout the experiment to obtain samples for PXRD. A second almost identical experiment was run which greatly reduced the number of times the sample jar was opened was designed. This second experiment milled the reaction for a total of 4.5 hours before opening for the first time. The diffraction patterns of this second experiment are shown in Figure 100. The assumption that opening the milling jar was impeding the milling reaction seems plausible as the reaction progressed significantly faster in the second experiment; however, for unknown reasons the reaction still did not progress to completion. Regardless, across the in-situ milling reaction experiments a number of crystalline intermediate phases were found which were further investigated.

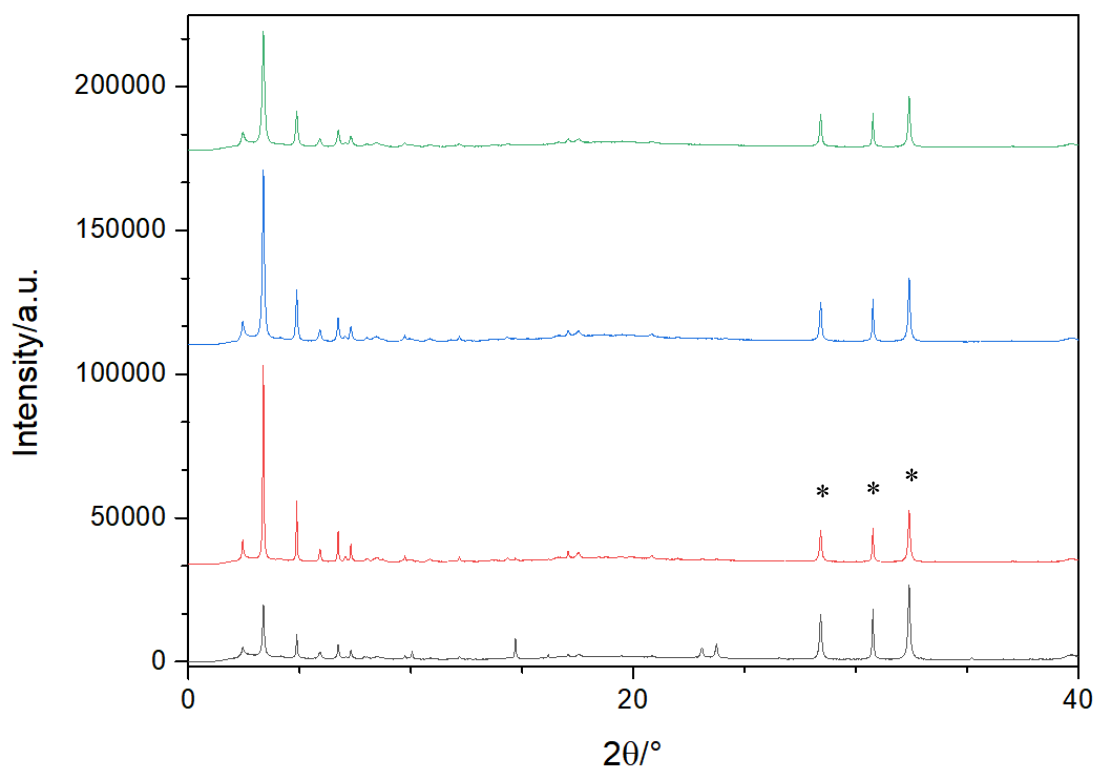


Figure 100 Second milling reaction to attempt to produce IR-MOF-74-Zn, data collected at Diamond Lightsource beamline I11. Milling reaction was sealed and milled for 4.5 hours before opening. All powder patterns are a mixture of (3) and ZnO, ZnO peaks are marked with stars (\*).

### 5.3.6.1 Characterisation of new phases

So far three new intermediate phases have been found in the IR-MOF-74-Zn mechanochemical synthesis. A single-crystal structure has only been found for one of the intermediates; descriptions of milling times to form and powder pattern refinements follow.

#### 5.3.6.1.1 IR-MOF-74-Zn 1<sup>st</sup> intermediate (**1**)

The powder pattern of (**1**) is shown in Figure 101 as isolated from the 1st milling experiment. The crystal structure of (**1**) corresponds to the DMF solvate of H<sub>4</sub>ODA as described in Section 5.2.1.1 (H<sub>4</sub>ODA.2(DMF) formula: C<sub>16</sub>H<sub>12</sub>N<sub>2</sub>O<sub>8</sub>.2(C<sub>3</sub>H<sub>7</sub>NO)).

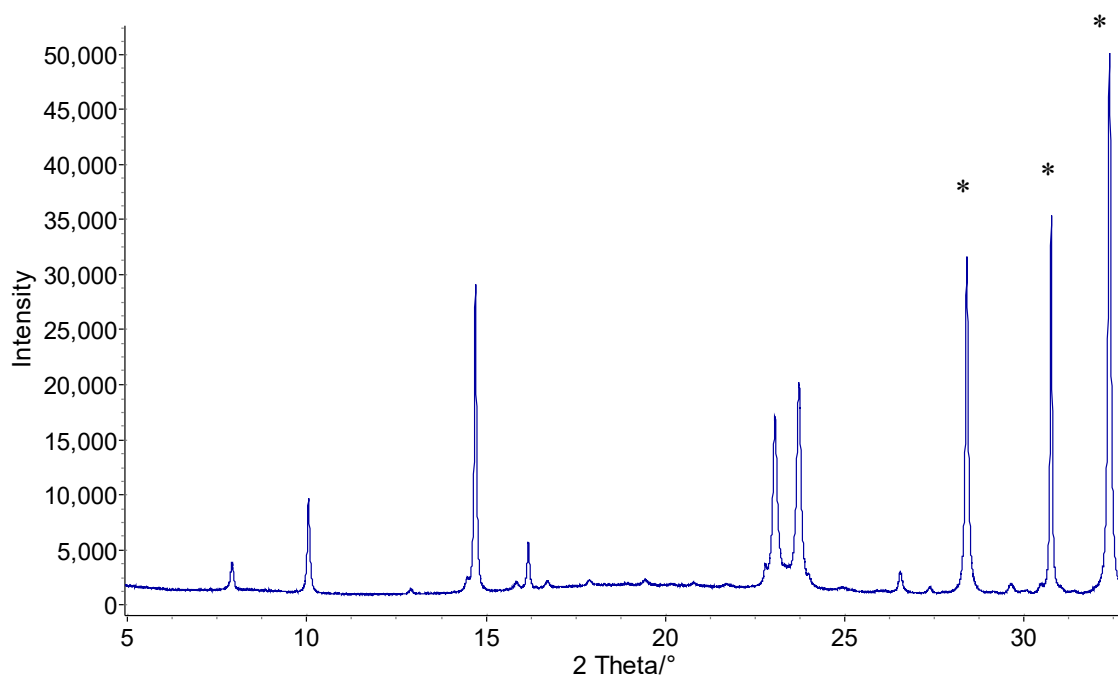


Figure 101 PXRD pattern of (**1**), collected on DLS I11. Starred peaks correspond to ZnO Wurtzite phase. A Rietveld refinement was performed (Figure 102) to compare the lattice parameters between the H<sub>4</sub>ODA.2(DMF) structure described in Section 5.3.1.2.2 and (**1**); this comparison is shown in Table 27. The similarity in lattice parameters confirms that the first intermediate formed in the synthesis of IR-MOF-74-Zn is H<sub>4</sub>ODA.2(DMF) .

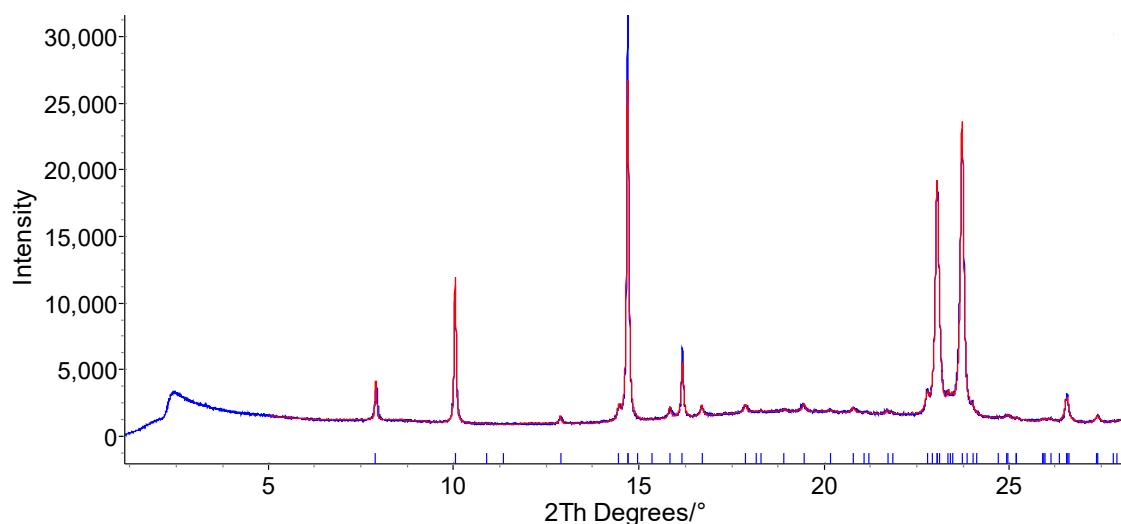


Figure 102 Rietveld refinement of (1) using DLS I11 data  $\lambda=1.38$  Å.

Table 27 Comparison of Rietveld lattice parameters of (1) between in-house X-ray data and DLS I11 data. In-house data collected on Bruker D8 Advance.

	<b>DLS I11 refinement</b>	<b>experiment</b>	<b>In-house Pawley refinement</b>
<b><i>a</i> (Å)</b>	7.075(1)		7.069(5)
<b><i>b</i> (Å)</b>	8.242(3)		8.244(7)
<b><i>c</i> (Å)</b>	10.574(3)		10.583(7)
<b><math>\alpha</math> (°)</b>	72.10(3)		73.07(4)
<b><math>\beta</math> (°)</b>	81.15(6)		81.23(5)
<b><math>\gamma</math> (°)</b>	86.00(6)		85.90(5)
<b>Volume (Å<sup>3</sup>)</b>	582.8(4)		582.9(8)
<b>R<sub>wp</sub> (%)</b>	6.27		8.244

#### 5.3.6.1.2 IR-MOF-74-Zn 2<sup>nd</sup> intermediate (2)

(2) is the second intermediate which forms during the mechanochemical synthesis of IR-MOF-74-Zn. So far, the crystal structure of (2) has yet to be determined, but the following are the current best fitting lattice parameters along with the Pawley refinement comparison to the experimental data. Figure 103 shows the collected powder pattern along with Pawley refinement of (2) as collected at DLS I11. Lattice parameters were

indexed using DICVOL as implemented in DASH and used as part of a Pawley refinement. The lattice parameters are shown in Table 28

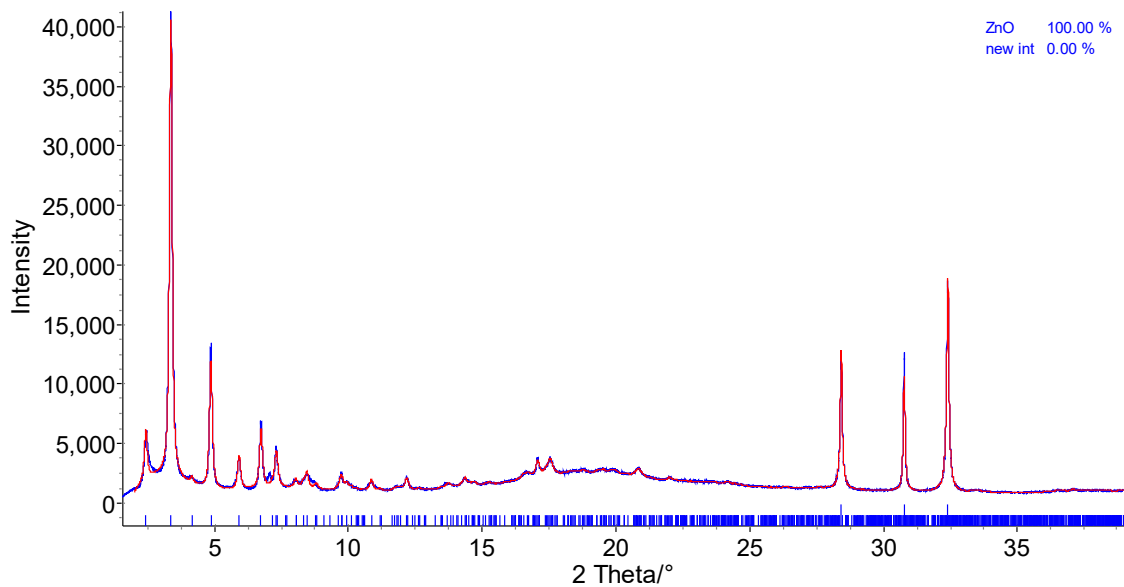


Figure 103 Experimental powder pattern and Pawley refinement of (2). Experimental (blue), calculated (red), hkl indices (tick marks): (2) (lower ticks), ZnO (upper ticks).

Table 28 Refined lattice parameters for (2)

Crystal system	Monoclinic
Space group	<i>P</i> 2
<i>a</i> (Å)	23.70(4)
<i>b</i> (Å)	32.53(4)
<i>c</i> (Å)	10.90(5)
$\beta$ (°)	97.4(4)
Volume (Å <sup>3</sup> )	8330(4)
$R_{wp}$ (%)	5.056

### 5.3.6.1.3 IR-MOF-74-Zn 3<sup>rd</sup> intermediate (**3**)

(**3**) is seemingly the final intermediate that forms in the synthesis of IR-MOF-74-Zn. As with (**2**), the crystal structure of (**3**) has yet to be solved. (**3**) formed in lab experiments in 5 hours of milling in the IR-MOF-74-Zn experiment. It was also possible to synthesise (**3**) by milling a 1.5:1 mixture of Zn: H<sub>4</sub>ODA for 6 hours. Lattice parameters of (**3**) were obtained using DICVOL as implanted in DASH. The lattice parameters were used in a Pawley refinement which shows good agreement to the experimental data (Figure 104, Table 29).

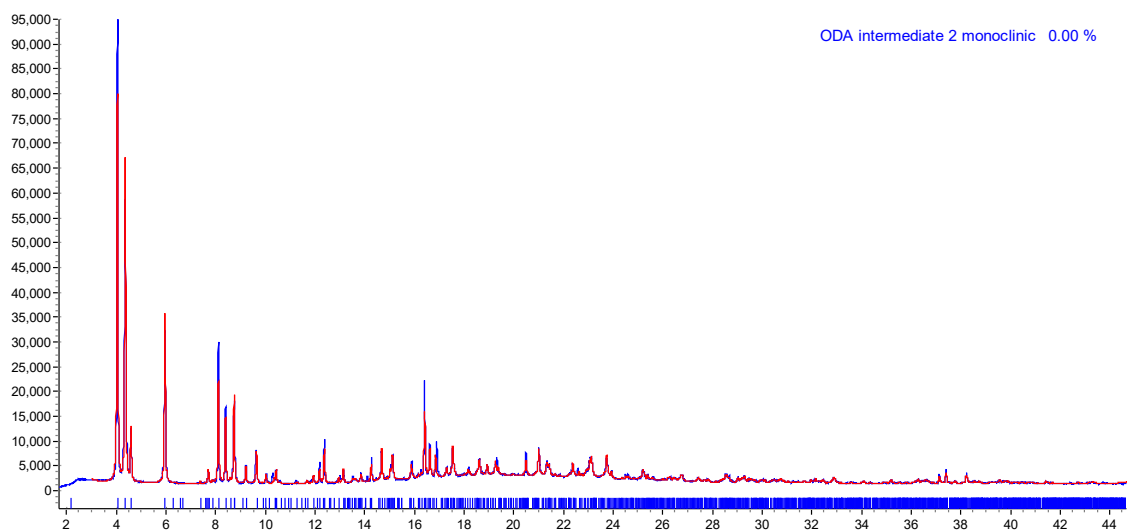


Figure 104 PXR D pattern and Pawley refinement of (**3**). Experimental (blue), calculated (red), hkl indices (tick marks). Collected on DLS I11  $\lambda=1.38$  Å.

Table 29 Refined lattice parameters of (3).

<b>Crystal system</b>	<b>Triclinic</b>
<b>Space group</b>	<i>P</i> -1
<i>a</i> (Å)	7.92(3)
<i>b</i> (Å)	19.77(4)
<i>c</i> (Å)	36.21(3)
$\alpha$ (°)	89.9(6)
$\beta$ (°)	88.2(5)
$\gamma$ (°)	80.7(2)
<b>Volume (Å<sup>3</sup>)</b>	5590(7)
<b>R<sub>wp</sub> (%)</b>	7.74

Attempts were made at solving (3) using DASH<sup>141</sup> and EXPO<sup>146</sup>; however, both methods were unsuccessful at solving the crystal structure. The refined volume of (3) made predicting the contents of the unit-cell impossible from a combinatorial perspective. (3) is potentially a framework type structure, though no similar structures exist on the CSD<sup>3</sup> which would aid in structure identification.



## 5.4 Discussion

### 5.4.1 Discussion on the synthesis of IR-MOF-74-Zn

This chapter provides compelling evidence that isorecticular MOF-74-Zn structures can be synthesised via mechanochemical methods. This mechanochemical synthesis is novel as apart from MOF-74-Zn no other frameworks in the MOF-74 family have been synthesised via a mechanochemical method; Furthermore, this is the first reported synthesis of IR-MOF-74-Zn.

Finding a successful synthesis method required working through several factors. It was found that the factors that affected the synthesis most were milling reaction time and milling ball size and mass. Changing solvent volume had little effect on the total reaction time providing that a minimum of 0.5  $\mu\text{L}/\text{mg}$  of DMF was used in the reaction. In theory rate of milling might also be an important factor, but the shaker mill used in the synthesis had a max rate of 30 Hz which was used in all experiments. Reaction temperature could also be an important factor as recently published data suggests that reaction mixture initial temperature can have a large influence on total reaction time.<sup>186</sup> As with mechanochemical reactions of MOF-74-Zn (Section 3.4.1), DMF purity was a major factor in the success rate of the mechanochemical synthesis. Water contaminated DMF would significantly hinder the reaction speed and produce different reaction intermediates. This effect on reaction intermediates is not surprising as solvents have a huge effect on hydrating reaction mixtures and producing solvated intermediates.<sup>187</sup>

Studying the synthesis of IR-MOF-74-Zn using in-situ PXRD monitoring gave insight into the reaction pathways of the synthesis. Most importantly, it established that crystalline intermediates formed during the synthesis. The presence of crystalline intermediates was not guaranteed as many mechanochemical reactions only form amorphous intermediate phases,<sup>188</sup> if intermediates are formed at all.

The result of the systematic study of the factors influencing the synthesis is the IR-MOF-74-Zn framework. Although confirmation of the structure of the framework has not yet been achieved, the strongest piece of evidence for the successful synthesis of IR-MOF-74-Zn is the analysis of the PXRD data along with similar trends in intermediate formation, as for MOF-74-Zn. Unfortunately, thus far, we have been unable to activate the framework to access the very large internal surface area. Solvent instability of IR-MOF-74-Zn seems to be a large factor as PXRD demonstrates that the framework crystalline phase decomposes very quickly in many common solvents. However, this might be a result of removing coordinated DMF from the pores of the framework too forcefully. Supercritical CO<sub>2</sub> extraction has been proven to be an effective activation method for delicate MOF structures;<sup>123</sup> and this is therefore an avenue well worth exploring in the future.

#### **5.4.2 IR-MOF-74-Zn intermediates**

In this chapter, intermediates formed during the mechanochemical synthesis of IR-MOF-74-Zn have been studied. Three crystalline intermediate phases have been found, with each appearing and disappearing throughout the reaction. So far, only one crystal structure has been determined, which corresponds the first intermediate which formed within the first sampling of the reaction. The crystal structure of the first intermediate is a DMF solvate of the H<sub>4</sub>ODA linker, which gives evidence that solvation effects are very important for mechanochemical reactions. Unfortunately, the crystal structures of the final two crystalline intermediates have yet to be solved. The largest hurdle in solving the final two intermediates crystal structure is unit-cell size, which, in these cases pushes up to the limits of structures that can easily be solved using powder X-ray diffraction structure solution methods (in both cases simulated annealing runs which account for

possible unit-cell contents are in excess of 40 degrees of freedom, and the success rate for simulated annealing runs in DASH approaches sub 1% after 30 degrees of freedom).

As the final frameworks of MOF-74-Zn and IR-MOF-74-Zn are very similar it is worth comparing the two frameworks intermediates to work out if the reaction route is also similar. As with MOF-74-Zn, crystalline intermediates are formed during the synthesis of IR-MOF-74-Zn. In both cases the first intermediate that forms are DMF solvates of the linker used to make the framework (Figure 105), and in both cases the linker solvate disappears early in the reaction to be fully replaced by a second intermediate. Unfortunately, the first intermediate is as far as we can compare for crystal structures.

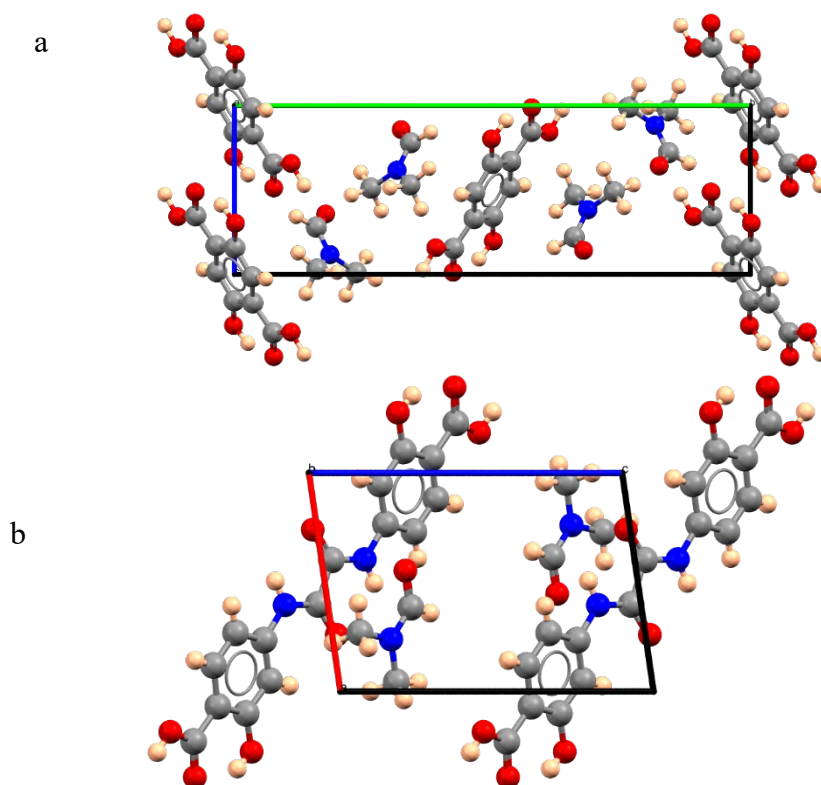


Figure 105 Structures of the first intermediates in the mechanochemical synthesis of the IR-MOF-74-Zn family of frameworks. 1st intermediate of MOF-74 viewed down the *b*-axis ( $H_4DHTA \cdot 2(DMF)$  Formula  $C_8H_6O_6, 2(C_3H_7NO)$ ) (a). 1st intermediate of IR-MOF-74 synthesis as viewed down *c*-axis ( $H_4ODA \cdot 2(DMF)$  formula:  $C_{16}H_{12}N_2O_8, 2(C_3H_7NO)$ ) (b). Cell axis labels: a (red), b (green), c (blue). Atoms present: carbon (grey), oxygen (red), nitrogen (blue), hydrogen (pink).

However, we can also see the trend that the unit-cell volume of the intermediates increases throughout the milling reactions, and in both cases the first intermediate has the smallest unit-cell volume and the final intermediate has the largest unit-cell volume.

## 5.5 Further work

The work discussed in this chapter describes the first steps toward the synthesis and characterisation of a new microporous metal-organic framework. There is evidence that the framework was successfully synthesised, but the crystal structure has yet to be solved. Attempts were made at solving the crystal structure using PXRD structure solution, but lack of information made total structure solution impossible. To sidestep this issue growth of single-crystals of IR-MOF-74-Zn would be required, most likely with a solvothermal method. It would also be ideal to solve the crystal structure of the remaining intermediates, though single-crystal growth would also be necessary. Finally, further experimentation is required in order find a suitable activation method for the framework. Most mesoporous frameworks use a supercritical CO<sub>2</sub> activation method which might be met with more success than the simple solvent exchange, vacuum oven heat method.

## 5.6 Conclusion

In this chapter the synthesis and characterisation of IR-MOF-74-Zn has been reported. IR-MOF-74-Zn is a new metal-organic framework that has been synthesised via a mechanochemical method. The synthesis method was based on the mechanochemical synthesis of MOF-74-Zn. A number of similarities exist between the synthesis of the two frameworks which might indicate that a whole new series of isorecticular MOF-74-Zn structures can be synthesised via mechanochemical methods. In addition to the successful synthesis of IR-MOF-74 three new intermediate structures have been isolated, with the crystal structure of the first intermediate ( $\text{H}_4\text{ODA} \cdot 2(\text{DMF})$  formula:  $\text{C}_{16}\text{H}_{12}\text{N}_2\text{O}_8 \cdot 2(\text{C}_3\text{H}_7\text{NO})$ ) solved via PXRD structure solution methods.

## Chapter 6- Miscellaneous crystal structures containing MOF linkers

### 6.1 Introduction

Presented in this chapter are a collection of novel crystal structures which were solved throughout the PhD. The structures described fall in to three Sections: the crystal structure of 2,5-dihydroxyterephthalic acid (H<sub>4</sub>DHTA) and the crystal structure of its potassium salt, the crystal structure of a novel 1D coordination polymer made using 4,4'-oxalylbis(imino)]bis(2-hydroxybenzoic acid) (H<sub>4</sub>ODA, the linker used to synthesise IR-MOF-74-Zn), and the crystal structure of a DMF solvate of H<sub>4</sub>TDA.

H<sub>4</sub>DHTA is the linker used to synthesise MOF-74-Zn and so knowing the crystal structure is very useful, because it allows for a Rietveld refinement of the MOF-74 reaction mixture from the very beginning of synthesis. The potassium salt of H<sub>4</sub>DHTA was found in a contaminated batch of H<sub>4</sub>DHTA. Analysis of the contaminated batch revealed that it was a novel crystal structure, so is reported here.

The 1D coordination polymer of zinc and H<sub>4</sub>ODA, which can be formulated as  $Zn_2Ac_2H_2ODA(DMF)_2$ , is a paddlewheel coordination polymer which forms when zinc acetate dihydrate is used during the attempted mechanochemical synthesis of IR-MOF-74-Zn instead of zinc oxide.

The H<sub>4</sub>TDA DMF solvate formula  $H_4TDA(DMF)_4$  is a novel crystal structure of a linker which can be used to make large MOF-74 isorecticular frameworks.

## 6.2 Experimental

### 6.2.1 Structure solution of H<sub>4</sub>DHTA

H<sub>4</sub>DHTA was purchased from Alfa Aesar and used without any further purification. PXRD data were collected on the Bruker D8 Advance according to Section 2.9.2.5 and on DLS I11 according to 2.9.2.5. Data were indexed using DICVOL as implemented in DASH. Simulated annealing as implemented in TOPAS was run and final result refined using DFT according to Section 2.9.2.3. <sup>1</sup>H NMR and <sup>13</sup>C NMR were collected according to Section 2.11.1, both 5 mg of each sample were dissolved in 5 mL of deuterated DMSO.

### 6.2.2 Structure solution of KH<sub>3</sub>DHTA·(H<sub>2</sub>O)

A batch of H<sub>4</sub>DHTA purchased from Alfa Aesar was contaminated upon arrival. It was determined to be KH<sub>3</sub>DHTA via structure solution from single-crystal X-ray diffraction. Single-crystals of KH<sub>3</sub>DHTA·(H<sub>2</sub>O) were grown by dissolving 100 mg of KH<sub>3</sub>DHTA in 20 mL of hot deionised water. The solution was hot filtered and left to cool for 4 days after which small single-crystals (colourless needles) suitable for single-crystal X-ray diffraction were found. Single-crystal X-ray diffraction and structure solution were performed according to the procedure outlined in 2.9.1.1. As purchased “H<sub>4</sub>DHTA” was compared to the solved crystal structure using Rietveld refinement in Topas according to the procedure outlined in Section 2.9.2.5. 2 mg KH<sub>3</sub>DHTA was dissolved in 5 mL d<sub>6</sub>-DMSO for NMR. <sup>1</sup>H NMR and <sup>13</sup>C NMR were performed according to Section 2.11.1.

### 6.2.3 Synthesis and Structure solution of Zn<sub>2</sub>H<sub>2</sub>ODA·DMF<sub>2</sub>(H<sub>2</sub>O)<sub>2</sub>

2.2 mmol ZnAc<sub>2</sub>·H<sub>2</sub>O and 1.1 mmol H<sub>4</sub>ODA were added to a 25 mL stainless steel milling jar along with a single 9 g stainless steel milling ball and 300 μL DMF. The jar was sealed and milled for 120 minutes on the Retsch MM 400 shaker mill. A PXRD pattern of the resultant powder was performed on the Bruker D8 Advance according to the procedure outlined in Section 2.9.2.3. Lattice parameters were determined using the DICVOL

function as implemented in DASH and a Pawley refinement performed using TOPAS 4.2. A simulated annealing run was performed using the refined lattice parameters. The fragments used in the simulated annealing run were as follows: Half H<sub>2</sub>ODA molecule with dummy atom to anchor fragment to centre of inversion, one DMF molecule, one O atom representing an H<sub>2</sub>O molecule, and one Zn atom. H<sub>2</sub>ODA fragment was fixed to special position but otherwise all components were allowed to move freely during simulated annealing (degrees of freedom= 17). The resultant structure was further refined by adding missing hydrogen atoms to water molecules; then structure refined using DFT. A rigid body refinement was performed on the DFT energy minimised structure to give the final crystal structure and CIF (see appendix). A Rietveld refinement using TOPAS was performed to confirm the agreement of the determined crystal structures with the experimental powder pattern.

#### **6.2.4 Synthesis of H<sub>4</sub>TDA**

H<sub>4</sub>TDA (4,4'-[1,4-phenylenebis-(carbonylimino)]bis(2-hydroxybenzoic acid)) was synthesised following the method described by Nguyen<sup>180</sup> *et al* with no alterations made.

##### **6.2.4.1 Synthesis and structure solution of H<sub>4</sub>TDA(DMF)<sub>2</sub>**

10 mg H<sub>4</sub>TDA was dissolved in 20 mL hot DMF. The solution was hot filtered and left to cool partially uncovered for 5 days. After cooling colourless needle-like single-crystals suitable for single-crystal X-ray diffraction were found. Single-crystal X-ray diffraction and structure solution was performed according to the procedure outlined in Section 2.9.1.1.



Table 30 Crystallographic and refinement details for the crystal structures described in this chapter. Powder diffraction Data/restraints/parameters field corresponds to number of refined parameters.

Identifier	H <sub>4</sub> DHTA	KH <sub>3</sub> DHTA·(H <sub>2</sub> O)	Zn <sub>2</sub> H <sub>2</sub> ODA·DMF <sub>2</sub> (H <sub>2</sub> O) <sub>2</sub>	H <sub>4</sub> TDA(DMF) <sub>2</sub>
<b>Solution method</b>	Powder diffraction	Single-crystal	Powder diffraction	Single-crystal
<b>Empirical formula</b>	C <sub>8</sub> H <sub>6</sub> O <sub>6</sub>	C <sub>8</sub> H <sub>7</sub> KO <sub>7</sub>	C <sub>26</sub> H <sub>30</sub> N <sub>4</sub> O <sub>14</sub> Zn <sub>2</sub>	C <sub>34</sub> H <sub>44</sub> N <sub>6</sub> O <sub>12</sub>
<b>Formula weight</b>	198.13	254.24	753.31	728.75
<b>Temperature (K)</b>	293	150.00(10)	293	155(8)
<b>Crystal system</b>	Triclinic	Triclinic	Triclinic	Triclinic
<b>Space group</b>	<i>P</i> -1	<i>P</i> -1	<i>P</i> -1	<i>P</i> -1
<b><i>a</i> (Å)</b>	4.2824(2)	6.6993(10)	8.1713(5)	7.7582(4)
<b><i>b</i> (Å)</b>	5.5514(2)	8.6495(17)	8.9405(7)	9.9345(6)
<b><i>c</i> (Å)</b>	8.1931(3)	9.0380(16)	11.7390(7)	12.9348(8)
<b><i>α</i> (°)</b>	93.45(2)	65.763(18)	103.083(5)	68.299(6)
<b><i>β</i> (°)</b>	102.22(2)	74.448(14)	102.571(4)	78.096(5)
<b><i>γ</i> (°)</b>	96.84(2)	78.465(15)	105.152(3)	72.020(5)
<b>Volume (Å<sup>3</sup>)</b>	188.28(2)	457.65(16)	770.56(10)	876.242
<b>Z</b>	1	2	1	1
<b>ρ<sub>calc</sub> g (cm<sup>3</sup>)</b>		1.845		1.381
<b>μ (mm<sup>-1</sup>)</b>		5.354		0.106
<b>F(000)</b>		260.0		386.0
<b>Crystal size/mm</b>		0.45 × 0.03 × 0.02		0.14 × 0.12 × 0.07
<b>Radiation (Å)</b>	CuKα (λ = 1.54184)	CuKα (λ = 1.54184)	CuKα (λ = 1.54184)	MoKα (λ = 0.71073)
<b>2θ range for data collection (°)</b>		10.976 to 122.538		6.534 to 58.656
<b>Index ranges</b>		-7 ≤ h ≤ 7, -9 ≤ k ≤ 9, -10 ≤ l ≤ 9		-10 ≤ h ≤ 10, -13 ≤ k ≤ 13, -17 ≤ l ≤ 17
<b>Reflections collected</b>	114	3992	687	22954
<b>Independent reflections</b>		1381 [R <sub>int</sub> = 0.0700, R <sub>sigma</sub> = 0.0786]		4338 [R <sub>int</sub> = 0.0547, R <sub>sigma</sub> = 0.0405]
<b>Data/restraints/parameters</b>	54	1381/0/152	54	4338/0/279
<b>Goodness-of-fit on F<sup>2</sup></b>		1.032		1.041
<b>Final R indexes [I ≥ 2σ (I)]</b>		R <sub>1</sub> = 0.0452, wR <sub>2</sub> = 0.0960		R <sub>1</sub> = 0.0551, wR <sub>2</sub> = 0.1249
<b>Final R indexes [all data]</b>		R <sub>1</sub> = 0.0690, wR <sub>2</sub> = 0.1095		R <sub>1</sub> = 0.0741, wR <sub>2</sub> = 0.1380
<b>Largest diff. peak/hole (e Å<sup>-3</sup>)</b>				0.74/-0.30
<b>R factors(Pawley, Rietveld) (%)</b>	4.04, 4.95	4.53	3.95, 5.39	5.59

## 6.3 Results

### 6.3.1 H<sub>4</sub>DHTA

#### 6.3.1.1 NMR

<sup>13</sup>C NMR of H<sub>4</sub>DHTA (Figure 106a) indicates that there are 4 carbon environments plus the environment for the deuterated DMSO used to dissolve H<sub>4</sub>DHTA (DMSO-d<sub>6</sub> multiplet at 40 ppm). Peaks were assigned to the relevant carbon environments (Figure 106b).

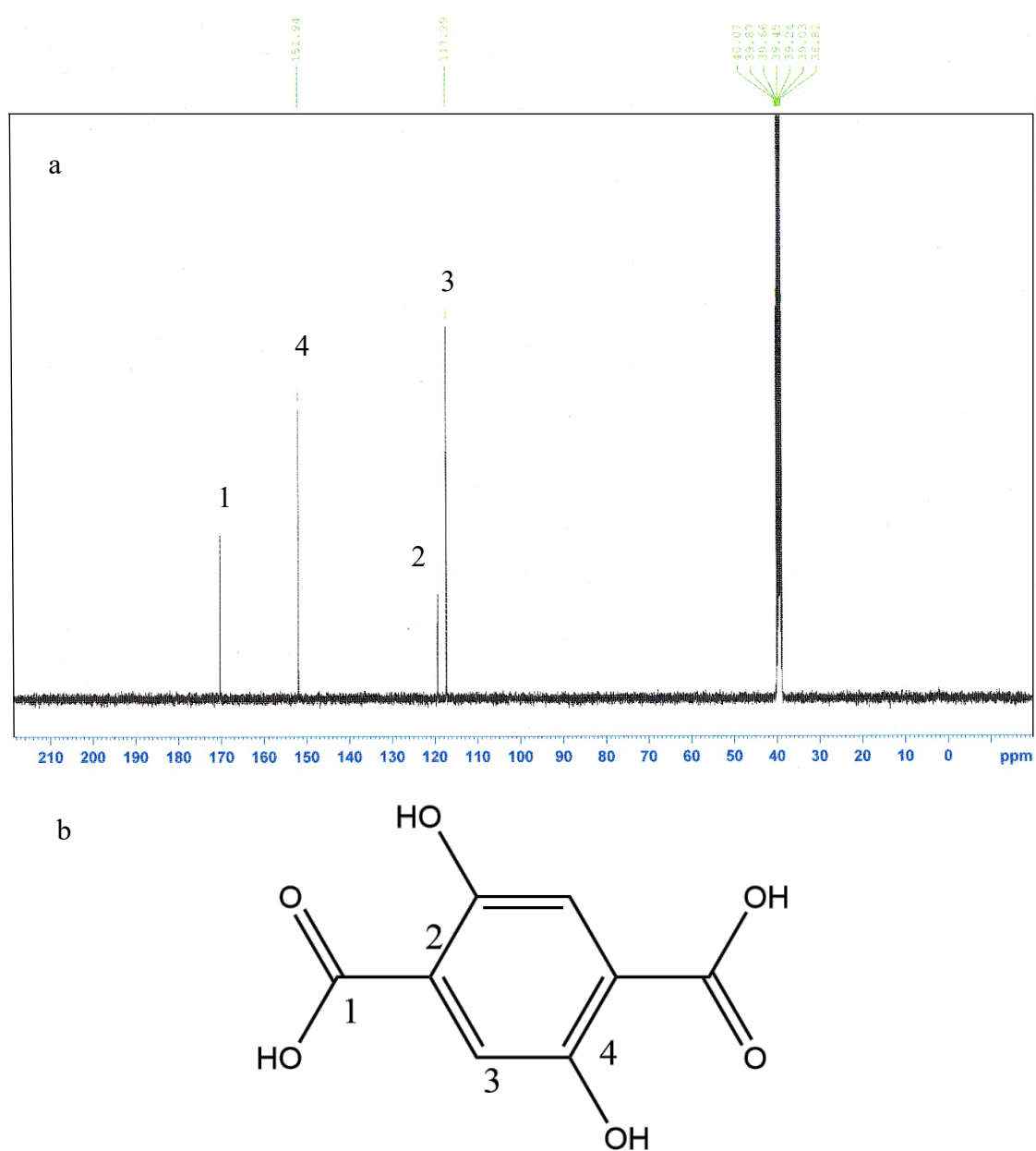


Figure 106. (a) <sup>13</sup>C NMR of H<sub>4</sub>DHTA; (b) <sup>13</sup>C environment assignment for H<sub>4</sub>DHTA.

Presented in Figure 107a are the  $^1\text{H}$  NMR data of  $\text{H}_4\text{DHTA}$ . Peaks were assigned to the structure of  $\text{H}_4\text{DHTA}$  (Figure 107b). Only one peak corresponding to  $\text{H}_4\text{DHTA}$  is visible in the  $^1\text{H}$  NMR, the peak for environment 3 on the diagram (Figure 107b); the other two peaks correspond to water (broad peak at 3.3 ppm) and DMSO- $\text{d}_6$  (peak at 2.3 ppm). Environments 1 and 2 appear as an extremely broad peak centred around 11 ppm. This extreme peak broadening is commonly seen with carboxylic groups exchanging hydrogens.<sup>189</sup>

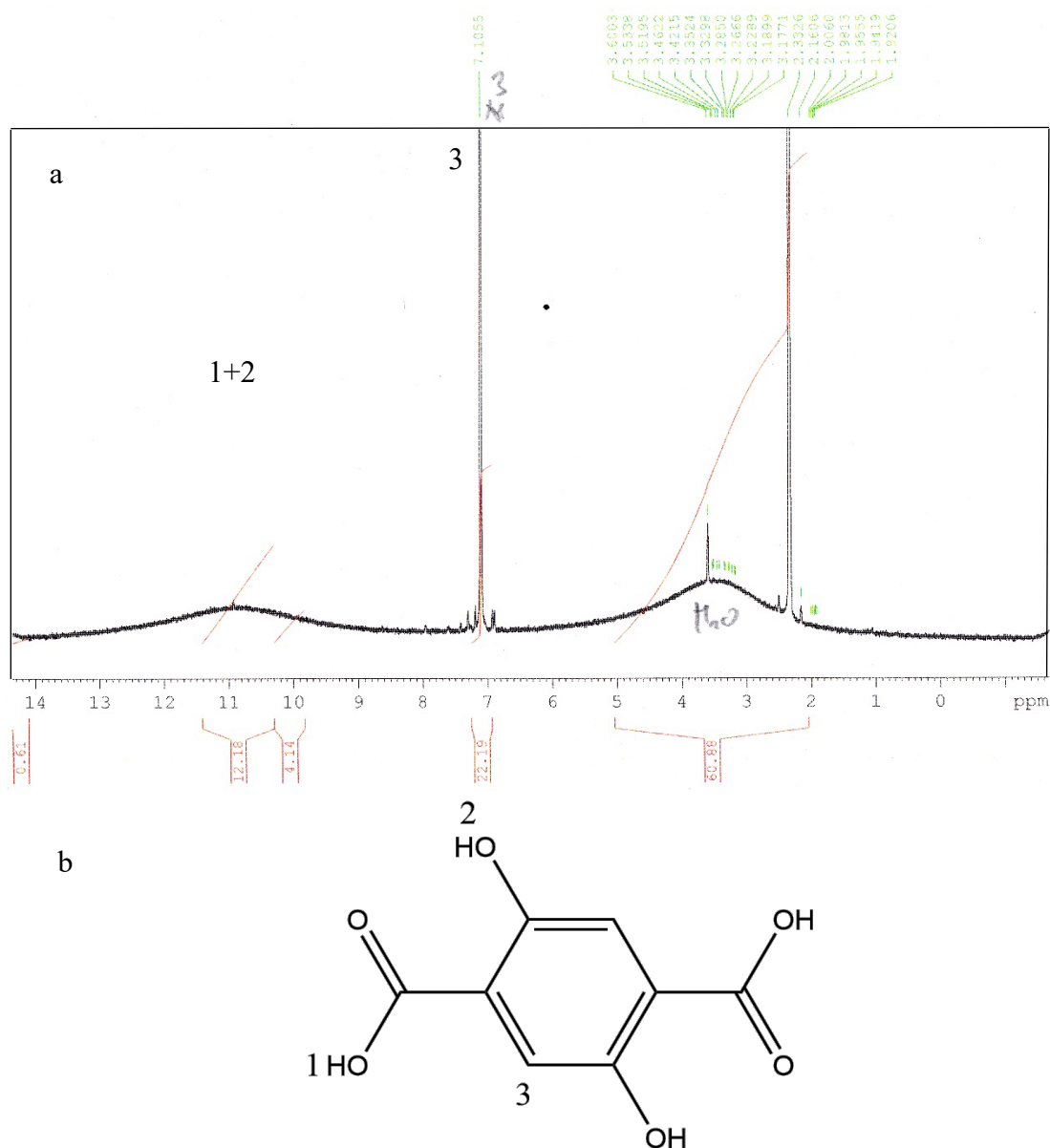


Figure 107. (a)  $^1\text{H}$  NMR of  $\text{H}_4\text{DHTA}$ ; (b) H environment assignment of  $\text{H}_4\text{DHTA}$ .

### 6.3.1.2 PXRD

Figure 108 shows the collected PXRD pattern of the as-purchased from supplier H<sub>4</sub>DHTA.

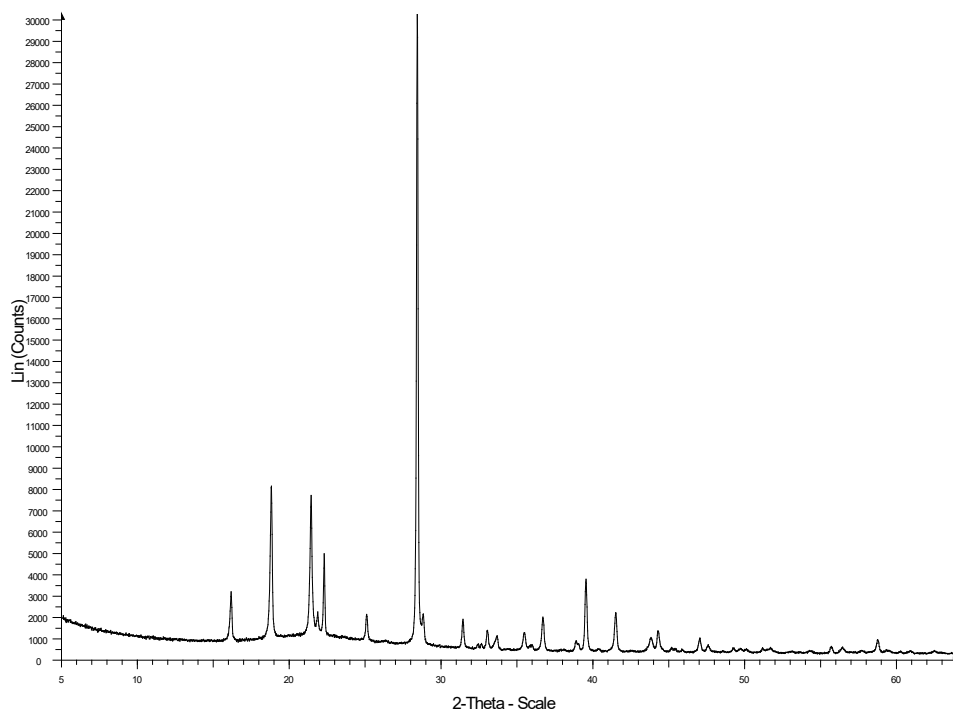


Figure 108 PXRD pattern of H<sub>4</sub>DHTA as collected on Bruker D8 Advance ( $\lambda = 1.5406 \text{ \AA}$ )

A search on the CCDC CSD<sup>3</sup> for the crystal structure of H<sub>4</sub>DHTA revealed that no such structure had been deposited on the database, so an effort was made to solve the crystal structure using powder structure solution. Lattice parameters for the phase were indexed using DICVOL as implemented in DASH<sup>141</sup> and a Pawley refinement was used to confirm the found lattice parameters.

### 6.3.1.3 Structure solution process

Data shown in Figure 108 were first indexed using DASH DICVOL indexing function. This gave reasonable starting lattice parameters (Table 31, second column). Using the lattice parameters and the area under each peak, a TOPAS simulated annealing run was created. A quick initial run was conducted using a complete linker rigid body, but it was

determined that the molecule was sitting on a centre of inversion, effectively producing doubled atomic sites (Figure 109). Therefore, in the subsequent run half of a 2,5-dihydroxyterephthalic acid linker was used as the rigid body input.

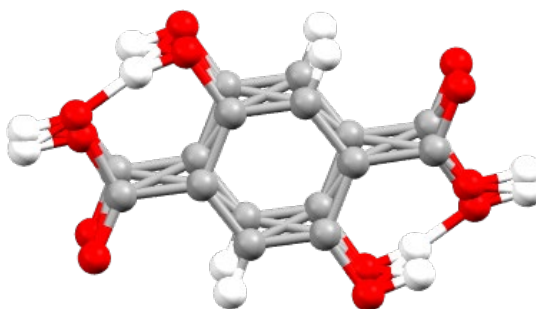


Figure 109 First structure solution with doubled sites. Atoms present carbon (grey), oxygen (red), hydrogen (white).

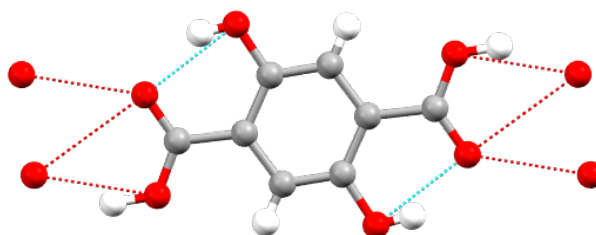


Figure 110 Final Topas simulated annealing solution, showing H-bonding (internal, blue lines)(external red lines). Atoms present carbon (grey), oxygen (red), hydrogen (white).

Shown in Figure 110 is the final simulated annealing solution. The hydrogen position on the carboxyl group is clearly incorrect as it lies far from the predicted H-bonding lines. To improve and confirm the solution, DFT was run to minimise the energy of the structure.

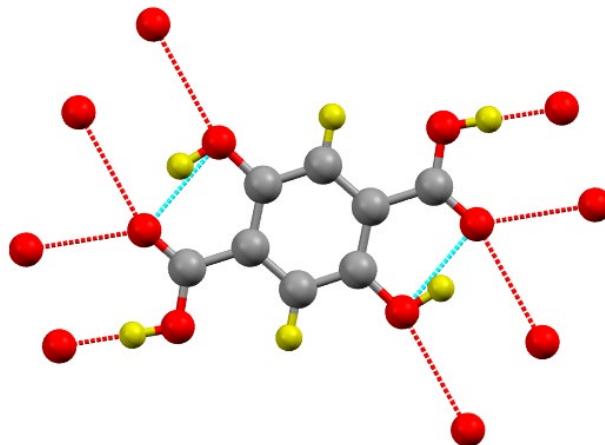


Figure 111 DFT optimised structure of 2,5-dihydroxyterephthalic acid showing H-bonding (internal – blue lines) (external – red lines). Atoms present: carbon (grey), oxygen (red), hydrogen (yellow).

Shown in Figure 111 is the optimised structure following DFT calculations. Bond lengths in the optimised structure are all slightly shorter, except for H-O hydroxyl bonds which have increased from  $0.8\text{\AA}$  to  $1.0\text{\AA}$ . The other large difference is in the carboxyl hydrogen angle which has decreased from  $120^\circ$  to  $109^\circ$ . These optimisations are not easily achievable using simulated annealing.

Although powder diffraction data had been collected on I11, the structure solution was carried out using laboratory X-ray data, as refinements using I11 data were not satisfactory, either due to radiation damage from the beam or due to the geometry of the MYTHEN detector setup.

A Rietveld refinement using laboratory powder X-ray diffraction data, together with the lattice parameters from the Pawley refinement, and the atomic coordinates from DFT, was carried out (Figure 112). Scale parameter, spherical harmonics for preferred orientation, a simple axial model for peak shapes, and thermal parameters of atom coordinates were refined. This resulted in good agreement with the experimental data, and gave a final  $R_{wp}$  of 4.96%, only 0.95 higher than the Pawley refinement.

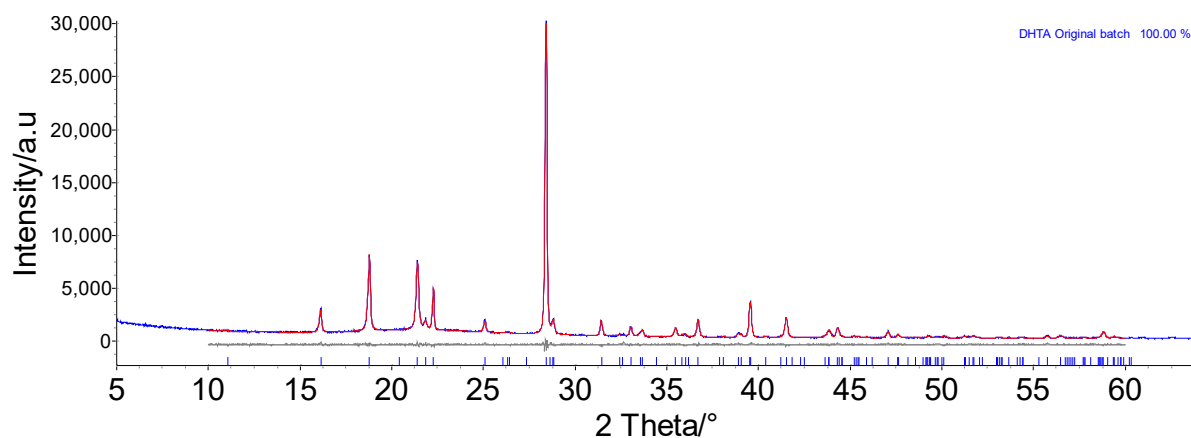


Figure 112 Final PXRD Rietveld refinement of bulk powder of H<sub>4</sub>DHTA (C<sub>8</sub>H<sub>6</sub>O<sub>6</sub>). Observed data (blue), model (red), difference (grey). Data collected on the Bruker D8 Advance.

Table 31 Lattice parameters as used through refinements. (Initial from indexing, Final Pawley from Topas Pawley refinement, Final Rietveld from final refinement).

Parameter	Initial	Final Pawley	Final Rietveld
$a$ (Å)	5.5624	5.55	5.55
$b$ (Å)	8.2017	8.19	8.19
$c$ (Å)	4.2829	4.28	4.28
$\alpha$ (°)	102.23	102.2	102.2
$\beta$ (°)	96.73	96.8	96.8
$\gamma$ (°)	93.52	93.4	93.4
Volume (Å <sup>3</sup> )	188.8883	188.283	188.283
Rwp		4.011	4.96

#### 6.3.1.4 Description of the crystal structure of H<sub>4</sub>DHTA

The CIF of H<sub>4</sub>DHTA can be found in the appendix (formula C<sub>8</sub>H<sub>6</sub>O<sub>6</sub>). H<sub>4</sub>DHTA crystallises in the *P*-1 space group (Figure 113), with the centre of the H<sub>4</sub>DHTA molecule located at the centre of inversion, at  $(\frac{1}{2} \frac{1}{2} 0)$ .

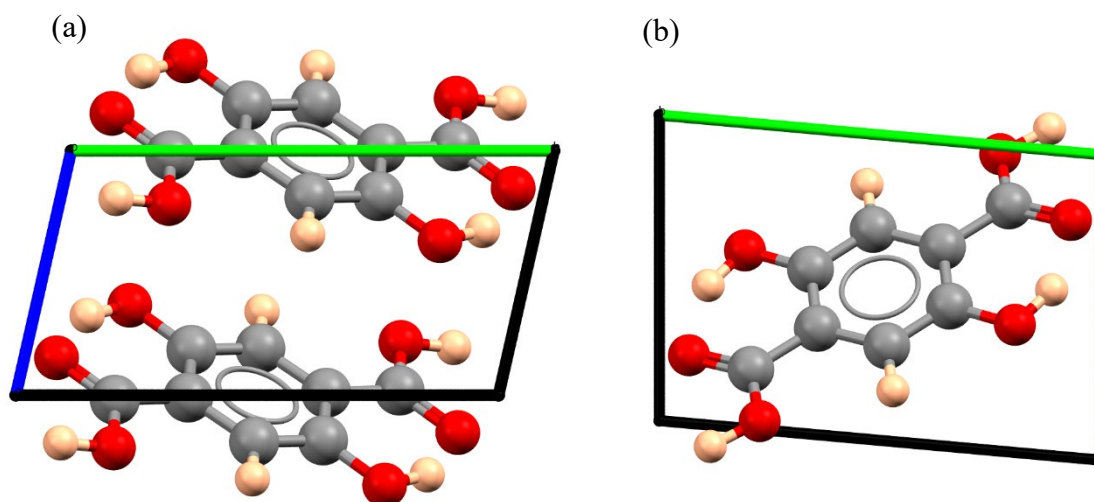


Figure 113 Crystal structure of H<sub>4</sub>DHTA. (a) Packing of H<sub>4</sub>DHTA as viewed down the *a*-axis. (b) Packing of H<sub>4</sub>DHTA as viewed down the *c*-axis. Key for elements: carbon (grey), oxygen (red), hydrogen (pink) Key for axis: *a*-axis (blue), *b*-axis (red), *c*-axis (green).



The structure exhibits both intramolecular and intermolecular H-bonding (Figure 114). Intermolecular H-bonding occurs between neighbouring carboxylic and hydroxyl groups;

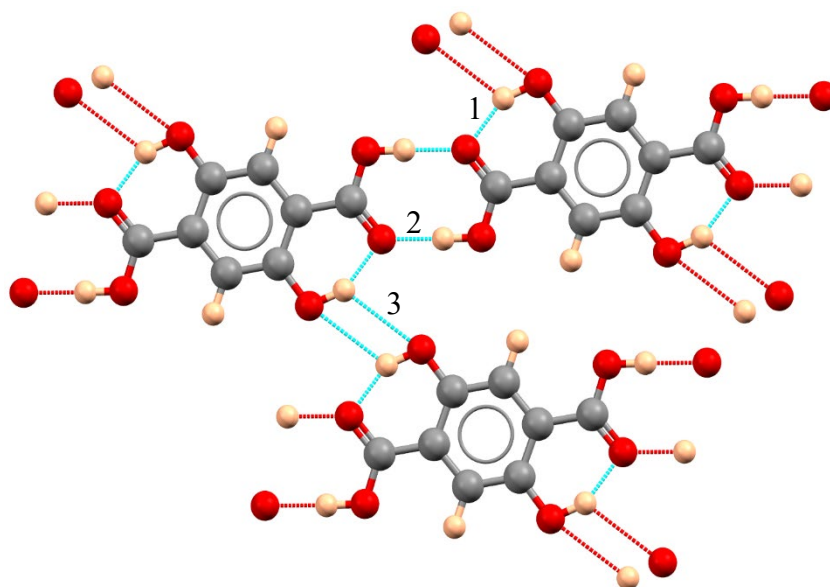


Figure 114 H-Bonding in the crystal structure of H<sub>4</sub>DHTA showing H-bonding between three neighbouring H<sub>4</sub>DHTA molecules. Intramolecular H-bonds (blue), intermolecular H-bonds (red). Key for elements: carbon (grey), oxygen (red), hydrogen (pink)

intramolecular H-bonding occurs between the hydroxyl group and carboxyl group (Table 32). The hydrogen bonding in this crystal structure is very similar to the H-bonding seen in other DHTA based structures, such as the DMF solvate of H<sub>4</sub>DTA and ZnH<sub>2</sub>DHTA(DMF)<sub>2</sub>(H<sub>2</sub>O)<sub>2</sub> (see Sections 3.3.7.2. and 3.3.7.4.).

Table 32 List of bond hydrogen bond lengths present in H<sub>4</sub>DHTA. Numbers refer to Figure 114.

Hydrogen bonding environment	Distance (Å)
1	1.627
2	1.638
3	2.542

### 6.3.2 $\text{KH}_3\text{DHTA}(\text{H}_2\text{O})$

One of the batches of  $\text{H}_4\text{DHTA}$  purchased from Alfa Aesar had unexpected properties: the powder was a far paler yellow than previous  $\text{H}_4\text{DHTA}$  batches received and did not form MOF-74 in the usual 90-minute reaction time. It was suspected that this batch was contaminated in some way, and therefore a range of analytical techniques were exploited to investigate this.

#### 6.3.2.1 NMR

The first analytical technique used was NMR to confirm that 2,5-dihydroxyterephthalic acid was present.

The collected  $^{13}\text{C}$  NMR for  $\text{KH}_3\text{DHTA}(\text{H}_2\text{O})$  is shown in Figure 115(a). The experimental  $^{13}\text{C}$  NMR is very similar to that previously collected for  $\text{H}_4\text{DHTA}$  (Section 6.3.1.1) and the peak assignments are the same. The only difference is a slight shift of all peaks upfield by 5 ppm. As the  $\text{DMSO-d}_6$  peaks have also shifted, this is a difference in collection parameters and not a substantial change in the composition of the molecule.

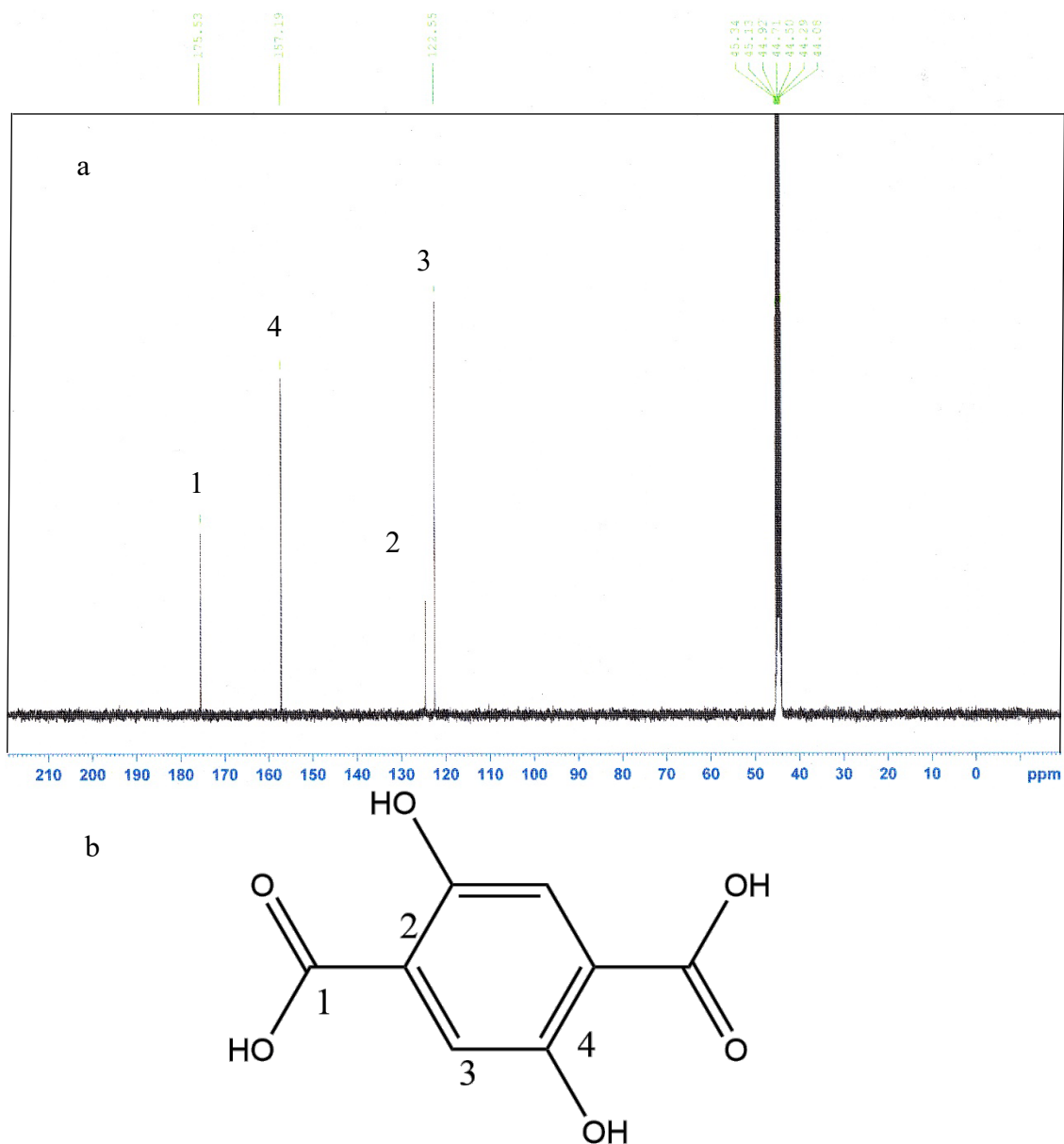


Figure 115(a)  $^{13}\text{C}$  NMR of  $\text{KH}_3\text{DHTA}(\text{H}_2\text{O})$ . (b) Structural formula of  $\text{H}_4\text{DHTA}$  used for peak assignment. Shown in Figure 116a is the experimental  $^1\text{H}$  NMR spectrum for  $\text{KH}_3\text{DHTA}$ . The spectrum is again very similar to the  $^1\text{H}$  NMR spectrum for  $\text{H}_4\text{DHTA}$  (Section 6.3.1.1); the only meaningful difference between the two is the much smaller peak corresponding to environment 3. This reduction in relative peak height is due to the lower concentration of  $\text{KH}_3\text{DHTA}(\text{H}_2\text{O})$  used in this measurements when compared to the initial  $\text{H}_4\text{DHTA}$  data collection. ; The lower concentration is consequence of the lower solubility in  $\text{DMSO-d}_6$  of  $\text{KH}_3\text{DHTA}(\text{H}_2\text{O})$  when compared to  $\text{H}_4\text{DHTA}$ .

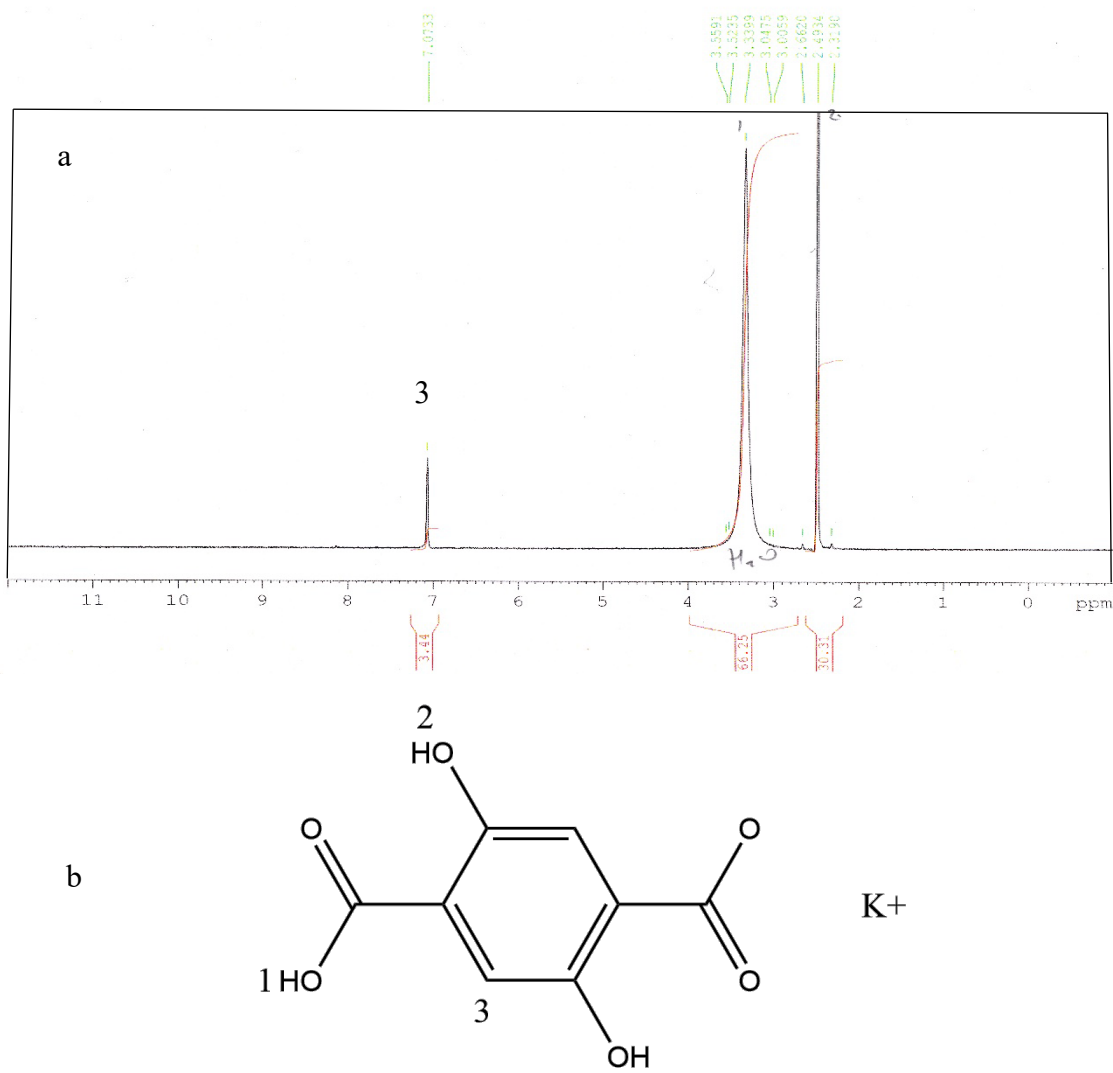


Figure 116a:  $^1\text{H}$  NMR of  $\text{KH}_3\text{DHTA}(\text{H}_2\text{O})$ . Figure 12b: Structural formula of  $\text{KH}_3\text{DHTA}$  used for peak assignment.

### 6.3.2.2 PXRD

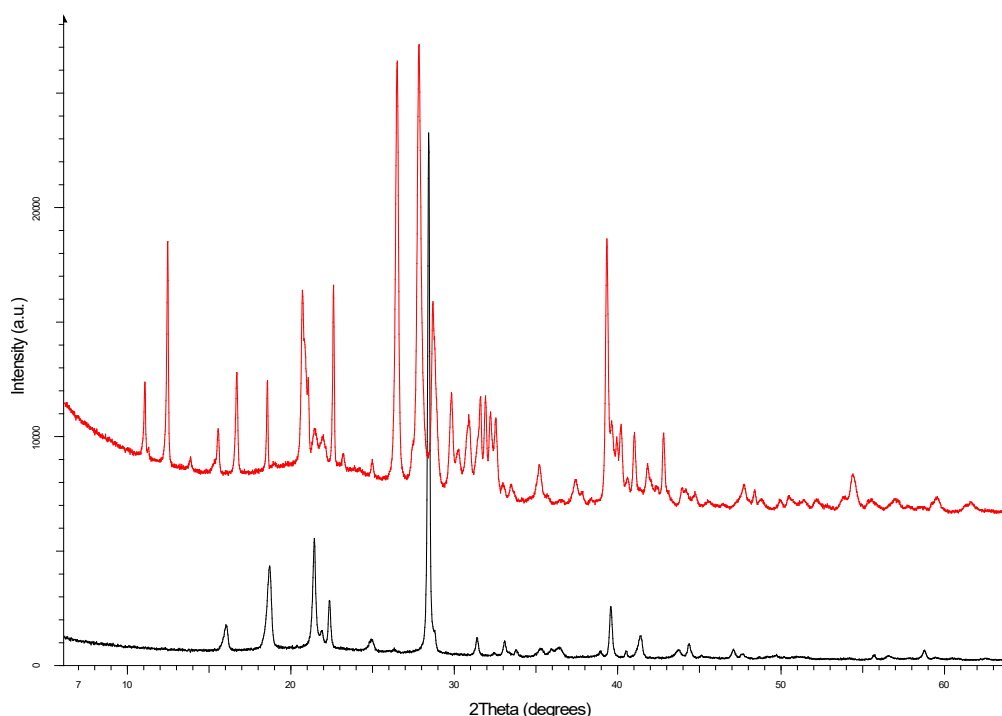


Figure 117 Comparison PXRD patterns of two H<sub>4</sub>DHTA batches. Red: contaminated H<sub>4</sub>DHTA batch. Blue: non-contaminated H<sub>4</sub>DHTA. Collected on the Bruker D8 Advance.

Comparing the experimental diffractograms of the contaminated H<sub>4</sub>DHTA and a previous H<sub>4</sub>DHTA batch indicated that the former was an entirely different phase (Figure 117). The powder diffraction pattern for the contaminated H<sub>4</sub>DHTA contains none of the peaks found for the crystalline H<sub>4</sub>DHTA phase (Section 6.3.1), indicating that this is a different phase. The lattice parameters of the contaminated H<sub>4</sub>DHTA phase were determined using TOPAS and used to search the CCDC CSD. Without knowing the elemental composition of the phase solving from powder X-ray diffraction data was impossible and therefore attempts to grow single-crystals were consequently carried out.

### 6.3.2.3 Single-crystal X-ray Diffraction



Figure 118 Single-crystal used to solve the  $\text{KH}_3\text{DHTA}(\text{H}_2\text{O})$  structure, mounted for data collection. Crystal is a colourless needle.

Figure 118 shows the crystal on which single-crystal X-ray diffraction was performed. Olex2 was used to solve the crystal structure from the data collected. There was uncertainty as to what the counter ion in the salt was present in the structure. The possible counter ions were K, Ca, Na, and Mg. There was the possibility that both the carboxylic acid groups on the DHTA molecule were deprotonated to form  $\text{H}_2\text{DHTA}^{2-}$  allowing for calcium and magnesium salts (see CCDC refcodes: EXUFEK,<sup>190</sup> EMEZAX<sup>191</sup> for calcium and magnesium terephthalic acid salts). Through trial and error it was determined that potassium gave the lowest R value; potassium and sodium salts have been reported for terephthalic acid but not 2,5-dihydroxyterephthalic acid (see CCDC refcode HUKYOB<sup>192</sup> for sodium and ZEFNIH<sup>193</sup> for potassium respectively). Further evidence that the cation was potassium comes from the synthesis method for  $\text{H}_4\text{DHTA}$  which uses potassium carbonate.<sup>111</sup>

### 6.3.2.4 Description of the crystal structure

The potassium salt of  $\text{H}_4\text{DHTA}$  crystallises as a monohydrate in space group *P*-1 (Table 30 column 3). The asymmetric unit contains one potassium cation, one DHTA molecule, and one water molecule (Figure 119a). The DHTA molecules are linked by symmetric

and very short H-bonds to form long chains. The unit-cell centre of symmetry is located between neighbouring DHTA molecules. All contents of the unit-cell sit on general positions (Figure 121b). The potassium ion also sits on a general position and is surrounded by 6 oxygens of the nearby carboxyls and one water (Figure 119b).

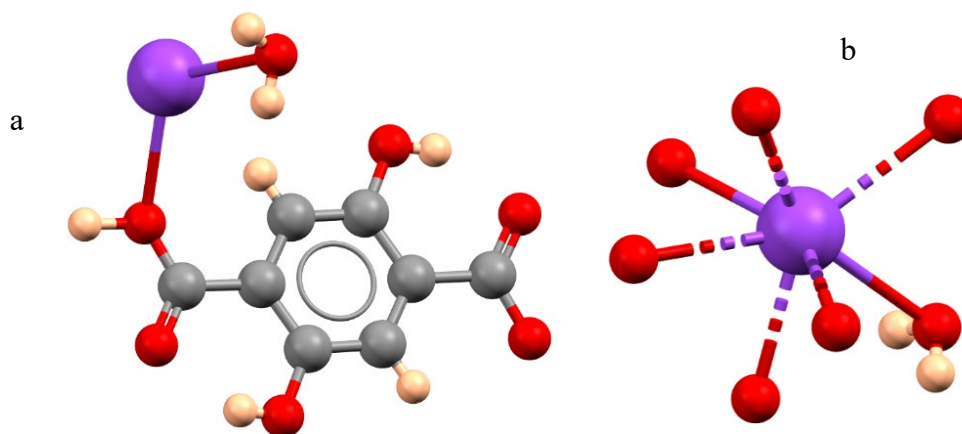


Figure 119a: asymmetric unit of  $K_3DHTA(H_2O)$ . 15b: oxygens surrounding potassium cation. Elements present: Potassium (purple), carbon (grey), oxygen (red), hydrogen (pink).

The DHTA molecules form infinite chains aligned between the crystallographic  $b$  and  $c$ -axes. These chains are formed due to the hydrogen bonds of neighbouring carboxyl groups (Figure 121a). The potassium ion sits in between the  $H_3DHTA$  chains coordinating to the carboxyl groups of  $H_3DHTA$ .

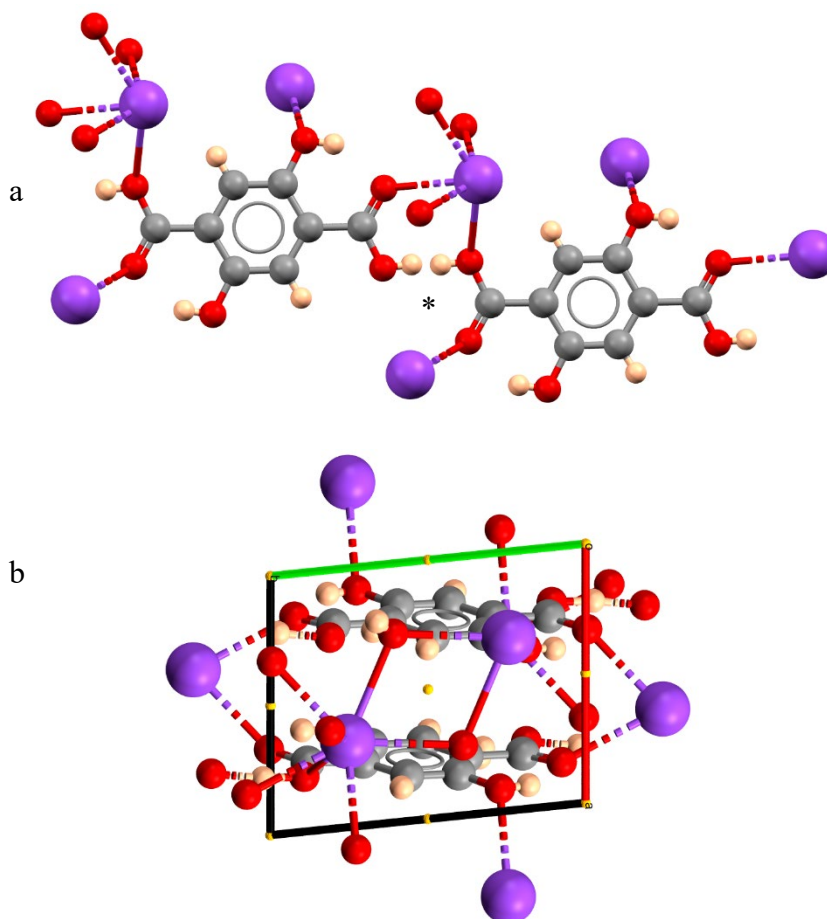


Figure 121a: Chains of H<sub>3</sub>DHTA showing the close hydrogen-hydrogen distance indicated by star. Figure 121b: packing of KH<sub>3</sub>DHTA(H<sub>2</sub>O) as viewed down the *c*-axis. Yellow spheres represent crystallographic centres of inversion. Elements present: Carbon (grey), oxygen (red), hydrogen (pink), potassium (purple).

The structure has further hydrogen bonding with hydroxyl groups, which form hydrogen bonds to each other as well as their neighbouring carboxyl groups (Figure 120).

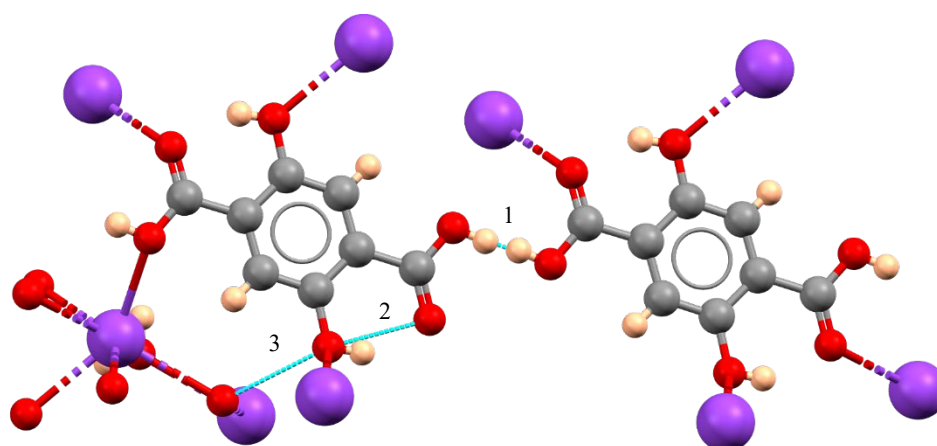


Figure 120 KH<sub>3</sub>DHTA(H<sub>2</sub>O) demonstrates extensive hydrogen bonding. Hydrogen bonds are shown as blue dotted lines. Red dashed lines represent intermolecular hydrogen bonding. Elements present: Carbon (grey), oxygen (red), hydrogen (pink), potassium (purple). Numbers on hydrogen bonds correspond to Table 33



Table 33 Hydrogen bond lengths for KH<sub>3</sub>DHTA(H<sub>2</sub>O) corresponding to numbers on Figure 122.

<b>Hydrogen bonding environment</b>	<b>Distance (Å)</b>
<b>1</b>	1.639
<b>2</b>	2.595
<b>3</b>	2.954

### 6.3.3 ZnAcH<sub>2</sub>ODA(DMF)

During the initial attempts to synthesise IR-MOF-74-Zn (Chapter 5), reactions with different zinc metal sources were performed. In particular, zinc acetate was used instead of zinc oxide (zinc oxide was used in all other MOF-74 syntheses) to find out if it would result in the formation of IR-MOF-74. Instead of IR-MOF-74-Zn, a new, unreported phase was produced. PXRD was performed on the product to try to determine the nature of the new phase.

#### 6.3.3.1 PXRD

Shown in Figure 122a is the collected PXRD pattern for Zn<sub>2</sub>AcH<sub>2</sub>ODA(DMF).

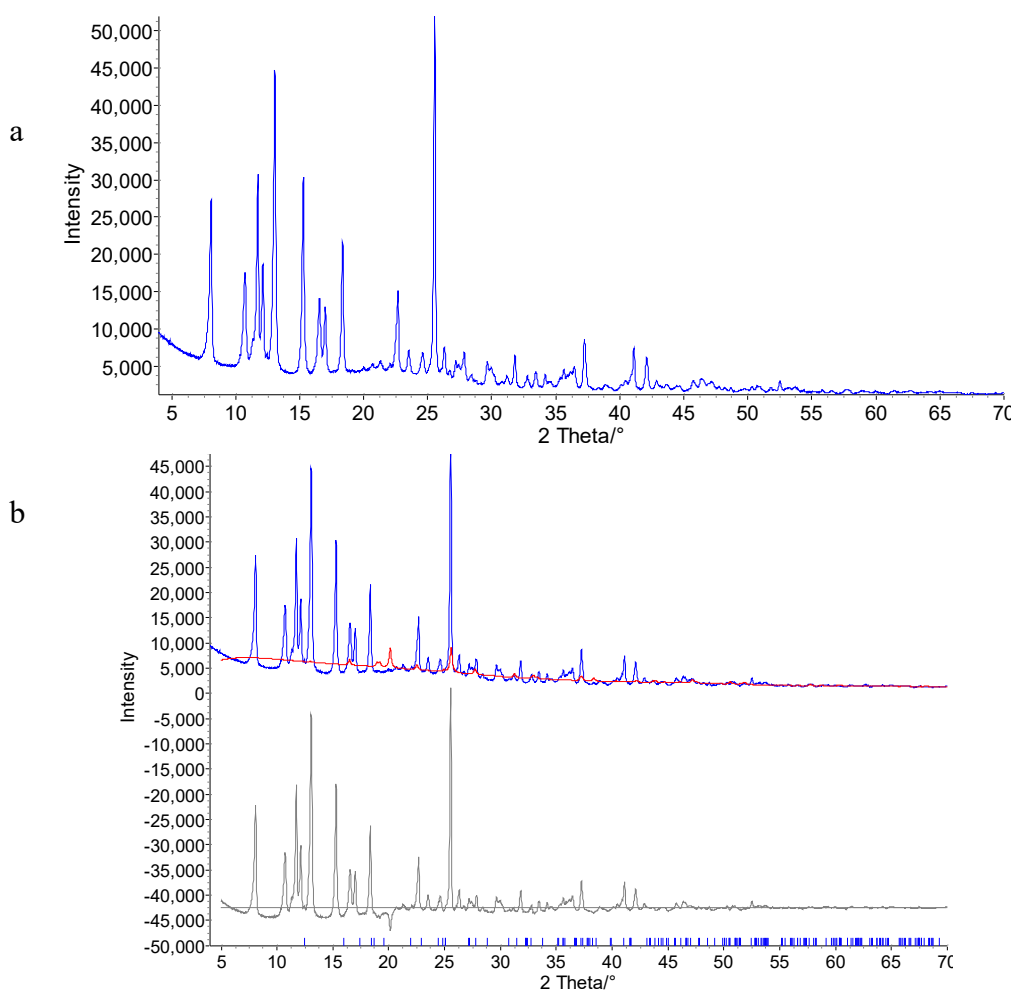


Figure 122. (a) PXRD pattern of ZnAcH<sub>2</sub>ODA(DMF) as collected on Bruker D8 Advance. Figure 122(b) Rietveld refinement using zinc acetate dihydrate as the starting model. Curves present: Experimental (blue), calculated (red), difference (grey).

Table 34 Comparison of lattice parameters for Zn<sub>2</sub>AcH<sub>2</sub>ODA(DMF) determined using a Pawley refinement and a Rietveld refinement. Pawley and Rietveld refinements prior to DFT energy minimisation did not have cell parameters in standard settings.

<b>Refinement method</b>	<b>Pawley</b>	<b>Rietveld before DFT</b>	<b>Final Rietveld</b>
<b>Crystal system</b>	Triclinic	Triclinic	Triclinic
<b>Space group</b>	<i>P-1</i>	<i>P-1</i>	<i>P-1</i>
<b><i>a</i> (Å)</b>	12.76(11)	12.760(6)	8.1713(5)
<b><i>b</i> (Å)</b>	8.941(7)	8.940(3)	8.9405(7)
<b><i>c</i> (Å)</b>	8.171(5)	8.171(3)	11.7390(7)
<b><i>α</i> (°)</b>	74.85(4)	74.84(3)	103.083(5)
<b><i>β</i> (°)</b>	116.12(4)	116.12(4)	102.571(4)
<b><i>γ</i> (°)</b>	112.07(5)	112.06(3)	105.152(3)
<b>Volume (Å<sup>3</sup>)</b>	770(11)	770.50(6)	770.56(10)
<b>Rwp</b>	4.533	6.875	5.39

### 6.3.3.2 Description of the crystal structure of Zn<sub>2</sub>Ac<sub>2</sub>H<sub>2</sub>ODA(DMF)<sub>2</sub>

A Rietveld refinement using zinc acetate dihydrate was attempted, but this refinement revealed that the zinc acetate phase had been completely consumed during the reaction (Figure 122b). The loss of zinc acetate indicated that, provided the product of the reaction was a single phase, this product had a 2:1 ratio of zinc to ODA. The powder diffraction pattern for this product was indexed using DICVOL as implemented in DASH (Table 34 second column) and a Pawley refinement using the lattice parameters run in TOPAS (Figure 123). The Pawley refinement was in excellent agreement with the experimental data ( $R_{wp} = 4.53\%$ ), so a structure solution using DASH was attempted.

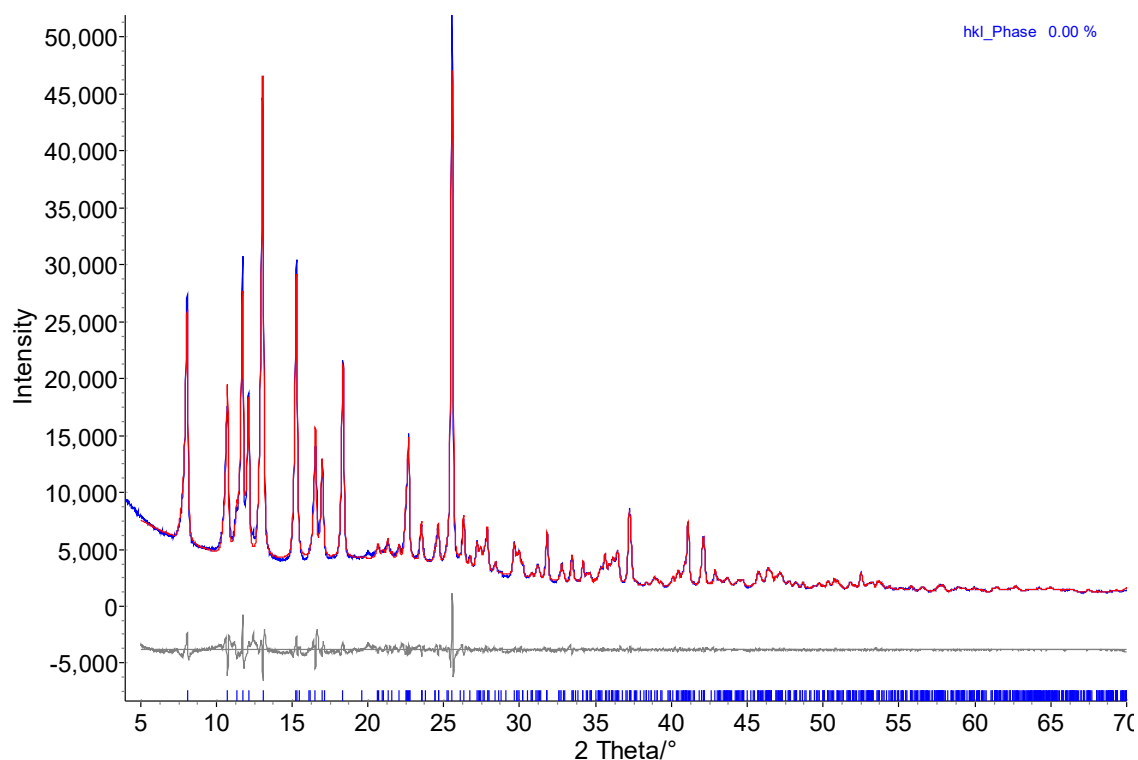


Figure 123 PXRD pattern of Zn<sub>2</sub>AcH<sub>2</sub>ODA(DMF) and Pawley refinement using lattice parameters determined by indexing in Topas. Curves present: Experimental (blue), calculated (red), difference (grey), reflection markers (tick marks).

Based on the volume of the unit cell and the likely components of the crystal structure, the fragments used in the simulated annealing runs were as follows: half an H<sub>2</sub>ODA molecule bonded to one zinc atom, one acetate ion, and one DMF molecule (Figure 124). The half H<sub>2</sub>ODA fragment was created using the atom coordinates from the H<sub>4</sub>ODA(DMF)<sub>2</sub> structure described in Section 5.3.1.2.2 with a zinc atom added at the end of the carboxyl group. Given the ratio of H<sub>4</sub>ODA to zinc in the reaction mixture, and the presence of acetate in the reaction mixture, it was assumed that the structure would contain a paddlewheel, and so the zinc atom was added at the average distance and bond angle found across all structures in the CCDC CSD<sup>3</sup> containing zinc paddlewheels.

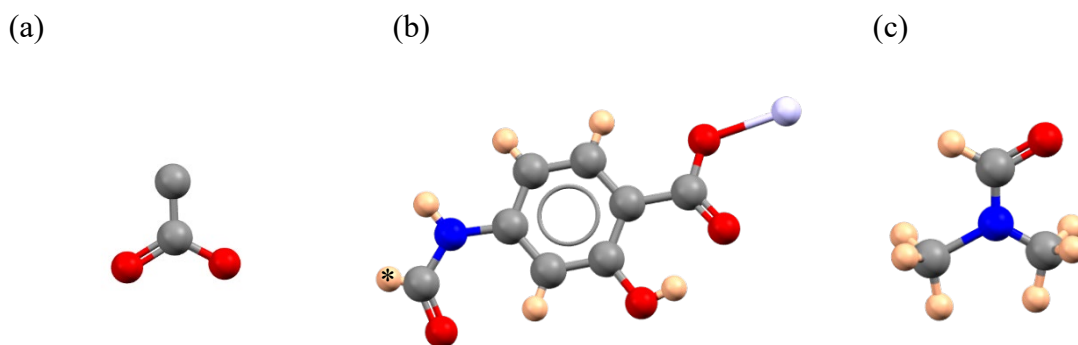


Figure 124 Fragments used in DASH structure solution of  $Zn_2AcH_2ODA(DMF)$ . (a) Acetate fragment; (b) Half  $H_2ODA$  molecule with zinc atom. Atom with star is the dummy atom used to anchor unit cell; (c) DMF molecule. Key: carbon (grey), oxygen (red), nitrogen (blue), zinc (light blue), hydrogen (pink).

After 400 runs the best solution reached a  $\chi^2$  value 23.18. The structure looked chemically sensible, and the DMF and acetate fragments had formed into a paddlewheel during the simulated annealing. A scale-only Rietveld refinement was performed to confirm that the structure described the bulk powder. The Rietveld refinement ( $R_{wp}$  6.875) was poorer than the Pawley refinement meaning that the model could be improved (Table 34 column 3).

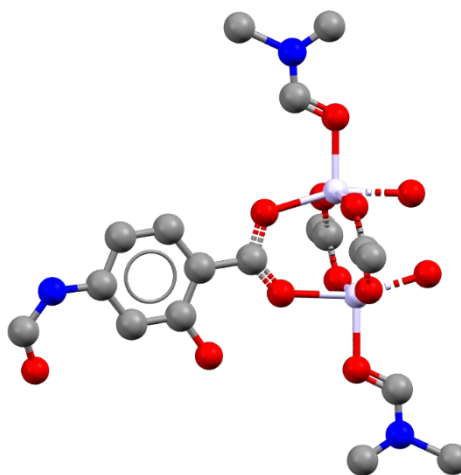


Figure 125 DASH simulated annealing structure for  $Zn_2AcH_2ODA(DMF)$  showing coordination around zinc paddlewheel. Elements present: carbon (grey), oxygen (red), nitrogen (dark blue), zinc (light blue) hydrogens omitted for clarity.

As individual atoms in fragments do not move during simulated annealing, individual atom coordinates, especially hydrogens, can often be improved. A DFT energy minimisation was performed on the DASH solution to try and improve the fit.

After DFT energy minimisation, the largest changes in the structure came from hydrogen positions and bond angles around the paddlewheel. This is unsurprising as the

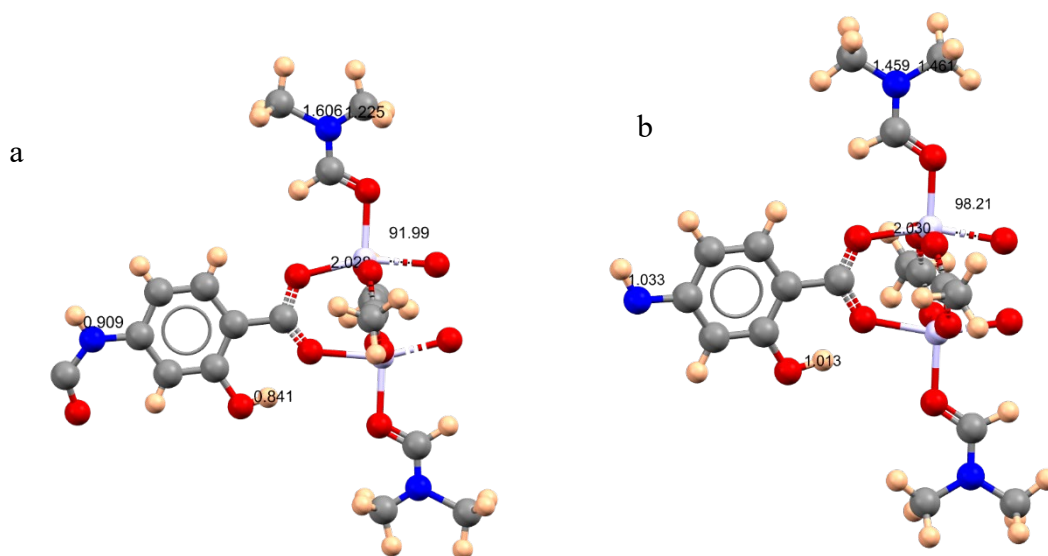


Figure 126 Comparison of the between DASH solution and DFT energy minimisation for the structure of Zn<sub>2</sub>AcH<sub>2</sub>ODA(DMF), illustrating changes in bond lengths and angles. DASH simulated annealing solution (left), DFT energy minimisation (right). Key: carbon (grey), oxygen (red), nitrogen (dark blue), zinc (light blue).

paddlewheel bond angles and lengths were set to the average values from the CCDC CSD for paddlewheel structures (Figure 126). After minimisation, the bond angles around the paddlewheel changed significantly, in particular the angle (ODA)O-Zn-O(DMF) changed from 92 ° to 98 °; while both values are in the accepted range 98 ° is much more reasonable.<sup>194</sup> After energy minimisation, a final Rietveld rigid-body refinement was performed to ensure that the refined model correctly described the data. The final fit ( $R_{wp} = 5.39$ ) constitutes a significant an improvement over the initial Rietveld using the simulated annealing structure (Table 34 column 4).

Table 34 Comparison of lattice parameters for Zn<sub>2</sub>AcH<sub>2</sub>ODA(DMF) determined using a Pawley refinement and a Rietveld refinement. Pawley and Rietveld refinements prior to DFT energy minimisation did not have cell parameters in standard settings.

<b>Refinement method</b>	<b>Pawley</b>	<b>Rietveld DFT</b>	<b>before Final Rietveld</b>
<b>Crystal system</b>	Triclinic	Triclinic	Triclinic
<b>Space group</b>	<i>P</i> -1	<i>P</i> -1	<i>P</i> -1
<b><i>a</i> (Å)</b>	12.76(11)	12.760(6)	8.1713(5)
<b><i>b</i> (Å)</b>	8.941(7)	8.940(3)	8.9405(7)
<b><i>c</i> (Å)</b>	8.171(5)	8.171(3)	11.7390(7)
<b><i>α</i> (°)</b>	74.85(4)	74.84(3)	103.083(5)
<b><i>β</i> (°)</b>	116.12(4)	116.12(4)	102.571(4)
<b><i>γ</i> (°)</b>	112.07(5)	112.06(3)	105.152(3)
<b>Volume (Å<sup>3</sup>)</b>	770(11)	770.50(6)	770.56(10)
<b>R<sub>wp</sub></b>	4.533	6.875	5.39

### 6.3.3.2 Description of the crystal structure of $\text{Zn}_2\text{Ac}_2\text{H}_2\text{ODA}(\text{DMF})_2$

$\text{Zn}_2\text{Ac}_2\text{H}_2\text{ODA}(\text{DMF})_2$  crystallises in the triclinic  $P-1$  space group. The asymmetric unit contains one zinc atom, one acetate ion, one DMF molecule, and half an  $\text{H}_2\text{ODA}$  molecule (Figure 127a). The middle of the  $\text{H}_2\text{ODA}$  molecule and the centre of the zinc paddlewheel sit on centres of inversion.

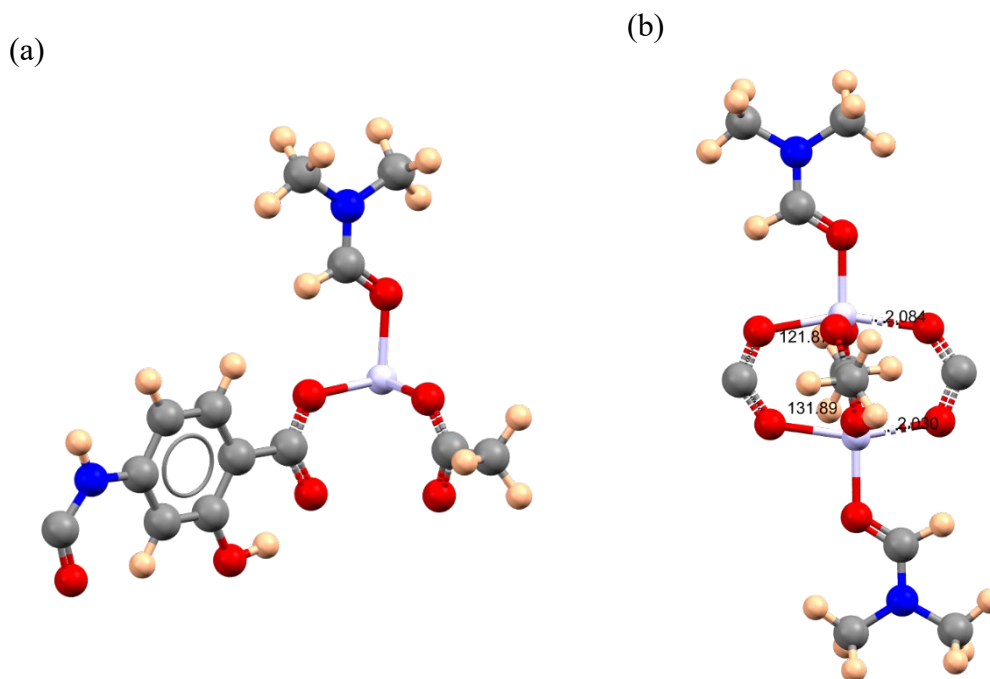


Figure 127 Structure of  $\text{Zn}_2\text{Ac}_2\text{H}_2\text{ODA}(\text{DMF})_2$ . (a) Asymmetric unit of  $\text{Zn}_2\text{Ac}_2\text{H}_2\text{ODA}(\text{DMF})_2$ . Figure 127(b) Coordination around the zinc paddlewheel showing bond Zn-O bond lengths. Key: carbon (grey), oxygen (red), nitrogen (dark blue), zinc (light blue).

The two zinc atoms in the paddlewheel are slightly offset and the bond lengths vary on each side (Figure 127b). This type of distorted paddlewheel is observed in a number of other zinc paddlewheel structures including: CCDC refcode AGOMAN,<sup>195</sup> CCDC refcode CIRBUD,<sup>196</sup> CCDC refcode FISNUT.<sup>197</sup> Shown in Figure 129 are the coordination around the zinc paddlewheels in the three examples mentioned previously. In all cases the C-O-Zn bond angles deviate from each other significantly with largest difference occurring in AGOMAN where the bond angles are  $138^\circ$  and  $116^\circ$ .



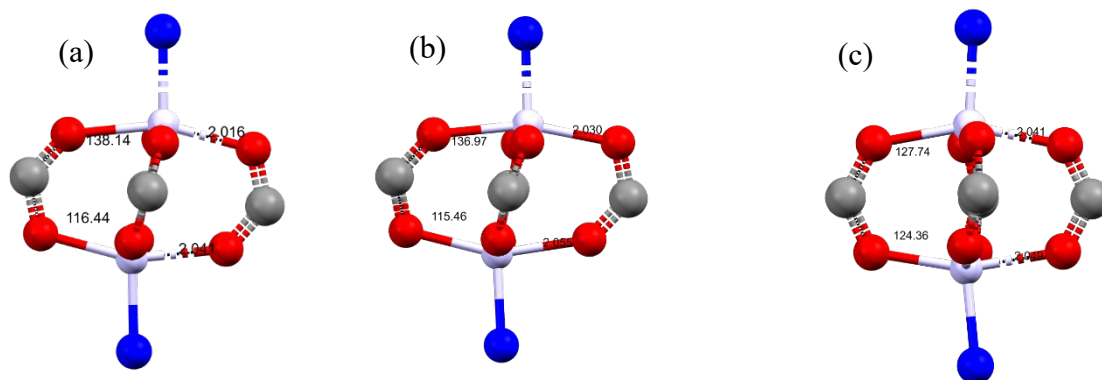


Figure 129 Spatial arrangement of several paddlewheel structures taken from the CCDC CSD. (a) AGOMAN, (b) CIRBUD, (c) FISNUT. Key: carbon (grey), oxygen (red), nitrogen (dark blue), zinc (light blue).

In the structure described here,  $\text{H}_2\text{ODA}^{2-}$  anions link the paddlewheels into infinite one-dimensional chains, as shown in Figure 128c. Figure 128a shows the packing of the unit-cell down the crystallographic  $a$ -axis showing the aforementioned chains offset from each other, with the paddlewheel located at opposite corners of the unit-cell. Figure 128b

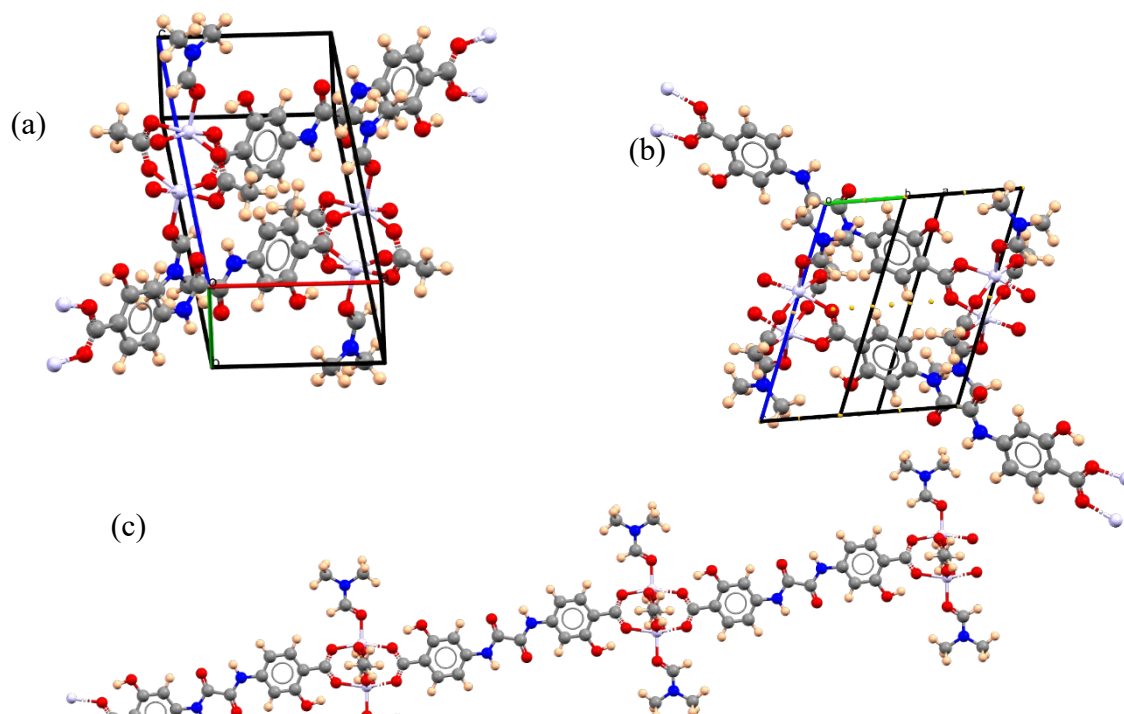


Figure 128a Packing of  $\text{Zn}_2\text{Ac}_2\text{H}_2\text{ODA}(\text{DMF})_2$  showing chains packing across unit-cell. Figure 128b Packing of  $\text{Zn}_2\text{Ac}_2\text{H}_2\text{ODA}(\text{DMF})_2$  showing crystallographic centres of inversion as yellow spheres to show symmetry present in unit-cell. Figure 128c single chain of  $\text{Zn}_2\text{Ac}_2\text{H}_2\text{ODA}(\text{DMF})_2$  to show how a 1 d chain forms through the zinc paddlewheel. Elements present: carbon (grey), oxygen (red), nitrogen (dark blue), zinc (light blue).

shows the centres of inversion in the unit-cell as yellow spheres to make the points of inversion clearer.

$Zn_2Ac_2H_2ODA(DMF)_2$  exhibits extensive hydrogen bonding (Figure 130). This hydrogen bonding occurs between chains, from the nitrogen on the  $H_2ODA$  amide group to the acetate groups of the paddlewheel. This hydrogen bonding is likely to stabilise the packing of the chains. Additionally, hydrogen bonding occurs between neighbouring  $H_2ODA$  hydroxyl and carboxyl groups.

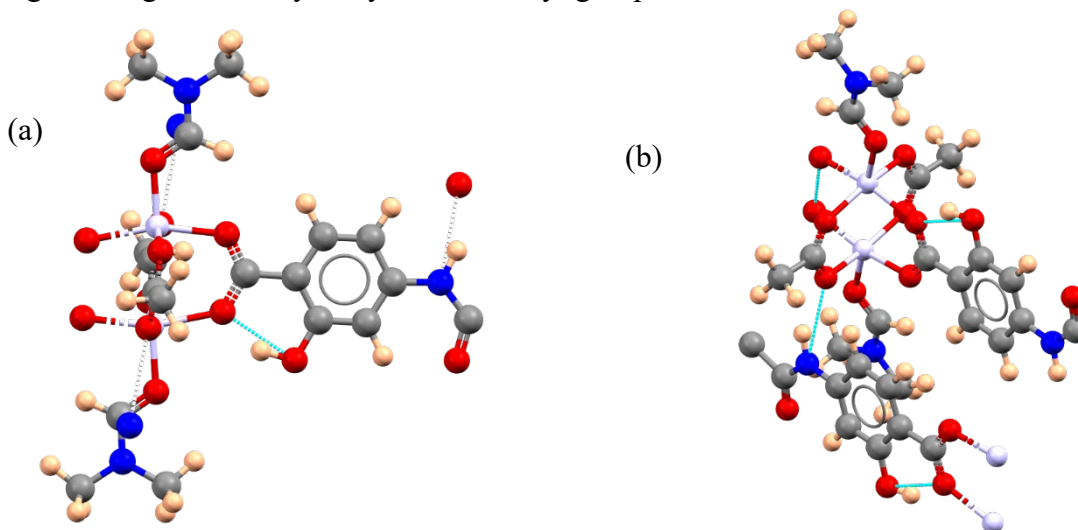


Figure 130 Hydrogen bonding present in  $Zn_2Ac_2H_2ODA(DMF)_2$ . The dashed blue lines correspond to hydrogen bonding of shown chains, while white dashed lines correspond to hydrogen bonding of unshown chains. Figure 131(a) intra molecular hydrogen bonding. Figure 132(b) intermolecular hydrogen bonding. Elements present: carbon (grey), oxygen (red), hydrogen (pink), nitrogen (dark blue), zinc (light blue).

As the with other  $H_4ODA$  structure described in this thesis (Section 5.3.1.2.2) the  $H_4ODA$  linker exhibits a twist around the amide – benzene ring in the structure (Figure 132). In

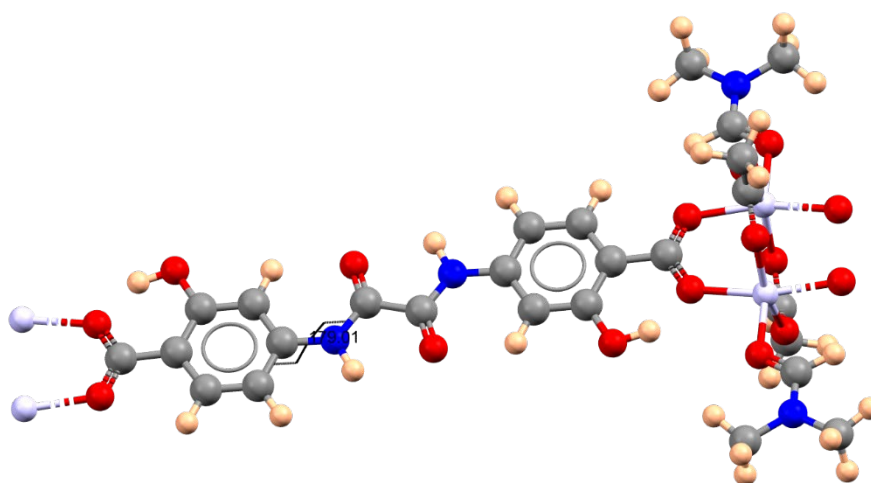


Figure 132  $Zn_2Ac_2H_2ODA(DMF)_2$  bond angle around amide group to benzene ring to show twist of the  $H_2ODA$  molecule. Elements present: carbon (grey), oxygen (red), nitrogen (dark blue), zinc (light blue).

this structure the twist is much less extreme, only deviating from  $180^\circ$  by  $1^\circ$ , while the DMF solvate of H<sub>4</sub>ODA had a bond angle of  $168^\circ$ .

### 6.3.4 H<sub>4</sub>TDA(DMF)

H<sub>4</sub>TDA is a MOF linker which can be used to synthesise IR-MOF-74 frameworks. H<sub>4</sub>TDA has the same functional groups as H<sub>4</sub>ODA, which is discussed in Chapter 5.

#### 6.3.4.1 Single-crystal X-ray diffraction

Crystals suitable for single-crystal X-ray diffraction were grown by dissolving H<sub>4</sub>TDA in hot DMF, hot filtering and then leaving to cool for several days. X-ray diffraction was performed on these crystals.

#### 6.3.4.2 Description of the crystal structure

H<sub>4</sub>TDA(DMF) crystallises in a triclinic *P*-1 unit-cell in which the H<sub>4</sub>TDA molecules sit on crystallographic centres of inversion (Figure 133b). The asymmetric unit contains half

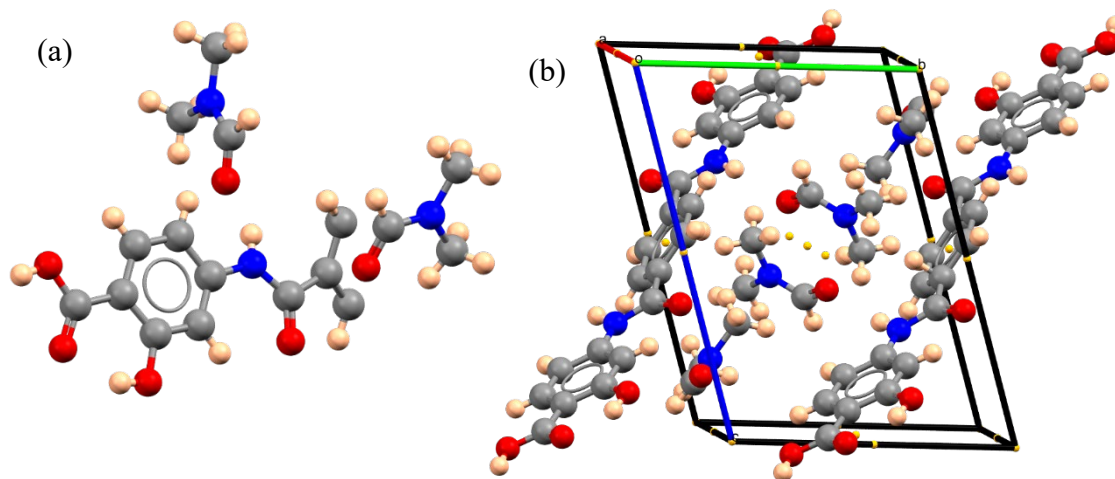


Figure 133a: Asymmetric unit of H<sub>4</sub>TDA(DMF)<sub>4</sub>. Figure 133b: Packing of H<sub>4</sub>TDA(DMF)<sub>4</sub> showing centres of inversion as yellow spheres. Elements present: Carbon(grey), oxygen (red), hydrogen (pink), nitrogen (blue).

an H<sub>4</sub>TDA and two DMF molecules; the atoms of the DMF molecules sit on general positions (Figure 133a). One of the four methyl groups on the DMF molecules is disordered, and has its hydrogens split over 6 sites. H<sub>4</sub>TDA molecules pack into chains

with DMF molecules taking up the space between the chains (Figure 134a). This means that chains are sandwiched between DMF molecules (Figure 134b).

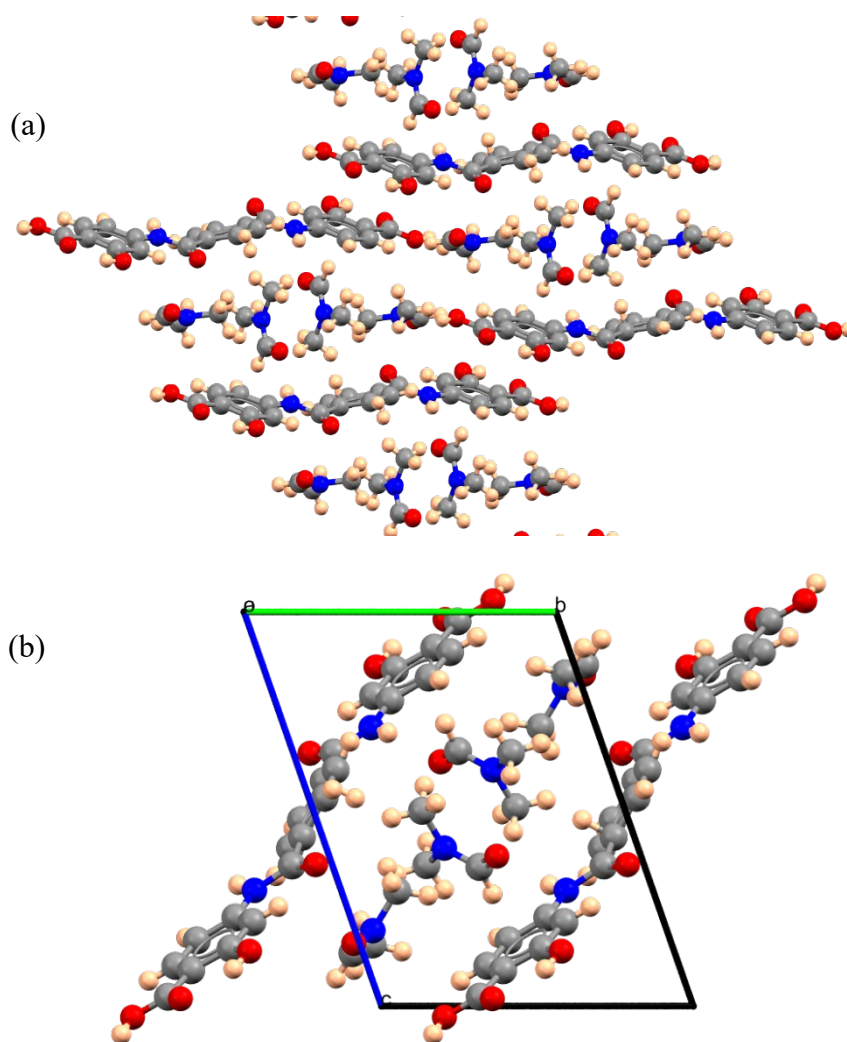


Figure 134 Packing of chains in  $H_4TDA(DMF)_4$ . Figure 19b: packing of  $H_4TDA(DMF)_4$  as viewed down the crystallographic a-axis. Elements present: Carbon(grey), oxygen (red), hydrogen (pink), nitrogen (blue).

The crystal structure exhibits hydrogen bonding between  $H_4TDA$  molecules and DMF molecules. The  $H_4TDA$  molecules do not have a hydrogen bonding between each other

and do not exhibit any  $\pi$ -stacking. Each H<sub>4</sub>TDA molecule has hydrogen bonding with four DMF molecules.

The H<sub>4</sub>TDA molecule exhibits a torsion around the amide linkage of 30 °. This torsion is unusual as the most common torsion angle for this type of amide bond is 0 °, but still in an accepted range.<sup>182</sup>

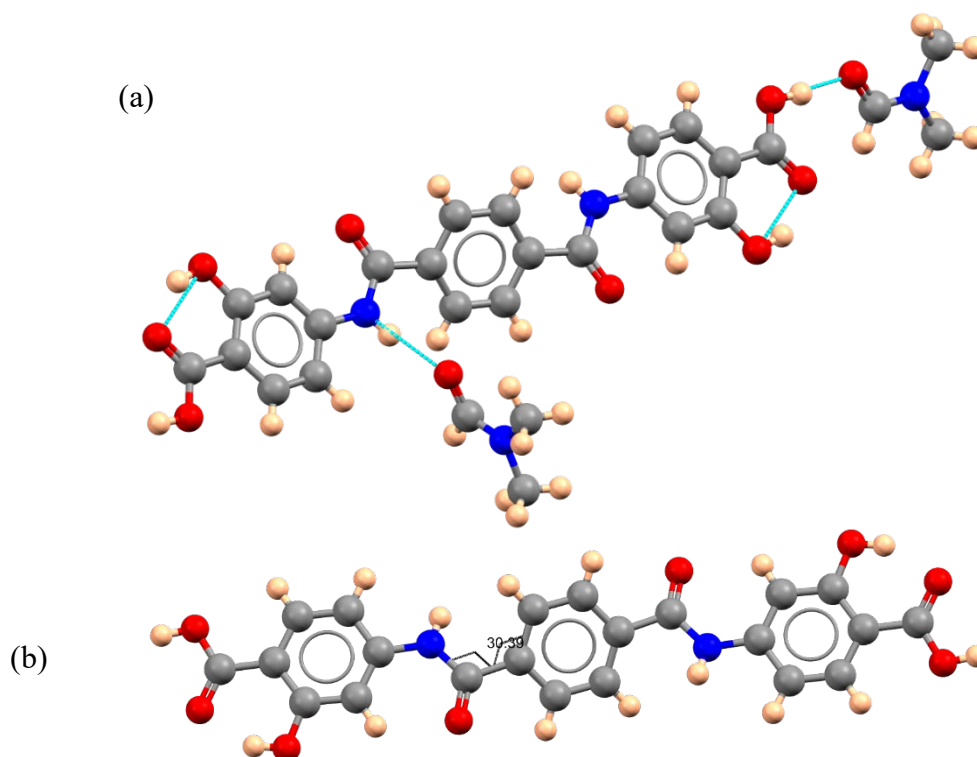


Figure 135 Hydrogen bonding present in H<sub>4</sub>TDA(DMF)<sub>4</sub>. Elements present: Carbon(grey), oxygen (red), hydrogen (pink), nitrogen (blue).

## 6.4 Discussion

### 6.4.1 H<sub>4</sub>DHTA and KH<sub>3</sub>DHTA(H<sub>2</sub>O)

The crystal structures of H<sub>4</sub>DHTA and KH<sub>3</sub>DHTA(H<sub>2</sub>O) were successfully solved using a combination of X-ray diffraction and NMR spectroscopy. The need for solving these crystal structures was to work out why a contaminated batch of H<sub>4</sub>DHTA would not produce MOF-74-Zn. The only visual difference between the “good” H<sub>4</sub>DHTA and contaminated H<sub>4</sub>DHTA was a paler yellow colour for the contaminated batch. NMR was initially employed to try and work out what was wrong with the contaminated batch, but both NMR spectra were almost identical; this at least meant that the contaminated batch had DHTA in it. Following the inability to find out the contaminant using NMR, X-ray diffraction was used. The crystal structure was successfully solved using single-crystal X-ray diffraction by growing crystals of the contaminated compound. The crystal structure is new, the only other reported salt of H<sub>4</sub>TDA is an ammonium salt with formula: H<sub>3</sub>DHTA(NH<sub>4</sub>)(H<sub>2</sub>O) CCDC refcode GUSVOH.<sup>198</sup> The two salts are extremely similar with almost identical lattice parameters and unit-cell volume.

After solving the structure of KH<sub>3</sub>DHTA(H<sub>2</sub>O), it was found that the structure of H<sub>4</sub>DHTA was yet to be reported. As H<sub>4</sub>DHTA very commonly forms solvates when crystallised (see DMF solvate in Section 3.3.7.1 and H<sub>2</sub>O solvate CCDC refcode DUSJUX<sup>159</sup>) structure solution from powder X-ray diffraction was used.

### 6.4.2 Zn<sub>2</sub>Ac<sub>2</sub>H<sub>2</sub>ODA(DMF)<sub>2</sub>

Zn<sub>2</sub>Ac<sub>2</sub>H<sub>2</sub>ODA(DMF)<sub>2</sub> is a novel one-dimensional coordination polymer which was solved using powder X-ray diffraction structure-solution methods. When attempting to synthesise IR-MOF-74-Zn (see chapter 5) zinc acetate dihydrate was substituted for zinc oxide to see if IR-MOF-74-Zn would form. Even after milling the reaction mixture for

10 hours the reaction did not progress beyond  $\text{Zn}_2\text{Ac}_2\text{H}_2\text{ODA}(\text{DMF})_2$ , as established by examination of the PXRD patterns collected as a function of milling time.

### 6.4.3 $\text{H}_4\text{TDA}(\text{DMF})$

The crystal structure of  $\text{H}_4\text{TDA}(\text{DMF})$  was determined by single-crystal X-ray diffraction.  $\text{H}_4\text{TDA}$  is the continuation of the work outlined in Chapter 5 of synthesising new isorecticular MOF-74 frameworks using mechanochemical synthesis.  $\text{H}_4\text{TDA}$  is very similar to both  $\text{H}_4\text{DHTA}$  and  $\text{H}_4\text{ODA}$ , with the same functional groups for coordinating to zinc, but with a large distance between the ends of the molecule (Figure 136).

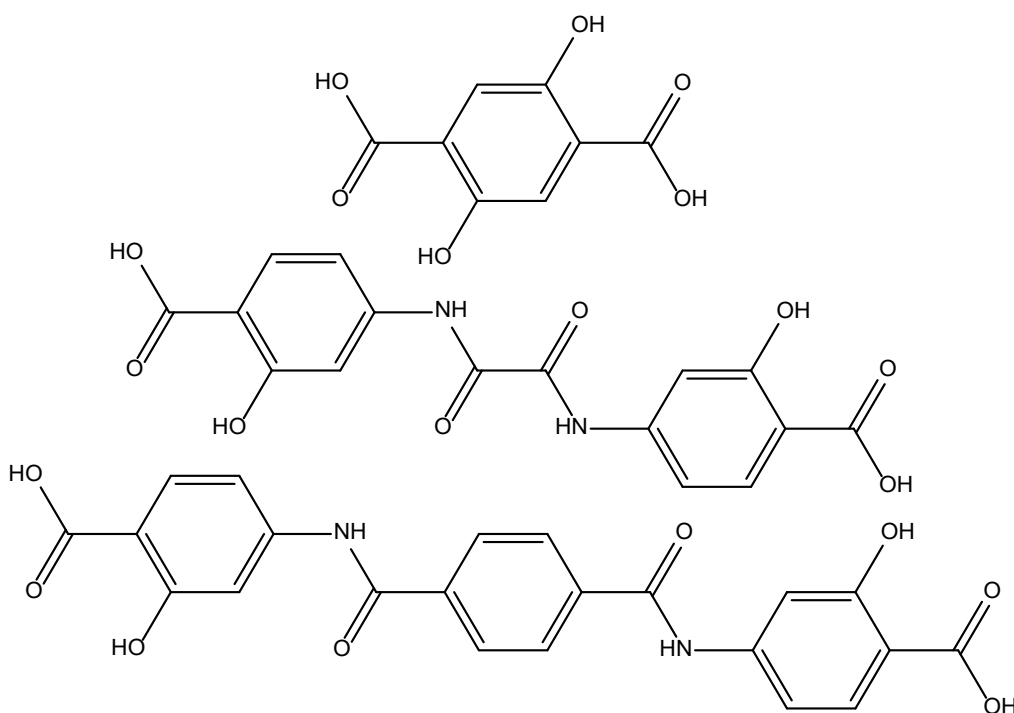


Figure 136 sketches of  $\text{H}_4\text{DHTA}$  (top),  $\text{H}_4\text{ODA}$  (middle), and  $\text{H}_4\text{TDA}$  (bottom).

To confirm the synthesis of  $\text{H}_4\text{TDA}$ , as with  $\text{H}_4\text{ODA}$ , a DMF solvate was prepared and single-crystal X-ray diffraction performed. This resulted in new crystal structure, which is similar to the  $\text{H}_4\text{DHTA}(\text{DMF})_2$  and  $\text{H}_4\text{ODA}(\text{DMF})_2$  structures as described in sections 3.3.7.1 and 5.3.1 respectively (Table 35).  $\text{H}_4\text{ODA}(\text{DMF})_2$  and  $\text{H}_4\text{TDA}(\text{DMF})_2$  are very

similar, both crystallising in triclinic space groups, while H<sub>4</sub>DHTA(DMF)<sub>2</sub> crystallised in a monoclinic space group (Table 30).

Table 35 Comparison of lattice parameters for series of DMF solvates of linkers used in isorecticular MOF-74 synthesis.

	<b>H<sub>4</sub>DHTA(DMF)<sub>2</sub></b>	<b>H<sub>4</sub>ODA(DMF)<sub>2</sub></b>	<b>H<sub>4</sub>TDA(DMF)<sub>4</sub></b>
<b>Crystal system</b>	Monoclinic	Triclinic	Triclinic
<b>Space group</b>	<i>P2<sub>1</sub>/n</i>	<i>P-1</i>	<i>P-1</i>
<b><i>a</i> (Å)</b>	6.879(8)	7.0517(1)	7.7582(4)
<b><i>b</i> (Å)</b>	20.818(7)	8.154(2)	9.9345(6)
<b><i>c</i> (Å)</b>	5.920(7)	10.483(2)	12.9348(8)
<b><i>α</i> (°)</b>	90	72.31(2)	68.299(6)
<b><i>β</i> (°)</b>	98.095(4)	81.22(2)	78.096(5)
<b><i>γ</i> (°)</b>	90	86.73(2)	72.020(5)
<b>Volume (Å<sup>3</sup>)</b>	839.57(3)	567.46(1)	876.24(2)

## 6.5 Conclusion

### 6.5.1 Structures of H<sub>4</sub>DHTA and KH<sub>3</sub>DHTA(H<sub>2</sub>O)

The key lesson arising from this piece of work is to run always analysis on any chemicals purchased from suppliers as, in this instance, time was wasted trying to use contaminated H<sub>4</sub>DHTA, which would never produce MOF-74 for a number of weeks before realising the cause. Out of the mistake two new crystal structures have been determined, one of which, the structure of H<sub>4</sub>DHTA, is important for understanding the process by which MOF-74 forms. KH<sub>3</sub>DHTA(H<sub>2</sub>O) is very similar to other salts of terephthalic acid forming layered structures. This find fills out the picture further as it confirms that the crystal structures of 2,5-dihydroxyterephthalic acid salts are very similar to those of terephthalic acid salts.

### 6.5.2 Zn<sub>2</sub>Ac<sub>2</sub>H<sub>2</sub>ODA(DMF)<sub>2</sub>

Zn<sub>2</sub>Ac<sub>2</sub>H<sub>2</sub>ODA(DMF)<sub>2</sub> is a novel 1-D coordination polymer built from zinc paddlewheels.



### 6.5.3 H<sub>4</sub>TDA(DMF)<sub>4</sub>

H<sub>4</sub>TDA(DMF)<sub>4</sub> is a new crystal structure for the DMF solvate of this linker, which can be used to synthesise an isorecticular MOF-74 framework. Based on previous evidence of linker DMF solvates discussed in this thesis, this structure will most likely correspond to the first intermediate which forms during a mechanochemical synthesis.

As the framework that could be synthesised from this linker contains significantly larger channels than the isorecticular MOF-74 framework described in Chapter 5, further investigation using the H<sub>4</sub>TDA linker is worth pursuing.

## Chapter 7- Conclusions and further work

### 7.1 Conclusions

The applications of MOFs are showing significant industrial interest as several companies begin to produce MOFs on large-scale for many purposes. The mechanochemical synthesis of MOFs is already being exploited by one company, MOF technologies ltd, and undoubtedly more companies will switch to mechanochemical synthesis in the coming years. Understanding how MOFs form during mechanochemical synthesis gives transferrable knowledge for how other potential MOFs might form; to this end this thesis presents the mechanochemical synthesis of two MOFs, one previously synthesised and one novel. Both of these MOFs (MOF-74-Zn and IR-MOF-74-Zn) form crystalline intermediates which have been indexed and several solved using powder X-ray diffraction and single-crystal X-ray diffraction.

In Chapter 1, the existing drug loading studies of MOFs are presented. The list of drug loading studies of MOFs is small, with most of the studies measuring ibuprofen loading. As most MOFs are synthesised from toxic metals, or toxic linkers, the MOF-74 family of frameworks is presented as a strong candidate for drug loading applications.

In Chapter 3, the mechanochemical synthesis of MOF-74-Zn  $Zn_2H_2DHTA$  ( $Zn_2C_8H_2O_6$ ) is described. MOF-74-Zn was synthesised from an existing mechanochemical method and its properties characterised by ChemBET surface area analysis and SEM and compared to conventionally synthesised MOF-74-Zn reported in literature. The results indicated that the BET surface area of the mechanochemically synthesised samples was consistent with the reported solvothermally synthesised MOF-74 values. Unsurprisingly, the particle size of mechanochemically synthesised MOF-74-Zn were found to be significantly smaller than solvothermally synthesised MOF-74-Zn. It was found that the

mechanochemically synthesised MOF particle sizes were influenced by the particle size of the starting materials, namely the zinc oxide, allowing for synthesis of MOF-74 with particle sizes as small as 200 nm synthesised using 100 nm zinc oxide.

Furthermore, several new MOF-74 crystalline intermediate structures were found and solved using a combination of powder X-ray and single-crystal X-ray diffraction structure solution. Three novel crystal structures have been solved:  $C_{14}H_{20}N_2O_8$ , and two polymorphs of  $C_{14}H_{22}N_2O_{10}Zn$ . These solved structures showed a clear progression through the reaction as intermediates transitioned from a DMF solvate of  $H_4DHTA$  to 1D coordination polymers involving the zinc. Investigation of the progression of intermediates revealed that the solvation of the linker is a very important step in the mechanochemical synthesis as MOF-74 does not form when no solvent is used. A final intermediate has been indexed, but yet to be solved. Examination of the final intermediate's unit cell suggests the intermediate could also be a porous structure.

Chapter 4 reports the loading of MOF-74-Zn with ibuprofen for the first time. Several analytical techniques were used to measure both the rate of ibuprofen uptake as well as maximum loading. UV-Vis spectroscopy was used to measure both the rate and maximum loading which suggested the maximum ibuprofen loading was 0.29 g/g (g of ibuprofen per g of MOF-74); it was found that the ibuprofen reached 80% of its maximum loading in only three hours, but the loading continued throughout a full 100 hours in the experiment. This ibuprofen loading value exceeds the reported ibuprofen values of MOF-74-Fe and MOF-74-Ni. The surface interactions of ibuprofen and MOF were examined using solid-state NMR and inelastic neutron spectroscopy. Analysis of the results indicates that the ibuprofen has extensive interactions with the surface of the MOF similar to the ibuprofen-surface interactions found in porous silica materials with

ibuprofen carboxylic acid functionality interacting most significantly to the porous materials surface.<sup>85</sup>

Chapter 5 presents the mechanochemical synthesis of a novel isoreticular MOF-74 framework based on the VNU-74 family of frameworks. This is the first reported synthesis of VNU-II-74-Zn (IR-MOF-74-Zn) through any synthesis method. Finding the reaction parameters that would actually synthesis IR-MOF-74-Zn was a challenge which involved permuting nearly all the reaction parameters. The synthesis method is very similar to the mechanochemical synthesis of MOF-74-Zn. The framework has a suggested as-synthesised formula of  $Zn_2(ODA)(DMF)_2(NH_3)_{2.5}(H_2O)_2$  with the DMF,  $NH_3$ , and  $H_2O$  being solvents present in the pores. The presence of  $NH_3$  is justified by the breakdown of DMF in acidic conditions during the mechanochemical synthesis. Attempts to activate IR-MOF-74-Zn have so far been unsuccessful using solvent exchange and vacuum oven as tested using ChemBET surface area analysis. The stability of IR-MOF-74-Zn in various solvents has been investigated using powder X-ray diffraction. IR-MOF-74-Zn was found to be most stable in DMF and hexane.

Chapter 6 presents four novel crystal structures which were solved as part of the synthesis of MOF-74-Zn and IR-MOF-74-Zn. The crystal structures of 2,5-dihydroxyterephthalic acid ( $C_8H_6O_6$ ) and its potassium salt ( $C_8H_6O_6K(H_2O)$ ) are reported. Additionally, the crystal structure of the DMF solvate of 4,4'-oxalylbis(imino)]bis(2-hydroxybenzoic acid ( $C_{16}H_{12}N_2O_8(C_3H_7O)_2$ ) and its zinc paddlewheel coordination polymer ( $Zn_2(C_2H_3O_2)_2C_{16}H_{12}N_2O_8(C_3H_7O)_2$ ) have also been reported and characterised.

## 7.2 Future work

Several MOF-74 and IR-MOF-74 intermediates were found and discussed in this thesis; however, only half of the crystal structures have been solved so far. Further structure solution would most likely require the growth of single-crystals of the intermediate phases, meaning solvothermal synthesis would likely be required. In particular, the IR-MOF-74-Zn intermediates have such large unit-cells that structure solution using the powder diffraction structure solution methods outlined in this thesis are not viable.

MOF-74-Zn was successfully loaded with ibuprofen with several pieces of compelling evidence including CHN elemental analysis, SS-NMR, UV-Vis spectroscopy, and INS spectroscopy all supporting ibuprofen being present in the MOF sample. Ibuprofen unloading was, however, not successfully presented as the framework decayed in phosphate buffer solution making detection of ibuprofen concentration impossible with UV-Vis spectroscopy alone. To circumvent this issue, HPLC connected to UV-VIS could be a credible strategy to separate H<sub>4</sub>DHTA and ibuprofen UV-Vis signals.

While IR-MOF-74-Zn has been successfully synthesised using a mechanochemical method, the exact crystal structure has not been solved. The technique used for creating crystal structures for other isorecticular MOF-74 frameworks involved creating simulated models of the framework and minimising their energy using DFT methods.<sup>94, 180</sup> This method could be applied to the IR-MOF-74-Zn framework for the purposes of solving the crystal structure, direct solvothermal synthesis of the framework is also an option.

Activation of the IR-MOF-74-Zn framework is also required as the potential surface area is totally inaccessible in its current state. Attempts to activate the framework described in this thesis were unsuccessful and resulted in the collapse of the framework, however, other activation methods exist which are better suited to unstable frameworks. The

method which will probably have the highest chance of success is supercritical CO<sub>2</sub> extraction which has been used in multiple instances of difficult to activate frameworks.<sup>122, 123, 199</sup> After activation ChemBET could then be used to measure the internal surface area of the IR-MOF-74-Zn framework.

## References

1. Ferey, G., Hybrid porous solids: past, present, future. *Chemical Society Reviews* **2008**, *37* (1), 191-214.
2. Kitagawa, S.; Kitaura, R.; Noro, S., Functional porous coordination polymers. *Angewandte Chemie-International Edition* **2004**, *43* (18), 2334-2375.
3. Groom, C. R.; Bruno, I. J.; Lightfoot, M. P.; Ward, S. C., The Cambridge Structural Database. *Acta Crystallographica Section B-Structural Science Crystal Engineering and Materials* **2016**, *72*, 171-179.
4. Kaye, S. S.; Dailly, A.; Yaghi, O. M.; Long, J. R., Impact of preparation and handling on the hydrogen storage properties of Zn<sub>4</sub>O(1,4-benzenedicarboxylate)<sub>3</sub> (MOF-5). *Journal of the American Chemical Society* **2007**, *129* (46), 14176-14186.
5. An, J.; Farha, O. K.; Hupp, J. T.; Pohl, E.; Yeh, J. I.; Rosi, N. L., Metal-adeninate vertices for the construction of an exceptionally porous metal-organic framework. *Nature Communications* **2012**, *3*, 604.
6. Chui, S. S. Y.; Lo, S. M. F.; Charmant, J. P. H.; Orpen, A. G.; Williams, I. D., A chemically functionalizable nanoporous material Cu-3(TMA)<sub>2</sub>(H<sub>2</sub>O)<sub>3</sub> (n). *Science* **1999**, *283* (5405), 1148-1150.
7. Zhang, C. F.; Qiu, L. G.; Ke, F.; Zhu, Y. J.; Yuan, Y. P.; Xu, G. S.; Jiang, X., A novel magnetic recyclable photocatalyst based on a core-shell metal-organic framework Fe<sub>3</sub>O<sub>4</sub>@MIL-100(Fe) for the decolorization of methylene blue dye. *Journal of Materials Chemistry A* **2013**, *1* (45), 14329-14334.
8. Cavka, J. H.; Jakobsen, S.; Olsbye, U.; Guillou, N.; Lamberti, C.; Bordiga, S.; Lillerud, K. P., A new zirconium inorganic building brick forming metal organic frameworks with exceptional stability. *Journal of the American Chemical Society* **2008**, *130* (42), 13850-13851.
9. Honicke, I. M.; Senkovska, I.; Bon, V.; Baburin, I. A.; Bonisch, N.; Raschke, S.; Evans, J. D.; Kaskel, S., Balancing Mechanical Stability and Ultrahigh Porosity in Crystalline Framework Materials. *Angewandte Chemie-International Edition* **2018**, *57* (42), 13780-13783.
10. An, J. Y.; Shade, C. M.; Chengelis-Czegan, D. A.; Petoud, S.; Rosi, N. L., Zinc-Adeninate Metal-Organic Framework for Aqueous Encapsulation and Sensitization of Near-infrared and Visible Emitting Lanthanide Cations. *Journal of the American Chemical Society* **2011**, *133* (5), 1220-1223.
11. Liu, L.; Wang, J. C.; Xu, C. Y.; Zhang, Y. Q.; Li, Y.; Li, C. G.; Wang, J. J.; Zhang, Y. P., Six 1D/2D Zinc(II) coordination complexes constructed based on semirigid Bis(dimethylbenzimidazole) ligand and different carboxylates: Syntheses, structures, and photoluminescence properties. *Journal of Molecular Structure* **2019**, *1180*, 7-14.
12. Wang, T.; Zhang, C. X.; Deng, S. J.; Liu, Y. J.; Xiao, W. M.; Zhang, N., A Novel 3D Coordination Polymer Bearing Rare NbO-x-d Subnets: Synthesis, Structure, and Properties. *Journal of Inorganic and Organometallic Polymers and Materials* **2018**, *28* (1), 308-313.
13. Ongari, D.; Tiana, D.; Stoneburner, S. J.; Gagliardi, L.; Smit, B., Origin of the Strong Interaction between Polar Molecules and Copper(II) Paddle-Wheels in Metal Organic Frameworks. *Journal of Physical Chemistry C* **2017**, *121* (28), 15135-15144.
14. Bureekaew, S.; Amirjalayer, S.; Schmid, R., Orbital directing effects in copper and zinc based paddle-wheel metal organic frameworks: the origin of flexibility. *Journal of Materials Chemistry* **2012**, *22* (20), 10249-10254.
15. Gao, W. Y.; Cai, R.; Pham, T.; Forrest, K. A.; Hogan, A.; Nugent, P.; Williams, K.; Wojtas, L.; Luebke, R.; Weselinski, L. J.; Zaworotko, M. J.; Space, B.; Chen, Y. S.; Eddaoudi, M.; Shi, X. D.; Ma, S. Q., Remote Stabilization of Copper Paddlewheel Based Molecular Building Blocks in Metal-Organic Frameworks. *Chemistry of Materials* **2015**, *27* (6), 2144-2151.
16. Eddaoudi, M.; Kim, J.; Rosi, N.; Vodak, D.; Wachter, J.; O'Keeffe, M.; Yaghi, O. M., Systematic design of pore size and functionality in isorecticular MOFs and their application in methane storage. *Science* **2002**, *295* (5554), 469-472.
17. Lock, N.; Wu, Y.; Christensen, M.; Cameron, L. J.; Peterson, V. K.; Bridgeman, A. J.; Kepert, C. J.; Iversen, B. B., Elucidating Negative Thermal Expansion in MOF-5. *Journal of Physical Chemistry C* **2010**, *114* (39), 16181-16186.
18. Macrae, C. F.; Bruno, I. J.; Chisholm, J. A.; Edgington, P. R.; McCabe, P.; Pidcock, E.; Rodriguez-Monge, L.; Taylor, R.; van de Streek, J.; Wood, P. A., Mercury CSD 2.0 - new features for the visualization and investigation of crystal structures. *Journal of Applied Crystallography* **2008**, *41*, 466-470.

19. Dietzel, P. D. C.; Panella, B.; Hirscher, M.; Blom, R.; Fjellvag, H., Hydrogen adsorption in a nickel based coordination polymer with open metal sites in the cylindrical cavities of the desolvated framework. *Chemical Communications* **2006**, (9), 959-961.
20. MOF-74 properties. <https://www.sigmaaldrich.com/technical-documents/articles/materials-science/metal-organic-frameworks/mof-74-zn.html> (accessed 10th December 2019).
21. Park, K. S.; Ni, Z.; Cote, A. P.; Choi, J. Y.; Huang, R. D.; Uribe-Romo, F. J.; Chae, H. K.; O'Keeffe, M.; Yaghi, O. M., Exceptional chemical and thermal stability of zeolitic imidazolate frameworks. *Proceedings of the National Academy of Sciences of the United States of America* **2006**, *103* (27), 10186-10191.
22. ZIF-8 properties. <https://www.sigmaaldrich.com/technical-documents/articles/materials-science/metal-organic-frameworks/zif-8.html> (accessed 10th December 2019).
23. Yang, Q. Y.; Wiersum, A. D.; Jobic, H.; Guillerm, V.; Serre, C.; Llewellyn, P. L.; Maurin, G., Understanding the Thermodynamic and Kinetic Behavior of the CO<sub>2</sub>/CH<sub>4</sub> Gas Mixture within the Porous Zirconium Terephthalate UiO-66(Zr): A Joint Experimental and Modeling Approach. *Journal of Physical Chemistry C* **2011**, *115* (28), 13768-13774.
24. Xiang, S. C.; Zhou, W.; Gallegos, J. M.; Liu, Y.; Chen, B. L., Exceptionally High Acetylene Uptake in a Microporous Metal-Organic Framework with Open Metal Sites. *Journal of the American Chemical Society* **2009**, *131* (34), 12415-12419.
25. Dhakshinamoorthy, A.; Alvaro, M.; Garcia, H., Claisen-Schmidt Condensation Catalyzed by Metal-Organic Frameworks. *Advanced Synthesis & Catalysis* **2010**, *352* (4), 711-717.
26. Liu, J. C.; Culp, J. T.; Natesakhawat, S.; Bockrath, B. C.; Zande, B.; Sankar, S. G.; Garberoglio, G.; Johnson, J. K., Experimental and theoretical studies of gas adsorption in Cu-3(BTC)(2): An effective activation procedure. *Journal of Physical Chemistry C* **2007**, *111* (26), 9305-9313.
27. Serre, C.; Millange, F.; Thouvenot, C.; Nogues, M.; Marsolier, G.; Louer, D.; Ferey, G., Very large breathing effect in the first nanoporous chromium(III)-based solids: MIL-53 or Cr-III(OH)(O<sub>2</sub>C-C<sub>6</sub>H<sub>4</sub>-CO<sub>2</sub>)-(HO<sub>2</sub>C-C<sub>6</sub>H<sub>4</sub>-CO<sub>2</sub>H)<sub>x</sub>(H<sub>2</sub>O)<sub>y</sub>. *Journal of the American Chemical Society* **2002**, *124* (45), 13519-13526.
28. Loiseau, T.; Serre, C.; Huguénard, C.; Fink, G.; Taulelle, F.; Henry, M.; Bataille, T.; Ferey, G., A rationale for the large breathing of the porous aluminum terephthalate (MIL-53) upon hydration. *Chemistry-a European Journal* **2004**, *10* (6), 1373-1382.
29. Guo, Y. Y.; Zhang, J.; Dong, L. Z.; Xu, Y.; Han, W.; Fang, M.; Liu, H. K.; Wu, Y.; Lan, Y. Q., Syntheses of Exceptionally Stable Aluminum(III) Metal-Organic Frameworks: How to Grow High-Quality, Large, Single Crystals. *Chemistry-a European Journal* **2017**, *23* (61), 15518-15528.
30. Lin, K. S.; Adhikari, A. K.; Tu, M. T.; Wang, C. H.; Chiang, C. L., Preparation, Characterization, and Hydrogen Storage Capacity of MIL-53 Metal-Organic Frameworks. *Journal of Nanoscience and Nanotechnology* **2013**, *13* (4), 2549-2556.
31. Llewellyn, P. L.; Bourrelly, S.; Serre, C.; Vimont, A.; Daturi, M.; Hamon, L.; De Weireld, G.; Chang, J. S.; Hong, D. Y.; Hwang, Y. K.; Jung, S. H.; Ferey, G., High uptakes of CO<sub>2</sub> and CH<sub>4</sub> in mesoporous metal-organic frameworks MIL-100 and MIL-101. *Langmuir* **2008**, *24* (14), 7245-7250.
32. Liang, R. W.; Chen, R.; Jing, F. F.; Qin, N.; Wu, L., Multifunctional polyoxometalates encapsulated in MIL-100(Fe): highly efficient photocatalysts for selective transformation under visible light. *Dalton Transactions* **2015**, (41), 18227-18236.
33. Gersten, B. *Chemfiles Volume 5 article 13*, <http://www.sigmaaldrich.com/technical-documents/articles/chemfiles/solvothermal-synthesis.html>, (accessed 21<sup>st</sup> August 2019)
34. Oregon State University autoclave training course. <https://chemsafety.chem.oregonstate.edu/content/osp-autoclave-hydrothermal-experiments> (accessed 15/11/2019).
35. Zhang, H.; Zhong, J.; Zhou, G. X.; Wu, J. L.; Yang, Z. Y.; Shi, X. M., Microwave-Assisted Solvent-Free Synthesis of Zeolitic Imidazolate Framework-67. *Journal of Nanomaterials* **2016**, 48386-48386.
36. Tranchemontagne, D. J.; Hunt, J. R.; Yaghi, O. M., Room temperature synthesis of metal-organic frameworks: MOF-5, MOF-74, MOF-177, MOF-199, and IRMOF-0. *Tetrahedron* **2008**, *64* (36), 8553-8557.
37. James, S. L.; Adams, C. J.; Bolm, C.; Braga, D.; Collier, P.; Friscic, T.; Grepioni, F.; Harris, K. D. M.; Hyett, G.; Jones, W.; Krebs, A.; Mack, J.; Maini, L.; Orpen, A. G.; Parkin, I. P.; Shearouse, W. C.; Steed, J. W.; Waddell, D. C., Mechanochemistry: opportunities for new and cleaner synthesis. *Chemical Society Reviews* **2012**, *41* (1), 413-447.
38. D., M. A.; A., W., *IUPAC. Compendium of Chemical Terminology, 2nd ed. (the "Gold Book")*. 1997.
39. Friscic, T., New opportunities for materials synthesis using mechanochemistry. *Journal of Materials Chemistry* **2010**, *20* (36), 7599-7605.



40. Pilloni, M.; Padella, F.; Ennas, G.; Lai, S. R.; Bellusci, M.; Rombi, E.; Sini, F.; Pentimalli, M.; Delitala, C.; Scano, A.; Cabras, V.; Ferino, I., Liquid-assisted mechanochemical synthesis of an iron carboxylate Metal Organic Framework and its evaluation in diesel fuel desulfurization. *Microporous and Mesoporous Materials* **2015**, *213*, 14-21.
41. Do, J. L.; Friscic, T., Mechanochemistry: A Force of Synthesis. *Acs Central Science* **2017**, *3* (1), 13-19.
42. Julien, P. A.; Uzarevic, K.; Katsenis, A. D.; Kimber, S. A. J.; Wang, T.; Farha, O. K.; Zhang, Y. C.; Casaban, J.; Germann, L. S.; Etter, M.; Dinnebier, R. E.; James, S. L.; Halasz, I.; Friscic, T., In Situ Monitoring and Mechanism of the Mechanochemical Formation of a Microporous MOF-74 Framework. *Journal of the American Chemical Society* **2016**, *138* (9), 2929-2932.
43. Uzarevic, K.; Halasz, I.; Friscic, T., Real-Time and In Situ Monitoring of Mechanochemical Reactions: A New Playground for All Chemists. *Journal of Physical Chemistry Letters* **2015**, *6* (20), 4129-4140.
44. Batzdorf, L.; Fischer, F.; Wilke, M.; Wenzel, K. J.; Emmerling, F., Direct In Situ Investigation of Milling Reactions Using Combined X-ray Diffraction and Raman Spectroscopy. *Angewandte Chemie-International Edition* **2015**, *54* (6), 1799-1802.
45. Lukin, S.; Stolar, T.; Tireli, M.; Blanco, M. V.; Babic, D.; Friscic, T.; Uzarevic, K.; Halasz, I., Tandem In Situ Monitoring for Quantitative Assessment of Mechanochemical Reactions Involving Structurally Unknown Phases. *Chemistry-a European Journal* **2017**, *23* (56), 13941-13949.
46. Wang, G. W., Mechanochemical organic synthesis. *Chemical Society Reviews* **2013**, *42* (18), 7668-7700.
47. Belsky, A.; Hellenbrandt, M.; Karen, V. L.; Luksch, P., New developments in the Inorganic Crystal Structure Database (ICSD): accessibility in support of materials research and design. *Acta Crystallographica Section B-Structural Science* **2002**, *58*, 364-369.
48. Mueller, U.; Schubert, M.; Teich, F.; Puetter, H.; Schierle-Arndt, K.; Pastre, J., Metal-organic frameworks - prospective industrial applications. *Journal of Materials Chemistry* **2006**, *16* (7), 626-636.
49. Reinsch, H.; Waitschat, S.; Chavan, S. M.; Lillerud, K. P.; Stock, N., A Facile "Green" Route for Scalable Batch Production and Continuous Synthesis of Zirconium MOFs. *European Journal of Inorganic Chemistry* **2016**, (27), 4490-4498.
50. Taddei, M.; Steitz, D. A.; van Bokhoven, J. A.; Ranocchiari, M., Continuous-Flow Microwave Synthesis of Metal-Organic Frameworks: A Highly Efficient Method for Large-Scale Production. *Chemistry-a European Journal* **2016**, *22* (10), 3245-3249.
51. Klinowski, J.; Paz, F. A. A.; Silva, P.; Rocha, J., Microwave-Assisted Synthesis of Metal-Organic Frameworks. *Dalton Transactions* **2011**, *40* (2), 321-330.
52. de la Hoz, A.; Diaz-Ortiz, A.; Moreno, A., Microwaves in organic synthesis. Thermal and non-thermal microwave effects. *Chemical Society Reviews* **2005**, *34* (2), 164-178.
53. Ren, J. W.; Segakweng, T.; Langmi, H. W.; Musyoka, N. M.; North, B. C.; Mathe, M.; Bessarabov, D., Microwave-assisted modulated synthesis of zirconium-based metal-organic framework (Zr-MOF) for hydrogen storage applications. *International Journal of Materials Research* **2014**, *105* (5), 516-519.
54. Jhung, S. H.; Lee, J. H.; Yoon, J. W.; Serre, C.; Ferey, G.; Chang, J. S., Microwave synthesis of chromium terephthalate MIL-101 and its benzene sorption ability. *Advanced Materials* **2007**, *19* (1), 121-124.
55. Albuquerque, G. H.; Fitzmorris, R. C.; Ahmadi, M.; Wannemacher, N.; Thallapally, P. K.; McGrail, B. P.; Herman, G. S., Gas-liquid segmented flow microwave-assisted synthesis of MOF-74(Ni) under moderate pressures. *Crystengcomm* **2015**, *17* (29), 5502-5510.
56. Ren, J. W.; Dyosiba, X.; Musyoka, N. M.; Langmi, H. W.; Mathe, M.; Liao, S. J., Review on the current practices and efforts towards pilot-scale production of metal-organic frameworks (MOFs). *Coordination Chemistry Reviews* **2017**, *352*, 187-219.
57. Sigma Aldrich. <http://www.sigmaaldrich.com/>.
58. MOF technologies. <https://www.moftechnologies.com/manufacturing/> (accessed 25th November 2019).
59. Strem Chemicals. [https://www.strem.com/uploads/resources/documents/catalog\\_26\\_2017-2019\\_.pdf](https://www.strem.com/uploads/resources/documents/catalog_26_2017-2019_.pdf) (accessed 25th November 2019).
60. Promethean particles. <http://www.prometheanparticles.co.uk>.
61. Lu, K. D.; Aung, T.; Guo, N. N.; Weichselbaum, R.; Lin, W. B., Nanoscale Metal-Organic Frameworks for Therapeutic, Imaging, and Sensing Applications. *Advanced Materials* **2018**, *30* (37), 20.

62. Espallargas, G. M.; Coronado, E., Magnetic functionalities in MOFs: from the framework to the pore. *Chemical Society Reviews* **2018**, *47* (2), 533-557.
63. Sun, C. Y.; Wang, X. L.; Zhang, X.; Qin, C.; Li, P.; Su, Z. M.; Zhu, D. X.; Shan, G. G.; Shao, K. Z.; Wu, H.; Li, J., Efficient and tunable white-light emission of metal-organic frameworks by iridium-complex encapsulation. *Nature Communications* **2013**, *4*, 2717.
64. He, H. M.; Sun, F. X.; Borjigin, T.; Zhao, N.; Zhu, G. S., Tunable colors and white-light emission based on a microporous luminescent Zn(II)-MOF. *Dalton Transactions* **2014**, *43* (9), 3716-3721.
65. Liu, X. C.; Zhou, Y. Y.; Zhang, J. C.; Tang, L.; Luo, L.; Zeng, G. M., Iron Containing Metal-Organic Frameworks: Structure, Synthesis, and Applications in Environmental Remediation. *Acs Applied Materials & Interfaces* **2017**, *9* (24), 20255-20275.
66. Wang, C. C.; Li, J. R.; Lv, X. L.; Zhang, Y. Q.; Guo, G. S., Photocatalytic organic pollutants degradation in metal-organic frameworks. *Energy & Environmental Science* **2014**, *7* (9), 2831-2867.
67. Wang, H.; Yuan, X. Z.; Wu, Y.; Chen, X. H.; Leng, L. J.; Zeng, G. M., Photodeposition of metal sulfides on titanium metal-organic frameworks for excellent visible-light-driven photocatalytic Cr(VI) reduction. *Rsc Advances* **2015**, *5* (41), 32531-32535.
68. Liang, R. W.; Jing, F. F.; Shen, L. J.; Qin, N.; Wu, L., M@MIL-100(Fe) (M = Au, Pd, Pt) nanocomposites fabricated by a facile photodeposition process: Efficient visible-light photocatalysts for redox reactions in water. *Nano Research* **2015**, *8* (10), 3237-3249.
69. Shen, L. J.; Liang, S. J.; Wu, W. M.; Liang, R. W.; Wu, L., Multifunctional NH<sub>2</sub>-mediated zirconium metal-organic framework as an efficient visible-light-driven photocatalyst for selective oxidation of alcohols and reduction of aqueous Cr(VI). *Dalton Transactions* **2013**, *42* (37), 13649-13657.
70. Wang, H.; Yuan, X. Z.; Wu, Y.; Zeng, G. M.; Chen, X. H.; Leng, L. J.; Wu, Z. B.; Jiang, L. B.; Li, H., Facile synthesis of amino-functionalized titanium metal-organic frameworks and their superior visible-light photocatalytic activity for Cr(VI) reduction. *Journal of Hazardous Materials* **2015**, *286*, 187-194.
71. Bai, Z. Q.; Yuan, L. Y.; Zhu, L.; Liu, Z. R.; Chu, S. Q.; Zheng, L. R.; Zhang, J.; Chai, Z. F.; Shi, W. Q., Introduction of amino groups into acid-resistant MOFs for enhanced U(VI) sorption. *Journal of Materials Chemistry A* **2015**, *3* (2), 525-534.
72. Howarth, A. J.; Katz, M. J.; Wang, T. C.; Platero-Prats, A. E.; Chapman, K. W.; Hupp, J. T.; Farha, O. K., High Efficiency Adsorption and Removal of Selenate and Selenite from Water Using Metal-Organic Frameworks. *Journal of the American Chemical Society* **2015**, *137* (23), 7488-7494.
73. Zhang, N.; Yuan, L. Y.; Guo, W. L.; Luo, S. Z.; Chai, Z. F.; Shi, W. Q., Extending the Use of Highly Porous and Functionalized MOFs to Th(IV) Capture. *Acs Applied Materials & Interfaces* **2017**, *9* (30), 25216-25224.
74. Ma, S. Q.; Zhou, H. C., Gas storage in porous metal-organic frameworks for clean energy applications. *Chemical Communications* **2010**, *46* (1), 44-53.
75. Zhou, W.; Wu, H.; Yildirim, T., Enhanced H<sub>2</sub> Adsorption in Isostructural Metal-Organic Frameworks with Open Metal Sites: Strong Dependence of the Binding Strength on Metal Ions. *Journal of the American Chemical Society* **2008**, *130* (46), 15268-15269.
76. Ahmed, A.; Liu, Y. Y.; Purewal, J.; Tran, L. D.; Wong-Foy, A. G.; Veenstra, M.; Matzger, A. J.; Siegel, D. J., Balancing gravimetric and volumetric hydrogen density in MOFs. *Energy & Environmental Science* **2017**, *10* (11), 2459-2471.
77. Xiao, B.; Wheatley, P. S.; Zhao, X. B.; Fletcher, A. J.; Fox, S.; Rossi, A. G.; Megson, I. L.; Bordiga, S.; Regli, L.; Thomas, K. M.; Morris, R. E., High-capacity hydrogen and nitric oxide adsorption and storage in a metal-organic framework. *Journal of the American Chemical Society* **2007**, *129* (5), 1203-1209.
78. Adhikari, A. K.; Lin, K. S., Synthesis, Fine Structural Characterization, and CO<sub>2</sub> Adsorption Capacity of Metal Organic Frameworks-74. *Journal of Nanoscience and Nanotechnology* **2014**, *14* (4), 2709-2717.
79. An, J.; Geib, S. J.; Rosi, N. L., High and Selective CO<sub>2</sub> Uptake in a Cobalt Adeninate Metal-Organic Framework Exhibiting Pyrimidine- and Amino-Decorated Pores. *Journal of the American Chemical Society* **2010**, *132* (1), 38-39.
80. Dietzel, P. D. C.; Johnsen, R. E.; Fjellvag, H.; Bordiga, S.; Groppo, E.; Chavan, S.; Blom, R., Adsorption properties and structure of CO<sub>2</sub> adsorbed on open coordination sites of metal-organic framework Ni<sub>2</sub>(dhtp) from gas adsorption, IR spectroscopy and X-ray diffraction. *Chemical Communications* **2008**, (41), 5125-5127.

81. Caskey, S. R.; Wong-Foy, A. G.; Matzger, A. J., Dramatic tuning of carbon dioxide uptake via metal substitution in a coordination polymer with cylindrical pores. *Journal of the American Chemical Society* **2008**, *130* (33), 10870-10871.
82. Wu, M. X.; Yang, Y. W., Metal-Organic Framework (MOF)-Based Drug/Cargo Delivery and Cancer Therapy. *Advanced Materials* **2017**, *29* (23), 20-28.
83. Horcajada, P.; Serre, C.; Vallet-Regi, M.; Sebban, M.; Taulelle, F.; Ferey, G., Metal-organic frameworks as efficient materials for drug delivery. *Angewandte Chemie-International Edition* **2006**, *45* (36), 5974-5978.
84. Vilaca, N.; Amorim, R.; Machado, A. F.; Parpot, P.; Pereira, M. F. R.; Sardo, M.; Rocha, J.; Fonseca, A. M.; Neves, I. C.; Baltazar, F., Potentiation of 5-fluorouracil encapsulated in zeolites as drug delivery systems for in vitro models of colorectal carcinoma. *Colloids and Surfaces B-Biointerfaces* **2013**, *112*, 237-244.
85. Qian, K. K.; Zhou, W.; Xu, X. M.; Udovic, T. J., Characterization of Medicinal Compounds Confined in Porous Media by Neutron Vibrational Spectroscopy and First-Principles Calculations: A Case Study with Ibuprofen. *Pharmaceutical Research* **2012**, *29* (9), 2432-2444.
86. Liechty, W. B.; Kryscio, D. R.; Slaughter, B. V.; Peppas, N. A., Polymers for Drug Delivery Systems. In *Annual Review of Chemical and Biomolecular Engineering, Vol 1*, Prausnitz, J. M.; Doherty, M. F.; Segalman, R. A., Eds. Annual Reviews: Palo Alto, 2010; Vol. 1, pp 149-173.
87. Oh, H.; Li, T.; An, J., Drug Release Properties of a Series of Adenine-Based Metal-Organic Frameworks. *Chemistry-a European Journal* **2015**, *21* (47), 17010-17015.
88. Cunha, D.; Ben Yahia, M.; Hall, S.; Miller, S. R.; Chevreau, H.; Elkaim, E.; Maurin, G.; Horcajada, P.; Serre, C., Rationale of Drug Encapsulation and Release from Biocompatible Porous Metal-Organic Frameworks. *Chemistry of Materials* **2013**, *25* (14), 2767-2776.
89. Tan, L. L.; Li, H. W.; Zhou, Y.; Zhang, Y. Y.; Feng, X.; Wang, B.; Yang, Y. W., Zn<sup>2+</sup>-Triggered Drug Release from Biocompatible Zirconium MOFs Equipped with Supramolecular Gates. *Small* **2015**, *11* (31), 3807-3813.
90. Hu, Q.; Yu, J. C.; Liu, M.; Liu, A. P.; Dou, Z. S.; Yang, Y., A Low Cytotoxic Cationic Metal-Organic Framework Carrier for Controllable Drug Release. *Journal of Medicinal Chemistry* **2014**, *57* (13), 5679-5685.
91. McKinlay, A.; thesis for Chemistry, P. New Nitric Oxide Releasing Materials. University of St. Andrews, 2010.
92. Gomar, M.; Yeganegi, S., Adsorption of 5-fluorouracil, hydroxyurea and mercaptopurine drugs on zeolitic imidazolate frameworks (ZIF-7, ZIF-8 and ZIF-9). *Microporous and Mesoporous Materials* **2017**, *252*, 167-172.
93. Horcajada, P.; Chalati, T.; Serre, C.; Gillet, B.; Sebrie, C.; Baati, T.; Eubank, J. F.; Heurtaux, D.; Clayette, P.; Kreuz, C.; Chang, J. S.; Hwang, Y. K.; Marsaud, V.; Bories, P. N.; Cynober, L.; Gil, S.; Ferey, G.; Couvreur, P.; Gref, R., Porous metal-organic-framework nanoscale carriers as a potential platform for drug delivery and imaging. *Nature Materials* **2010**, *9* (2), 172-178.
94. Levine, D. J.; Runcevski, T.; Kapelewski, M. T.; Keitz, B. K.; Oktawiec, J.; Reed, D. A.; Mason, J. A.; Jiang, H. Z. H.; Colwell, K. A.; Legendre, C. M.; FitzGerald, S. A.; Long, J. R., Olsalazine-Based Metal-Organic Frameworks as Biocompatible Platforms for H<sub>2</sub> Adsorption and Drug Delivery. *Journal of the American Chemical Society* **2016**, *138* (32), 10143-10150.
95. Lu, K. D.; He, C. B.; Guo, N. N.; Chan, C.; Ni, K. Y.; Weichselbaum, R. R.; Lin, W. B., Chlorin-Based Nanoscale Metal-Organic Framework Systemically Rejects Colorectal Cancers via Synergistic Photodynamic Therapy and Checkpoint Blockade Immunotherapy. *Journal of the American Chemical Society* **2016**, *138* (38), 12502-12510.
96. Wu, W.; Perrin-Sarrado, C.; Lartaud, I.; Sapin-Minet, A.; Gaucher, C., Polymer nanocomposites enhance GSNO intestinal absorption and promotes the formation of releasable nitric oxide stores in rat aorta. *Fundamental & Clinical Pharmacology* **2016**, *30*, 1795-1803.
97. Cattaneo, D.; Warrender, S. J.; Duncan, M. J.; Castledine, R.; Parkinson, N.; Haley, I.; Morris, R. E., Water based scale-up of CPO-27 synthesis for nitric oxide delivery. *Dalton Transactions* **2016**, *45* (2), 618-629.
98. Sagir, T.; Huysal, M.; Durmus, Z.; Kurt, B. Z.; Senel, M.; Isik, S., Preparation and in vitro evaluation of 5-fluorouracil loaded magnetite-zeolite nanocomposite (5-FU-MZNC) for cancer drug delivery applications. *Biomedicine & Pharmacotherapy* **2016**, *77*, 182-190.

99. Salleh, N.; Jais, U. S.; Sarijo, S. H.; Ieee, Gelatin-Coated Zeolite Y For Controlled Release of Anticancer Drug (Zerumbone). *Ieee Symposium on Business, Engineering and Industrial Applications (Isbeia 2012)* **2012**, 124-129.
100. de Gennaro, B.; Catalanotti, L.; Cappelletti, P.; Langella, A.; Mercurio, M.; Serri, C.; Biondi, M.; Mayol, L., Surface modified natural zeolite as a carrier for sustained diclofenac release: A preliminary feasibility study. *Colloids and Surfaces B-Biointerfaces* **2015**, *130*, 101-109.
101. Zhou, Y. X.; Quan, G. L.; Wu, Q. L.; Zhang, X. X.; Niu, B. Y.; Wu, B. Y.; Huang, Y.; Pan, X.; Wu, C. B., Mesoporous silica nanoparticles for drug and gene delivery. *Acta Pharmaceutica Sinica B* **2018**, *8* (2), 165-177.
102. Miriyala, N.; Ouyang, D. F.; Perrie, Y.; Lowry, D.; Kirby, D. J., Activated carbon as a carrier for amorphous drug delivery: Effect of drug characteristics and carrier wettability. *European Journal of Pharmaceutics and Biopharmaceutics* **2017**, *115*, 197-205.
103. Hagiwara, A.; Ahn, T.; Ueda, T.; Iwamoto, A.; Torii, T.; Takahashi, T., anticancer agents adsorbed by activated carbon particles, a new form of dosage enhancing efficacy on lymph-nodal metastases. *Anticancer Research* **1986**, *6* (5), 1005-1008.
104. Yadavalli, T.; Ames, J.; Agelidis, A.; Suryawanshi, R.; Jaishankar, D.; Hopkins, J.; Thakkar, N.; Koujah, L.; Shukla, D., Drug-encapsulated carbon (DECON): A novel platform for enhanced drug delivery. *Science Advances* **2019**, *5* (8), 12.
105. Siegel, R. A., hydrophobic weak polyelectrolyte gels - studies of swelling equilibria and kinetics. *Advances in Polymer Science* **1993**, *109*, 233-267.
106. Tanaka, T.; Fillmore, D.; Sun, S. T.; Nishio, I.; Swislow, G.; Shah, A., PHASE-TRANSITIONS IN IONIC GELS. *Physical Review Letters* **1980**, *45* (20), 1636-1639.
107. Chen, G. H.; Hoffman, A. S., graft-copolymers that exhibit temperature-induced phase-transitions over a wide-range of ph. *Nature* **1995**, *373* (6509), 49-52.
108. Schmaljohann, D., Thermo- and pH-responsive polymers in drug delivery. *Advanced Drug Delivery Reviews* **2006**, *58* (15), 1655-1670.
109. Mellot-Draznieks, C.; Dutour, J.; Ferey, G. R., Hybrid organic-inorganic frameworks: Routes for computational design and structure prediction. *Angewandte Chemie-International Edition* **2004**, *43* (46), 6290-6296.
110. Rosi, N. L.; Kim, J.; Eddaoudi, M.; Chen, B. L.; O'Keeffe, M.; Yaghi, O. M., Rod packings and metal-organic frameworks constructed from rod-shaped secondary building units. *Journal of the American Chemical Society* **2005**, *127* (5), 1504-1518.
111. Cadot, S.; Veyre, L.; Luneau, D.; Farrusseng, D.; Quadrelli, E. A., A water-based and high space-time yield synthetic route to MOF Ni-2(dhtp) and its linker 2,5-dihydroxyterephthalic acid. *Journal of Materials Chemistry A* **2014**, *2* (42), 17757-17763.
112. Dietzel, P. D. C.; Blom, R.; Fjellvag, H., Base-induced formation of two magnesium metal-organic framework compounds with a bifunctional tetratopic ligand. *European Journal of Inorganic Chemistry* **2008**, *1* (23), 3624-3632.
113. Diaz-Garcia, M.; Mayoral, A.; Diaz, I.; Sanchez-Sanchez, M., Nanoscaled M-MOF-74 Materials Prepared at Room Temperature. *Crystal Growth & Design* **2014**, *14* (5), 2479-2487.
114. Dietzel, P. D. C.; Morita, Y.; Blom, R.; Fjellvag, H., An in situ high-temperature single-crystal investigation of a dehydrated metal-organic framework compound and field-induced magnetization of one-dimensional metal-oxo chains. *Angewandte Chemie-International Edition* **2005**, *44* (39), 6354-6358.
115. Bhattacharjee, S.; Choi, J. S.; Yang, S. T.; Choi, S. B.; Kim, J.; Ahn, W. S., Solvothermal Synthesis of Fe-MOF-74 and Its Catalytic Properties in Phenol Hydroxylation. *Journal of Nanoscience and Nanotechnology* **2010**, *10* (1), 135-141.
116. Wang, L. J.; Deng, H. X.; Furukawa, H.; Gandara, F.; Cordova, K. E.; Peri, D.; Yaghi, O. M., Synthesis and Characterization of Metal-Organic Framework-74 Containing 2, 4, 6, 8, and 10 Different Metals. *Inorganic Chemistry* **2014**, *53* (12), 5881-5883.
117. Zuluaga, S.; Fuentes-Fernandez, E. M. A.; Tan, K.; Xu, F.; Li, J.; Chabal, Y. J.; Thonhauser, T., Understanding and controlling water stability of MOF-74. *Journal of Materials Chemistry A* **2016**, *4* (14), 5176-5183.
118. Deng, H. X.; Grunder, S.; Cordova, K. E.; Valente, C.; Furukawa, H.; Hmadeh, M.; Gandara, F.; Whalley, A. C.; Liu, Z.; Asahina, S.; Kazumori, H.; O'Keeffe, M.; Terasaki, O.; Stoddart, J. F.; Yaghi, O. M., Large-Pore Apertures in a Series of Metal-Organic Frameworks. *Science* **2012**, *336* (6084), 1018-1023.

119. Gheorghe, A.; Imaz, I.; van der Vlugt, J. I.; Maspoch, D.; Tanase, S., Tuning the supramolecular isomerism of MOF-74 by controlling the synthesis conditions. *Dalton Transactions* **2019**, 48 (27), 10043-10050.
120. Luo, F.; Yan, C. S.; Dang, L. L.; Krishna, R.; Zhou, W.; Wu, H.; Dong, X. L.; Han, Y.; Hu, T. L.; O'Keeffe, M.; Wang, L. L.; Luo, M. B.; Lin, R. B.; Chen, B. L., UTSA-74: A MOF-74 Isomer with Two Accessible Binding Sites per Metal Center for Highly Selective Gas Separation. *Journal of the American Chemical Society* **2016**, 138 (17), 5678-5684.
121. Sun, Y. J.; Zhou, H. C., Recent progress in the synthesis of metal-organic frameworks. *Science and Technology of Advanced Materials* **2015**, 16 (5), 054202.
122. Mondloch, J. E.; Karagiari, O.; Farha, O. K.; Hupp, J. T., Activation of metal-organic framework materials. *Crystengcomm* **2013**, 15 (45), 9258-9264.
123. Farha, O. K.; Hupp, J. T., Rational Design, Synthesis, Purification, and Activation of Metal-Organic Framework Materials. *Accounts of Chemical Research* **2010**, 43 (8), 1166-1175.
124. Coats, A. W.; Redfern, J. P., Thermogravimetric analysis. A review. In *Analyst*, 1963; Vol. 88, pp 906-924.
125. *T.A. Instruments Universal Analysis user manual*, 1998-1999.
126. Kemp, W., *Organic Spectroscopy*. 3rd ed.; Macmillan Publishing: UK, 1991.
127. *Cary WinUV software*, Agilent Technologies inc: 2002.
128. Parker, S. F.; Lennon, D.; Albers, P. W., Vibrational Spectroscopy with Neutrons: A Review of New Directions. *Applied Spectroscopy* **2011**, 65 (12), 1325-1341.
129. F., P. S., *Encyclopaedia of spectroscopy and spectrometry*. 1999.
130. Parker, S. F.; Carlile, C. J.; Pike, T.; Tomkinson, J.; Newport, R. J.; Andreani, C.; Ricci, F. P.; Sacchetti, F.; Zoppi, M., TOSCA: a world class inelastic neutron spectrometer. *Physica B* **1997**, 241, 154-156.
131. Arnold, O.; Bilheux, J. C.; Borreguero, J. M.; Buts, A.; Campbell, S. I.; Chapon, L.; Doucet, M.; Draper, N.; Leal, R. F.; Gigg, M. A.; Lynch, V. E.; Markvardsen, A.; Mikkelsen, D. J.; Mikkelsen, R. L.; Miller, R.; Palmen, K.; Parker, P.; Passos, G.; Perring, T. G.; Peterson, P. F.; Ren, S.; Reuter, M. A.; Savici, A. T.; Taylor, J. W.; Taylor, R. J.; Tolchenoy, R.; Zhou, W.; Zikoysky, J., Mantid-Data analysis and visualization package for neutron scattering and mu SR experiments. *Nuclear Instruments & Methods in Physics Research Section a-Accelerators Spectrometers Detectors and Associated Equipment* **2014**, 764, 156-166.
132. *Origin*, OriginLab corporation: 2010.
133. Egerton, R. F., *Physical principles of electron microscopy : an introduction to TEM, SEM, and AEM*. Springer 2005.
134. Hammond C., Oxford University Press, *The basics of Crystallography and Diffraction*. 2015.
135. *CrysAlis PRO*, Agilent: 2014. Agilent Technologies Ltd, Yarnton, Oxfordshire, England.
136. *ShelXT*, Sheldrick: 2015.
137. Sheldrick, G. M., ShelXL. *Acta Cryst.*, 2015; Vol. C71, pp 3-8.
138. Dolomanov, O. V.; Bourhis, L. J.; Gildea, R. J.; Howard, J. A. K.; Puschmann, H., OLEX2: a complete structure solution, refinement and analysis program. *Journal of Applied Crystallography* **2009**, 42, 339-341.
139. *CrystalMaker*, Palmer D. C., CrystalMaker Software Ltd, Begbroke, Oxfordshire, England: 2014.
140. Young R.A., Oxford University Press, *The Rietveld Method*. 1995.
141. David, W. I. F.; Shankland, K.; van de Streek, J.; Pidcock, E.; Motherwell, W. D. S.; Cole, J. C., DASH: a program for crystal structure determination from powder diffraction data. *Journal of Applied Crystallography* **2006**, 39, 910-915.
142. Coelho, A. A., TOPAS and TOPAS-Academic: an optimization program integrating computer algebra and crystallographic objects written in C plus. *Journal of Applied Crystallography* **2018**, 51, 210-218.
143. *EVA*, Version 3, Bruker AXS, 1996-2007.
144. Evans, J. S. O., Advanced Input Files & Parametric Quantitative Analysis Using Topas. In *Extending the Reach of Powder Diffraction Modelling by User Defined Macros*, Scardi, P.; Dinnebier, R. E., Eds. Trans Tech Publications Ltd: Stafa-Zurich, 2010; Vol. 651, pp 1-9.
145. Kirkpatrick, S.; Gelatt, C. D.; Vecchi, M. P., Optimization by Simulated Annealing. *Science* **1983**, 220 (4598), 671-680.

146. Altomare, A.; Cuocci, C.; Giacobuzzo, C.; Moliterni, A.; Rizzi, R.; Corriero, N.; Falcicchio, A., EXPO2013: a kit of tools for phasing crystal structures from powder data. *Journal of Applied Crystallography* **2013**, *46*, 1231-1235.
147. Giannozzi, P.; Baroni, S.; Bonini, N.; Calandra, M.; Car, R.; Cavazzoni, C.; Ceresoli, D.; Chiarotti, G. L.; Cococcioni, M.; Dabo, I.; Dal Corso, A.; de Gironcoli, S.; Fabris, S.; Fratesi, G.; Gebauer, R.; Gerstmann, U.; Gougoussis, C.; Kokalj, A.; Lazzeri, M.; Martin-Samos, L.; Marzari, N.; Mauri, F.; Mazzarello, R.; Paolini, S.; Pasquarello, A.; Paulatto, L.; Sbraccia, C.; Scandolo, S.; Sclauzero, G.; Seitsonen, A. P.; Smogunov, A.; Umari, P.; Wentzcovitch, R. M., Quantum Espresso: a modular and open-source software project for quantum simulations of materials. *Journal of Physics-Condensed Matter* **2009**, *21* (39), 19.
148. Dinnebier, R.; Leineweber, A.; Evans, J., *Rietveld Refinement practical powder diffraction pattern analysis using TOPAS*. 3 ed.; Walter de Gruyter GmbH & Co: 2018.
149. Thompson, S. P.; Parker, J. E.; Potter, J.; Hill, T. P.; Birt, A.; Cobb, T. M.; Yuan, F.; Tang, C. C., Beamline I11 at Diamond: A new instrument for high resolution powder diffraction. *Review of Scientific Instruments* **2009**, *80* (7), 075107.
150. Tartoni, N.; Thompson, S. P.; Tang, C. C.; Willis, B. L.; Derbyshire, G. E.; Wright, A. G.; Jaye, S. C.; Homer, J. M.; Pizzev, J. D.; Bell, A. M. T., High-performance X-ray detectors for the new powder diffraction beamline I11 at Diamond. *Journal of Synchrotron Radiation* **2008**, *15*, 43-49.
151. Malvern *Zetasizer software*, 2018.
152. Bruker *TopSpin*, 2019.
153. Sing, K. S. W., Adsorption methods for the characterization of porous materials. *Advances in Colloid and Interface Science* **1998**, *76*, 3-11.
154. Sing, K. S. W.; Everett, D. H.; Haul, R. A. W.; Moscou, L.; Pierotti, R. A.; Rouquerol, J.; Siemieniewska, T., Reporting Physisorption Data for Gas Solid Systems with Special Reference to the Determination of Surface-area and Porosity (Recommendations 1984). *Pure and Applied Chemistry* **1985**, *57* (4), 603-619.
155. Dietzel, P. D. C.; Johnsen, R. E.; Blom, R.; Fjellvag, H., Structural changes and coordinatively unsaturated metal atoms on dehydration of honeycomb analogous microporous metal-organic frameworks. *Chemistry-a European Journal* **2008**, *14* (8), 2389-2397.
156. Glover, T. G.; Peterson, G. W.; Schindler, B. J.; Britt, D.; Yaghi, O., MOF-74 building unit has a direct impact on toxic gas adsorption. *Chemical Engineering Science* **2011**, *66* (2), 163-170.
157. Thommes, M.; Kaneko, K.; Neimark, A. V.; Olivier, J. P.; Rodriguez-Reinoso, F.; Rouquerol, J.; Sing, K. S. W., Physisorption of gases, with special reference to the evaluation of surface area and pore size distribution (IUPAC Technical Report). *Pure and Applied Chemistry* **2015**, *87* (9-10), 1051-1069.
158. Ghermani, N. E.; Morgant, G.; d'Angelo, J.; Desmaele, D.; Fraisse, B.; Bonhomme, F.; Dichi, E.; Sgahier, M., Covalently bonded infinite zigzag chain structure in a novel Zn(II) complex of 2,5-dihydroxy-1,6-benzenedicarboxylic acid. *Polyhedron* **2007**, *26* (12), 2880-2884.
159. Cheng, P.-W.; Cheng, C.-F.; Chun-Ting, Y.; Lin, C.-H., 2,5-Dihydroxyterephthalic acid dihydrate. *Acta Crystallographica Section E* **2010**, *66* (8), o1928.
160. Maximoff, S. N.; Smit, B., Redox chemistry and metal-insulator transitions intertwined in a nanoporous material. *Nature Communications* **2014**, *5*, 4032.
161. Hofmann, D. W. M., Fast estimation of crystal densities. *Acta Crystallographica Section B-Structural Science* **2002**, *58*, 489-493.
162. Sun, H. Y.; Li, X.; Wang, Z. R.; Sun, S. Q.; Li, C. B.; Wang, J. J., Synthesis, Crystal Structure and Theoretical Calculations of Two Zn (II) Coordination Polymers Based on 2,5-Dihydroxyterephthalic Acid. *Journal of Cluster Science* **2018**, *29* (6), 1275-1283.
163. Bhattacharya, B.; Halder, A.; Paul, L.; Chakrabarti, S.; Ghoshal, D., Eye-Catching Dual-Fluorescent Dynamic Metal-Organic Framework Senses Traces of Water: Experimental Findings and Theoretical Correlation. *Chemistry-a European Journal* **2016**, *22* (42), 14998-15005.
164. Zhai, Q. G.; Bu, X. H.; Mao, C. Y.; Zhao, X.; Daemen, L.; Cheng, Y. Q.; Ramirez-Cuesta, A. J.; Feng, P. Y., An ultra-tunable platform for molecular engineering of high-performance crystalline porous materials. *Nature Communications* **2016**, *7*, 13645.
165. Dale, S. H.; Elsegood, M. R. J., Hydrogen-bonding adducts of benzenepolycarboxylic acids with N,N-dimethylformamide: benzene-1,4-dicarboxylic acid N,N-dimethylformamide disolvate, benzene-1,2,4,5-tetracarboxylic acid N,N-dimethylformamide tetrasolvate and benzene-1,2,3-tricarboxylic acid N,N-dimethylformamide disolvate monohydrate. *Acta Crystallographica Section C* **2004**, *60* (6), o444-o448.

166. Ranft, A.; Betzler, S. B.; Haase, F.; Lotsch, B. V., Additive-mediated size control of MOF nanoparticles. *Crystengcomm* **2013**, *15* (45), 9296-9300.
167. Paulet, C.; Loiseau, T.; Ferey, G., Hydrothermal synthesis (in water-dimethylformamide) and crystal structure of MIL-30, a new layered fluorinated gallium phosphate with 1,3-diaminopropane and dimethylamine as templates. *Journal of Materials Chemistry* **2000**, *10* (5), 1225-1229.
168. Gimenez-Marques, M.; Hidalgo, T.; Serre, C.; Horcajada, P., Nanostructured metal-organic frameworks and their bio-related applications. *Coordination Chemistry Reviews* **2016**, *307*, 342-360.
169. Horcajada, P.; Serre, C.; Maurin, G.; Ramsahye, N. A.; Balas, F.; Vallet-Regi, M.; Sebban, M.; Taulelle, F.; Ferey, G., Flexible porous metal-organic frameworks for a controlled drug delivery. *Journal of the American Chemical Society* **2008**, *130* (21), 6774-6780.
170. Shankland, N.; Florence, A. J.; Cox, P. J.; Sheen, D. B.; Love, S. W.; Stewart, N. S.; Wilson, C. C., Crystal morphology of ibuprofen predicted from single-crystal pulsed neutron diffraction data. *Chemical Communications* **1996**, (7), 855-856.
171. Rossi, B.; Verrocchio, P.; Viliani, G.; Mancini, I.; Guella, G.; Rigo, E.; Scarduelli, G.; Mariotto, G., Vibrational properties of ibuprofen-cyclodextrin inclusion complexes investigated by Raman scattering and numerical simulation. *Journal of Raman Spectroscopy* **2009**, *40* (4), 453-458.
172. Mallick, S.; Pattnaik, S.; Swain, K.; De, P. K.; Saha, A.; Ghoshal, G.; Mondal, A., Formation of physically stable amorphous phase of ibuprofen by solid state milling with kaolin. *European Journal of Pharmaceutics and Biopharmaceutics* **2008**, *68* (2), 346-351.
173. Wiranidchamong, C.; Ruangpayungsak, N.; Suwattanasuk, P.; Shuwisitkul, D.; Tanvichien, S., Plasticizing effect of ibuprofen induced an alteration of drug released from Kollidon SR matrices produced by direct compression. *Drug Development and Industrial Pharmacy* **2015**, *41* (6), 1037-1046.
174. Pang, J. M.; Luan, Y. X.; Li, F. F.; Cai, X. Q.; Du, J. M.; Li, Z. H., Ibuprofen-loaded poly(lactic-co-glycolic acid) films for controlled drug release. *International Journal of Nanomedicine* **2011**, *6*, 659-665.
175. Bag, P. P.; Wang, D.; Chen, Z.; Cao, R., Outstanding drug loading capacity by water stable microporous MOF: a potential drug carrier. *Chemical Communications* **2016**, *52* (18), 3669-3672.
176. Pham, T.; Forrest, K. A.; Banerjee, R.; Orcajo, G.; Eckert, J.; Space, B., Understanding the H<sub>2</sub> Sorption Trends in the M-MOF-74 Series (M = Mg, Ni, Co, Zn). *Journal of Physical Chemistry C* **2015**, *119* (2), 1078-1090.
177. Erucar, I.; Keskin, S., Efficient Storage of Drug and Cosmetic Molecules in Biocompatible Metal Organic Frameworks: A Molecular Simulation Study. *Industrial & Engineering Chemistry Research* **2016**, *55* (7), 1929-1939.
178. Erucar, I.; Keskin, S., Computational investigation of metal organic frameworks for storage and delivery of anticancer drugs. *Journal of Materials Chemistry B* **2017**, *5* (35), 7342-7351.
179. Li, T.; Kozłowski, M. T.; Doud, E. A.; Blakely, M. N.; Rosi, N. L., Stepwise Ligand Exchange for the Preparation of a Family of Mesoporous MOFs. *Journal of the American Chemical Society* **2013**, *135* (32), 11688-11691.
180. Nguyen, B. T.; Nguyen, H. L.; Nguyen, T. C.; Cordova, K. E.; Furukawa, H., High Methanol Uptake Capacity in Two New Series of Metal-Organic Frameworks: Promising Materials for Adsorption-Driven Heat Pump Applications. *Chemistry of Materials* **2016**, *28* (17), 6243-6249.
181. 3 - Computational Techniques. **1999**, 91 - cp1.
182. Chakrabarti, P.; Dunitz, J. D., Structural Characteristics of the Carboxylic Amide Group. *Helvetica Chimica Acta* **1982**, *65* (5), 1555-1562.
183. Hamon, L.; Llewellyn, P. L.; Devic, T.; Ghoufi, A.; Clet, G.; Guillerm, V.; Pirngruber, G. D.; Maurin, G.; Serre, C.; Driver, G.; van Beek, W.; Jolimaître, E.; Vimont, A.; Daturi, M.; Ferey, G., Co-adsorption and Separation of CO<sub>2</sub>-CH<sub>4</sub> Mixtures in the Highly Flexible MIL-53(Cr) MOF. *Journal of the American Chemical Society* **2009**, *131* (47), 17490-17499.
184. Juillard, J.; Dimethylformamide- Purification, Tests for Purity and Physical-Properties. *Pure and Applied Chemistry* **1977**, *49* (6), 887-892.
185. Montis, R.; Hursthouse, M. B., Surprisingly complex supramolecular behaviour in the crystal structures of a family of mono-substituted salicylic acids. *Crystengcomm* **2012**, *14* (16), 5242-5254.
186. Uzarevic, K.; Ferdelji, N.; Mrla, T.; Julien, P. A.; Halasz, B.; Friscic, T.; Halasz, I., Enthalpy vs. friction: heat flow modelling of unexpected temperature profiles in mechanochemistry of metal-organic frameworks. *Chemical Science* **2018**, *9* (9), 2525-2532.
187. Strobridge, F. C.; Judas, N.; Friscic, T., A stepwise mechanism and the role of water in the liquid-assisted grinding synthesis of metal-organic materials. *Crystengcomm* **2010**, *12* (8), 2409-2418.

188. Jayasankar, A.; Somwangthanaroj, A.; Shao, Z. J.; Rodriguez-Hornedo, N., Cocrystal formation during cogrinding and storage is mediated by amorphous phase. *Pharmaceutical Research* **2006**, *23* (10), 2381-2392.
189. H-NMR chemical shifts chart. <https://www.chem.wisc.edu/areas/reich/nmr/05-hmr-02-delta.htm> (accessed 28th November 2019).
190. Du, S. F.; Ji, C. Q.; Xin, X. L.; Zhuang, M.; Yu, X. Y.; Lu, J. T.; Lu, Y. K.; Sun, D. F., Syntheses, structures and characteristics of four alkaline-earth metal-organic frameworks (MOFs) based on benzene-1,2,4,5-tetracarboxylic acid and its derivative ligand. *Journal of Molecular Structure* **2017**, *1130*, 565-572.
191. Dale, S. H.; Elsegood, M. R. J.; Kainth, S., Group 2 metal salts of pyromellitic acid:  $Mg(H_2O)_6(C_{10}H_4O_8)$  and  $Ba(C_{10}H_4O_8)(H_2O)_5$ . *Acta Crystallographica Section C-Crystal Structure Communications* **2003**, *59*, M505-M508.
192. Hu, M.-L.; Ng, S. W., Disodium dihydrogen 1,2,4,5-benzenetetracarboxylate dihydrate. *Acta Crystallographica Section E* **2002**, *58* (11), m616-m618.
193. Miyakubo, K.; Takeda, S.; Nakamura, N., Crystal-Structure of Potassium Hydrogen Terephthalate - Symmetrical Hydrogen-Bond in One-Dimensional Chain. *Bulletin of the Chemical Society of Japan* **1994**, *67* (8), 2301-2303.
194. Alzahrani, K. A. H.; Deeth, R. J., Molecular modeling of zinc paddlewheel molecular complexes and the pores of a flexible metal organic framework. *Journal of Molecular Modeling* **2016**, *22* (4), 13.
195. Abdolalian, P.; Morsali, A.; Makhloufi, G.; Janiak, C., Acid- and base-stable porous mechanically interlocked 2D metal-organic polyrotaxane for in situ organochlorine insecticide encapsulation, sensing and removal. *New Journal of Chemistry* **2018**, *42* (22), 18152-18158.
196. Tehrani, A. A.; Abbasi, H.; Esrafil, L.; Morsali, A., Urea-containing metal-organic frameworks for carbonyl compounds sensing. *Sensors and Actuators B-Chemical* **2018**, *256*, 706-710.
197. Abdolalian, P.; Morsali, A., Flexible and breathing metal-organic framework with high and selective carbon dioxide storage versus nitrogen. *Polyhedron* **2019**, *161*, 56-62.
198. Shustova, N. B.; Cozzolino, A. F.; Reineke, S.; Baldo, M.; Dinca, M., Selective Turn-On Ammonia Sensing Enabled by High-Temperature Fluorescence in Metal-Organic Frameworks with Open Metal Sites. *Journal of the American Chemical Society* **2013**, *135* (36), 13326-13329.
199. Howarth, A. J.; Peters, A. W.; Vermeulen, N. A.; Wang, T. C.; Hupp, J. T.; Farha, O. K., Best Practices for the Synthesis, Activation, and Characterization of Metal-Organic Frameworks. *Chemistry of Materials* **2017**, *29* (1), 26-39.